

Ultrasonic-Assisted Freezing of Micro-sized Water Droplets

Shaolei Gai

BSc (MechEng) (SAU); MSc (MechEng) (SAU)

A thesis submitted in fulfilment of the requirements for the degree of

Doctor of Philosophy



**Discipline of Chemical Engineering, School of Engineering,
The University of Newcastle, Australia**

August 2020

Statement of Originality

I hereby certify that the work embodied in the thesis is my own work, conducted under normal supervision.

The thesis contains no material which has been accepted, or is being examined, for the award of any other degree or diploma in any university or other tertiary institution and, to the best of my knowledge and belief, contains no material previously published or written by another person, except where due reference has been made. I give consent to the final version of my thesis being made available worldwide when deposited in the University's Digital Repository, subject to the provisions of the Copyright Act 1968 and any approved embargo.

Signature: **Shaolei Gai**

Acknowledgment of Authorship

I hereby certify that the work embodied in this thesis contains published paper/s/scholarly work of which I am a joint author. I have included as part of the thesis a written declaration endorsed in writing by my supervisor, attesting to my contribution to the joint publication/s/scholarly work.

By signing below I confirm that Shaolei Gai contributed to the papers/ publications entitled:

(1) “LBM modelling of supercooled water freezing with inclusion of the recalescence stage”

	Shaolei Gai contribution	Supervisory team contribution
Conception and design	75%	25%
Analysis and interpretation	70%	30%
Drafting and production	70%	30%

(2) “Ice nucleation of water droplet containing solid particles under weak ultrasonic vibration”

	Shaolei Gai contribution	Supervisory team contribution
Conception and design	75%	25%
Analysis and interpretation	70%	30%
Drafting and production	70%	30%

(3) *“A theoretical model for predicting homogeneous ice nucleation rate based on molecular kinetic energy distribution”*

	Shaolei Gai contribution	Supervisory team contribution
Conception and design	75%	25%
Analysis and interpretation	75%	25%
Drafting and production	75%	25%

(4) *“LBM study of ice nucleation induced by the collapse of cavitation bubbles”*

	Shaolei Gai contribution	Supervisory team contribution
Conception and design	75%	25%
Analysis and interpretation	75%	25%
Drafting and production	75%	25%

(5) *“Effect of ultrasonic vibration on the nucleation onset of temperature of micro-sized water droplets”*

	Shaolei Gai contribution	Supervisory team contribution
Conception and design	75%	25%
Analysis and interpretation	75%	25%
Drafting and production	75%	25%

Signature: Elham Doroodchi

Acknowledgements

I would like to acknowledge the financial support of the University of Newcastle and the genuine support of the people mentioned below who all contributed to the accomplishment of this thesis.

First and foremost, I would like to express my sincere gratitude to my principal supervisor, Associate Professor Elham Doroodchi, for her continuous support of my research and her patience, motivation and immense knowledge. Her invaluable guidance has assisted me immensely with my research and in my writing of this thesis. I could not imagine having a better mentor for my research studies. I also wish to thank my co-supervisors, Dr Zhengbiao Peng, Professor Behdad Moghtaderi and Professor Jianglong Yu, for their encouragement and insightful comments and questions. They gave me the incentive to approach my research from various perspectives. I especially wish to thank Professor Jianglong Yu for recommending me to my principal supervisor and for being responsible for a turning point in my career.

I would also like to thank Dr Khadijeh Paymooni for her training and guidance in doing experiments and her invaluable comments on my research. I would also like to thank my laboratory colleagues, Milan Barma and Mostafizur Rahman, for their help and insightful discussions. I would also like to give my special thanks to Jim Todhunter for his assistance in developing my experimental rigs.

I would also like to thank my good friends Dr Wei Xie, Dr Hui Song, Dr Fengkui Yin and Dr Soonho Lee for their immense help in both my life and studies.

I also wish to acknowledge the financial support by Australian Research Council (ARC) (Project ID: DP200102605).

Last, but not least, I wish to thank my all of my family, especially my wife Yunxin Bo, who have always cared for me during my overseas study. Without their support and encouragement, I would never have been able to complete my thesis.

Publications

Journal articles

1. **Shaolei Gai**, Zhengbiao Peng, Behdad Moghtaderi, Jianglong Yu, & Elham Doroodchi. (2020). LBM modelling of supercooled water freezing with inclusion of the recalescence stage. *International Journal of Heat and Mass Transfer*, 146, 118839. (Q1, IF:4.947)
2. **Shaolei Gai**, Zhengbiao Peng, Behdad Moghtaderi, Jianglong Yu, & Elham Doroodchi. (2020). Ice nucleation of water droplet containing solid particles under weak ultrasonic vibration. *Ultrasonics Sonochemistry*, 70, 105301. (Q1, IF:6.513)
3. **Shaolei Gai**, Zhengbiao Peng, Behdad Moghtaderi, Jianglong Yu, & Elham Doroodchi. (2020). A theoretical model for predicting homogeneous ice nucleation rate based on molecular kinetic energy distribution. *Journal of the Atmospheric Sciences*. (Under review)
4. **Shaolei Gai**, Zhengbiao Peng, Behdad Moghtaderi, Jianglong Yu, & Elham Doroodchi. (2020). LBM study of ice nucleation induced by the collapse of cavitation bubbles. *Ultrasonics Sonochemistry*. (Under review)
5. **Shaolei Gai**, Zhengbiao Peng, Behdad Moghtaderi, Jianglong Yu, & Elham Doroodchi. (2020). Experimental Study on the ultrasonic-assisted freezing of micro-sized water droplets. (In preparation)

Conference papers

1. **Shaolei Gai**, Zhengbiao Peng, Behdad Moghtaderi, Jianglong Yu, & Elham Doroodchi. (2018). Effect of ultrasonic vibration on the nucleation onset of temperature of micro-sized water droplets. *Chemeca 2018*, 234.

Abstract

This research is concerned with a combined theoretical, experimental and numerical study of the ultrasonic-assisted freezing of micro-sized water droplets. The main objectives of the study are to gain an improved understanding of ice nucleation and the freezing of micro-sized water droplets induced by the high pressures from acoustic cavitation, and the subsequent effects on the freezing temperatures of the droplets. This work is motivated by the need to develop effective approaches to generating engineered ice particles with uniform sizes and spherical shapes for a range of industrial applications, such as in air-conditioning systems, medical cooling, food storage, ice pigging, and the broader field of cold energy storage.

In this study, a theoretical framework was developed to describe the relationship between ice nucleation and pressure. Specifically, fundamental improvements were incorporated into the existing models to capture the transition of the ice-water interface using an approach based on the distribution of the molecular kinetic energy which, in turn, eliminated the need to specify the ice-water interface energy and activation energy typically required in conventional methods. A good agreement was obtained between the predictions of the model and the experimental data from the literature for temperatures down to 190 K, indicating that the model was able to capture all of the essential elements of the ice nucleation phenomenon using a simplified approach. With the measurable parameters as the inputs, including the enthalpy of fusion, the hydrogen-bond energy, the pressure-dependent melting temperatures and the pressure-dependent densities of the solids/liquids, this theoretical framework can be readily extended and applied to analyse the nucleation of other liquids with hydrogen-bonds.

The experimental work is focused on the adaptation of the classic ice nucleation triggering techniques, which are based on acoustic cavitation, to systems with confined volumes of water (i.e., micro-sized droplets). In particular, two mechanical triggering methods were developed. In the first method, the fine solid particles submerged in a droplet were used to provide free sites for the inception of cavitation bubbles. In the second method, cavitation bubbles were formed within a continuous medium carrying the suspended droplets. Both methods used acoustic vibrations to trigger the ice nucleation. In the first method, it was found that the fraction of the frozen droplets increased with an increase in the concentration of the particle numbers, the intensity of the vibrations and the vibration induction time. It was evident that the nucleation sites in this approach were limited to the regions between the solid particles and the vibrating substrate which, in turn, indicated that the contact pressures due to the collisions of the particles with the substrate greatly influenced the onset of the ice nucleation. In the second method, the fraction of the frozen droplets was also found to increase with an increase in the intensity of the vibrations and the vibration induction time. The experimental observations showed that the sites of the onset of the ice nucleation were on the droplet's surface, where strong interactions were encountered between the cavitation bubbles (formed in the continuous phase) and the droplets (in the dispersed phase). It was evident that the cavitation bubbles triggered the onset of the ice nucleation.

Numerical studies based on the lattice Boltzmann method (LBM) were carried out to gain a better understanding of the underlying mesoscale physics of the ice nucleation and freezing processes for the above approaches. Specifically, the study developed a model which coupled the conventional pseudo-potential multi-relaxation-time LBM (MRT-LBM) with a thermal LBM to investigate the dynamics of the cavitation bubbles, including their growth and collapse and the subsequent ice nucleation and freezing

processes. The thermal LBM was extended by: (i) the inclusion of the recalescence stage (rapid growth of dendritic ice); and (ii) the inclusion of a criterion for the pressure-dependent onset of the ice nucleation. In this model, the Stefan number was used to determine the initial ice fraction for the entire spectrum of the degrees of supercooling in the recalescence stage. The Simon-Glatzel equation was applied to correlate the ice melting curve with the local pressure field which, in turn, governed the onset of the ice nucleation. Both the data in the literature data and the experimental data collected as part of this study were used to validate the model. It was found that the deviations fell within the limits of experimental error.

The model was then used to gain insights into a number of phenomena, including: (i) the effects of the recalescence stage on the freezing process; (ii) the ice nucleation induced by the cavitation bubbles; (iii) the evolution of the pressures of the cavitation bubbles inside the crevices; and (iv) the evolution of the pressures on the surfaces of the droplets in the vicinity of the collapsing cavitation bubbles. The simulation results showed that the inclusion of the recalescence stage had a significant effect on the accuracy of predicting ice-water interface evolution for supercooling degrees greater than 20 K. Given that the freezing of a small droplet often bears a supercooling degree of more than 30 K, and the local supercooling degree could be significantly increased by the high pressures created by the collapse of the cavitation bubbles, therefore an accurate description of the freezing can be achieved only when the recalescence stage has been taken into account. Simulation results also captured the sudden rise in local temperature following the rapid (isentropic) process of cavitation bubble collapse. The local temperature rose significantly exceeded the ice melting temperature preventing the freezing process to proceed. These results suggest that maintaining a sufficiently large initial supercooling degree or use of additional mechanisms to force the ice crystals to migrate to the low-temperature regions

are essential to achieve complete freezing of water droplets. The collapse dynamics of the air bubbles trapped in the crevices on the surfaces of the solid particles was found to be sensitive to the morphological characteristics of the crevices, with the collapse of the bubbles in a hemispherical crevice generating the highest pressures. More importantly, the results provided a potential theoretical explanation on how the presence of solid particles assists with the initialisation of the ice nucleation in a droplet. Lastly, the simulation results showed that the onset of the ice nucleation on the surfaces of the droplets was strongly dependent on the distance between the bubble collapse point and the surface of the droplet. The simulation results were used to develop a correlation for predicting the minimum distance required to initiate ice nucleation in the droplet as a function of the key operating parameters, including the sizes of the cavitation bubbles and the amplitudes of the external pressures.

The effectiveness of the method of triggering the ice nucleation with the cavitation bubbles for continuous production of micro-sized ice particles dispersed in an immiscible liquid was examined experimentally. Specifically, the yield and quality of ice particles, in terms of the fractions of the frozen droplets, the distributions of the particle sizes and the roundness ratios of the ice particles, were examined as a function of the characteristics of the ultrasonic vibrations, namely the power output of the sonicator, the duty cycle of the vibrations and the offset distance of the sonicator probe. It was found that the production yield could be increased with increases in the power output of the sonicator, the duty cycle of the vibrations and the offset distance of the sonicator, but that it was decreased with a reduction in the temperature of the cooling module. However, the increase in the yield led to a loss of quality as the mean diameter of the water droplets used for producing the ice particles was in a range from 535 μm to 567 μm . After the ice nucleation using the cavitation bubbles, the mean diameters of the ice particles produced were measured in a

range from 450 μm to 590 μm . The freezing temperature achieved was as high as 269 K with a fraction of frozen droplets of 2% and a roundness ratio for the ice particles of 1. The highest fraction of frozen droplets was about 92% which was obtained at 262 K, whereas the roundness ratio of the ice particles decreased drastically to around 45%.

The results of the present study should prove useful in the application of the ultrasonic vibration-assisted nucleation of supercooled liquids in other fields, such as freezing of saline water droplets, solidification of molten metals, and freezing of biomaterials, in which the supercooling phenomenon is often encountered.

Table of Contents

Statement of Originality	i
Acknowledgment of Authorship	ii
Acknowledgements.....	iv
Publications.....	vi
Abstract.....	vii
Table of Contents.....	xii
List of Figures	xvii
List of Tables.....	xxv
Nomenclature.....	xxvi
Chapter 1. INTRODUCTION	1
1.1 Background.....	2
1.2 Aims and objectives	6
1.3 Thesis outline	7
Chapter 2. LITERATURE REVIEW	9
2.1 Introduction.....	10
2.2 Ice nucleation of water droplets.....	10
2.2.1 Homogeneous ice nucleation.....	10
2.2.2 Heterogeneous ice nucleation.....	14
2.2.2.1 Catalysts with an ice-like crystal structure.....	15
2.2.2.2 Electric fields	18
2.2.2.3 Magnetic fields.....	20

2.2.2.4 Structure of the contact surface.....	22
2.2.2.5 Acoustic cavitation bubbles.....	23
2.2.3 Ice nucleation in small water droplets	26
2.3 Mathematical models for cavitation bubbles	30
2.3.1 Theoretical background	31
2.3.1.1 Rayleigh-Plesset equation	31
2.3.1.2 Bubble thermodynamics.....	33
2.3.1.3 Equations of state	36
2.3.2 Numerical methods for the liquid-gas movable interface	37
2.3.2.1 Conventional methods.....	37
2.3.2.2 Lattice Boltzmann method	43
2.3.2.3 Comparison of numerical methods	48
2.3.3 Numerical study of cavitation bubbles.....	49
2.3.3.1 Cavitation bubble collapse in the neighbourhood of a solid wall	49
2.3.3.2 Bubble collapses near a soft boundary.....	53

Chapter 3. THEORETICAL MODEL FOR PRESSURE-DEPENDENT ICE

NUCLEATION	57
3.1 Introduction.....	58
3.2 Theory and mathematical models	60
3.2.1 Homogeneous ice nucleation.....	60
3.2.2 Pressure dependent homogeneous ice nucleation temperatures.....	64
3.2.3 Formation of ice germs.....	67
3.2.4 Homogeneous ice nucleation rate.....	73
3.3 Results and discussion	76
3.4 Conclusions.....	83

Chapter 4. EXPERIMENTAL STUDY OF THE ICE NUCLEATION OF WATER	
DROPLETS.....	85
4.1 Introduction.....	86
4.2 Ice nucleation assisted by the coupled effects of ultrasonic vibrations and solid particles.....	86
4.2.1 Experimental set-up.....	86
4.2.2 Materials.....	88
4.2.3 Experimental conditions and procedures.....	89
4.2.4 Results and discussion.....	90
4.3 Ice nucleation assisted by cavitation bubbles formed in the continuous medium.....	93
4.3.1 Experimental set-up.....	93
4.3.2 Material.....	95
4.3.3 Experimental conditions and procedures.....	96
4.3.4 Results and discussion.....	97
4.4 Chapter summary.....	103
Chapter 5. NUMERICAL STUDY OF ICE NUCLEATION INDUCED BY CAVITATION BUBBLES.....	106
5.1 Introduction.....	107
5.2 Development of a numerical model.....	107
5.2.1 Pseudo-potential MRT-LBM.....	108
5.2.2 Thermal field.....	111
5.2.3 Inclusion of the recalescence stage.....	113
5.2.4 Ice nucleation onset temperature under pressure.....	116
5.3 Model validation.....	117
5.3.1 Thermodynamic consistency.....	117

5.3.2 Free bubble growth and shrinkage	119
5.3.3 Evolution of the bubble profile in the neighbourhood of a solid boundary ..	122
5.3.4 Evolution of the ice-water interface	124
5.4 Numerical studies	126
5.4.1 Effects of the recalescence stage on the freezing process	126
5.4.1.1 Numerical modelling.....	128
5.4.1.2 Results and discussion	128
5.4.2 Ice nucleation induced by the collapse of cavitation bubbles	138
5.4.2.1 Numerical modelling.....	140
5.4.2.2 Results and discussion	143
5.4.3 Evolution of the pressures of the cavitation bubbles inside the crevice.....	157
5.4.3.1 Numerical modelling.....	158
5.4.3.2 Results and discussion	161
5.4.4 Evolution of the pressures on the surfaces of a droplet in the vicinity of a collapsing cavitation bubble	168
5.4.4.1 Numerical modelling.....	169
5.4.4.2 Results and discussion	170
5.5 Chapter summary.....	173
Chapter 6. EXPERIMENTAL STUDY ON THE CONTINUOUS PRODUCTION OF ICE PARTICLES	177
6.1 Introduction.....	178
6.2 Experimental study	178
6.2.1 Experimental conditions and procedures	178
6.2.2 Stability analysis of the experimental set-up.....	179
6.3 Results and discussion	183

6.3.1 Initial bubble formation and distribution of sizes.....	183
6.3.2 Influential parameters and the quality of the ice particles.....	185
6.3.3 Characterisation of the ice particles	192
6.4 Chapter summary.....	194
Chapter 7. CONCLUSIONS AND RECOMMENDATIONS	196
7.1 Conclusions.....	197
7.2 Recommendations for future work	203
References	206
Appendix A: Experimental set-up for recalescence stage analysis	230

List of Figures

Figure 2.1. Comparison between the classical nucleation theory and the experimental data. The dashed line is a theoretical estimation and the symbols are the experimental data. 13

Figure 2.2. Ice nucleation on the basal faces of silver iodide (AgI). Snapshots after $t = 3$ ps of: (a) the whole simulation box, and the adsorbed layers on the (b) Γ^- -terminated and (c) Ag^+ -terminated faces; (d) snapshot of the whole box; and (e) local density variations along z at $t = 160$ ns. The box contained 4914 water molecules and 960 ions in the AgI crystal [21]. 16

Figure 2.3. Microscopic images of induced ice nucleation at an electrode: (a) the cylindrical platinum electrode visible as a black silhouette, (b) a thin ice layer, developed at the electrode's front directly after the application of an electric pulse, (c) star-shaped ice dendrites growing out of the primary crystal [92]. 19

Figure 2.4. Sequence showing the onset of solidification induced by a cavitation bubble. The water temperature was 268.15 K and the bubble oscillated in the non-luminescing volume mode. The time interval between two consecutive frames was 1/30 s [119]. 24

Figure 2.5. Density as a function of temperature for isobars from 0 MPa to - 110 MPa. The solid part of the isobars is the measurements by Pallares et al. [120], and the dashed portion is an extrapolation. The solid black line gives the density of the ice. The red dots indicate the HoN temperature for each isobar for a nucleation rate coefficient of $10^8 \text{ cm}^{-3} \text{ s}^{-1}$ for the pressure of the isobar derived by shifting the melting curve by 307 MPa to a lower pressure. The black dot on the ice density line indicates the temperature above which cavitation instead of freezing is expected to occur to relax the exerted negative pressure [41]. 25

Figure 2.6. Schematic diagram depicting the temperature profile of a spherical bubble. 33

Figure 2.7. Discretisation of the bubble boundary and the interface between the liquid phase and the rigid boundary. 40

Figure 2.8. Schematic structure of the D2Q9 lattice and the discrete nodes and velocities. 45

Figure 2.9. (Colour online) Pressure distribution in the liquid during jet formation. The zone of high pressure on top of the bubble moves downwards jointly with the bubble [159].	51
Figure 2.10. The vector fields at different moments [207].	51
Figure 2.11. Velocity contours and vectors for a cavitation bubble interacting with a solid dirt particle [209].	53
Figure 2.12. Schematic representation of a single bubble near a membrane [212].	54
Figure 2.13. Interaction of a single bubble near a membrane [212].	55
Figure 2.14. Development of the toruses after a jet impact [213].	56
Figure 3.1. Schematic diagram of the control volume.	67
Figure 3.2. Control volume for describing the evolution of the size of an IG. The different transparencies of the contact layer indicate the different temperatures.	71
Figure 3.3. Evolution of the HoN temperature over a range of pressures.	77
Figure 3.4. Variations in the sizes and number concentrations of the IGs against the temperature: (a) sizes, (b) number concentrations.	78
Figure 3.5. HoN rates for supercooled water over temperature at the atmospheric pressure. Scattered data are the experimental data from the literature; the broken lines are the theoretical prediction results from the CNTs; the inset represents the nucleation rate with and without consideration of the thermal fluctuations in the transition.	80
Figure 3.6. HoN rates for supercooled water over a range of high pressures. Scattered data are the experimental data from the literature; black line and lines with symbols represent the predicted results using the present model; and the yellow dashed line is the results predicted using Jeffery and Austin’s theoretical model (1997) [216].	82
Figure 4.1. Schematic of the experimental set-up. WD-1 is a water droplet with glass beads and WD-2 is the reference droplet without any particles.	88
Figure 4.2. SEM images of particles: (a) scaled at 100 μm , and (b) scaled at 1 μm [D_p : 180 – 250 μm].	89
Figure 4.3. Evolution of the ice nucleation process under the coupled effects of the ultrasonic vibration field and particles: (a) $T_o = 268.15 \text{ K}$, $D_p: 90 - 150 \mu\text{m}$, $N_p: 5 -$	

10 particles/droplet; (b) $T_o = 271.15$ K, $D_p: 90 - 150$ μm , $N_p: 3$ particles/droplet. Scale bar: 100 μm	91
Figure 4.4. Fractions of the frozen droplets over the temperatures and number concentrations and sizes of the particles: (a) $E_v: 0.0011$ W/cm ² , droplet size: 0.8 mm, $t_v: 10$ s, $D_p: 180 - 250$ μm ; (b) $E_v: 0.0011$ W/cm ² , $N_p: 10-15$ particles/droplet, $t_v: 10$ s, droplet size: 0.8 mm.	92
Figure 4.5. Effects of the intensity of the ultrasonic vibrations on the fraction of the frozen droplets over the vibration induction time [$T_o = 269.15$ K, droplet size: 0.8 mm, $N_p: 10-15$ particle/droplet].....	93
Figure 4.6. Schematic diagram of the experimental set-up for ice nucleation in tubes assisted by ultrasonic vibrations.....	95
Figure 4.7. Ice nucleation of water droplets over temperatures without ultrasonic vibrations.....	98
Figure 4.8. Effects of the temperature and sonicator power output on the ice nucleation of water droplets [pre-existing bubble size: 0.2 mm].....	99
Figure 4.9. Effects of the pre-existing bubble sizes and vibration induction times on the ice nucleation of water droplets [$P_p = 15\%$, $T = 369.65$ K].....	100
Figure 4.10. Time sequences for the ice nucleation of water droplets triggered by cavitation bubbles [$P_p = 15\%$].....	102
Figure 4.11. Distribution of the ice nucleation onset sites induced by cavitation bubbles.	103
Figure 5.1. Thermodynamic consistencies: (a) comparison of the coexistence curve of the MRT-LBM with the Maxwell construction, (b) pressure differences between the liquid drop and the vapour phase as a function of $1/r$ at $T_o = 0.6T_c$	119
Figure 5.2. Comparison of the evolution of the sizes of the cavitation bubbles between the simulation results and the analytical solutions.	122
Figure 5.3. Comparison of the evolution of the bubble profiles between the simulation results and the experimental data: (a) experimental data, (b) LBM simulation results.	124
Figure 5.4. Schematic illustration of the computational domain.	124

Figure 5.5. Comparison between the experimental data and the simulation results considering the recalescence stage [$T_0 = 293$ K, $T_{cp} = 228$ K, $T_{nuc} = 239$ K and $d_t = 0.4$ mm].	126
Figure 5.6. Cooling time (t_{nuc}) required to reach T_{nuc} at different T_{cp} ($T_0 = 293$ K and $d_t = 0.4$ mm). The <i>Ste</i> method was used to calculate the initial ice fraction generated in the recalescence stage. The dots represent the experimental data; the dashed-line represents the fitting curve.	129
Figure 5.7. Time series of the ice-water interface captured in simulations and experiments ($T_0 = 293$ K, $T_{cp} = 228$ K, $T_{nuc} = 239$ K and $d_t = 0.4$ mm). At each time instant, the image on the left-hand side is the predicted result using the model without considering the recalescence stage; the image in the middle is the results predicted by the extended LBM using the <i>Ste</i> method for calculating the initial ice fraction generated in the recalescence stage; and the image on the right-hand side is the raw data captured in experiments.	131
Figure 5.8. Comparison between the experimental data and the simulation results, with and without consideration of the recalescence stage [$T_0 = 293$ K, $T_{cp} = 228$ K, $T_{nuc} = 239$ K and $d_t = 0.4$ mm].	133
Figure 5.9. Initial ice fractions predicted by the enthalpy method and the <i>Ste</i> method over a wide range of temperatures.	134
Figure 5.10. Comparison of the results predicted by the LBM model with and without consideration of the recalescence stage ($T_0 = 293$ K, $T_{cp} = 228$ K and $d_t = 0.4$ mm). The <i>Ste</i> method was used to calculate the initial ice fractions in the model considering the recalescence stage.	135
Figure 5.11. Evolution of the ice-water interface for different T_{cp} . [$T_0 = 293$ K, $T_{nuc} = 239$ K, and $d_t = 0.4$ mm; the <i>Ste</i> method was used to calculate the initial ice fractions generated in the recalescence stage; T1, T2 and T3 were $T_{cp} = 230$ K, $T_{cp} = 228$ K, and $T_{cp} = 226$ K, respectively].	137
Figure 5.12. Temperature field at $t = 0.19$ s for three different T_{cp} after the onset of the nucleation: (a) $T_{cp} = 230$ K, (b) $T_{cp} = 228$ K, and (c) $T_{cp} = 226$ K. The room	

temperature was set at 293 K, and the <i>Ste</i> method was used to calculate the initial ice fractions generated in the recalescence stage.....	137
Figure 5.13. Computational domains for simulations of the collapse of cavitation bubbles and ice nucleation: (i) near a solid boundary, and (ii) within a pressurised space.	141
Figure 5.14. Effects of k and σ on the spurious current.....	143
Figure 5.15. Effects of λ on p_{\max} [$\Delta p = 0.0027$, $T_0 = 0.4175T_c$, $R_0 = 80$].....	144
Figure 5.16. Effects of the initial Δp on p_{\max} and T [$\lambda = 2.5$, $T_0 = 0.4175T_c$, $R_0 = 80$].....	145
Figure 5.17. Effects of R_0 on p_{\max} [$\Delta p = 0.0027$, $T_0 = 0.4175T_c$, $\lambda = 2.5$].....	146
Figure 5.18. Pressure fields, temperature fields and distributions of the ice fractions before and after ice nucleation induced by the collapse of cavitation bubbles near a solid boundary [$T_0 = 0.4175T_c$, $\lambda = 3.5$, $\Delta p = 0.0027$ and $R_0 = 80$]: (a) pressure fields; (b) temperature fields; and (c) distributions of ice fractions.....	149
Figure 5.19. Effects of Δp on the p_{\max} , T_{high} and T_{low} of the cavitation bubble [$T_0 = 0.4175T_c$, $R_0 = 80$].....	151
Figure 5.20. Effects of R_0 on the p_{\max} [$T_0 = 0.4175T_c$, $\Delta p = 0.00176$].....	151
Figure 5.21. Pressure fields, temperature fields and distributions of the ice fractions before and after ice nucleation induced by the collapse of cavitation bubbles within a pressurised space [$T_0 = 0.4175T_c$, $\Delta p = 0.00176$ and $R_0 = 80$]: (a) pressure fields; (b) temperature fields; and (c) distributions of the ice fractions.....	153
Figure 5.22. Evolution of the T_{high} values and the corresponding T_{hom} values at the centre of the cavitation bubble upon ice nucleation [Dashed line represents the bulk water temperature].	154
Figure 5.23. Evolution of $f_{\text{ice-sum}}$ over time [1, 2 and 3 in the figure represent the three stages of the evolution of $f_{\text{ice-sum}}$]: (a) Scenario I [$R_0 = 80$, $\lambda = 2.5$ and $\Delta p = 0.00344$]; (b) Scenario II [$R_0 = 80$ and $\Delta p = 0.00176$].	156
Figure 5.24. Simplified basic structures of the asperity crevices on the rough surfaces of the particles [Grey colour represents the body of the particle; light blue colour represents the liquid film; black colour represents the solid substrate].	158

Figure 5.25. SEM images of glass beads in different groups [Scaled at 10 μm].	160
Figure 5.26. Effects of the asperity equivalent diameter on p_d [$E_v = 0.0011 \text{ W/cm}^2$].	160
Figure 5.27. Boundary conditions of the computational domain.	161
Figure 5.28. Effects of the height and width of the square-shape crevice on p_{max} at $p_d = 0.08 \text{ GPa}$: (a) height effect on p_{max} with width fixed at $0.80 \mu\text{m}$; (b) width effect on p_{max} with height fixed at $0.64 \mu\text{m}$ [i: primary collapse dominant; ii: transition from dominant primary collapse to dominant secondary collapse; iii: secondary collapse dominant].	163
Figure 5.29. Pressure fields for the collapse of a cavitation bubble in a square-shape crevice [$H_{\text{sq}}: 0.64 \mu\text{m}$, $W_{\text{sq}}: 0.8 \mu\text{m}$; pressure unit: GPa]. The primary collapse is circled by the red dashed line and the secondary collapse is circled by the solid red line.	163
Figure 5.30. Collapse of cavitation bubbles in the cone-shape crevice at $p_d = 0.08 \text{ GPa}$: (a) effects of the crevice height on p_{max} with width fixed at $0.8 \mu\text{m}$; (b) effects of the crevice radius on p_{max} with height fixed at $0.72 \mu\text{m}$.	164
Figure 5.31. Pressure fields for the collapse of a cavitation bubble in a cone-shape crevice [$R: 0.4 \mu\text{m}$; $H: 0.72 \mu\text{m}$; pressure unit: GPa].	165
Figure 5.32. Maximum collapse pressures of cavitation bubbles in the hemisphere-shape crevice: (a) effects of the crevice radius on p_{max} at $p_d = 0.05 \text{ GPa}$; (b) effects of p_d on p_{max} with crevice radius fixed at $0.4 \mu\text{m}$.	166
Figure 5.33. Pressure fields for the collapse of a cavitation bubble in a hemisphere-shape crevice [$R: 0.4 \mu\text{m}$; pressure unit: GPa].	167
Figure 5.34. Effects of the initial sizes of the cavitation bubbles of the collapsed spherical bubbles on the propagation of the collapse pressure over L_b .	171
Figure 5.35. Effects of the initial sizes of the cavitation bubbles of the collapsed non-spherical bubbles on the propagation of the collapse pressure over L_b .	172
Figure 5.36. Effects of the collapse pressure on the critical distance between the surface of the droplet and the collapse point of the cavitation bubbles.	172

Figure 6.1. Evolution of the driving pressure amplitudes over different distances from the sonicator probe [$V_{\text{duty}}=10\%$].	180
Figure 6.2. Effects of the water flowrate on the size distribution of the water droplets with $q_o = 11$ mL/h [$P_p = 0$].	181
Figure 6.3. Effects of the oil flowrate on the size distribution of the water droplets with $q_w = 0.2$ mL/h [$P_p = 0$].	182
Figure 6.4. Effects of the temperature of the ice nucleation module on the distribution of water droplet sizes [$P_p = 0$; $q_o = 12$ mL/h; b: $q_w = 0.5$ mL/h].	183
Figure 6.5. Formation of a cavitation bubble in a crevice without ultrasonic vibrations [$q_o = 12$ mL/h].	185
Figure 6.6. Effects of the flowrate on f_{ice} [$q_o:q_w = 12:0.36$; $P_p = 20\%$; $V_{\text{duty}} = 10\%$; $L_p = 0$ mm].	187
Figure 6.7. Effects of the flowrate on R_r [$q_o:q_w = 12:0.36$; $P_p = 20\%$; $V_{\text{duty}} = 10\%$; $L_p = 0$ mm].	187
Figure 6.8. Effects of the vibration intensity on the f_{ice} at different temperatures [$q_o:q_w = 12:0.36$; $V_{\text{duty}} = 10\%$, $L_p = 0$ mm].	188
Figure 6.9. Effects of the intensity of the ultrasonic vibrations on the R_r at different temperatures [$q_o:q_w = 12:0.36$; $V_{\text{duty}} = 10\%$, $L_p = 0$ mm].	189
Figure 6.10. Effects of the vibration duty cycle on the f_{ice} [$q_o:q_w = 12:0.36$; $L_p = 0$ mm].	190
Figure 6.11. Effects of the vibration duty cycle on the R_r [$q_o:q_w = 12:0.36$; $L_p = 0$ mm].	190
Figure 6.12. Effects of the offset distance of the sonicator probe on f_{ice} [$q_o:q_w = 12:0.36$; $P_p = 10\%$; $V_{\text{duty}} = 10\%$].	191
Figure 6.13. Effects of the offset distance of the sonicator probe on R_r [$q_o:q_w = 12:0.36$; $P_p = 10\%$; $V_{\text{duty}} = 10\%$].	192
Figure 6.14. Morphology of ice particles [scale bar: 0.4 mm].	193

Figure 6.15. Ice particle mean-diameter over temperature and water flowrate [$q_o = 12$ mL/h; $P_p = 10\%$; $V_{\text{duty}}=10\%$]..... 194

Figure 6.16. Recollection process by an ice particle of the small droplets [Time interval: 0.033 s; scale bar: 0.4 mm]. 194

List of Tables

Table 1.1. Comparison of some representative ice particle generators.	3
Table 2.1. List of ice nucleation catalysts.....	16
Table 2.2. Experimental data for the ice nucleation of small water droplets using different methods.	28
Table 3.1. Simon-Glatzel equation parameters for the melting curve of ices [231].....	65
Table 3.2. Parameters for the density equations of the ice and water [231].....	66
Table 4.1. Applied driving pressure varying against the power output of the sonicator.	89
Table 4.2. Physical properties of Fluoridrop 7500.	96
Table 5.1. Unit conversion table.....	117
Table 5.2. Unit conversion table.....	125

Nomenclature

Symbol	Description	Units
D_p	Solid particle diameter	μm
E_k	Molecular kinetic energy	J/mol
E_{ice}	Hydrogen bond energy	J/mol
E_v	Vibration intensity	W/cm^2
f_α	Discrete velocity distribution	-
f_{ice}	Fraction of frozen droplets	-
f_n	Net flux of water molecules that could potentially attach to the IG surface	-
ΔG	Free energy of critical ice nucleus formation	J/mol
Δg	Free energy of activation for the diffusion of water molecules across the ice-water interface	J/mol
h_i	Discrete temperature distribution	-
J_h	Homogeneous ice nucleation rate	$\text{cm}^{-3} \text{ s}^{-1}$
N_{ag}	Avogadro constant	-
N_c	Number concentration of IG	-
P_{EOS}	Reduced pressure from the equation of state	-
p_{max}	Maximum collapse pressure by a cavitation bubble	GPa
P_p	Sonicator power output	-
q_o	Oil flowrate	mL/h
q_w	Water flowrate	mL/h
R_r	Roundness ratio	-

R_{ig}	Initial IG radius	nm
T_{hom}	Homogeneous ice nucleation onset temperature	K
T_m	Melting temperature	K
T_{nuc}	Ice nucleation temperature	K
T_c	Cooling temperature	

Abbreviations

COP	Coefficient of performance	-
CNT	Classical nucleation theory	-
EoS	Equations of state	-
HoN	Homogeneous ice nucleation	-
HeN	Heterogeneous ice nucleation	-
HB	Hydrogen bonds	-
IG	Ice germ	-
LBM	Lattice Boltzmann Method	-
MRT	Multi-relaxation-time	-
MD	Molecular dynamic	-
MBD	Maxwell Boltzmann distribution	-
SCC	Specific chiller capacity	-
<i>Ste</i>	Stefan number	-

Greek Letters

$\tilde{\alpha}$	Thermal diffusivity	-
k	Boltzmann constant	J/K
λ	Standoff distance	-

$\Delta\mu$	Chemical-potential difference between ice and liquid water	J
$\sigma_{i/w}$	Ice-water interface tension	N/m
τ	Relaxiation time	-
φ	Water molecule fraction that can form HBs	-
\emptyset	Source term	-
<i>Subscripts</i>		
α	Discrete velocity direction	-
c	Concentration for N_c	-
cri	Critical value	-
hom	Homogeneous	-
i	Discrete velocity direction	-
inm	Ice nucleation module	-
max	Maximum value	-
nuc	Nucleation	-
<i>Superscripts</i>		
eq	Equilibrium	-

CHAPTER 1. INTRODUCTION

1.1 Background

As a kind of promising eco-friendly phase-changing medium, ice particles have been studied widely for decades, from their fundamental thermal properties to their practical applications [1]. Ice particles have been used worldwide in a range of fields in industry, including in air-conditioning systems, medical cooling, food storage, ice pigging, and the broader field of cold energy storage [2, 3].

In particular, ice particles are often used after mixing with a binary solution consisting of water and anti-freezing agent, i.e., in the form of ice slurry, which has proved to be a promising technique in a range of environmental and engineering sectors. The literature reports that the application of ice slurry could directly reduce the emissions of environment-negative-impact refrigerants like chlorofluorocarbons (CFCs) and hydrochlorofluorocarbons (HCFCs) up to a 90% [1]. Due to the large latent heat of fusion contained in the ice particles, which is up to 333.55 kJ/kg [1], the capacity to store huge amounts of cold energy makes the ice slurry able to shift peak electricity usage to an off-peak time by simply using off-peak electricity to generate ice slurry, thus realising an effective electricity management. In addition, unlike in traditional cold energy storage methods, such as ice-on-coil [4] which is normally in the form of chunk ice, ice particles could be directly pumped into pipelines [5-7]. As a consequence, the heat transfer coefficient between the ice particles and the pipes could be significantly increased, leading to a downsizing of the pipe and heat exchanger dimensions, which would drop the required pumping power and the operating costs [8]. Because of these traits, the application of ice particles in air-conditioning systems in large buildings could save up to 55% of the air conditioning electricity costs [9, 10].

Despite the worldwide applications, there is a high demand for engineered ice particles with uniform sizes and spherical shapes which aim to greatly improve their performance. To date, there have been a large number of ice particle generators that have been developed around the world, such as the scraped surface generator [11], orbiting rod generator [11], fluidised bed generator [12], supercooling generator [13], direct contact generator [14], and vacuum type generator [15] (as listed in Table 1.1). The generators are evaluated in Table 1.1 in terms of the ice particle size and shape, specific chiller capacity (SCC) and coefficient of performance (COP).

Table 1.1. Comparison of some representative ice particle generators.

Generator type	Scraped surface	Orbiting rod	Fluidised bed	Supercooling	Direct contact	Vacuum
Ice particle size (μm)	250 to 500	50 to 100	100 to 300	NA	1000 to 4000	500 to 1000
Ice particle shape	irregular	irregular	irregular	irregular	irregular	spherical
COP	≈ 4.5	≈ 3.0	NA	≈ 4.45	NA	≈ 8.0
SCC (kWm^{-3})	≈ 50	≈ 700	≈ 398	≈ 1500	≈ 1300	≈ 14
Supercooling (K)	10 to 19	10 to 8	10	3.65	5	NA
Coolant	R22, R404, R717	R22, R717, R134a	Potassium formate solution	R134a	FC-84	water
Reference	[11]	[11]	[12]	[13]	[14]	[15]

As shown in Table 1-1, all the current generators with the exception of the vacuum type generator produce ice particles with uniform sizes and shapes which leads to a dramatic decrease in the quality of the ice particles. For example, it has been reported that ice slurry with irregularly shaped ice particles has resulted in poor fluidity and easy agglomeration and clogging, even though the ice particle size was small [1]. Small and globular ice particles are usually used for easy pumping through tubes as well as in heat exchangers

[1]. The vacuum type generator can produce ice particles with uniform sizes and spherical shapes, and the coolant is the water itself. However, its low SCC ($\approx 14 \text{ kWm}^{-3}$) means it has a large footprint and its huge equipment cost and high maintenance requirements significantly limit its applications to only large factories.

In recent years, efforts have mainly been directed towards generating ice particles from micro-sized water droplets in order to enhance the quality of the ice particles in terms of creating uniform sizes and spherical shapes [1, 2, 16-18]. The well-established microfluidics can be applied to generate droplets with controlled sizes and shapes, and can greatly reduce the footprint of the generator through the mass integration of microfluidic channels. However, ice nucleation in micro-sized water droplets has proved challenging [19], and has often required a degree of supercooling greater than 30 K, leading to an increase in energy input and a reduction in the COP. Driven by this, the current research delves into the development of heterogeneous ice nucleation methods to bring up the freezing temperature of the micro-sized water droplets. Up to now, a variety of heterogeneous methods have been developed to increase the ice nucleation rate of small water droplets, including the freezing catalyst [20, 21], electro/magnetic field [22-24] and cavitation bubbles [25]. The electro/magnetic-based nucleation techniques, however, are still under study and require a deep understanding of the nucleation mechanism [26]. One commonly used active method for triggering ice nucleation is based on the addition of catalysts which have structures similar to the ice (ice-like) [27-30], such as silver iodide [31]. However, it is still challenging to achieve a relatively high freezing temperature for small water droplets [30]. Another promising approach to reducing the supercooling degree for ice nucleation is based on acoustic cavitation bubbles [32]. It has been reported

that the presence of cavitation bubbles could produce a nucleation onset temperature of close to 273.15 K [33-35].

Although laudable efforts have been directed to understanding the cavitation bubble induced ice nucleation experimentally [32, 36-38] and theoretically [39, 40], the underlying physics is still poorly understood. Many different theories have been proposed to describe the mechanisms of acoustic cavitation induced ice nucleation, including the high positive/negative pressure generated by the collapse of the cavitation bubbles [36] and the microstreaming of stable cavitation bubbles [38]. Based on Hickling's theory, the local positive high pressure generated (up to 10 GPa) could produce a very high supercooling degree which drives the instantaneous ice nucleation [32, 36, 37]. The high negative pressure requires a temperature of lower than 262 K [41], which cannot explain the experimental results with small degrees of supercooling. Although the microstreaming theory can be applied to explain some of the experimental observations, there are still contradictions and debates about the underlying phenomenon that drives heterogeneous ice nucleation with lower supercooling degrees [38]. Therefore, for vigorous collapses of cavitation bubbles, the theory based on the high positive pressure could be the primary ice nucleation mechanism, but further study is required for a quantitative evaluation, i.e., clarifying the relationship between the ice nucleation and the pressure. Other theories might also contribute to the initialisation of the ice nucleation, however significant further work is required to confirm and elucidate their contributions, which exceeds much beyond the scope of the current effort.

In addition, it is rather challenging to directly generate cavitation bubbles in a small water droplet due to insufficient cavitation inception sites, such as pre-existing bubbles and particles. Therefore, the development of effective approaches to applying the cavitation

bubbles to micro-sized water droplets are needed and must hinge on a deep understanding of the mechanisms of cavitation bubble induced ice nucleation. Moreover, numerical models are often adopted to examine the evolution of the pressure and temperature fields before and after the collapse of the cavitation bubbles. However, few of them have made further attempts to examine the cavitation bubble induced ice nucleation process as it requires the prediction of the local ice nucleation onset temperature. For an accurate prediction of the freezing dynamics after the onset of the ice nucleation, the ice solidification process also needs to be well understood, particularly the recalescence stage in the solidification process as its effects on the subsequent freezing process is not yet well understood.

1.2 Aims and objectives

The main aim of this research project is to successfully trigger the ice nucleation inside the micro-sized water droplets using acoustic vibration. To achieve this aim, a combined theoretical, experimental and numerical study is performed.

The principal objectives of the study are to:

- i. Theoretically establish the relationship between ice nucleation and pressure;
- ii. Experimentally understand the ice nucleation of water droplets induced by mechanical ice triggering methods;
- iii. Experimentally and numerically quantify the effect of recalescence stage on the prediction of the initial ice distribution and the subsequent freezing process;

- iv. Numerically obtain the evolution of the pressures and temperatures of the collapsing cavitation bubbles, and the subsequent ice nucleation triggered by the high pressures generated in the last stage of the collapse of the bubbles;
- v. Apply the fundamental knowledge gained in this work to generate micro-sized ice particles continuously.

1.3 Thesis outline

This thesis is organised into seven chapters, with each chapter containing one specific topic concerning the objectives of the research. A short outline of the chapters in this thesis is given below:

Chapter 1 provides an overview of the production and applications of engineered ice particles and provides a background to cavitation bubble induced ice nucleation.

Chapter 2 presents a thorough literature review of the various aspects of the project, such as the homogeneous and heterogeneous ice nucleation methods of water droplets, the mathematical models for cavitation bubbles, and the challenges which are faced in the course of this research.

Chapter 3 focuses on the development of a theoretical framework for pressure-dependent homogeneous ice nucleation.

Chapter 4 provides the experiments and discussions on the ice nucleation of water droplets assisted by ultrasonic vibrations, including the: (i) ice nucleation of water droplets assisted by the coupling of the ultrasonic vibrations and the solid particles; and (ii) ice nucleation of water droplets assisted by the cavitation bubbles in a continuous medium.

Chapter 5 is dedicated to the development of a numerical model to examine the dynamics of the cavitation bubbles, the onset of the ice nucleation and the freezing process.

Chapter 6 focuses on the experiments and discussion on continuous ice particle generation assisted by acoustic cavitation bubbles in a continuous medium.

Chapter 7 presents the key conclusions derived from this research study and provides a series of recommendations for future work in this area.

CHAPTER 2. LITERATURE REVIEW

2.1 Introduction

Based on the aims and objectives outlined in Chapter 1, this chapter presents a thorough literature review on two main subjects, namely the methods of ice nucleation for small water droplets, and the numerical models of the cavitation bubbles. The review begins with the current pathways of ice nucleation for water, including homogeneous ice nucleation (HoN) and heterogeneous ice nucleation (HeN). HeN consists of five main methods (ice nucleation catalyst, cavitation bubbles, electric field, magnetic field, and the structure of the contact surface) which is followed by the application of the HeN methods to the small water droplets. Amongst the HeN methods, the cavitation bubble method is superior to the others in the simplicity of its implementation, environment-friendliness and cost-effectiveness. Because of the small scale of the cavitation bubbles, experimental investigations of the pressure and temperature fields are rather difficult. Consequently, numerical models as useful tools which are usually adopted. Therefore, the literature on the cavitation bubbles numerical models is reviewed, including the theoretical background, numerical models for the liquid-gas movable interface, and the numerical studies on the physical problems related to cavitation bubbles.

2.2 Ice nucleation of water droplets

2.2.1 Homogeneous ice nucleation

If a water sample is ultra pure and not exposed to external excitations, it can be supercooled to a very low temperature (~ 235 K) and be maintained in this metastable state for a certain time before the onset of HoN. The HoN is triggered once a sufficient number of relatively long-lived hydrogen bonds are present at the same location to form a fairly compact initial ice germ (IG) and reach a stage that allows rapid crystal growth

[42]. The growth of an IG is described by the HoN rate, $J(T)$. In calculating the HoN rate at a given temperature, there are two factors which need to be considered: (i) the steady state IG size distribution calculated from the maximum formation energy; and (ii) the net flux of the water molecules that attach on the surface of the critical nucleus. Based on this, the classical nucleation theory (CNT) was adapted for HoN in supercooled liquid water [43-46], in which the assumed basic mechanism is that the small water clusters grow and decay by the absorption or emission of single molecules [46]. The steady-state nucleation rate is then given by:

$$J(T) = c_g \cdot f \cdot \Omega_g = \frac{NkT}{h} \exp\left(\frac{-(\Delta G + \Delta g)}{kT}\right) \quad (2.1)$$

c_g : the concentration of critical IGs per unit volume (mol/cm³);

f : the net flux of water molecules on the surface of the critical germ (mol/cm²·s);

Ω_g : the surface area of the critical IG (cm²/mol);

N : total number of water molecules in the system (-);

k : Boltzmann constant (J/K);

T : temperature in kelvins (K);

h : Planck constant (Js);

ΔG : free energy of the critical ice nucleus formation (J/mol);

Δg : free energy of the activation for the diffusion of water molecules across the ice-water interface (J/mol).

In a water system at a given temperature, ΔG and Δg are the only two factors needed to be determined. The free energy ΔG of the critical ice nucleus formation from n water molecules is given by:

$$\Delta G = \sigma_{i/w}A_n + n\Delta\mu \quad (2.2)$$

$\sigma_{i/w}$: ice-water interface tension (N/m);

A_n : surface area of the ice nucleus composed of n water molecules (m^2);

$\Delta\mu$: chemical-potential difference between the ice and liquid water (J);

n : the number of water molecules (-).

The chemical potential, $\Delta\mu$, is expressed as a function of the temperature [47]. However, the $\sigma_{i/w}$ is difficult to obtain experimentally due to the rapid freezing. The normal approach is to use either theoretically estimated values or fitted values from the experimental data, which inevitably causes deviations and depends largely on the kinetic model used [46]. In ice nucleation from supercooled liquid water, the diffusion of the water molecules across the ice-water interface is subject to an activation energy barrier, Δg [48], in which the molecule diffusion is under the force field created by the surrounding water molecules. The Δg can be obtained experimentally from the slope of the Arrhenius diagram for the temperature dependence of the self-diffusion constant of the liquid water. Different approaches to estimating the thermodynamic and kinetic parameters of the CNT are reviewed by Ickes et al. [49], as well as the sensitivity of the choice of parameters to the calculated nucleation rate.

HoN in supercooled water has been experimentally studied for many years [50-53], and this has provided sufficient nucleation rate data to check the validity of theoretical models. As shown in Figure 2.1, the ice nucleation rate, $J(T)$, represented by the scattered data, increases rapidly as it approaches $T = 228$ K and undergoes an ease in the increase for $T < 228$ K. The dozens of theoretical models proposed so far could well explain the experimental observations. For example, the CNT based nucleation model of Murray et

al. [45] could cover most of the experimental data points [30, 51, 53-56] and it can be seen that the $J(T)$ decreases by about 30 orders of magnitude, from 230 K to 245 K. It can be reasonably inferred that, at relatively high temperatures, the time required for freezing one micro-sized water droplet would be extremely long, hence one can only resort to lowering the temperature to increase the $J(T)$. However, such techniques are not favourable for practical applications due to the low COP incurred in producing the ice particles. Therefore, HeN methods have been intensely studied with the aim of increasing the ice nucleation rate at a relatively high temperature.

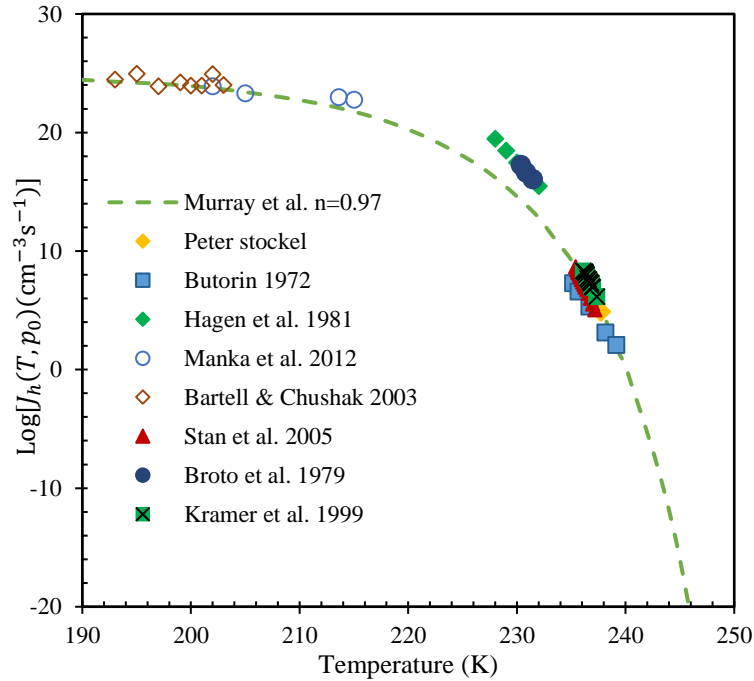


Figure 2.1. Comparison between the CNT and the experimental data. The dashed line is a theoretical estimation and the symbols are the experimental data.

According to Equation (2.1), the ΔG and Δg are the two main thermodynamic parameters controlling the $J(T)$. For HeN methods to take effect, efforts should be directed to ways of changing the ΔG and Δg . Taking ΔG for example, the expression

of Equation (2.1) indicates that, at a certain temperature, a potential approach to changing the free energy of the formation is to change the size of the IG. To change the size, solid particles with a crystal structure similar to ice are frequently used, such as mineral particles [57-59]. As previously mentioned, the diffusion of water molecules is heavily affected by the activation energy barrier exerted by the surrounding molecules, i.e., the transient water-water hydrogen bonds [46]. Therefore, for the water molecule to diffuse across the ice-water interface, the Δg could be greatly reduced by rearranging the local molecules. It is well known that a water molecule is composed of one oxygen atom and two hydrogen atoms. The hydrogen atom is slightly positively charged while the oxygen atom is slightly negative charged due to the large electronegativity of the oxygen atom, which makes the water molecule subject to the effects of electric or magnetic fields [60]. Other than efforts to change the ΔG and Δg , the changing of the freezing point and the subsequent supercooling is also of great interest to researchers. The variation of the freezing point is intimately related to the local pressure and is dominated by the density ratio between the ice and the liquid water. If the substance contracts during freezing in the presence of the Δp , the resulting work done by the Δp is stored as an increase in the latent heat [61]. The opposite happens if the substance expands during freezing. The experimental results have proved that the ice nucleation temperature increased at ultra-high pressures (> 1 GPa) [62], which has suggested a promising way of realising controlled ice nucleation by manipulating the local pressures. Based on the above discussions, the factors that can influence the $J(T)$ can be categorised into five different types: (i) catalysts with an ice-like crystal structure; (ii) cavitation bubbles; (iii) electric fields; (iv) magnetic fields; and (v) contact surface structure.

2.2.2 Heterogeneous ice nucleation

Almost all of the cases of water freezing on earth can be attributed to the onset of HeN. HeN is the result of the presence of alien particles or external stimuli. In order to increase the nucleation rate at high temperatures, there are a number of HeN methods which have been developed to break the metastable state of supercooled water. The methods which apply the aforementioned five major influencing factors are reviewed in the following sections.

2.2.2.1 Catalysts with an ice-like crystal structure

Materials with crystal structures similar to ice (ice Ih, space group: P63/mmc) which are immersed in or in contact with supercooled water could act as an ice nucleation catalyst. This was first discovered and confirmed by Vonnegut in 1947 [63] by using β -AgI as the nucleation catalyst. An ice-like bilayer of strongly adsorbed water molecules is first formed on the matching surface, which can be viewed as the surface of a stable ice nucleus. The ice nucleation then starts on top of this bilayer, as shown in the molecular dynamics simulation results for ice nucleation on AgI-like surfaces (see Figure 2.2). It can clearly be seen that the crystallography of the Ih ice lattice structure matches very well with the hexagonal surface of the AgI, and from where it rapidly grows. This molecular dynamic simulation also reveals that the ice formation prefers an Ag^+ -terminated face to other faces due to: (i) the close lattice match ($\sim 3\%$); and (ii) the strongly constrained molecule positions rendered by the strong interaction between the Ag^+ ions and the oxygens [21].

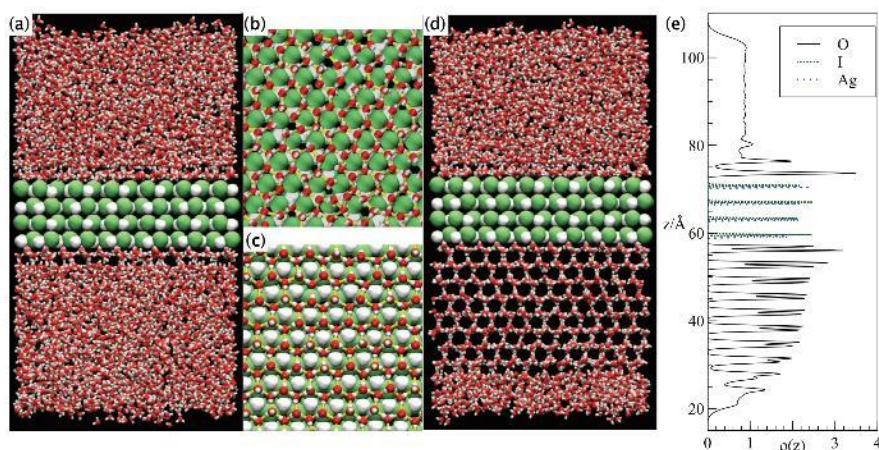


Figure 2.2. Ice nucleation on the basal faces of silver iodide (AgI). Snapshots after $t = 3$ ps of: (a) the whole simulation box, and the adsorbed layers on the (b) Γ -terminated and (c) Ag^+ -terminated faces; (d) snapshot of the whole box; and (e) local density variations along z at $t = 160$ ns. The box contained 4914 water molecules and 960 ions in the AgI crystal [21].

To date, a wide range of materials have been investigated and have shown their abilities to induce ice nucleation, such as carbonaceous particles [64], kaolinite particles [20], micas [65], and many other minerals [65-68] or biological particles [58, 69]. Some examples of these catalysts are listed in Table 2.1. The average nucleation onset temperature can reach as high as 272 K with F-phlogopite and 271 K with silver-iodide [65], which exemplify the success of using such ice-like materials as the catalyst for ice nucleation.

Table 2.1. List of ice nucleation catalysts.

Substances	Lattice parameter (a, b, c) Å	Ice nucleation onset temperature	^a Ref.	^b Ref.
Ice <i>Ih</i>	4.5, 4.5, 7.3	273.15 K	[70]	-
Fluorine Phlogopite	5.3, 9.2, 10.1	272 K	[71]	[65]
Silver Iodide	4.6, 4.6, 7.5	271 K	[72]	[65]

Muscovite	5.2, 9.0, 20.0	268 K	[73]	[65]
Pollen	-	264 K	-	[74]
Barium Fluoride	6.2, 6.2, 6.2	258 K	[75]	[76]
K-feldspar	8.6, 13.0, 7.2	250 K	[77]	[59]
Quartz	-	243 K	-	[59]
Kaolinite	5.2, 9.0, 7.4	241 K	[78]	[79]

^a References for lattice parameters; ^b References for ice nucleation onset temperatures

However, some authors have argued that the crystallographic match does not explain the kaolinite's ice nucleation abilities as the adsorbed water molecules do not always make ice-like structures [80, 81], rather the ice nucleation only takes place at some active sites. Edwards et al. [82, 83] suggested that, due to the non-uniform electrical properties of the surfaces of AgI, the ice nucleation sites are limited to those weakest adsorption points where the monolayer should be able to reorient for the crystal growth. Therefore, it can be expected that the modification of the electrical properties of the surfaces could significantly change the catalyst's nucleation abilities. For example, Curland et al. [84] designed polar crystalline ceramic pellets of AgI, and the experiment results showed that the positive pyroelectric charge on the silver-enriched side elevated the ice nucleation onset temperature. In contrast, the negative charge on the iodide side decreased the ice nucleation onset temperature.

The above discussion may suggest that, for an ice nucleation catalyst, a lattice match is not the only factor that influences the ice nucleation and that the surface electrical properties also play a key role [85]. The catalyst can be viewed as a stable existing IG in supercooled water. If the size of the catalyst goes over a critical value, the ice nucleation will be irreversible; while if the size is under a critical value, the nucleation will not start unless the temperature is low enough. Hence, for an ice nucleation catalyst to perform

well, the effects of the size need to be considered and investigated. In 1958, Fletcher [86] theoretically studied the effects of the sizes of alien particles (nuclei) with different surface properties. It was found that for most nuclei to have a significant effect, the particle diameter should be above 200 nm [86]. Welti et al. [87] experimentally investigated the effects of the sizes of four mineral particles on their ice formation (montmorillonite, kaolinite, illite and Arizona test dust), with diameters ranging from 100 nm to 800 nm. The experimental results showed that for the larger particles, the ice formation was more efficient, which corroborated the findings of Fletcher. Hence, the structure of the catalyst crystals and the particle size are of great importance in inducing ice nucleation.

2.2.2.2 Electric fields

As discussed in Section 2.2.2.1, ice nucleation could be significantly affected by the electric field. Due to the polar nature of water molecules, the electric field can realign the water molecules along the direction of the field and change the connections of the hydrogen bonds [60]. The electrofreezing phenomenon has been known since 1861 [88], however it was not until the mid-20th century that electrofreezing was used in the ice nucleation of water [89].

In applying electric fields for the ice nucleation, a pulsed or continuous DC electric field (10^5 V/m - 10^9 V/m) is applied to the water sample while the sample is continuously cooled down. Electrofreezing can be divided into two types according to the position of the electrode, i.e., the immersed electrodes and the external electrodes. Both types of electrodes can reach an increased ice nucleation temperature [90, 91]. Specifically, the ice nucleation temperature increases with an increase in the strength of the electric field.

For an immersed electrode, the ice nucleation occurs at the highly charged surface of the tip of the electrode, as shown in Figure 2.3.

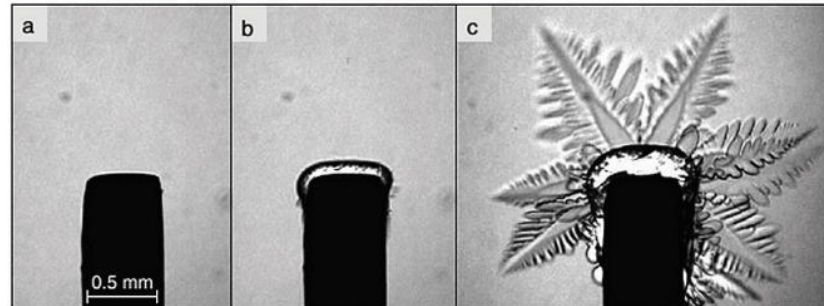


Figure 2.3. Microscopic images of induced ice nucleation at an electrode: (a) the cylindrical platinum electrode visible as a black silhouette, (b) a thin ice layer, developed at the electrode's front directly after the application of an electric pulse, (c) star-shaped ice dendrites growing out of the primary crystal [92].

Unlike the highly charged AgI which inhibits ice nucleation, the high strength of the electrostatic field is, obviously, in favour of ice nucleation. Generally, it is believed that spontaneous ice nucleation is caused due to the stronger bonds in the direction of the electric field [60] or the formation of an enhanced nucleus [90]. It has also been argued that, for immersed electrodes, the tiny bubbles formed through electrolysis also affect the nucleation [91]. However, the question arises if the electrodes are placed outside the water sample, i.e., the external electrode, what will happen? The ice nucleation experiments using an external electrostatic field carried out by Wei et al. [90] confirmed the same nucleating ability using an external electrostatic field. Apparently, it is only the electrostatic field that matters. However, it can be noticed that almost all of the electrofreezing cases are confined in a container or are in contact with a solid surface. Therefore, is it possible that the nucleation is caused by the interaction with the solid surface? In 1963, Pruppacher [93] suggested that the electrofreezing effect is the

consequence of the movements of the droplets in the electric field along the solid surface. To isolate the water from the solid surface, Rzesanke et al. [24] designed an experimental setup in which water droplets could fall freely through an experimental area where the droplet's surface could be highly charged equal to an electrostatic field ranging from 2×10^4 V/m to 2×10^5 V/m. In another approach by Stan et al. [94], the water droplets were carefully placed in a carrier fluid where the applied electric field was up to 1.6×10^5 V/m. However, the nucleation rates achieved by these authors did not show any evidence of being positively influenced by the static electric field [24, 94]. Interestingly, similar results were also obtained by using certain kinds of substrates [95-97], where the surface was planar with very low roughness. The experimental results of Zhang et al. [23] showed that with a relatively higher roughness, the ice nucleation temperature was relatively higher as well. Thus, this might imply that the surface roughness plays an important role in electrofreezing. When a rough surface is placed inbetween the water and the electric field, due to the electrostatic pull the water molecules tend to squeeze into small concaves on the rough surface, leading to a surge in the local pressure which can be high enough to induce ice nucleation. Without the roughness or a similar structure, the required electric field strength may reach $\sim 5 \times 10^9$ V/m, which has been confirmed by a molecular dynamic simulation [85].

2.2.2.3 Magnetic fields

Due to the diamagnetic property of water molecules, the application of magnetic fields have been shown to affect the physical properties of confined water [98], such as the melting point [99], the specific heat and the surface tension [100, 101]. Molecular dynamic and Monte Carlo simulations [102-104] have shown that the hydrogen bonds

can be affected by a magnetic field and, consequently, the networks of hydrogen bonds can be rearranged, weakened or strengthened. The magnetic fields applied are generally in the range of 0 T – 10 T [98]. To date, numerous experiments have been done to reproduce such effects on the process of ice nucleation, however no consistent results have been found.

Inaba et al. [99] measured the melting point of water in a magnetic field, which they found, and at 6 T the melting point increased by 5.6×10^{-3} K. Chang and Weng [104] also found that the number of hydrogen bonds increased by approximately 0.34% when the magnetic field was increased from 1 T to 10 T. Hence, it can be concluded that magnetic fields can strengthen hydrogen bonds. Zhang et al. [105] investigated the freezing of confined water exposed to a magnetic field of 10 T and found that a bilayer crystalline ice phase could be induced at 340 K. However, different molecular dynamic simulation results were reported by Hu et al. [106], who found that the effects of a magnetic field on hydrogen bonds are marginal, even at 10 T. However, experiments have demonstrated that the ice nucleation in large levitated water droplets can be triggered at 23 T [107], where the increase in nucleation temperature was minimum, or even negative, compared to the experiment done by Aleksandrov et al. [22]. In pinpointing the underlying ice nucleation mechanism with a magnetic field, caution is needed when carrying out experiments as suspended impurities can affect the results [108, 109]. Other than insoluble impurities, the air nanobubbles naturally present in water are believed to be the primary target of the magnetic field [110-112]. A magnetic field can cause the destabilisation of air nanobubbles by disturbing the ionic balance between the negative ions adsorbed on the bubbles and the shell of the counter ions. These changes to the bubble-water interface may lead to the modification of the size of the water cluster.

Obviously, the magnetic field can affect the ice nucleation to some extent, however how the magnetic field induces ice nucleation is not clear. Furthermore, it is essential to have a well-designed experiment that can be replicated and confirmed by different laboratories.

2.2.2.4 Structure of the contact surface

As discussed above, contact freezing normally occurs when the material has an ice-like crystal structure or an appropriate surface charge. The participants of the non-planar surfaces in contact freezing cases are of great importance, and have been poorly understood so far. According to molecular dynamic simulation results, the ice nucleation can be significantly enhanced by anatomically sharp, concave edges [113]. However, the enhancements found have only taken place at certain degrees, such as 110°, 75° and 45°, where the formation of special topological defects can be facilitated [113]. These critical geometrical conditions determine that the effects of the geometry of most common surfaces on the ice nucleation might be very little. This has been confirmed by the freezing of droplets on specially roughed substrates [114].

If non-planar surfaces work in conjunction with other active methods of ice nucleation, such as ultrasonic cavitation bubbles and electrostatic fields, their ability to increase the temperature of the ice nucleation can be augmented. It has been reported that placing the rough surfaces of a solid particle in an ultrasonic vibration field can considerably enhance the inception of cavitation bubbles[115], and that the cavitation bubbles are believed to be very efficient in ice nucleation [116, 117]. Likewise, in electrostatic fields, the surface roughness of a solid particle was also found to favour ice nucleation at relatively high temperatures [23]. Therefore, the special design or treatment of contact surfaces can be utilised to facilitate ice nucleation in certain circumstances.

2.2.2.5 Acoustic cavitation bubbles

The presence of acoustic cavitation bubbles in water has proved capable of greatly increasing the onset temperature of ice nucleation to close to 273.15 K [33, 34]. The acoustic cavitation phenomena can also be applied to control the ice nucleation and turn its stochastic behaviour into a repeatable event. However, the underlying physics has not yet been fully understood. To date, a number of theories on the phenomenon of ice nucleation which has been induced by cavitation bubbles have been proposed, including: (i) the high positive pressure [37]; (ii) the high negative pressure [41]; and (iii) the microstreaming [39].

According to Hickling's theory [36], the dramatic increase in the onset temperature of ice nucleation can be attributed to the increased equilibrium freezing temperature resulting from the positive pressure change. The pressure pulses generated by the collapse of ultrasonic cavitation bubbles have been reported to reach up to 10 GPa [32, 34]. Pecha and Gompf investigated the collapse of cavitation bubbles driven by two 20 kHz piezoelectric disks [118]. By analysing the last phase of the collapse captured by a streak camera, the relationship between the pressure amplitude of the shock wave and its velocity, v , can be formulated as [118]:

$$p = B \left[2 \frac{n-1}{n+1} \left(\frac{v}{c} - 1 \right) + 1 \right]^{2n/(n-1)} \quad (2.3)$$

where $B = 2750$ bar, $n = 7.44$ and $c = 1430$ m/s is the speed of the sound. Shock wave pressure values of up to 60 kbar can be reached at a driving pressure of 1.39 bar. It has been found that the ensuing pressure shock wave took effect instantly at the onset temperature of the ice nucleation [119] (see Figure 2.4).

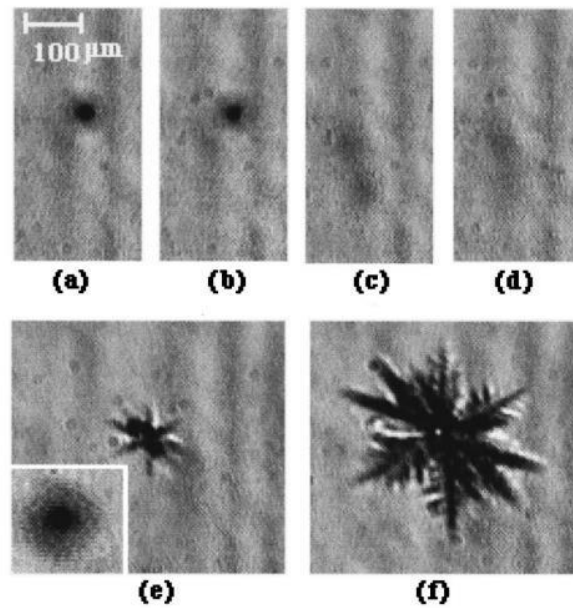


Figure 2.4. Sequence showing the onset of solidification induced by a cavitation bubble. The water temperature was 268.15 K and the bubble oscillated in the non-luminescing volume mode. The time interval between two consecutive frames was $1/30\text{ s}$ [119].

This theory appears to be qualitatively reasonable, but further study is required to dig deeper into the theory and to undertake a quantitative evaluation. However, there are still doubts over exactly where and when the nucleation starts during the collapse of the cavitation bubbles due to the lack of key experimental data. It has also been argued that a very high negative pressure followed by the high positive pressure after a collapse is also able to trigger local ice nucleation. Claudia Marcolli [41] investigated the effects of negative pressures on ice nucleation and found that increasing the negative pressure at temperatures below about 262 K eventually resulted in HoN, whereas at above 262 K negative pressure triggers cavitation rather than ice nucleation. As seen in Figure 2.5, the HoN temperature gradually shifts to the warmer side with an increase in the negative pressure.

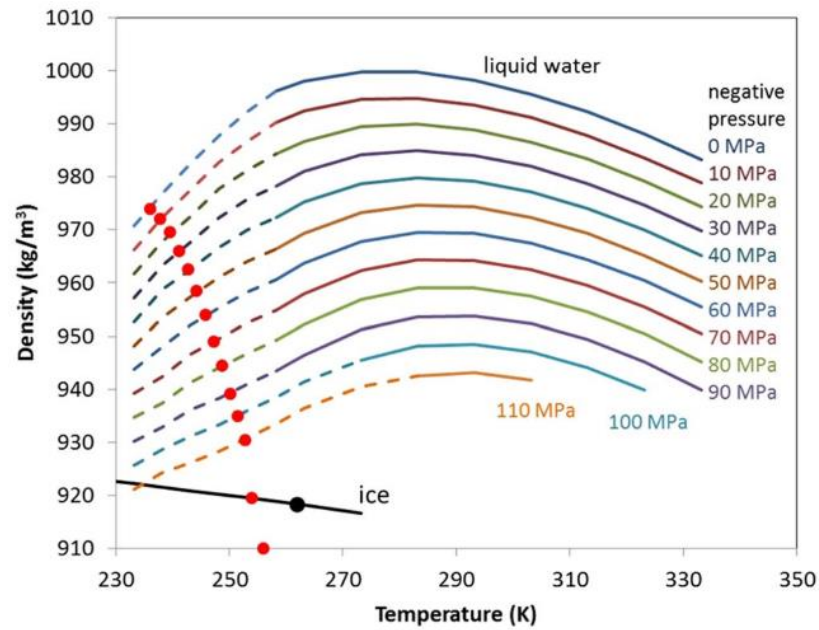


Figure 2.5. Density as a function of temperature for isobars from 0 MPa to - 110 MPa. The solid part of the isobars is the measurements by Pallares et al. [120], and the dashed portion is an extrapolation. The solid black line gives the density of the ice. The red dots indicate the HoN temperature for each isobar for a nucleation rate coefficient of $108 \text{ cm}^{-3} \text{ s}^{-1}$ for the pressure of the isobar derived by shifting the melting curve by 307 MPa to a lower pressure. The black dot on the ice density line indicates the temperature above which cavitation instead of freezing is expected to occur to relax the exerted negative pressure [41].

It has also been reported that ice nucleation can be triggered by stable bubble oscillation, i.e., the microstreaming (or flow streams) generated by the motion of stable cavitation bubbles [39]. Zhang et al. [38] examined ice nucleation in two types of water samples: (i) filtered deionised water, and (ii) supersaturated deionised water (by mechanically adding air bubbles). The microstreaming was captured by particle image velocimetry in both of the water samples, but it was only found to affect the ice nucleation in the sample of supersaturated deionised water.

Although the underlying mechanism has not been fully elucidated, it is clear that the ice nucleation rate is positively related to the cavitation bubbles that are generated at a given

time and volume [34]. Therefore, the ice nucleation hinges on the presence and population of the cavitation bubbles. The size of the cavitation bubbles as a function of the frequency and intensity of the vibrations has been elucidated by Brotchie et al. [121], who found that the bubble sizes decreased with an increase in the frequency of the vibrations, while the bubble sizes increased and then plateaued with an increase in the intensity of the vibrations. For natural water, it has been found that the generation of the cavitation bubbles can be greatly enhanced by dissolving gas in the water [116, 122]. To the contrary, if the water is degassed and placed in an ultrasonic field, it is rather difficult to get the cavitation bubbles to occur, thus leading to a delay in the ice nucleation [33]. Apart from dissolving gas, alien particles are also of great importance in boosting the generation of cavitation bubbles. Particles with hydrophobic and rough surfaces are thought to be very effective in providing the cavitation bubbles with active inception sites [123-125]. Both dissolved gas and alien particles are direct ways of reducing the tensile strength of water.

2.2.3 Ice nucleation in small water droplets

Small ice particles, particularly micro-sized ice particles, are useful in many ways, although producing them directly from water droplets is a great challenge. The various methods that have been employed in realising controlled ice nucleation in small water droplets, as well as a summary of the experimental data, are listed in Table 2.2 below. The application of catalysts for ice nucleation has proved effective in reducing the supercooling degrees of the small water droplets. However, due to the limited active sites contained on each particle of the catalyst [82, 83], the particles are required to be crushed into micro- or even nano-scale particles [126] to gain enough surface area. In such cases, Stan et al. [30] found that for water droplets of 80 μm , the most effective nucleation temperature for AgI particles is as high as 263 K. Considering that the smallest effective

particle size is around 1 μm [86, 87], the concentration of the catalyst particles added in each water droplet is inevitably high. The smaller the droplet, the higher the concentration of the catalyst. Moreover, the catalyst may be toxic, such as AgI [31], which has a silver ion which is among the most toxic of heavy metal ions. Hence, it is vital to make sure the concentration of the catalyst is lower than the harmful level. Further, during the production cycle of the ice particles, the added catalyst may end up as sediment. The accrued sediment may then block the tubing system and increase maintenance costs. Therefore, a conclusion can be drawn that the use of catalysts in ice nucleation is not suitable in terms of their toxicity and production costs.

There is a prominent use of electric fields in ice nucleation, where the nucleation ability is not restrained by the volume of the water and can avoid the shortcomings of catalysts. The operating range of the DC voltage strength in the electric field normally varies from 10^5 V/m to 10^7 V/m, which may exceed the dielectric breakdown strength of pure water [94]. The electric field can be imposed on water droplets either by placing the electrodes inside or outside the water samples. Regardless of which way is used, the nucleation temperature positively hinges on the electrostatic field strength. However, for the electric field to take effect, the prerequisite is that the water droplets must be in contact with a solid surface rather than suspended in another fluid because these suspended water droplets appear to be immune to the electrical field [24, 94], and may start merging due to the electrical field [127]. The biggest challenges for electrofreezing lie in how to maintain the spherical shapes of the water droplets on the solid surface during freezing and how to avoid the dielectric breakdown.

Table 2.2. Experimental data for the ice nucleation of small water droplets using different methods.

Methods applied	Condition	Generation mode	Droplet size (μm)	ΔT (K)	Ref.
Catalyst	Kaolinite: 1 wt%	batch	10 - 40	32.65	[79]
	Kaolinite: $\sim 10/\text{cm}^{-3}$	batch	60	6.0	[20]
	1-Nonadecanol: Monolayer	batch	60 - 96	~ 25	[126]
	AgI	continuous (in oil)	~ 100	10 - 19	[30]
	Pollen	continuous (in air)	~ 500	14	[128]
Electric field	Feldspar	batch	14 - 16	~ 22.65	[59]
	DC 4.2×10^5 V/m	batch	~ 1000	17 (30% freezing)	[23]
	DC 8.0×10^7 V/m	batch	~ 1000	~ 15	[129]
	AC 1.6×10^5 V/m (3-100 kHz)	continuous (in carrier fluid)	70	~ 36	[94]
	$\pm 2 \times 10^4$ C/m ²	continuous (in air)	70 - 100	~ 33	[24]
Magnetic field	DC 3.0×10^5 V/m	continuous (in air)	~ 2000	10 (60% freezing)	[130]
	0.5 T	batch	~ 5000	~ 0	[22]
Ultrasonic vibration	17.9 T	continuous (antifreezing liquid)	~ 6000	~ 10	[107]
	800 kHz, 0.15 W/m ²	batch	~ 1500	~ 16	[131]

Despite the contradictory results arising from the multiplicity of experimental conditions, magnetic fields do have the potential to induce ice nucleation [26]. As listed in Table 2.2, ice nucleation has been successfully triggered in relatively large water drops at a surprisingly low degree of supercooling, i.e., ~ 0 K [22], if not containerless [107]. It can be expected that it is also feasible to employ magnetic fields to nucleate micro-sized droplets, as it is believed that it is the increased density of the nuclei under the effects of the magnetic field that pulls the trigger [22]. It has also been reported that the presence of nanobubbles has been responsible for strengthened water clusters [110-112]. Hence, prior to producing water droplets, water samples should be filled with nano-scale air bubbles, which can be done either by air pumping or by water electrolysis. This approach seems promising, although further repeatable experiments are warranted to elucidate the nucleation mechanism of magnetic fields. However, the nucleation techniques which use electric and magnetic fields are still at the stage of laboratory investigations, and they require a deeper understanding of the nucleation mechanisms [26].

Another commonly used approach to inducing ice nucleation is employing ultrasonic cavitation bubbles. It has been found that using ultrasonic vibrations to induce ice nucleation is remarkable for bulk water [34, 116]. However, for micro-sized water droplets, using the ultrasonic cavitation method for ice nucleation has scarcely been reported on. In exploiting the high pressure generated by the collapse of cavitation bubbles, ultrasound waves with frequencies of 20 kHz to 40 kHz and vibration intensities of 0.1 to 0.5 W/cm² are typically used to form and collapse the cavitation bubbles. As discussed, the ice nucleation was attributed to the cavitation bubbles which tend to form at the antinodes along the waves [32]. Hence, if the droplet size is smaller than the wavelength, the cavitation bubbles are highly unlikely to be generated. This is

because cavitation in the water droplets is expected to be rather difficult due to the fewer number of impurities contained in such small-sized water droplets, such as pre-existing bubbles or hydrophobic particles [132]. The smaller the water droplet, the less impurities and the higher the tensile strength of the water [132]. One may resort to increasing the intensity of the vibrations, however, at such high driving pressures, the water droplets may break up and atomise [133]. Alternatively, high-frequency vibrations can be applied to increase the concentration of the cavitation bubble inside the droplets [131]. Under such conditions, the existing problems of the fast heating effect and the tendency for the emulsification [134] of the binary fluid (water droplets are usually carried by another immiscible fluid) make this approach less feasible.

Given the difficulties in the direct generation of cavitation bubbles inside the small water droplets, alternative methods are required to take advantage of the ultra-high pressure generated by the collapse of cavitation bubbles. To induce ice nucleation inside a water droplet, the cavitation bubbles could be: (i) generated outside the droplet (i.e., by generating cavitation bubbles inside the continuous medium), or (ii) introduced into the droplets through raw solid particles, where the tiny bubbles are attached onto the surfaces of the particles. In comparison to the other HeN methods, the cavitation bubbles method is superior to the others in the simplicity of its implementation, environmental friendliness and cost-effectiveness.

2.3 Mathematical models for cavitation bubbles

The phenomenon of cavitation is commonly encountered in natural and industrial processes [115, 135]. In theory, when the amplitude of the local pressure yields a tension that is equal to, or greater than, the tensile strength of the liquid, the cavitation occurs and

micro-sized bubbles are formed. As cavitation focuses the fluid flows down to microscopic scales and the bubbles concentrate the energy from the fluid during their shrinkage, the implosive collapse of the bubbles emits shock waves, resulting in severe damage to the surfaces of the material [115]. However, such well-known phenomenal features of cavitation bubbles have also been utilised to achieve many industrial outcomes, such as ultrasonic cleaning [136], sonochemistry [137] and shockwave therapy [138]. Remarkably, the ultrasonic collapse of cavitation bubbles has also been reported to successfully induce ice nucleation [25, 32, 34, 116]. Despite the laudable efforts conducted in the past decade [32, 34, 37], the physics underpinning the high efficiency of the ice nucleation triggered by the collapse of cavitation bubbles is yet to be fully understood, in particular the processes of the isentropic collapse of bubbles and the resultant ultra-high pressures and temperatures. Due to their small spatial and temporal scales, the direct measurement of the relevant quantities has proved extremely challenging (if not impossible) [139]. As a result, numerical approaches are often resorted to in order to gain insights into the underlying mechanisms that govern the processes of cavitation bubbles induced ice nucleation.

2.3.1 Theoretical background

2.3.1.1 Rayleigh-Plesset equation

The basic model for a spherical bubble was proposed by Lord Rayleigh in 1917 [140], which has the form of:

$$\rho R \ddot{R} + \frac{3}{2} \rho \dot{R}^2 + p_i - p_e \quad (2.4)$$

where ρ is the density of the liquid, R is the bubble radius, the overdot represents the differentiation with respect to time, and p_i and p_e are the internal and external pressures of the bubble, respectively, of which the difference drives the motion of the bubbles. The external driving pressures and the influence of the surface tension were later introduced into Equation (2.4) by Plesset and others [141-143]. Following Hilgenfeldt et al. [144], the Rayleigh-Plesset (R-P) equation is written as:

$$\rho_l \left(R\ddot{R} + \frac{3}{2}\dot{R}^2 \right) = p_b - p(t) - p_0 + \frac{R}{c_1} \frac{d}{dt} p_b - 4\eta_l \frac{\dot{R}}{R} - \frac{2\sigma}{R} \quad (2.5)$$

where p_b is the bubble pressure, $p(t)$ is the external driving pressure as a function of time, p_0 is the static pressure, c_1 is the sound velocity in the liquid, η_l is the viscosity of the liquid, and σ is the surface tension.

The standard R-P equation for spherical bubbles cannot reproduce rebound bubbles and shock waves as they require a noncondensable gas inside the bubble. This gas is assumed to be compressed and decompressed adiabatically [145]. Therefore, the bubble pressure is given as:

$$p_b = p_v + p_g \quad (2.6)$$

where the partial pressure, $p_g(t)$, of this noncondensable gas is given by [146]:

$$p_g(t) = p_{g0} \left(\frac{R_{\max}}{R} \right)^{3\gamma} \quad (2.7)$$

where p_{g0} is the pressure at the maximal initial bubble and γ is the adiabatic index.

To incorporate the shock wave, the R-P equation was extended to compressible liquids by Keller et al. [147] and can be written as [148]:

$$\ddot{R} = \frac{(p_g - \Delta p)(1 + \tilde{\nu}) + R\dot{p}_g/c - (3 - \tilde{\nu})\dot{R}^2 \rho/2}{(1 - \tilde{\nu})R\rho} \quad (2.8)$$

where $\tilde{\nu} \equiv \dot{R}(t)/c$. Tinguely et al. [145] suggested that the surface tension and viscosity could be neglected as they are insignificant in the last stage of the bubbles' collapse.

2.3.1.2 Bubble thermodynamics

Due to the evaporation and compression of the liquid, high temperatures occur on the bubble walls. A schematic diagram of the temperature profile of a spherical bubble is illustrated in Figure 2.6 below. The temperature distribution inside the bubble, T_{in} , is assumed to be spatially uniform, i.e., $T_{in} = T$, except for a thin boundary layer, $n\lambda$. λ is the mean free path of a gas molecule and n is a constant, having a value of between 0.95 and 7 [149]. The temperature distribution in this boundary layer is assumed to be:

$$T_{in} = T_w - \frac{\partial T_{in}}{\partial r} \Big|_{r=R} (r - R), \quad R - n\lambda \leq r \leq R \quad (2.9)$$

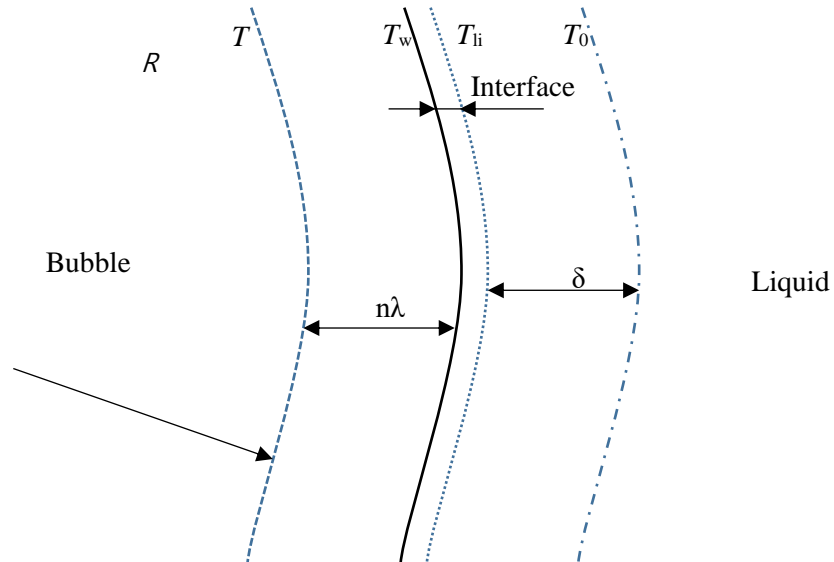


Figure 2.6. Schematic diagram depicting the temperature profile of a spherical bubble.

where T_w is the temperature of the walls of the bubble. According to the kinetic theory of gas, a temperature jump exists at the wall of a bubble [150-152]. Thus, T_w can be expressed as:

$$T_w = T_{li} + \Delta T \quad (2.10)$$

where T_{li} is the temperature of the liquid. ΔT is calculated by [149]:

$$\Delta T = -\frac{s}{2k} \sqrt{\frac{\pi m^*}{kT_w}} \frac{2 - a^* \alpha_e}{\alpha_e} \kappa \frac{T_w - T}{n} \quad (2.11)$$

where s is the cross-section of a molecule in the bubble, a^* is a constant, k is the Boltzmann constant and m^* is the mean mass of a molecule.

With a consideration of the effects of evaporation and condensation, the temperature inside a bubble is given as:

$$T_b = \frac{N_A^2 E V + (n_v + n_g)^2 a}{(n_v C_{s,v} + n_g C_{s,g}) N_A V} \quad (2.12)$$

where N_A is the Avogadro number, V is the volume of the bubble, E is the internal energy of the bubble, C_s is the heat capacity at a constant volume, n_v and n_g are the amounts of vapour molecules and gas molecules, respectively. The amount of the water vapour molecules, n_v , can be expressed as:

$$n_v(t + \Delta t) = n_v(t) + \frac{N_A}{M_v} 4\pi R^2 \dot{m} \Delta t \quad (2.13)$$

When a cavitation bubble grows or collapses, the volume change of the bubble is accompanied by changes in the mass of the vapour and the heat exchange. Hence, the thermal energy change of a bubble, ΔE , in time, Δt , can be expressed as:

$$\Delta E(t) = -p_b \Delta V(t) + \frac{N_A}{M_v} 4\pi R^2 \dot{m} e_v \Delta t + 4\pi R^2 \kappa \left. \frac{\partial T_m}{\partial r} \right|_{r=R} \Delta t \quad (2.14)$$

in which M_v is the molar mass of the water vapour and e_v is the energy carried by a vapour molecule, which is given as:

$$e_v = C_{s,v} T_w / N_A \quad (2.15)$$

The evaporation and condensation rate, \dot{m} , is calculated by [153]:

$$\dot{m} = \frac{\alpha_M}{\sqrt{2\pi R_v}} \left(\frac{p_v^*}{\sqrt{T_{li}}} - \frac{\Gamma p_v}{\sqrt{T_w}} \right) \quad (2.16)$$

where α_M is the accommodation coefficient for the evaporation or condensation, p_v is the actual vapour pressure, p_v^* is the saturated vapour pressure, R_v is the gas constant of the vapour and Γ is the correction factor.

For the simplicity of calculation, the temperature and pressure inside the bubble are assumed to be spatially uniform under the conditions and that the effects of inertia are negligible and that the velocity of the bubble wall is below the sound speed of the vapour/gas mixture [154]. Based on these assumptions, the bubble temperature can be simplified as:

$$T_b = T_\infty \left(\frac{R_{\max}}{R} \right)^{3(\gamma-1)} \quad (2.17)$$

where T_∞ is the temperature of the bulk liquid and R_{\max} is the maximum radius of the bubble.

2.3.1.3 Equations of state

The accurate description of the densities of the liquid and gas/vapour as a function of the temperature and pressure are vital to the prediction of the dynamics of the cavitation bubbles. Equations of state (EoS) attempt to describe the relationship between the temperature, pressure and density. For example, the van der Waals equation of state [155], which can be applied to obtain the pressure inside a bubble p_b :

$$p_b = \frac{R_g T}{v - b} - \frac{a}{v(v + b)} \quad (2.18)$$

where R_g is the gas constant, v is the molar volume and a and b are the van der Waals constants.

Upon the strong collapse of the bubbles, the co-volume should be included in the equation of state using the parameter β . This co-volume EoS can be described as:

$$R_{\text{spec}} T = p \left(\frac{1}{\rho_{gv}} - \frac{\beta}{\rho_n} \right) \quad (2.19)$$

where R_{spec} is the specific gas constant, ρ_{gv} is the density of the bubble, ρ_n is the equilibrium density of the bubble, and β is the co-volume dimensionalised with the molar volume at equilibrium. If it is assumed that the change in the state inside the bubble is adiabatic, then the above equation can be rewritten as:

$$p\left(\frac{1}{\rho_{gv}} - \frac{\beta}{\rho_n}\right)^\gamma = \text{const} \quad (2.20)$$

For the liquid, the Tait equation of state for water is used. The Tait equation includes nonlinear compressibility effects beyond the usual linear acoustics approximations for sound waves. This is a prerequisite to get the weak shock waves with a negative tension tail. The Tait equation can be expressed as [156]:

$$p_l(\rho) = (p_\infty - B) \left(\frac{\rho_l}{\rho_\infty}\right)^{n_T} - B \quad (2.21)$$

where p_∞ is the atmospheric pressure and ρ_∞ is the liquid equilibrium density. The values of the Tait exponent, n_T , and the Tait pressure, B , can be found in [156, 157].

2.3.2 Numerical methods for the liquid-gas movable interface

2.3.2.1 Conventional methods

2.3.2.1.1 Volume of fluid method

The the volume of fluid method was designed to capture the interface of two or more immiscible liquids based on the fluid volume fraction. The volume of fluid method has been successfully used in the investigation of bubble dynamics, including the evolution of the bubble profile, pressure shock, jet current and the temperature field [156-160]. The present research focuses on two-phase flows, namely the liquid and gas/vapour flows. The liquid is assumed to be incompressible, while the vapour bubble is compressible and conforms to the ideal gas law. The liquid and vapour are immiscible, and the mass transfer

between them is neglected [160]. The corresponding volume fraction function for the liquid phase can be written as [158]:

$$\alpha_l(\mathbf{x}, t) = \begin{cases} 1 & \text{liquid phase} \\ 0 < \alpha < 1 & \text{liquid - gas mixture} \\ 0 & \text{gas phase} \end{cases} \quad (2.22)$$

The volume fraction of the gas phase, α_g , is calculated by the following constraint:

$$\alpha_l + \alpha_g = 1 \quad (2.23)$$

The average density of the fluid, ρ , and the viscosity, μ , are calculated in each control volume by the following equations:

$$\rho = \rho_l \alpha_l + \rho_g \alpha_g \quad (2.24)$$

$$\mu = \mu_l \alpha_l + \mu_g \alpha_g \quad (2.25)$$

The evolution of the liquid-gas interface is updated by the volume of fluid equation:

$$\frac{\partial \alpha}{\partial t} + (\mathbf{v} \cdot \nabla) \alpha = 0 \quad (2.26)$$

where \mathbf{v} is the velocity of the fluid.

Once the α is obtained in each cell by the advection of the flow field, the interface can be reconstructed by different approximation schemes: the simple line interface calculation scheme [161], SOLA-VOF [162], the piecewise linear interface calculation scheme [163], and other higher-order differencing schemes.

2.3.2.1.2 Boundary integral method

The evolution of the cavitation bubbles feature in the large Reynolds numbers ($Re \sim 10^4$) [164, 165] associated with the motions of the bubbles and their short lifetimes in comparison to the viscous diffusion time. It is assumed that the liquid phase is inviscid, and that the motion of the bubbles is irrotational [166]. In addition, as the jet Mach number is larger than 0.1, accounting for about 0.1% of the lifetimes of the bubbles [164], hence the compressibility of the flow can be ignored. Therefore, the flow field of the liquid phase around the bubbles is governed by the Laplace equation. Hence, according to Green's integral formula, the velocity potential, ϕ , at any point in the domain can be expressed as:

$$c(p)\phi_p + \int_S \phi_q \frac{\partial}{\partial n} \left(\frac{1}{|p-q|} \right) ds = \int_S \frac{\partial}{\partial n} (\phi_q) \left(\frac{1}{|p-q|} \right) ds \quad (2.27)$$

where S denotes the boundary of the liquid phase, including the bubble boundary and the interface between the liquid phase and the rigid wall, p is any point in the liquid domain or on the boundary, q is any point on the boundary, and $\frac{\partial \phi}{\partial n}$ is the normal velocity of the bubble boundary. It should be noted that the discretisation of the rigid boundary is extended up to physical infinity, where the growth and collapse of the vapour bubbles have no considerable effect on the behaviour of the liquid domain. $c(p)$ is a coefficient depending on the location of the point p , and is given as:

$$c(p) = \begin{cases} 2\pi & \text{if } p \in S \\ 4\pi & \text{if } p \in \Omega \end{cases} \quad (2.28)$$

To numerically solve Equation (2.27), the bubble boundary is discretised by M cubic-spline elements, and the interface of the liquid domain with the rigid boundary is

discretised by N linear segments, as shown in Figure 2.7 below. The velocity potential and the normal derivative along each element are assumed to be constant and are in the middle of each element. Therefore Equation (2.27) is rewritten as:

$$c(p)\phi_i + \sum_{j=1}^N \phi_j \int_{S_i} \frac{\partial}{\partial n} \left(\frac{1}{|p_i - q_i|} \right) ds = \sum_{j=1}^N \frac{\partial}{\partial n} (\phi_j \int_S) \left(\frac{1}{|p_i - q_i|} \right) ds \quad (2.29)$$

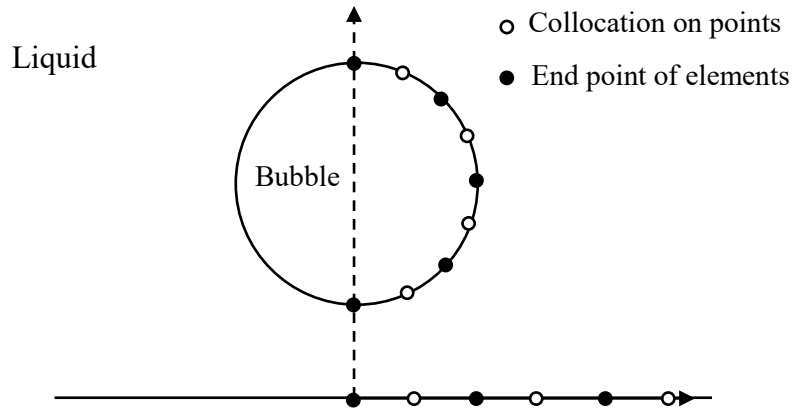


Figure 2.7. Discretisation of the bubble boundary and the interface between the liquid phase and the rigid boundary.

2.3.2.1.3 Level set method

The level set approach defines the interface of two fluids as a zero-level set of a smooth function. The level set function is the signed distance from the interface and can be simultaneously maintained. Hence, the interface can be implicitly tracked within a field which is interpolated with the finite element basis functions like any other state variable (e.g., pressure, velocity, temperature, etc.) [167]. The level set function is typically smooth, denoted as ψ , which eliminates the difficulties that conventional conservative schemes incur [167, 168].

The interface Γ' , namely the zero-level set of ψ , is given as:

$$\Gamma' = \{x | \psi(x, t) = 0\} \quad (2.30)$$

The level set function in the liquid phase is commonly set as positive values and is set as negative values in the gas phase. Thus, the level set function can be written as:

$$\psi(x, t) = \begin{cases} > 0 & x \in \text{liquid phase} \\ = 0 & x \in \Gamma' \\ < 0 & x \in \text{gas phase} \end{cases} \quad (2.31)$$

ψ is then initialised as the signed distance from the interface. The evolution of ψ with the moving interface can be obtained by a transport equation:

$$\frac{D\psi}{Dt} = \frac{\partial\psi}{\partial t} + \mathbf{u} \cdot \nabla\psi = 0 \quad (2.32)$$

The physical properties in each phase can be evaluated by:

$$\rho(\psi) = \rho_l H_\epsilon(\psi) + \rho_g (1 - H_\epsilon(\psi)) \quad (2.33)$$

$$\mu(\psi) = \mu_l H_\epsilon(\psi) + \mu_g (1 - H_\epsilon(\psi)) \quad (2.34)$$

where the smooth Heaviside function $H(\psi)$ [169] is defined as:

$$H_\epsilon(\psi) = \begin{cases} 0 & \psi < -\epsilon \\ \frac{1}{2} \left[1 + \frac{\psi}{\epsilon} + \frac{1}{\pi} \sin\left(\frac{\pi\psi}{\epsilon}\right) \right] & |\psi| \leq \epsilon \\ 1 & \psi > \epsilon \end{cases} \quad (2.35)$$

Unlike the exact Heaviside function, the 1/2 contour of the sharp Heaviside function $H(\psi)$ creates jagged or staircase contours on any discrete mesh of spacing [167]. However, by giving the interface a thickness of $\epsilon = \lambda\Delta x$, where $\lambda > 1$, the sharp changes across the interface are smoothed.

2.3.2.1.4 Moving particle semi-implicit method

The moving particle semi-implicit method was first proposed in 1996 by Koshizuka and Oka [170], based on smoothed-particle hydrodynamics. In the moving particle semi-implicit method, the liquid is described using moving particles, and for simplicity the bubble-liquid interface is set to be a vacuum pressure boundary without interfacial heat mass transfer. The continuity, Navier–Stokes and energy equations for incompressible viscous flows are:

$$\nabla \cdot \mathbf{u} = 0 \quad (2.36)$$

$$\rho \left(\frac{\partial \mathbf{u}}{\partial t} + (\mathbf{u} - \mathbf{u}^c) \cdot \nabla \mathbf{u} \right) = -\nabla p + \mu \nabla^2 \mathbf{u} + \sigma \kappa \cdot \mathbf{n} + \rho \mathbf{g} \quad (2.37)$$

$$\frac{\partial T}{\partial t} + (\mathbf{u} - \mathbf{u}^c) \cdot \nabla T = \alpha \nabla^2 T \quad (2.38)$$

where \mathbf{u} is the velocity of the fluid and \mathbf{u}^c represents the motion of a computing point which is adaptively configured during the calculation. An arbitrary calculation is allowed between the fully Lagrangian ($\mathbf{u}^c = \mathbf{u}$) and the Eulerian ($\mathbf{u}^c = \mathbf{0}$) calculations so that a sharp fluid front is calculated accurately by moving the computing points in Lagrangian coordinates while the computing point is fixed at the inlet and outlet boundaries.

The basic principle of the moving particle semi-implicit method is that the fluid is described using moving particles. The aforementioned governing equations are discretised using particle interaction models which include a gradient model, divergence model and Laplacian model, as shown below in Equations (2.39) – (2.41). Each particle only interacts with the surrounding particles in a limited region which is defined by the

weight function, as shown in Equation (2.42). The value of the effective radius, r_e , in Equation (2.42) usually varies from 2.0 to 3.0 times the local particle size [171].

Gradient model:

$$(\nabla\phi)_i = \frac{d}{n_i} \sum_{j \neq i} \left[\frac{\phi_j - \phi_i}{|\mathbf{r}_j - \mathbf{r}_i|^2} (\mathbf{r}_j - \mathbf{r}_i) w(|\mathbf{r}_j - \mathbf{r}_i|) \right] \quad (2.39)$$

Divergence model:

$$(\nabla \cdot \mathbf{u})_i = \frac{d}{n_i} \sum_{j \neq i} \left[\frac{(\mathbf{u}_j - \mathbf{u}_i) \cdot (\mathbf{r}_j - \mathbf{r}_i)}{|\mathbf{r}_j - \mathbf{r}_i|^2} w(|\mathbf{r}_j - \mathbf{r}_i|) \right] \quad (2.40)$$

Laplacian model:

$$(\nabla^2\phi)_i = \frac{2d}{\lambda n_i} \sum_{j \neq i} [(\phi_j - \phi_i) w(|\mathbf{r}_j - \mathbf{r}_i|)] \quad (2.41)$$

Weight function:

$$w(r) = \begin{cases} \frac{r_e}{r} - 1 & (0 \leq r \leq r_e) \\ 0 & (r_e \leq r) \end{cases} \quad (2.42)$$

2.3.2.2 Lattice Boltzmann method

The capability of the lattice Boltzmann method (LBM) to solve the Navier-Stokes equation started from a landmark paper published in 1986 by Frish et al. [172], which is commonly referred to as the ‘FHP model’. A triangular grid was used in the FHP model which restored some of the symmetry required to properly simulate the flows of fluids. Further modifications and extensions have been done to the FHP model since then. However, its inherent defects, such as the lack of Galilean invariance for fast flows and

statistical noise [173], have restrained more general applications. The statistical noise was completely eliminated by replacing the individual particles of the FHP model with an averaged, but still directionally discrete, distribution function. This breakthrough was made by McNamara and Zanetti in 1988 [174]. In 1992, Qian et al. [173] replaced the collision matrix developed by Higuera et al. [175] with single relaxation time, leading to the Bhatnagar, Gross and Krook (BGK) model. The BGK collision approximation treatment simplified the calculation of the Boltzmann equation to a great extent. From then on, the LBM underwent very fast growth.

The LBM is a mesoscopic numerical method based on statistical physics and can recover the Navier-Stokes equations at the macroscopic scale well [176]. In the LBM, a set of particle distribution functions are used in describing the density and velocity fields. The standard LBM with a force term based on the BGK model can be written as:

$$f_i(\mathbf{x} + \mathbf{e}_i \delta_t, t + \delta_t) = f_i(\mathbf{x}, t) - \frac{1}{\tau} [f_i(\mathbf{x}, t) - f_i^{eq}(\mathbf{x}, t)] + \delta_t \tilde{F}_i \quad (2.43)$$

where f_i is the particle distribution function, \tilde{F}_i is the forcing term and \mathbf{e}_i , \mathbf{x} , and t denote the discrete velocities, position and time, respectively. For a two-dimensional simulation case, the two-dimension and nine-velocity (D2Q9) lattice structure is illustrated below.

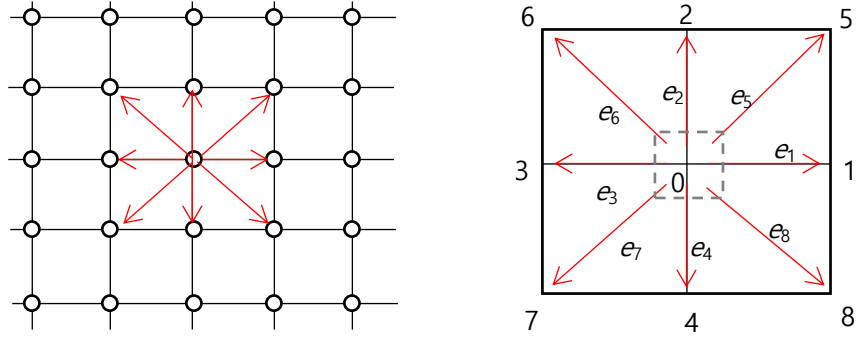


Figure 2.8. Schematic structure of the D2Q9 lattice and the discrete nodes and velocities.

The nine discrete velocities \mathbf{e}_i are expressed by:

$$\mathbf{e}_i = c \begin{bmatrix} 0 & 1 & 0 & -1 & 0 & 1 & -1 & -1 & 1 \\ 0 & 0 & 1 & 0 & -1 & 1 & 1 & -1 & -1 \end{bmatrix} \quad (2.44)$$

where $c = \delta_x/\delta_t$ is the lattice velocity, and δ_x is the lattice spacing.

In Equation (2.43), τ is the dimensionless relaxation time relating to the kinematic viscosity $\nu = c_s^2(\tau - 0.5)\delta_t$.

The equilibrium distribution function, f_i^{eq} , is described by:

$$f_i^{\text{eq}} = w_i \rho \left[1 + \frac{\mathbf{e}_i \cdot \mathbf{u}}{c_s^2} + \frac{(\mathbf{e}_i \cdot \mathbf{u})^2}{2c_s^4} - \frac{\mathbf{u}^2}{2c_s^2} \right] \quad (2.45)$$

where ρ , \mathbf{u} and T are the density, velocity and temperature, respectively. The isothermal sound velocity $c_s = \delta_x \sqrt{RT}/\delta_t$ with $RT = 1/3$. The weight coefficient, w_i , is set as: $w_i = 4/9$ ($i = 0$), $w_i = 1/9$ ($i = 1, 2, 3, 4$), $w_i = 1/36$ ($i = 5, 6, 7, 8$).

The local density of the fluid and the corresponding velocity of the flow are calculated by the following equations, respectively:

$$\rho = \sum_{i=0}^8 f_i \quad (2.46)$$

$$\mathbf{u} = \frac{1}{\rho} \left(\sum_{i=0}^8 f_i + \tau \mathbf{F} \right) \quad (2.47)$$

where \mathbf{F} is the total interaction force. Note that Equation (2.47) is called the direct velocity shift forcing scheme, which means using the forcing term, \tilde{F}_i , in Equation (2.43) can be neglected. Many different forcing schemes have been proposed to enhance the accuracy of the force implementation and numerical stability, such as the schemes of He et al. [177], Guo et al. [178], Wagner [179], and the MRT forcing scheme [180]. These forcing schemes have been critically reviewed by [181].

To date, a number of LBM-based multiphase multicomponent models have been developed, such as the colour-gradient model [182], the free-energy model [183], the interface tracking model [184] and the Shan-Chen model [185]. These models are briefly reviewed in the next section.

In the colour-gradient multicomponent model, one component is a red-coloured fluid and the other is blue-coloured, and each of the components needs one distribution function. Other than the common collision term in the LBM, there is also an extra collision term and it is followed by a re-colouring step. Grunau et al. [182] modified the model to deal with the components with different densities and viscosities. The pitfall of this model is that the spurious velocity is too high to ignore, which prohibits its application in cases with a high density ratio or a low capillary number. To deal with these disadvantages, a multiple relaxation time (MRT) was introduced into the model by Ahrenholz et al. in 2008 [186] and Huang et al. [187] also suggested a scheme to improve the model in 2013

which allows the model to be able to handle density ratios of the order of $O(10)$. One of the advantages of this model is that the interfacial tension and the viscosity ratio can be adjusted independently, which is important for multicomponent flows.

The thermodynamics issue of the non-monotonic EoS is incorporated into the pressure tensor in the N-S equations and the normal equilibrium distribution function was revised [188]. The original FE model was not Galilean invariant for the viscous term in the N-S equation. After redefining the stress tensor, the Galilean invariance was recovered to $O(u^2)$. In 2006, Zheng et al. [189] proposed an improved FE model, which was much simpler than the model of Inamuro et al. [190]. However, Zheng's model can only deal with density-matched cases, as indicated by Fakhari et al. [191]. In 2014, Shao et al. [192] improved Zheng's model by considering the local density variations, then the drawbacks of Zheng's model was successfully removed. The advantages of the FE LBM model are the low spurious currents and the independent adjusting of interfacial tension, viscosity and the density-ratio, and all of these make the FE LBM model promising for solving low Mach number flows and small capillary cases.

The interface-tracking model was first introduced in 1999 by He et al. [184]. This model uses two distribution functions and two corresponding LB equilibrium distribution functions. The Cahn-Hilliard interface tracking equation and the N-S equations can be recovered from the LBEs. Efforts are required to develop the interface-tracking based LBM models that can achieve a large density ratio.

An SC model can be used for solving single-component multiphase (SCMP) flow problems, and multi-component multiphase (MCMP) flows. In the SCMP model, the ideal gas equation state (EoS) in the single-phase LBM was replaced by a non-ideal non-

monotonic EoS [185] by incorporating a forcing term into the corresponding LB equation. In the MCMP SC model, each component has its own distribution function [193]. Due to the simple forcing term and high computing efficiency, the SC model has been widely used in various complex flows. However, the SC model could not adjust the surface tension and the ratio of densities independently, and the spurious currents are very high, and these drawbacks remain as obstacles in the way of further general use. Sbragaglia et al. [194] suggested a multi-range pseudo-potential form, the ratio of densities, and the surface tension could then be adjusted. In 2008, Shan [195] expanded the calculation of the pressure tensor with interactions beyond the nearest neighbours, which is able to eliminate the spurious currents.

2.3.2.3 Comparison of numerical methods

Conventional numerical methods are based on solving partial differential equations (PDE) [139]. In dealing with the two-phase flow, these methods need to couple with an interface tracking method such as volume of fluid and level-set methods [196] by additionally solving an equation of the phase-volume fraction, which further downgrades the computational efficiency [139, 197]. Alternatively, the LBM has emerged as a promising approach to simulating multiphase flow problems [176]. Compared to conventional computational fluid dynamics methods, the LBM has the advantages of simplicity, high efficiency and an easy implementation of boundary conditions. In the contexts of simulating gas-liquid flows, most importantly the LBM could automatically maintain the sharp interface, and an explicit interface tracking technique is not needed [198].

The LBM has become an increasingly efficient approach to solving a variety of complex fluid dynamics problems, particularly in the field of multiphysics. Compared with

classical flow solvers which discretise and solve the macroscopic Navier–Stokes equations on a continuum mechanics basis, the LBM tackles such problems on a mesoscopic scale and represents the fluid as a field of particle distribution functions. Particle motions are found by solving discrete Boltzmann equations. Nevertheless, the LBM essentially solves the same physics as the classical Navier–Stokes models. However, the LBM offers specific advantages regarding algorithmic operations and data locality. The efficiency and accuracy of the LBM method have been demonstrated in many publications. Moreover, the LBM is readily implemented in code programming and is inherently parallelizable, thus having the flexibility and capabilities to handle arbitrarily complex geometries and boundaries.

There are many LBM-based interface tracking methods, including the colour-gradient model [182], free-energy model [183], interface tracking model [184] and SC model [185]. Amongst these methods, the SC model is the most widely applied due to its simplicity, high efficiency and high flexibility. Another advantage of SC is that it works well with large density ratios [199], which cannot be conveniently treated by conventional interface tracking methods. In addition, the intrinsic high spurious current at the interface when using the SC model is significantly reduced by the MRT method [200]. Li et al. [201] further proposed an MRT forcing scheme that enables the SC model to achieve the thermodynamic consistency and numerical stability over a wide range of operating temperatures.

2.3.3 Numerical study of cavitation bubbles

2.3.3.1 Cavitation bubble collapse in the neighbourhood of a solid wall

The collapse of cavitation bubbles near a solid boundary has been a very hot research topic for decades due to its destructive action on the surfaces of materials such as ship propellers, turbine blades and the outlets of dams [202]. On the other hand, if well controlled, cavitation bubbles can also be used for surface cleaning [136] or ultrasonic lithotripsy [203]. The core of the collapse is the high pressure shock, high temperature and high jet current released in the last stage of the collapsing bubbles. When a cavitation bubble is formed near a solid boundary, it loses its initial spherical shape as the external pressure symmetry is destroyed by the presence of the solid surface. Consequently, a concave structure emerges on the top of the bubble interface (see Figure 2.9). The top interface keeps moving downwards as the pressure is higher than at the bottom interface. In the final stage of the collapse, the top interface severely strikes the bottom interface and hence penetrates the wall of the bubble. Thus, the bubble collapses and forms a high speed micro-jet (see Figure 2.10).

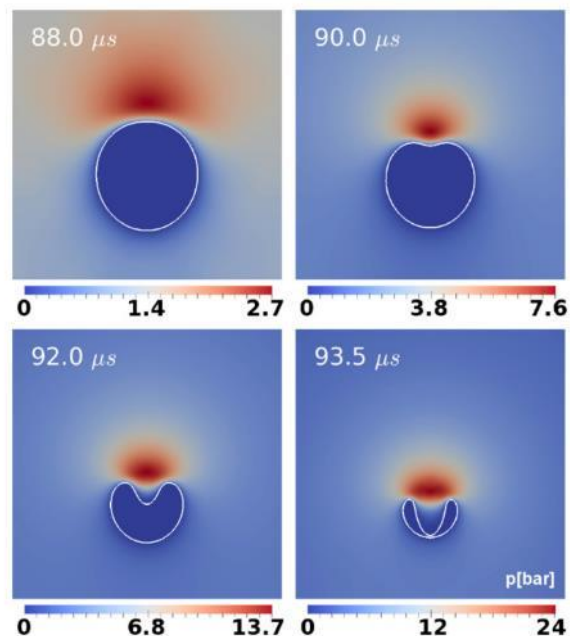


Figure 2.9. (Colour online) Pressure distribution in the liquid during jet formation. The zone of high pressure on top of the bubble moves downwards jointly with the bubble [156].

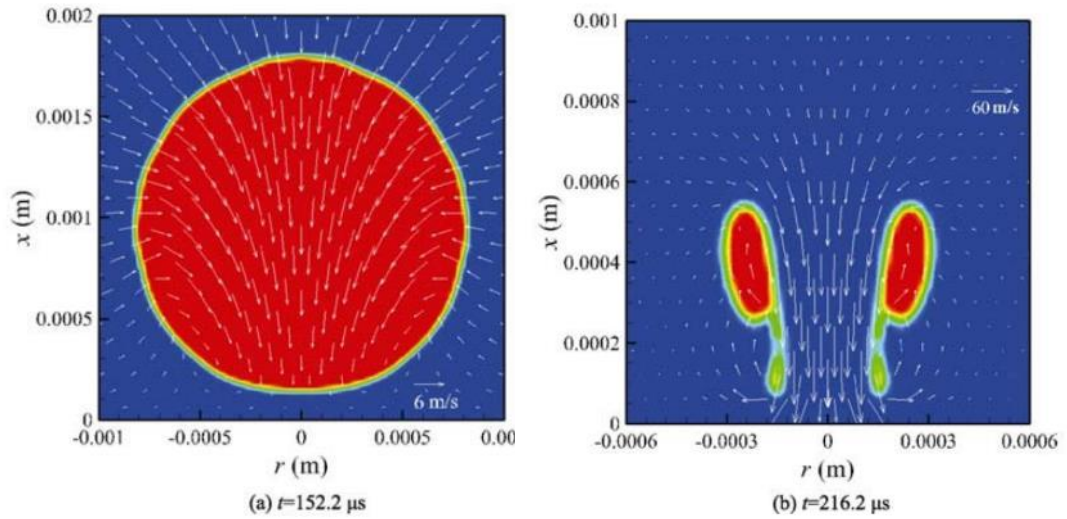


Figure 2.10. The vector fields at different moments [204].

The pressure, temperature and jet velocity of the collapse have been thoroughly examined and were found to be a function of the bubble standoff distance (λ) from the wall [139, 197, 205]. Yang et al. [139] found that the maximum temperature emerges at $\lambda \approx 2.4$ and increases with an increasing pressure difference between the bubble and the liquid. In addition, it was found that the smaller the standoff distance, the higher the temperature of the wall. For the jet velocity, Xue et al. [205] found that the highest jet velocity occurs at $\lambda \approx 2.4$ and increases with an increasing pressure difference as well. Liu et al. [204] investigated the effects of cavitation bubbles on the heat transfer near a heated wall. In the shrinkage stage, the surface heat transfer is enhanced due to the jet induced by the contraction of the bubbles. After the bubble has collapsed, the surface heat transfer coefficient inside the impinging area is significantly improved. However, in those regions far from the centre, the heat transfer is deteriorated because of the rotating flow. With an

increase of λ , the rate of heat transfer enhancement declines during the shrinkage stage. However, the heat transfer inside the deteriorated region is improved.

Ultrasonic cleaning is one of the most popular applications of cavitation bubbles. Despite the widespread use, the understanding of the physical phenomena involved is still limited due to the complexity and small scale of the process. In addition, the small spatial and fast temporal scales hinder a clear visualisation of the physical processes. Chahine et al. [206] systematically investigated the dynamics of the bubbles involved in the ultrasonic surface cleaning process and in the study the liquid-bubble interface was traced using the BIM. In addition, the numerical model for the rigid body is required in order to determine the torque, drag and lift forces imposed on the solid particles. The cavitation bubbles can generate suction and repulsion forces and pressure gradients that are strong enough to move the small particles toward or away from the bubbles depending on the original geometric configurations of the bubble/particle/wall. Bubble suction occurs mainly during the relatively slow bubble growth phase in particles very close to the bubble. In contrast, repulsion occurs during the highly inertial phases of the initial bubble growth and rebound and the collapse phase. In addition to the above, the formation and development of the bubble re-entrant jet is a strong source of much localised high shear which results in strong particle lifting from the surface, tumbling and repulsion away from the jet impact region at the wall (see Figure 2.11).

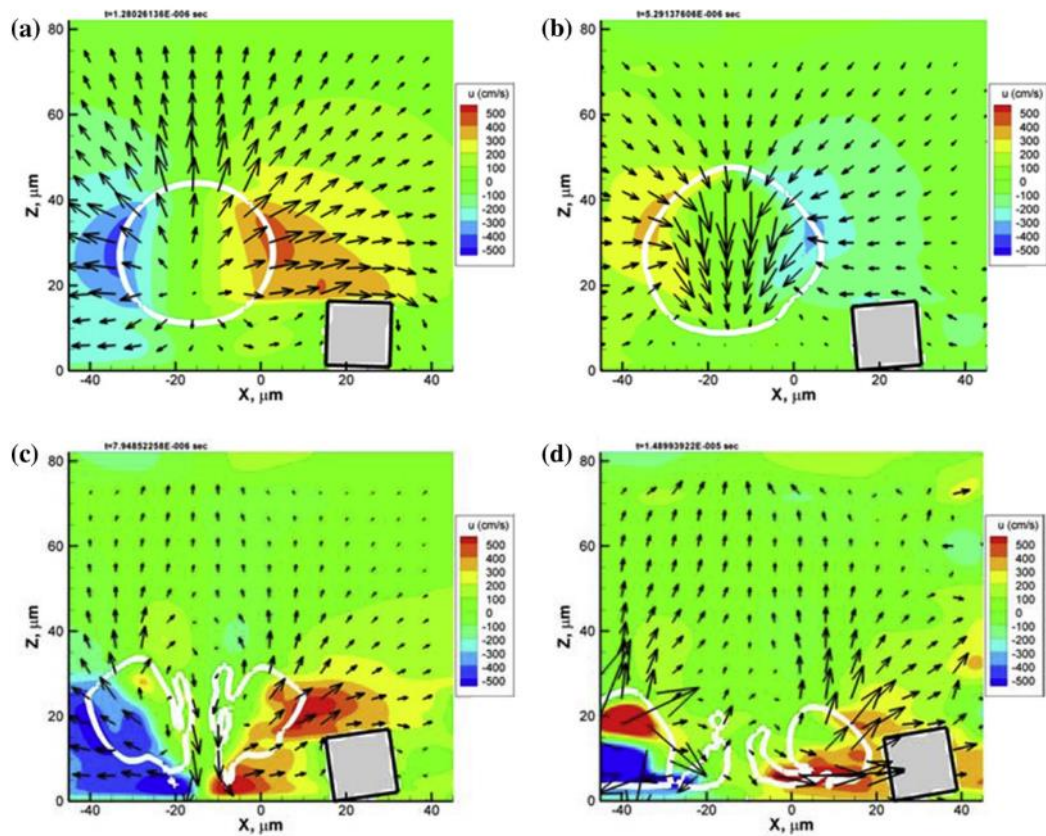


Figure 2.11. Velocity contours and vectors for a cavitation bubble interacting with a solid dirt particle [206].

2.3.3.2 Bubble collapses near a soft boundary

Cavitation bubbles can be found in medical applications, such as in laser treatments, high-intensity focused ultrasound and shock waves. The jets from the collapsing bubbles can be utilised for various purposes such as drug delivery or destroying tumour cells. Researchers have studied the dynamics of cavitation bubbles near biomaterials or tissues as thick elastic boundaries [207] or thin elastic boundaries [208]. A schematic representation of a bubble near the elastic boundary (membrane) is shown below in Figure 2.12. The bubble is in Fluid 1, and the elastic membrane is under the bubble at a distance

of H . The membrane between Fluid 1 and Fluid 2 is located initially at $z = 0$. The elevation of the membrane is denoted as $h(r,t)$.

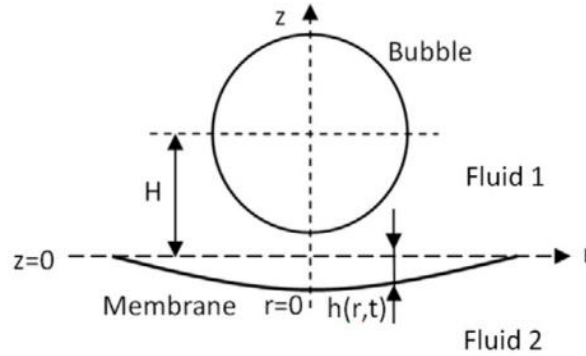


Figure 2.12. Schematic representation of a single bubble near a membrane [209].

Shervani-Tabar et al. [209] studied the collapse of an initially spherical bubble near an elastic membrane. As shown in Figure 2.13 below, a small bubble is generated at $t = 0 \mu s$ and expands spherically while the membrane is pushed downwards. The process of collapse begins when the bubble reaches its maximum size and the pressure inside the bubble becomes lower than that of the surrounding water. The membrane repulses back toward the bubble and transfers its momentum to the bubble in the form of a perturbation that propagates from the bottom to the top side of the surface of the bubble leading to the formation of a ‘mushroom’ shaped bubble in a necking form. Finally, the bubble splits into two smaller bubbles at the smallest volume.

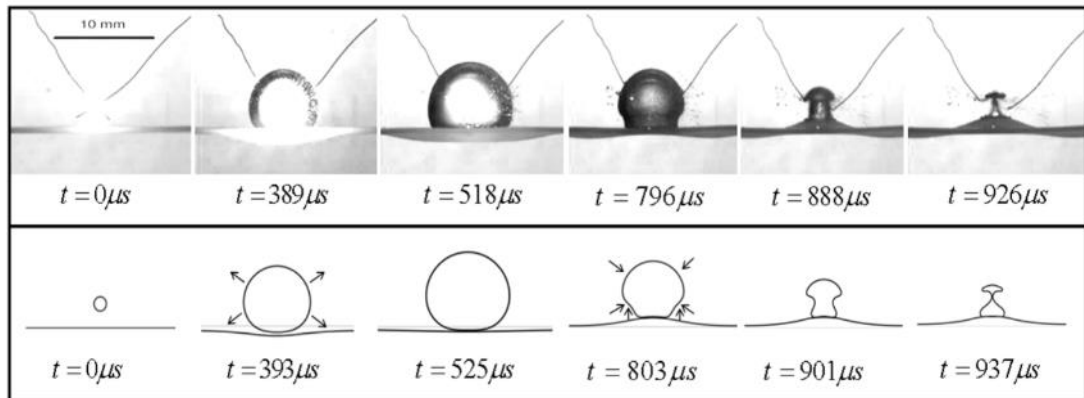


Figure 2.13. Interaction of a single bubble near a membrane [209].

Koukouvinis et al. [210] studied the evolution of a laser-generated cavitation bubble in the neighbourhood of a free surface (liquid-air interface). Similar to the cavitation bubbles near a solid wall or elastic membrane, a cavitation bubble near a free surface is also subjected to the destruction of the surrounding pressure field. An initially spherical bubble deforms due to the presence of the free surface, becoming an oval shape, then collapses. During the collapse a jet is formed at the top of the bubble which is directed towards the bottom of the container. After the jet impacts the bottom of the bubble, a gaseous pocket is formed (see Figure 2.14 (a) and (b)). The gaseous pocket then detaches from the initial bubble. After the initial bubble it has a toroidal structure (referenced to as Torus - 1) after it has been pierced by the jet. The authors also concluded that the effect of the surface tension is nearly unnoticeable, which is justified as the growth/collapse process for these bubble sizes is mainly inertially dominated.

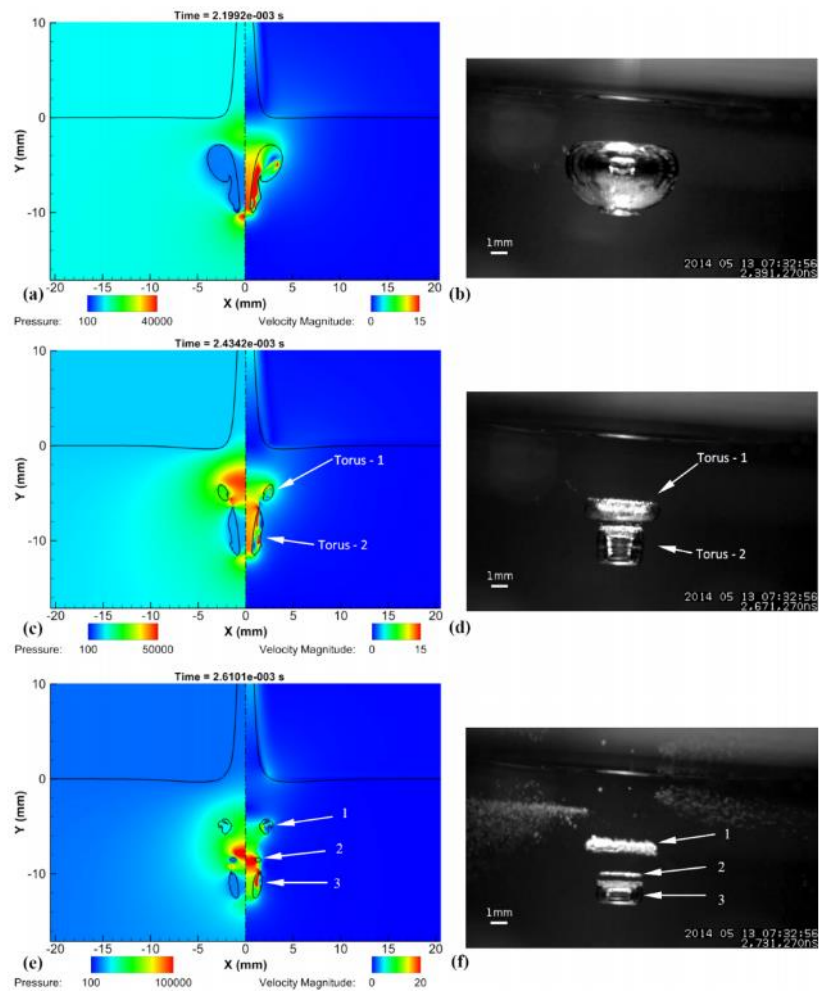


Figure 2.14. Development of the toruses after a jet impact [210].

**CHAPTER 3. THEORETICAL MODEL FOR
PRESSURE-DEPENDENT ICE NUCLEATION**

3.1 Introduction

According to the discussions in Section 2.2.2.5 of Chapter 2, the high positive pressure generated by the collapse of cavitation bubbles is believed to be the primary mechanism behind the cavitation bubble induced ice nucleation. To further elucidate this mechanism, in this chapter a theoretical model is developed based on the kinetic energy distribution of water molecules. Specifically, the pressure-dependent HoN temperature is obtained. The size distributions and concentrations of the IGs as functions of the temperature and pressure are calculated based on the thermodynamic equilibrium state of the IGs. Subsequently, a full expression of the HoN rates over the pressures and temperatures, including the supercooled regime ($T \in (273.15 \text{ K}, 232 \text{ K})$), transitional range ($T \in [232 \text{ K}, 227 \text{ K}]$) and No Man's Land ($T < 227 \text{ K}$), are formulated. The HoN rates predicted by the present model are compared against the experimental data and those predicted using the existing CNT with the internal pressure of the droplet considered.

Water, as one of the essentials of life, still has many uncertainties left unaddressed [211, 212]. In a supercooled state, amongst many abnormalities of water, it has been studied for decades, however, the underlying mechanisms that lead to the breaking of the supercooled state (or the onset of ice nucleation) have yet to be fully addressed [211]. Laudable efforts, using both theoretical [43, 44, 50] and experimental [30, 51, 54] approaches, have been directed towards comprehending the idealised HoN of supercooled water. The first theoretical estimation of the HoN rate was undertaken 70 years ago by Turnbull and Fischer [43] who proposed the CNT for supercooled water. Several improved versions of the CNT have subsequently emerged in the public domain which have been mainly focusing on elaborating the thermodynamic and kinetic properties of

water at temperatures lower than the melting point of water [49], e.g., the ice-water interface energy, $\sigma_{i/w}$, that determines the free energy, ΔG , of IG formation and the activation energy, Δg , required for water molecules to cross the ice-water interface. However, it has been well documented that the direct measurement of $\sigma_{i/w}$ and Δg in supercooled water are extremely difficult (if not impossible) due to the ultra-rapid freezing event [49].

Therefore, estimated values for $\sigma_{i/w}$ and Δg are still currently used, either through a theoretical derivation or an extrapolation from the fitting functions of the experimental data [46]. For instance, Pruppacher [44] estimated the activation energy, Δg , by fitting a series of experimental data from expanding cloud chambers and the observations at the cirrus cloud level for temperatures from 240.15 K down to 229.15 K. Jeffery and Austin [213] proposed a new analytic EoS for liquid water that is valid for pressures up to 3000 bars and temperatures up to 1200 K. The values for the latent heat, density of the liquid water and ice-water surface energy, $\sigma_{i/w}$, were inferred in order to estimate the HoN rates for large degrees of supercooling (up to 70 K).

However, significant discrepancies between the experimental data and the aforementioned CNT have been reported when the temperature decreases to the region of No Man's Land [54, 56]. Though the improved CNT developed by Murray et al. [45] and Huang and Bartell [50] have provided nucleation rates that partially match the experiment data in the No Man's Land, the deviation in the transition from the supercooled regime to the No Man's Land is too significant to ignore. The sensitivity of the predicted HoN rate to the input values of the $\sigma_{i/w}$ and Δg has been critically reviewed by Ickes et al. [49] who concluded that, depending on the value of the $\sigma_{i/w}$, the nucleation rate might differ

by more than $O(10^{25})$, whilst different values of Δg could lead to deviations of $O(10^{16})$. Evidently, the application of these estimated values results in uncertainties concerning the properties of the water which, in turn, might lead to completely erroneous predictions. Therefore, prior to the development of any new measuring technologies, it is vital to have a good understanding of the thermodynamics when water molecules are crossing the ice-water interface, and in particular the processes involved in the formation and decay of IGs.

According to the CNT, the growth of IGs is based on the diffusion of water molecules across the ice-water interface. However, studies by Langer et al. [214], Ohsaka and Trinh [215] and Shibkov et al. [216] have revealed that the measured velocities of the dendritic ice tip fall below the diffusion-based theoretical curve when the supercooling is greater than 4 K. In understanding this discrepancy between the theoretical predictions and the experimental measurements, Shibkov et al. [216] found that for cases with a large supercooling (i.e., > 4 K), there is a crossover from diffusion-limited to kinetics-limited growth at the ice-water interface. These findings have an analytical appeal in that the attachment of the water molecules to the ice crystals is determined by the kinetic energy of the water molecules which is transmitted across the interface through the rapid collisions of the molecules.

3.2 Theory and mathematical models

3.2.1 Homogeneous ice nucleation

The ice nucleation process relies on the continuous formation of hydrogen bonds (HBs). However, the formation of a HB leads to a decrease in entropy, which inevitably forms

an energy barrier to the ice nucleation. This energy barrier corresponds to the change in the Gibbs energy (ΔG) and is calculated by the chemical potential difference between the two species, i.e., the ice and water [49]. This energy barrier must be overcome when forming a HB in the liquid phase. Conventionally, the calculation of chemical potential is based on the equilibrium vapour pressures of ice and water [49], however, the use of macroscopic quantities for the microscopic IGs means that the bulk chemical potential applied to the IGs might fail [46]. In addressing this problem, the chemical potential needs to be redefined so as to correlate the microscopic quantities.

It has been reported that when the temperature reduces at the onset of HoN, the ice nuclei form faster than the liquid water can compensate [211]. This critically implies that when approaching the onset of HoN, the state of the supercooled water strongly hinges on the relationship between the kinetic energy of the water molecules and the total number of HBs. In liquid water, HBs are abundantly present in water and their number increases as the temperature is lowered [217]. However, the lifetime of the HBs is finite as the local HBs are known to be fleetingly forming and breaking [218]. The energy required for completely separating two bonded molecules is about 23.3 kJ mol^{-1} [219], equalling about half the enthalpy of vaporisation. Just breaking the HBs in liquid water to leave the molecules essentially at the same position and retaining the electrostatic attraction, requires much less energy, which has been estimated to be 6.28 kJ mol^{-1} [220] and is defined as the HB energy (E_{ice}). Assuming that in a water cluster, the cooperative effect [221] of surrounding HBs on a given HB is negligible, the energy required to break the HB is constant. Thus, the chemical potential can be defined as a kind of energy that governs the formation and breaking of the HBs, which has two species: kinetic energy and HB energy. The competition between these two energies determines the state of the

system. Consequently, the energy barrier or the chemical potential difference can be defined as the energy difference between the ice and the water. In the ice phase, the bonded water molecules still possess a certain amount of kinetic energy that is lower than the HB energy. In the water phase, however, the kinetic energy is the sole energy stored in the water molecules. Therefore, the Gibbs energy can then be given as:

$$\Delta G = n[\underbrace{\varphi(E_{\text{ice}} - E_{\text{k}})}_{\text{ice term}} - \underbrace{(1 - \varphi)E_{\text{k}}}_{\text{water term}}] \quad (3.1)$$

where n is the total number of water molecules in a water cluster or an IG, and φ is the fraction of the bonded water molecules.

Adopting the rigid water molecule model, the kinetic energy (E_{k}) of a single water molecule is calculated by:

$$E_{\text{k}} = E_{\text{k-tran}} + E_{\text{k-rot}} \quad (3.2)$$

where $E_{\text{k-tran}}$ is the translational energy of a water molecule and $E_{\text{k-rot}}$ is the rotational energy of a water molecule. According to the equipartition theorem, the translational energy equals the rotational energy [222]. Consequently, the kinetic energy required for a single water molecule to break a HB can be established as:

$$E_{\text{k}} = 2E_{\text{k-tran}} = m_{\text{H}_2\text{O}}v_{\text{c}}^2 = \frac{E_{\text{ice}}}{N_{\text{ag}}} \quad (3.3)$$

where $m_{\text{H}_2\text{O}}$ is the mass of a single water molecule, v_{c} is the critical molecule speed, and N_{ag} is the Avogadro constant. For water molecules with a speed of $v > v_{\text{c}}$, the HB is inevitably broken, while for water molecules with a speed of $v < v_{\text{c}}$, the HB is formed stably. However, upon the onset of HoN, each molecule can be viewed as being fully

bonded to other water molecules, given the high concentrations of HBs at large degrees of supercooling [217]. In such cases, a mole of water molecules averagely possesses two moles of HBs. Thus, for a single molecule to break its bonded state, it has to break two HBs. Consequently, for temperatures approaching the onset of HoN temperature, Equation (3.3) is modified as:

$$m_{\text{H}_2\text{O}}v_c'^2 = \frac{2E_{\text{ice}}}{N_{\text{ag}}} \quad (3.4)$$

Then the obtained $v_c' = 834.0 \text{ m s}^{-1}$. Water molecules with $v < v_c'$ cannot maintain their liquid state.

For a water system that contains a large number of water molecules, a speed distribution of water molecules is required for estimating the fraction of the water molecules ($\varphi(T, v_c')$) that can form HBs. As widely adopted in molecular dynamics (MD) simulations of liquid systems [223, 224], the Maxwell-Boltzmann distribution (MBD) equation [225] is employed for approximating the molecular speed distribution in water. At a certain temperature (T), the speed probability ($P(v)$) is calculated as:

$$P(v) = 4\pi \left(\frac{m_{\text{H}_2\text{O}}}{2\pi kT}\right)^{\frac{3}{2}} v^2 e^{\left(-\frac{m_{\text{H}_2\text{O}}v^2}{2kT}\right)} \quad (3.5)$$

Accordingly, the water molecule fraction ($\varphi(T, v_c')$) that can form HBs at the onset of HoN temperature (T_{hom}) is given as:

$$\varphi(T_{\text{hom}}, v_c') = \int_0^{v_c'} P(v) dv \quad (3.6)$$

This fraction indicates that, despite the capability of having $\varphi(T_{\text{hom}}, v_c')$ moles of bonded water molecules, the HBs cannot exist constantly, rather the total number of HBs

are kept constant through the rapid forming and breaking of the HBs between molecules. Assuming that, at a time instant, $\varphi(T, v'_c)$ moles of water molecules formed a cluster or a HB network that can have a long existence and a tendency to grow, then the total kinetic energy ($E_{k-t}(T)$) possessed by the water system must be high enough to counteract the freezing process. Therefore, the molar Gibbs energy (ΔG_k) of the water system must meet the following criterion to regain the liquid state:

$$\Delta G_k = E_{k-t}(T) - \Delta H\varphi(T, v'_c) > 0 \quad (3.7)$$

where $E_{k-t}(T)$ is described as:

$$E_{k-t}(T) = 3kTN_{ag} \quad (3.8)$$

Accordingly, in the present study a criterion for the onset of HoN is defined as:

$$E_{k-t}(T_{hom}) - \Delta H \cdot \varphi(T_{hom}, v'_c) = 0 \quad (3.9)$$

Thus, combining Equations (3.4), (3.5), (3.8) and (3.9) yields $T_{hom} = 230.0$ K.

It is worth noting that as the rigid model is applied, the vibrational degrees of freedom are not considered, thus not contributing to the total kinetic energy of the water molecules. Moreover, at low temperatures, the assumption of the classical rigid rotating water molecule might not hold, which in turn could lead to errors in the calculated $E_{k-t}(T_{hom})$. However, the T_{hom} predicted by Equation (3.9) (i.e., 230 K) agrees with the measured values (i.e., ~ 227.0 K [226, 227]), which suggests that the adoption of the classical rigid rotating water molecule to arrive at Equation (3.9) is theoretically acceptable.

3.2.2 Pressure dependent homogeneous ice nucleation temperatures

When the pressure changes, the densities of the water and ice change accordingly. In turn, this change leads to a change in the latent heat (enthalpy of fusion) which is realised by storing or releasing the work that is done during the ice expanding or contracting processes, respectively [61]. Thus, the pressure dependant latent heat can be given as:

$$\Delta H'(p) = \Delta H + 500 \left[\frac{1}{9\rho_{\text{H}_2\text{O}}(p)} - \frac{1}{9\rho_{\text{ice}}(p)} \right] (p - p_0) \quad (3.10)$$

where $p_0 = 1 \text{ atm}$ is the reference pressure and the density of the water ($\rho_{\text{H}_2\text{O}}(p)$) and density of the ice ($\rho_{\text{ice}}(p)$) are the values extracted along the curve of the melting temperature of the ice ($T_m(p)$). By inserting Equation (3.10) into Equation (3.9), the pressure dependant HoN temperature ($T_{\text{hom}}(p)$) can be obtained.

In this study, the Simon-Glatzel equation [228] is used to describe the ice melting curve as a function of the pressure:

$$T_m(p) = T_0 \left(\frac{\Delta p}{a^*} + 1 \right)^{1/b^*} \quad (3.11)$$

where $\Delta p = p - p'_0$. p'_0 and T_0 are the reference pressure and temperature, respectively. The values for the p'_0 , T_0 , a^* and b^* for the ice phases are listed in Table 3.1.

Table 3.1. Simon-Glatzel equation parameters for the melting curve of ices [228].

Ice form	Triple point	p'_0 (MPa)	T_0 (K)	a^* (MPa)	b^*
Ih	Gas-Ih-liq	6.11657×10^{-4}	273.15	-414.5	8.38
III	Ih-III-liq	209.5	251.15	101.1	42.86
V	III-V-liq	335.0	256.43	373.6	8.66
VI	V-VI-liq	618.4	272.73	661.4	4.69

The densities of the ice and liquid water against the pressure are described by [39]:

$$\rho(P, T) = \frac{\rho_0(p_{\text{ref}}, T_{\text{ref}})}{\zeta_T(p_{\text{ref}}, T)\zeta_P(p, T_{\text{ref}})} \quad (3.12)$$

where ζ_T and ζ_P are two functions describing the temperature and pressure dependence of the density, respectively, which are expressed as:

$$\zeta_T(p_{\text{ref}}, T) = a_{T1} + a_{T2}(T - T_{\text{ref}}) + a_{T3}(T - T_{\text{ref}})^{a_{T4}} \quad (3.13)$$

$$\zeta_P(p, T_{\text{ref}}) = a_{p1} + a_{p2}(p - p_{\text{ref}}) + a_{p3}(p - p_{\text{ref}})^{a_{p4}} \quad (3.14)$$

The unknown coefficients and other reference values in Equations (3.13) and (3.14) are given in Table 3.2.

Table 3.2. Parameters for the density equations of the ice and water [228].

Parameter (unit)	Liquid	Ice Ih	Ice III	Ice V	Ice VI	Eq.
p_{ref} (MPa)	0.1	6.12×10^{-4}	355.0	618.4	2216	(3.12)
T_{ref} (K)	180.00	273.16	256.43	272.73	356.15	
ρ_0 (kg m ⁻³)	1008	923	1151	1247	1355	
a_{T1}	1	1	1	1	1	(3.13)
a_{T2}	0	-1.0×10^{-4}	-9.95×10^{-5}	-8.33×10^{-4}	-1.8×10^{-4}	
a_{T3}	2.96×10^{-9}	-5.0×10^{-7}	-1.02×10^{-6}	-4.95×10^{-6}	3.82×10^{-8}	
a_{T4}	3.17	2	2	2	2	
p_{ref} (MPa)	2500	6.12×10^{-4}	355.01	618.4	2216	(3.14)
a_{p1}	0.75	1	1	1	1	
a_{p2}	-3.07×10^{-5}	-9.84×10^{-5}	-2.43×10^{-4}	-2.07×10^{-5}	0	

a_{p3}	-3.6 $\times 10^{-19}$	-2.15 $\times 10^{-7}$	-5.26 $\times 10^{-7}$	2.42 $\times 10^{-8}$	0
a_{p4}	5.2	2	2	2	2

3.2.3 Formation of ice germs

In a real water system, HBs exist primarily in the form of water clusters of various sizes. Though water clusters have a finite lifetime as they form and decay incessantly, the total number of HBs remains constant. Following the CNT, the water clusters or IGs are assumed to be spherical and of the same radius. For a real water system at $T > T_{\text{hom}}(p)$ (supercooled regime), an IG is formed at a cold spot where the local temperature transiently drops below $T_{\text{hom}}(p)$ due to thermal fluctuation. Let us define a control volume which consists of an IG and its surrounding contact layer. The contact layer is in the liquid state and of one molecule thickness, as shown in Figure 3.1.

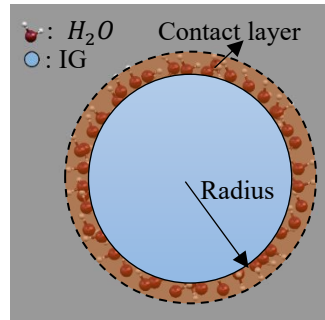


Figure 3.1. Schematic diagram of the control volume.

In the control volume, the size evolution of an IG can be described as follows (as illustrated in Figure 3.2):

- i. IG growth

During the growth of an IG, part of the kinetic energy of the water molecules with $v > v'_c$ are assumed to migrate into the contact layer. With the continuous growth of an IG, an energy balance is reached between $E_{k-t}(T, p)$ and $\Delta H'(p)$, which is given as:

$$\Delta H'(p) \frac{R_{ig}^3(T, p)}{d_{ice}^3(T, p) N_{ag}} = \frac{R_{ig}^3(T, p)}{d_{ice}^3(T, p)} m_{H_2O} \int_{v'_c}^{\infty} P(v) v^2 dv$$

$$+ 9kT \left\{ \frac{\left[R_{ig}(T, p) + \frac{d_{H_2O}(T, p)}{2} \right]^2}{d_{H_2O}^2(T, p)} \right. \quad (3.15)$$

$$\left. - \frac{R_{ig}^3(T, p) [1 - \varphi(T, v'_c)]}{3d_{ice}^3(T, p) \varphi(T, v'_c)} \right\}$$

where $R_{ig}(T, p)$ is the initial radius of the IG under such an energy balance, $d_{H_2O}(T, p)$ and $d_{ice}(T, p)$ are the water molecule and ice molecule diameters which are estimated based on the densities of the water and ice at $T_m(p)$, respectively. The term on the left-hand side of Equation (3.15) denotes the total enthalpy of the fusion in the control volume, whilst the terms on the right-hand side comprise the total kinetic energy of the water molecules in the control volume. With Equation (3.15), the $R_{ig}(T, p)$ can be obtained.

Meanwhile, the growth of the IG is assumed to be an adiabatic process in this study and the IG keeps growing until reaching the energy balance point, despite

the high temperature in the contact layer. Therefore, the contact layer temperature ($T_{\text{con}}(T, p)$) temporarily rises due to the acceptance of the migrated kinetic energy from the IG molecules during its growth. The transient temperature of the contact layer is then calculated by:

$$\begin{aligned}
 & T_{\text{con}}(T, p) \\
 &= T + \frac{TR_{\text{ig}}^3(T, p)[1 - \varphi(T, v'_c)] \left[\frac{m_{\text{H}_2\text{O}}}{3} \int_{v'_c}^{\infty} P(v)v^2 dv - 1 \right]}{3d_{\text{ice}}^3(T, p)\varphi(T, v'_c) \left[R_{\text{ig}}(T, p) + \frac{d_{\text{H}_2\text{O}}(T, p)}{2} \right]^2} \quad (3.16)
 \end{aligned}$$

It is worth noting that the adiabatic growth assumption for the IG process might be contradictory to thermophysics as the temperature of the contact layer could rise above the melting point, and the water can no longer freeze. It is used here as an intermediate variable just to simplify the analysis, including in Steps i and ii. In Step ii, the high kinetic energy in the contact layer will be transferred inwardly to the IG and outwardly to the bulk liquid (outside the control volume) as detailed below.

ii. IG decay

It is assumed that the heat transfer coefficient between the contact layer and the IG equals that between the contact layer and the bulk liquid. Due to the reabsorption of the high kinetic energy from the contact layer, the IG undergoes a melting process until $T_{\text{con}}(T, p)$ reduces to $T_{\text{m}}(p)$. Based on the amount of melted IG, the new IG size ($R'_{\text{ig}}(T, p)$) can be calculated by:

$$R'_{ig}(T, p) = \left\{ R_{ig}^3(T, p) - \frac{9kT_{con}(T, p)d_{ice}^3(T, p) \left[R_{ig}(T, p) + \frac{d_{H_2O}(T, p)}{2} \right]^2}{2d_{H_2O}^2(T, p) \left[\frac{3kT + E_{ice}(p)}{N_{ag}} \right]} \right\}^{\frac{1}{3}} \quad (3.17)$$

where the second term in the curly bracket denotes the volume of the melted IG.

Afterwards, the size of the IG remains stable at $R'_{ig}(T, p)$.

iii. IG cooling

After the size of the IG stabilises at $R'_{ig}(T, p)$, the control volume keeps cooling down to the macroscopic temperature (T_{bulk}) by heat exchange with the surrounding liquid.

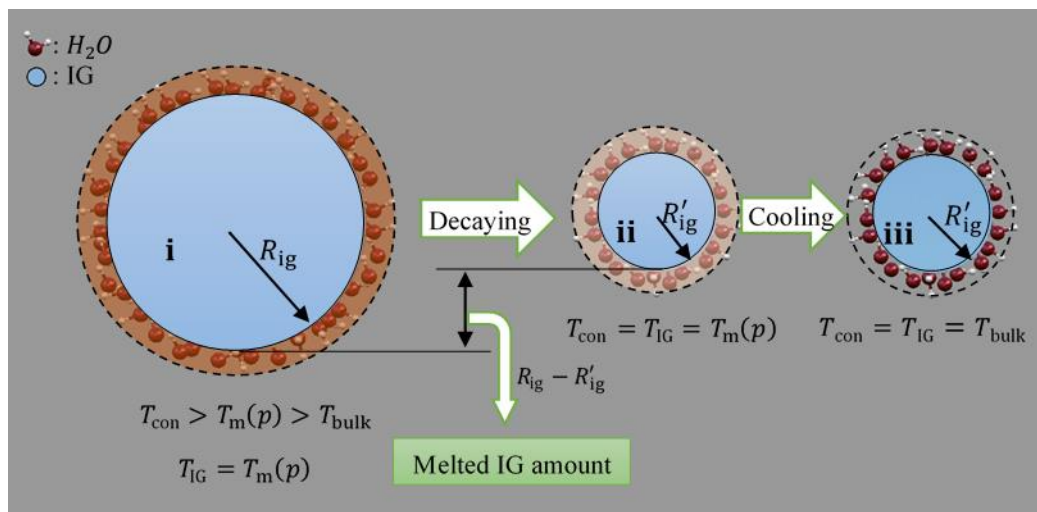


Figure 3.2. Control volume for describing the evolution of the size of an IG. The different transparencies of the contact layer indicate the different temperatures.

Based on the above discussions, the size distributions of the IGs over temperatures for $T > T_{\text{hom}}(p)$ can be obtained. For $T \leq T_{\text{hom}}(p)$, i.e., in No Man's Land, the ice nucleation is spontaneous. In the MD simulations, it was found that when the temperature decreases to $T_{\text{hom}}(p)$, there is a sharp increase in the amount of four-coordinated water clusters [42, 211]. This suggested that the four-coordinate water cluster $((H_2O)_4)$ could be the main IG structure for $T \leq T_{\text{hom}}(p_0)$. To simplify the calculation, in this study $(H_2O)_4$ is assumed to be the only form of IG in the No Man's Land. Once the IG is formed, its size also does not change ($R'_{\text{ig}}(T, p) = R_{\text{ig}}(T, p)$) given the almost identical temperatures of the IG and its contact layer [42, 211]. The $R'_{\text{ig}}(T, p)$ can be determined by the volume-equivalent radius of $(H_2O)_4$ which reads:

$$R'_{\text{ig}}(T, p) = R_{\text{ig}}(T, p) \approx \frac{1}{2} \sqrt[3]{\frac{16}{3} \pi \left(\frac{d_{\text{ice}}(p)}{2} \right)^3} = 0.64 d_{\text{ice}}(p) \quad T \leq T_{\text{hom}}(p) \quad (3.18)$$

Combining Equations (3.17) and (3.18), the sizes of the IG can be determined for both the supercooled regime and No Man's Land. Once the size is known, the number concentration of the IGs can be determined. For a given degree of supercooling, the concentration of the IGs ($N_c(T, p)$) hinges on the number variations of the HBs, which is directly determined by the density change over the temperature [229]. Accordingly, $N_c(T, p)$ is expressed by:

$$N_c(T, p) = \frac{3\Delta\rho(T, p)d_{\text{ice}}^3(T, p)}{4\pi[d_{\text{ice}}^3(T, p) - d_{\text{H}_2\text{O}}^3(T, p)]R_{\text{ig}}'^3(T, p)} + N_0(p) \quad (3.19)$$

where $\Delta\rho(T, p) = \rho_0(p) - \rho(T, p)$, $\rho_0(p)$ represents the density of the water at $T_m(p)$, $\rho(T, p)$ denotes the local density of the water and $N_0(p)$ is the number concentration of IGs at $T_m(p)$.

The density of the water, $\rho(T, p)$, at 1 atm is given in [229] for $T > T_{\text{hom}}(p_0)$. Due to the absence of data for supercooled water densities under high pressure, the density change is estimated based on the fraction of the water molecules that could potentially attach to an IG (i.e., $\varphi(T, v_c')$):

$$\Delta\rho(T, p) = [\rho_0(p) - \rho_{\text{ice}}(p)] \left[\frac{\varphi(T, v_c')\Delta T}{T_{\text{hom}}(p) - T_m(p)} \right] \quad T > T_{\text{hom}}(p), p > p_0 \quad (3.20)$$

where $\Delta T = T - T_m(p)$. For $T \leq T_{\text{hom}}(p)$, $\Delta\rho(T, p)$ is set to its value at $T_{\text{hom}}(p)$ as $\rho(T, p)$ infinitely approaches $\rho_{\text{ice}}(p)$ when the temperature decreases further after $T_{\text{hom}}(p)$ [44, 229].

To calculate $N_0(p)$, we assume that the water clusters at $T_m(p)$ have the same structure as a water dimer $((\text{H}_2\text{O})_2)$, as supported by [230]. In other words, each water molecule on average has only one HB. Thus, Equation (3.3) is adopted to calculate the critical speed at $T_m(p)$, leading to $v_c'' = 591.0 \text{ m s}^{-1}$. Subsequently, $N_0(p)$ has the form of:

$$N_0(p) = \frac{3\rho_0(p) \int_0^{v_c''} P(v) dv}{4\pi R_{ig}'^3(T_m, p)} \quad (3.21)$$

3.2.4 Homogeneous ice nucleation rate

The CNT is described by two components, as given in Equation (3.22) [46, 49]. One is the net flux of water molecules (f_n), i.e., the water molecules that can potentially be incorporated into the IG, and another one is the total number of IGs involved in the water system.

$$J_h = \overbrace{\frac{kT}{h} \cdot \exp\left(\frac{-\Delta g}{kT}\right)}^{\text{Flux of water molecule}} \cdot \overbrace{N \cdot \exp\left(\frac{-\Delta G}{kT}\right)}^{\text{Number of IG}} \quad (3.22)$$

where h is the Planck's constant. In Section 3.2.3, the IG critical size and concentration have been obtained. Thus the use of ΔG for obtaining the IG critical size is no longer necessary. Therefore, Equation (3.22) can be rewritten as

$$J_h(T, p) = 4\pi R_{ig}'^2(T, p) \cdot N_c(T, p) \cdot \frac{kT}{h} \exp\left(\frac{-\Delta g}{kT}\right) \quad (3.23)$$

In the present study, the focus is to bypass the application of Δg , which needs to be replaced by an alternative energy term.

For an IG, the molecular attachment to, and detachment from, the HB network all occur in the contact layer. Statistically, the attachment of an individual molecule to an IG forms

one HB, with the IG and one HB with another contact layer molecule. This yields the same critical molecule speed of $v'_c = 834.0 \text{ m s}^{-1}$ by using Equation (3.4) Given that all of the molecules in the contact layer still satisfy MBD, the criterion described by Equation (3.9) is applied to determine the phase state of the contact layer at any given temperature. Therefore, once the $E_{k-t}(T)$ is lower than $\Delta H'(p)\varphi(T, v'_c)$, this contact layer irreversibly turns into part of the IG. It thus seems plausible to determine Δg as the difference between the $E_{k-t}(T)$ and $\Delta H'(p)\varphi(T, v'_c)$ in the contact layer. As such, the model avoids the need to specify Δg . Therefore, a new expression for the HoN rate, $J_h(T, p)$, is arrived at:

$$J_h(T, p) = 4\pi R'_{ig}{}^2(T, p) \cdot N_c(T, p) \cdot \frac{kT}{h} e^{\left\{ \frac{-n_m [E_{k-t}(T) - \Delta H'(p)\varphi(T, v'_c)]}{kT} \right\}} \quad (3.24)$$

where n_m is the number of moles of the contact layer.

It is worth mentioning that the term $\frac{kT}{h}$ in Equation (3.24) originates in the transition state theory based on the concept of quantum chemistry which considers the vibrational motion of the water molecules at the saddle point of the potential energy surface while crossing the barrier. However, the term $[E_{k-t}(T) - \Delta H'(p)\varphi(T, v'_c)]$ is derived based on the classical kinetic energy theory, as discussed in Section 3.2.1. Despite the likelihood of incompatibility, the intention of combining the concept of quantum chemistry and the classical approach in this study is to bypass the need to specify the value of Δg .

With Equation (3.24), the HoN rate of a water system can be predicted as long as the temperature is fixed. However, it is physically impossible to maintain the local temperature at a constant value due to the thermal fluctuations. Thermal fluctuations make

the prediction of the sizes of the IGs extremely difficult for $T \approx T_{\text{hom}}(p)$ as the size predictions of Equations (3.17) and (3.18) differ significantly. Therefore, a temperature fluctuation range for the transition from the supercooled regime to the No Man's Land should be carefully chosen. Laksmono et al. [231] found the temperature in the transitional stage often sitting in the range of 227 K – 232 K under p_0 (1 atm). Hence, in this study, $T_{\text{hom-up}} = 232$ K was chosen as the fluctuation upper bound and $T_{\text{hom-down}} = 227$ K as the fluctuation lower bound. In this temperature range, the water system is a mixture of IGs with different sizes. The number concentrations of the IGs for each different size is impossible to estimate. To address this problem, a series of values for $J_h(T, p_0)$ are applied to obtain a fitting function. The first and foremost value is $J_h(T, p_0)$ at $T = T_{\text{hom}}$ as T_{hom} can be viewed as the centre point of the fluctuation range. Consequently, the $J_h(T_{\text{hom}}, p_0)$ can be obtained by averaging the values of the $J_h(T_{\text{hom-up}}, p_0)$ and $J_h(T_{\text{hom-down}}, p_0)$. Finally, a cubic polynomial fit of the $J_h(T, p_0)$ values at $225 \text{ K} \leq T \leq T_{\text{hom-down}}, T_{\text{hom}}$, and $T_{\text{hom-up}} \leq T \leq 234 \text{ K}$ was applied to estimate the $J_h(T, p_0)$ for the transitional stage. Further, for high pressure cases, the upper and lower bounds of the temperature fluctuations in the transitional range are set as $T_{\text{hom-down}} = T_{\text{hom}}(p) - 3 \text{ K}$ and $T_{\text{hom-up}} = T_{\text{hom}}(p) + 2 \text{ K}$, respectively, based on the transitional temperature at p_0 . The calculation of the $J_h(T, p)$ in the transition stage under a high pressure follows the same method as that under p_0 . Finally, a full expression of $J_h(T, p)$ is arrived at:

$$J_h(T, p) = \begin{cases} 4\pi R_{ig}^{\prime 2}(T, p) N_c(T, p) \frac{kT}{h} e^{\left\{ \frac{-n_m [E_{k-t}(T) - \Delta H'(p) \varphi(T, v_c')]}{kT} \right\}} & T \notin [T_{\text{hom-down}}, T_{\text{hom-up}}] \\ 10^{(a-b\Delta T+c\Delta T^2-d\Delta T^3)} & T \in [T_{\text{hom-down}}, T_{\text{hom-up}}] \end{cases} \quad (3.25)$$

where a , b , c and d are the constants of the fitting function, which is obtained under different pressures. With the absence of data on the sizes and concentrations of the IGs in the transition stage, the fitting function is deployed in this study as the seemingly unique alternative to interpolate $J_h(T, p)$, thus bridging the supercooled regime to the No Man's Land.

3.3 Results and discussion

The predicted pressure-dependent HoN temperatures ($T_{\text{hom}}(p)$) are shown below in Figure 3.3 in comparison to the experimental data. An empirical equation predicting the $T_{\text{hom}}(p)$ [37] is plotted for comparison. The melting curve ($T_m(p)$) estimated by the Simon-Glatzel equation [39] is also included as a reference. Good agreements were achieved between the predicted $T_{\text{hom}}(p)$ and the experimental data [213, 232], with deviations of less than 3% for pressures < 209.5 MPa. Under atmospheric pressure, the predicted $T_{\text{hom}}(p_0)$ equaled 230.0 K, just in the transitional range measured by Laksmono et al. [231] (i.e., 227 K – 232 K). However, the accuracy of the prediction strongly depends on the ΔH , which in this study is set as 6.28 kJ mol^{-1} , as rigorously measured by Smith et al. [220]. Both of the $T_m(p)$ and $T_{\text{hom}}(p)$ also decrease as the p increases. Such a descents in the nucleation temperature is attributed to the reduced $\Delta H'(p)$ due to the negative work done by the imposed high pressure (< 209.5 MPa) during the nucleating process [61]. The reduced $\Delta H'(p)$ requires a lower $E_{k-t}(T)$ to

reach a lower $T_{\text{hom}}(p)$. The present model cannot properly treat the ice nucleation in the pressure range $p_m \in (209.5, 625.9)$ MPa due to the complicated changes in the ice structures. For pressures above 625.9 MPa, the $T_{\text{hom}}(p)$ predicted by the present model and the empirical equation (i.e., $0.86T_m$) had very similar results with the discrepancy lower than 5.5%. Thus, the empirical equation was applied in all of the relevant simulations for simplicity and to save simulation time.

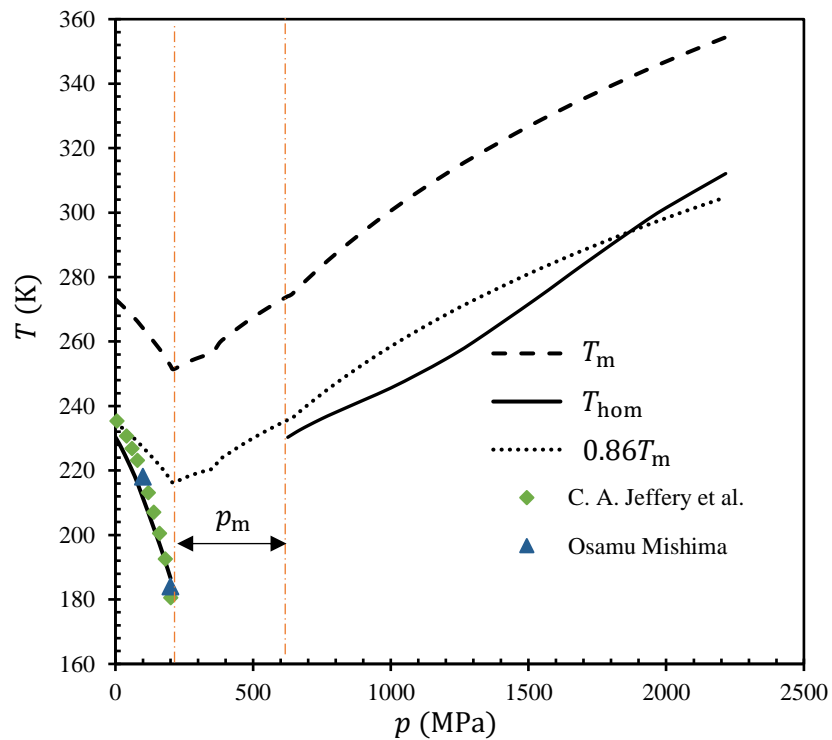


Figure 3.3. Evolution of the HoN temperature over a range of pressures.

The evolutions of the sizes of the IGs ($R_{\text{ig}}(T, p_0)$) and their number concentrations ($N_c(T, p_0)$) as a function of the temperature at p_0 are plotted in Figure 3.4 below. Clearly, the $R_{\text{ig}}(T, p_0)$ decreased as the temperature decreased, from 273.15 K to 232 K, resulting in an increase of $N_c(T, p_0)$ by about 4.4 times. In the transition range ($227 \text{ K} < T < 232 \text{ K}$), the $R_{\text{ig}}(T, p_0)$ dropped, from 1.27 nm to 0.204 nm,

which corresponded with a sharp rise in the $N_c(T, p_0)$, from $1.16 \times 10^{20} \text{ cm}^{-3}$ to $1.94 \times 10^{22} \text{ cm}^{-3}$. For temperatures lower than 227 K (in No Man's Land), the $R_{ig}(T, p_0)$ remained constant due to the dominant structure of the IGs, i.e., $(H_2O)_4$. Whilst the $R_{ig}(T, p_0)$ remained constant in No Man's Land, a steep increase in the $N_c(T, p_0)$ was observed due to the increased $\varphi(T, v'_c)$. The nonlinear variations of $R_{ig}(T, p_0)$ as a function of the temperature critically implied that the thermodynamic and kinetic properties of the supercooled water (e.g., $\sigma_{i/w}$ and Δg) at $T < 232 \text{ K}$ could not be estimated through linear extrapolations using the experimental data obtained at $T > 232 \text{ K}$, as has previously been done in the literature (e.g., [45, 50]).

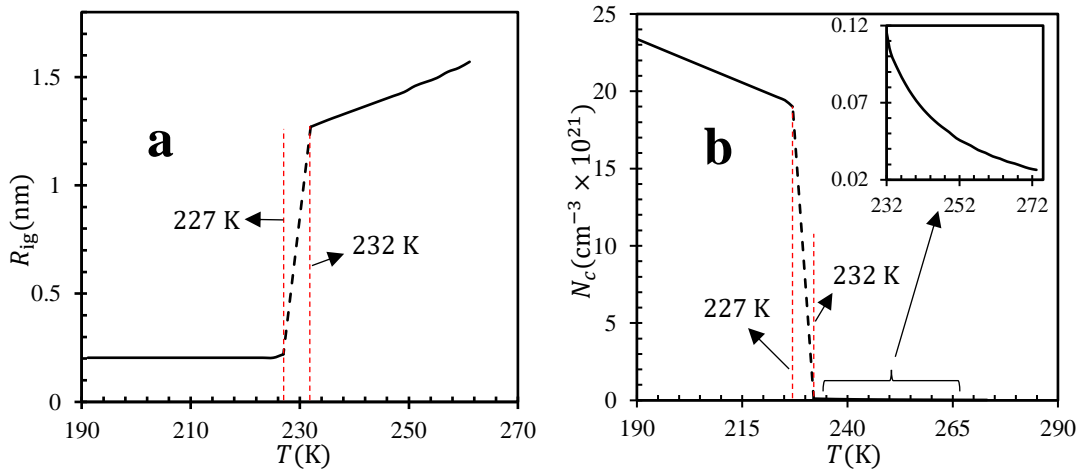


Figure 3.4. Variations in the sizes and number concentrations of the IGs against the temperature: (a) sizes, (b) number concentrations.

The predicted $J_h(T, p)$ at p_0 was compared to groups of published experimental data and the predicted results using existing theoretical models, as shown in Figure 3.5 below. Generally, the $J_h(T, p_0)$ increased sharply as the temperature dropped to $T_{hom}(p_0)$ and increased slowly after $T_{hom}(p_0)$, particularly in No Man's Land. The turning point took place around $T = 227 \text{ K}$ which was in line with the findings of Laksmono et al. [231].

In Figure 3-5, for $T \geq 232 \text{ K}$ (the supercooled regime), the present model as well as the theoretical models of Jeffery and Austin [213], Pruppacher [44], Huang and Bartell [50] and Murray et al. [45] all provided values of $J_h(T, p_0)$ (lines) that are in good agreement with the experiment data (scattered points) [30, 51, 52, 233]. However, for $215 \text{ K} < T < 236 \text{ K}$, the methods of Huang et al. [50] and Murray et al. [45] significantly underestimate the $J_h(T, p_0)$ due to their poorly estimated values of $\sigma_{i/w}$. The predicted results using the theoretical models of Pruppacher [44] and Jeffery and Austin [213] reasonably matched the experiment data for regions before the No Man's land ($T > 227 \text{ K}$), thanks to the consideration of the singularity of $T = 228 \text{ K}$ when calculating the free energy barrier to nucleation.

In the transition region of $227 \text{ K} < T < 232 \text{ K}$ (as shown in the inset in Figure 3.5), the $J_h(T, p_0)$ predicted using the present model, without considering the thermal fluctuation (orange dashed line), was greater than the experimental data of Hagen et al. [53] by $O(10^2)$. A significant improvement in the predictions was achieved after the temperature fluctuation was included through a cubic polynomial fitting function in the present model.

In No Man's Land ($T \leq 227 \text{ K}$), the $J_h(T, p_0)$ predicted by the present model was still in reasonable agreement with the experimental data of Manka et al. [54], Bartell and Chushak [56], Bhabhe et al. [234] and Amaya and Wyslouzil [235]. The values of $J_h(T, p_0)$ predicted by Jeffery and Austin's [213] theoretical model were several orders of magnitude higher than the experimental data for $200 \text{ K} < T < 227 \text{ K}$, while the theoretical predictions of Huang and Bartell [50] and Murray et al. [45] matched only a very small range of the experiment data ($190 \text{ K} < T < 215 \text{ K}$) in No Man's Land.

It is worth noting that the $J_h(T, p_0)$ predicted using the present model was slightly greater than most of the experimental data for $T < 215$ K. This overprediction was mainly attributed to a negligence of the high internal pressure inherently present inside the nanosized water droplets used in these experiments which suppresses the nucleation rate [236], as detailed in the following section.

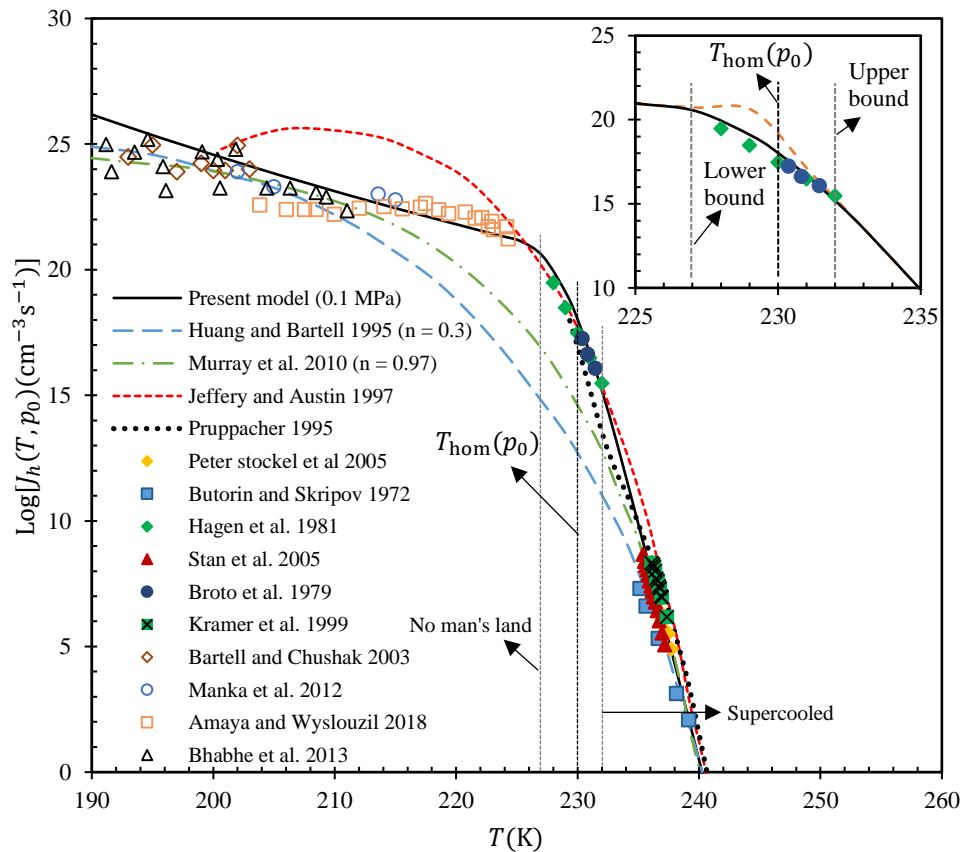


Figure 3.5. HoN rates for supercooled water over temperature at the atmospheric pressure. Scattered data are the experimental data from the literature; the broken lines are the theoretical prediction results from the CNTs; the inset represents the nucleation rate with and without consideration of the thermal fluctuations in the transition.

In natural and industrial processes, the freezing of micro-sized and nano-sized water droplets is commonly encountered. Due to the interfacial tension, there are ultrahigh internal pressures present inside these small droplets, as can be estimated by the Laplace

equation ($\Delta p = 2\sigma/\gamma$) [236]. Figure 3.6 shows the predicted $J_h(T, p)$ over a range of high pressures, which correspond to a broad range of droplet sizes (in nanoscale). The experimental data conducted for the nano-sized droplets are also summarised and included for comparison. The experiments were conducted at temperatures lower than 227 K and the ultrafine droplets with a radius from 3 nm to 100 nm were generated from vapour condensation in supersonic expansions [54], which corresponded to an internal pressure ranging from 1 MPa to 50 MPa. Evidently, a significant improvement in the predictions was achieved with the inclusion of the internal high pressure of the droplet and the scattered experimental data [54, 56, 234, 235] overlapped with most of the $J_h(T, p)$ predicted by the present model.

For $T > T_{\text{hom}}(p)$, the $J_h(T, p)$ decreased by $O(10^2)$ as the pressure increased. In other words, the ice nucleation rate was strongly pressure-dependent. This result was in line with the findings of the MD simulations of Li et al. [236] who investigated the effects of droplet sizes, from 2.4 nm to 6.1 nm, at 230 K, on the $J_h(T, p)$. For $T < T_{\text{hom}}(p)$, the $J_h(T, p)$ decreased slightly, by about 2.0 times, as the pressure increased by 10 MPa, which suggests a weak pressure dependence for $J_h(T, p)$ in No Man's Land.

Jeffery and Austin's theoretical model [213] provided similar results at the high pressure of 50 MPa for $T > T_{\text{hom}}(p)$, yet deviated significantly with the experimental data when $T < 215$ K. Indeed, Amaya and Wyslouzil [235] have recently conducted a comprehensive review of different theoretical models and concluded that the current nucleation theories or models cannot explain the experimental observations, even after the internal pressures of the droplets have been considered. However, the present model

proved capable of generating reasonably accurate predictions for $J_h(T,p)$ over temperatures down to 190 K.

For temperatures below 190 K, the assumption that $(H_2O)_4$ is the dominant IG structure might no longer hold due to the complexity of the transition from No Man's Land to the glassy water. At such low temperatures, the structures of the IGs might reduce to $(H_2O)_2$ or even $(H_2O)_1$, which would require significant work if one was to elucidate the evolution of the IGs under such low temperatures, which certainly exceeds beyond the scope of the present work. Therefore, due care is required when applying the present model to temperatures below 190 K.

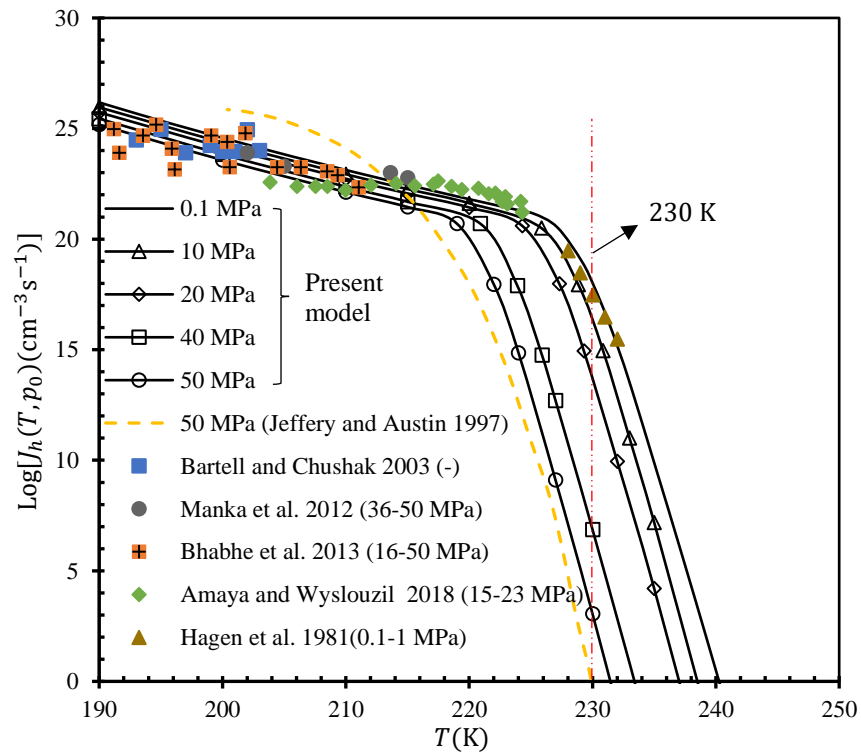


Figure 3.6. HoN rates for supercooled water over a range of high pressures. Scattered data are the experimental data from the literature; black line and lines with symbols represent the predicted results using the present model; and the yellow dashed line is the results predicted using Jeffery and Austin's theoretical model (1997) [213].

3.4 Conclusions

In this chapter, a theoretical framework was presented to clarify the relationship between the ice nucleation and the pressure based on the distribution of the molecular kinetic energy.

The predicted pressure-dependent HoN temperatures agreed well with the experimental data, with deviations of less than 3% for pressures lower than 209 MPa. For temperatures above 232 K, both the sizes of the IGs ($R_{ig}(T, p_0)$) and their number concentrations decreased with decreasing temperatures. For temperatures lower than 227 K, the $R_{ig}(T, p_0)$ remained constant due to the dominant structure of the IGs, i.e., $(H_2O)_4$, whereas a steep increase in the $N_c(T, p_0)$ was observed due to the increased $\varphi(T, v'_c)$. The nonlinear variations in the sizes and concentrations of the IGs indicated that the thermodynamic and kinetic characteristics of the IGs at $T < 232$ K cannot be estimated through extrapolations using the experimental data obtained at $T > 232$ K.

Under an atmospheric pressure, the predicted $J_h(T, p_0)$ increased sharply as the temperature dropped to $T_{hom}(p_0)$ and increased slowly after $T_{hom}(p_0)$. The turning took place at around $T = 227$ K. A significant improvement in the predictions was achieved after the temperature fluctuations were included in the model. The present model slightly over predicts $J_h(T, p_0)$ for temperatures below 215 K.

A significant improvement was achieved with the inclusion of the internal high pressure of the droplets. The $J_h(T, p)$ was found to be strongly pressure-dependent for $T > 232$ K, but appeared weakly dependent on the pressure for $T < 227$ K. The present model proved capable of generating reasonably accurate predictions for $J_h(T, p)$ for

temperatures down to 190 K. Due care is required when applying the present model to temperatures below 190 K.

The present model used measurable parameters for the inputs, including the enthalpy of the fusion, the hydrogen-bond energy, the pressure-dependent melting temperatures, and the pressure-dependent densities of the solids/liquids. Therefore, the model can be extended into a theoretical framework for other liquids with hydrogen-bonds.

**CHAPTER 4. EXPERIMENTAL STUDY OF THE ICE
NUCLEATION OF WATER DROPLETS**

4.1 Introduction

According to the theoretical predictions in Chapter 3, an extremely high-pressure field can trigger the ice nucleation in water at a relatively high temperature. In addition, the literature review in Chapter 2 has shown that the high-pressure field can be obtained through the collapse of acoustic cavitation bubbles. Therefore, in this chapter, the experimental work will focus on the investigation of ice nucleation in confined volumes of water (i.e., micro-sized droplets) triggered by two mechanical methods based on acoustic vibration. In the first method, the cavitation bubbles inception sites are provided by the fine solid particles that are submerged in a water droplet. In the second method, the cavitation bubbles are formed within a continuous medium carrying suspended droplets. The chapter provides details of the experimental set-ups, materials, equipment, and procedures for the experiments to test the above two methods. The experimental results are then presented, including the benchmark experiment where the ice nucleation of the water droplets is achieved without introducing ultrasonic vibrations, the ice nucleation of water droplets induced by the coupled effects of an ultrasonic vibration field and solid particles, and the ice nucleation of water droplets which has been assisted by cavitation bubbles formed in the continuous medium.

4.2 Ice nucleation assisted by the coupled effects of ultrasonic vibrations and solid particles

4.2.1 Experimental set-up

The design of the experimental set-up was based on an earlier study on water droplet ice nucleation by Olmo [131]. Figure 4.1 below shows the experimental set-up which

consisted of: (i) a sonicator (Branson Sonifier 450, Branson Ultrasonics, USA: 400 W, 20 kHz), (ii) a cooling module (MULTICOMP, MCPK2-15828NC-S, UK), (iii) a thermocouple, and (iv) a camera. The sonicator probe was positioned vertically against the left end of the substrate (a steel sheet) with dimensions of 0.1 cm in height, 8 cm in width and 2 cm in depth. The ultrasonic vibrations were transferred through the substrate at the right-hand end where the water droplets are located. The ultrasonic driving pressure was measured by a needle hydrophone system (Precision Ultrasonics, 4.0 mm Needle hydrophone, UK) over a range of sonicator power outputs. The top surface of the substrate at the right-hand end was coated with a hydrophobic layer (BOPP, Young's modulus: 1.7 – 2.5 GPa) to maintain the hemispherical shape of the droplets. Water droplets with an equivalent diameter of 800 μm were generated using a 0.5 μL syringe. Glass bead particles (Cospheric, USA) were picked up and injected into the droplet WD-1 using a wet syringe needle. The cooling module was placed underneath the right-hand end of the steel substrate and the temperature was precisely controlled by adjusting the input voltage and current. A k-type thermocouple (application range: 198 K – 523 K) was placed on the surface of the substrate close to the water droplets to monitor the operating temperatures (T_o). As the micro-sized water droplets were in direct contact with the surface of the substrate, T_o can be viewed as the droplet temperature. For each run, a reference droplet (WD-2) with no glass bead particles (henceforth called particles) was also placed in the vicinity of WD-1. The movements of the particles and the freezing behaviours inside WD-1 were captured using a digital microscope camera (RS Pro Wifi Microscope, RS Pro, AU) and a high-speed microscope (Meros, Dolomite, UK). A sealed enclosure minimised the influence on the droplet's freezing of natural convection between the droplets and the air. In addition, the chamber

was purged with nitrogen gas to reduce the condensation of water vapour on the substrate and any potential contamination from dust suspended in the air.

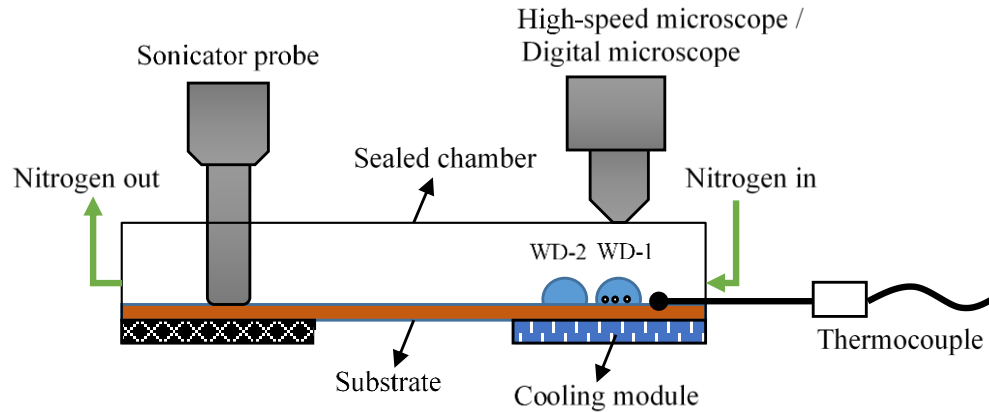


Figure 4.1. Schematic of the experimental set-up. WD-1 is a water droplet with glass beads and WD-2 is the reference droplet without any particles.

4.2.2 Materials

Particles with diameters (D_p) in four size groups (GB1: 63 – 75 μm , GB2: 90 – 150 μm , GB3: 180 – 250 μm and GB4: 250 – 300 μm) were used in present experiments. SEM images (see Figure 4.2) show that particles have a rough surface with asperities less than 10 μm in diameter (equivalent diameter). As exemplified in Figure 4.2(b), a large number of small crevices could exist amongst these asperities.

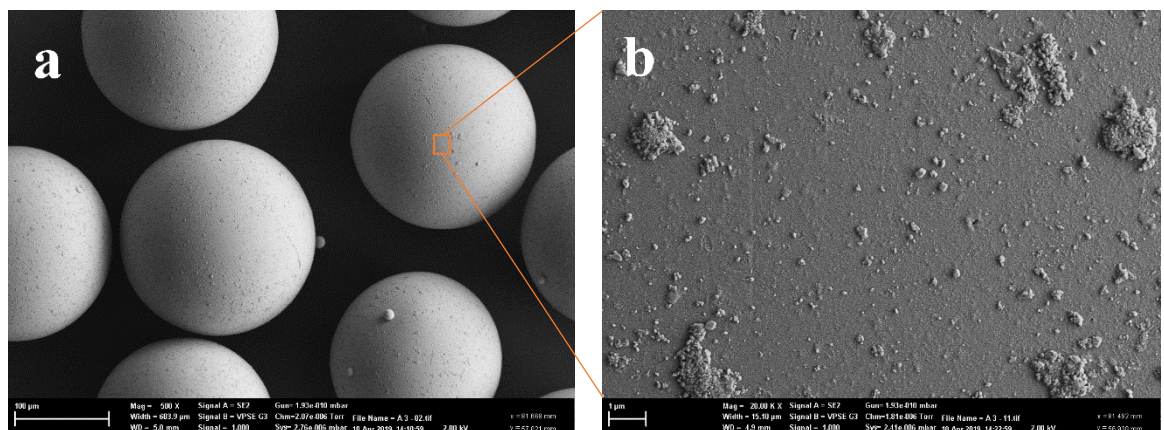


Figure 4.2. SEM images of particles: (a) scaled at 100 μm , and (b) scaled at 1 μm [D_p : 180 – 250 μm].

4.2.3 Experimental conditions and procedures

To exclude the influence of possible cavitation inception in the droplet (not in the crevice), the ultrasonic driving pressure in this study is set to be much lower than 0.12 MPa [237].

The applied sonication properties used in the study are detailed in Table 4.1.

Table 4.1. Applied driving pressure varying against the power output of the sonicator.

Sonicator power output (%)	Driving pressure (MPa)	Vibration intensity (W/cm ²)
10	0.0056 ± 0.00131	0.0011 ± 0.0003
13	0.00825 ± 0.00125	0.0023 ± 0.0003
15	0.00944 ± 0.0011	0.0031 ± 0.0004

For each experiment, the duty cycle (V_{duty}) was set at 10%, and the output power was changed between 10% and 15%. Furthermore, the effects of the T_o , vibration intensity (E_v), vibration induction time (t_v), particle number concentration (N_p) and D_p on the onset temperatures of the ice nucleation of the droplets were examined. A total sample population of 40 water droplets under each condition were examined and the number of frozen droplets (N_{drop}) were determined optically. This number was then used to calculate the fraction of frozen droplets, defined as $f_{\text{ice}} = \frac{N_{\text{drop}}}{40}$. A range of benchmark experiments was performed whereby the individual effects of the vibration field, with intensities of up to $E_v = 0.0031$ W/cm², and particles on the freezing of water droplets

(800 μm) were examined at as low as $T_o = 264$ K. The lower limit for the T_o was set at 264 K in order to avoid interference from condensation.

4.2.4 Results and discussion

Results of the benchmark experiments on the nucleation of 800 μm droplets using only the ultrasonic vibration field or particles showed no occurrence of ice nucleation. Specifically, when particles were injected into the water droplet without imposing the vibration field, the liquid state was maintained for over 5 minutes at $T_o = 264.15$ K, suggesting that impurities brought into the water droplet by particles have a marginal effect on water droplet ice nucleation. Similar results were obtained when the vibration field was applied solely with intensities up to $0.0031\text{W}/\text{cm}^2$ and $T_o = 264.15$ K. The study is then extended to examine the coupled effect of the vibration field and the presence of solid particles on ice nucleation of water droplet under the same operating conditions.

Figure 4.3 shows the ice nucleation evolution process under the coupled effect with $E_v = 0.0011$ W/cm^2 and $T_o = 268.15$ K. Clearly, even under such weak ultrasonic vibrations, the ice nucleation can be successfully induced with the assistance of particles. Figure 4.3(a) shows a typical evolution of ice nucleation and the freezing process within an 800 μm water droplet containing particles under the effect of ultrasonic vibration field. Prior to the onset of ice nucleation, particles move randomly in the water droplet. For each particle, the momentum is transferred from the vibrating substrate and its neighbouring particles. Under strong particle-particle and particle-substrate interactions, the ice nucleation is induced in the water droplet. The ice nucleation is seen starting from a single particle and spread rapidly through the entire supercooled space at a speed of \sim

0.8 cm/s. In addition, for all nucleation cases, the nucleation sites are constantly found to lie in the region between a particle and the substrate. This might suggest that the particle-substrate interaction is the main cause of ice nucleation. If the ice nucleation is triggered by the particle-particle interaction, ice should be found growing from the gap of two contact particles. However, this phenomenon was not observed in experiments.

To reveal the behaviour of ice nucleation induced by particle-substrate interaction, T_o is increased further to 271.15 K to slow down the ice growth rate and increase the chance of observing the initial stage of the ice nucleus. As shown in Figure 4.3(b), one tiny six-fold symmetrical snowflake ice crystal (around 50 μm) is formed. This snowflake indicates that the ice originates from a point ice nucleus. This point ice nucleus could be generated from the direct interaction between the substrate and the particle, or from the cavitation bubbles in the crevice [39, 40, 117, 238-243].

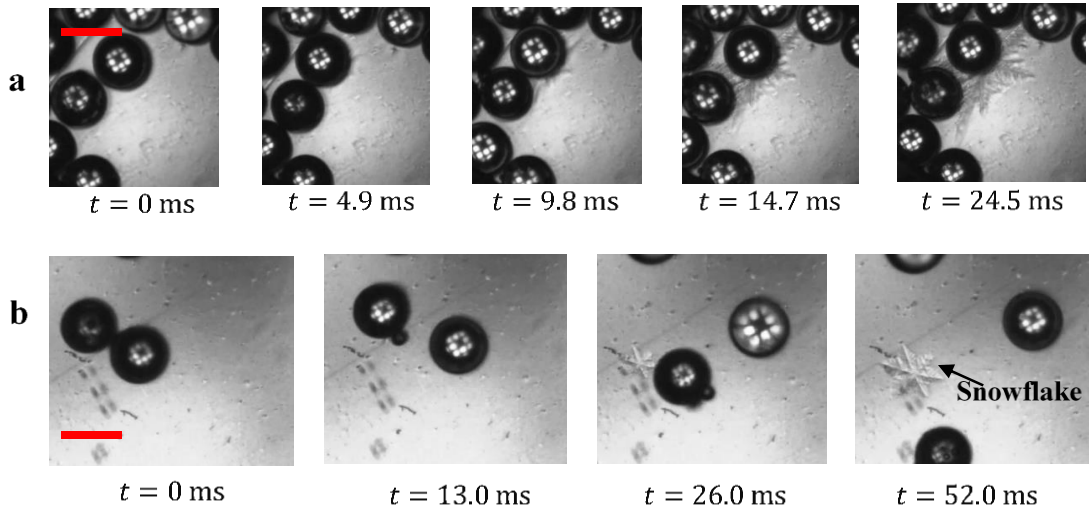


Figure 4.3. Evolution of the ice nucleation process under the coupled effects of the ultrasonic vibration field and particles: (a) $T_o = 268.15$ K, $D_p: 90 - 150$ μm , $N_p: 5 - 10$ particles/droplet; (b) $T_o = 271.15$ K, $D_p: 90 - 150$ μm , $N_p: 3$ particles/droplet. Scale bar: 100 μm .

In order to understand how the particle-substrate interaction affected the ice nucleation, key parameters including T_o , E_v , t_v , N_p and D_p were investigated in depth.

Figure 4.4(a) shows f_{ice} as a function of T_o with $E_v = 0.0011 \text{ W/cm}^2$ for different N_p . It can be seen that f_{ice} increased significantly, and doubled in value, as the number concentrations of the particles in the water droplets were increased from 2 – 3 to 10 – 15 particles per droplet. As the number concentrations of the particles decreased, lower freezing temperatures were required in order to maintain the same f_{ice} . It is noteworthy that the combined effect on the f_{ice} became significant only when there was more than one particle inside the water droplet. Water droplets containing one or no particles remained unfrozen, even with the T_o as low as 266.65 K. Figure 4.4(b) below shows the nucleation rate of a supercooled water droplet as a function of the sizes of the particles. As the particle sizes increased, the f_{ice} increased first and dropped at $D_p = 180\text{--}250 \text{ }\mu\text{m}$. This phenomenon was more pronounced when the droplet temperatures were reduced.

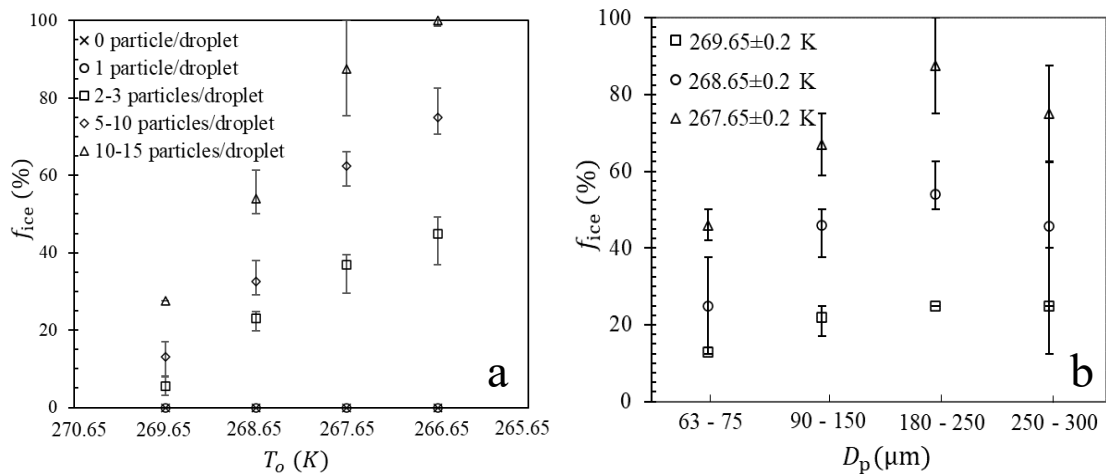


Figure 4.4. Fractions of the frozen droplets over the temperatures and number concentrations and sizes of the particles: (a) E_v : 0.0011 W/cm^2 , droplet size:

0.8 mm , t_v : 10 s , D_p : 180 – 250 μm ; (b) E_v : 0.0011 W/cm^2 , N_p : 10-15 particles/droplet, t_v : 10 s, droplet size: 0.8 mm.

The particle-substrate interactions were strongly influenced by the intensities of the ultrasonic vibrations. Figure 4.5 below shows the effects of the intensity of the ultrasonic vibrations and the induction time on f_{ice} . Clearly, f_{ice} increased with increasing E_v . Moreover, prolonging t_v further increased f_{ice} . These results indicated that the interactions between the particles and the substrate that can induce the ice nucleation are probabilistic.

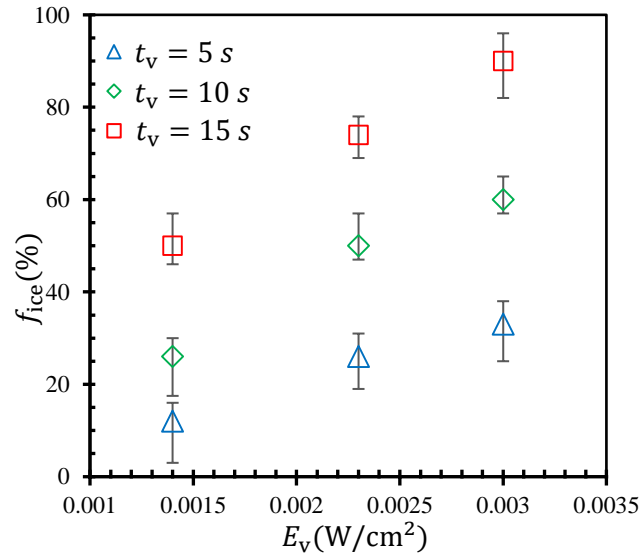


Figure 4.5. Effects of the intensity of the ultrasonic vibrations on the fraction of the frozen droplets over the vibration induction time [$T_o = 269.15$ K, droplet size: 0.8 mm, N_p : 10-15 particle/droplet].

4.3 Ice nucleation assisted by cavitation bubbles formed in the continuous medium

4.3.1 Experimental set-up

The experimental set-up consisted of the water droplet generation system, the ice nucleation module and the visualisation system. In the droplet generation system, two syringe pumps (NE-1000 Single Syringe Pump, Adelab, AU) were used to pump the continuous phase (Fluoridrop 7500, Dolomite Microfluidics, UK) and the dispersed phase (distilled water) to the microfluidic T-junction (Dolomite Microfluidics, UK). The microfluidic T-junction (ID: 0.5 mm) was made with hydrophobic surfaces. The water droplets were produced and introduced into an expansion tube (hydrophobic) with an ID of 0.8 mm. The expansion tube was introduced into the ice nucleation module, which was cooled down by a cooling module (Peltier cooling module, Multicomp, AU). The gap between the expansion tube and the ice nucleation module was filled with silicone thermal grease (5.0 W/mK) to enhance the heat exchange. However, to capture the evolution process of the cavitation bubbles induced ice nucleation using a high-speed camera (Phantom V1611, Vision Research, USA), the thermal grease needed to be replaced with nitrogen gas to ensure a clear viewport. Two K-type thermocouples (application range: 198 K – 523 K) were used to measure the surface temperatures of the cooling module and the top surfaces of the expansion tube. The sonicator probe (BRANSON SONIFIER 450, USA) sat directly on top of the expansion tube, whose position with respect to the left-hand boundary of the cooling module could be adjusted. The distance between the sonicator probe's centre line and the left-hand boundary of the cooling module was denoted as the sonicator offset distance, L_p . After nucleation, the expansion tube was instantly guided into an anti-condensation module. The anti-condensation module was filled with the same Fluoridrop 7500 as it has a thermal conductivity of close to 0.065 W/(mK). With the aid of the anti-condensation module, the morphology of the

water droplets and the ice particles could be monitored in real-time by a digital microscope (Dino-Lite, China).

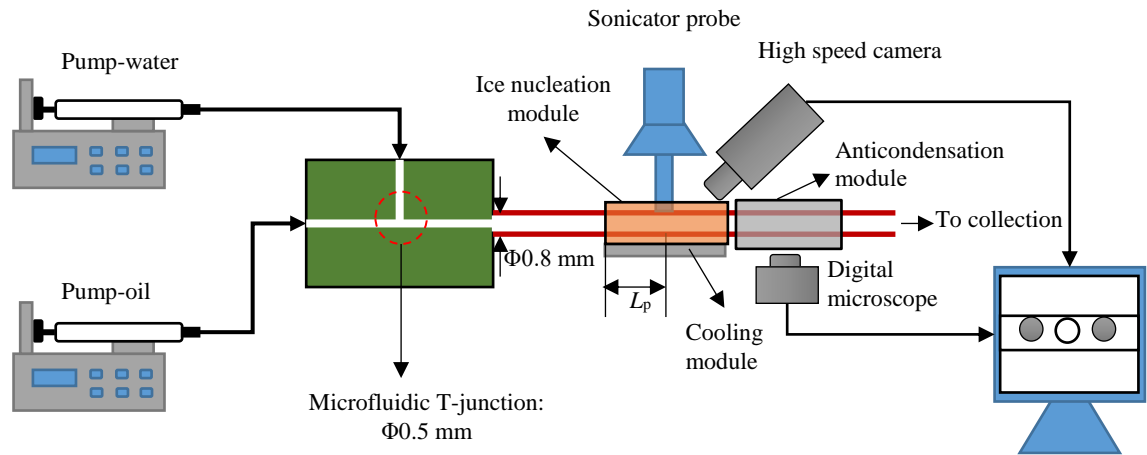


Figure 4.6. Schematic diagram of the experimental set-up for ice nucleation in tubes assisted by ultrasonic vibrations.

4.3.2 Material

The objective of the experiment was to investigate the feasibility of inducing ice nucleation triggered by cavitation bubbles outside the water droplets, i.e., in the oil phase. Hence, the oil phase must cavitate much easier than the water droplets, which required there to be abundant sites for the inception of cavitation bubbles present in the oil. To increase the number of cavitation inception sites, two methods are discussed in the literature. One is the introduction of solid particles, as described in Section 4.2, and the other one is to dissolve gas in the oil [122]. However, the solid particles will add complexities to the system which require a technique to introduce solid particles into every single water droplet and methods of avoiding particle depositions and system blockages. Therefore, the Fluoridrop 7500 was chosen due to its relatively high air solubility. The basic physical properties of Fluoridrop 7500 are listed in Table 4.2. The

air solubility is as high as 48 mL gas/100 mL. Fluoridrop 7500 also has features of a small kinematic viscosity (0.77 cSt) and a low pour point (173.15 K).

Table 4.2. Physical properties of Fluoridrop 7500.

Properties	Fluoridrop 7500
Density	1614 (kg/m ³)
Pour point	173.15 (K)
Kinematic viscosity	0.77 (cSt)
Specific heat	1128 (J/kg-K)
Thermal conductivity	0.065 (W/m-K)
Solubility in water	< 3 (ppm by weight)
Solubility of air	48 (ml gas/(100 ml liquid))
Surface tension	16.2 (mN/m)

4.3.3 Experimental conditions and procedures

The calculation of the residency time of the water droplets as a function of the flowrate in the nucleation module was vital to the heat exchange between the droplets and the ice nucleation module. However, in the ice nucleation module, the temperature distribution inside the expansion tube could not be obtained during the ice nucleation experiments as the presence of the thermocouple affected the flow patterns and the vibration field. Instead, the temperatures of the top surface and the bottom surface of the expansion tube were monitored in the experiments. The average value of these two temperatures was viewed as the temperature of the ice nucleation module and was denoted by T_{inm} .

Prior to carrying out the ice nucleation experiments, the distribution of the driving pressures needed to be characterised. The amplitude of the driving pressure (P_d), was

measured at a series of distances from the centre of the sonicator probe by a needle hydrophone (Precision Acoustics, UK).

To reveal the underlying mechanisms of the ice nucleation induced using cavitation bubbles, two water droplets (0.5 μL) were generated by controlling the dispersed volume of the syringe pumps. The gap between the two droplets was kept at 0.5 mm. After the two droplets were moved along the expansion tube to the nucleation module, the syringe pumps were turned off. An air bubble with a diameter of 0.5 mm was then manually injected in-between the two droplets by a microliter syringe (0.5 μL , Hamilton, USA). The ice nucleation module was then cooled down to a given temperature. Once the temperature was stabilised, the ultrasonic vibrations were turned on, and the evolution of the ice nucleation process was then recorded by the high-speed camera.

4.3.4 Results and discussion

The experiments investigated the freezing of water droplets without ultrasonic vibrations and pre-existing bubbles. The results for the two different oil types (air-pressurised oil and non-air-pressurised oil) are shown in Figure 4.7 below. Clearly, the ice nucleation events occurred for $T < 253.15$ K. The f_{ice} of the water droplets carried by both the air-pressurised oil and the non-air-pressurised oil rose exponentially when the temperature was lowered. For the non-air-pressurised oil, the f_{ice} was slightly higher than that of the air-pressurised oil, which might have been because the thermal conductivity was reduced by the air pressurised into the oil. Hence, the droplets required more time to reach an effective ice nucleation temperature. At $T_{\text{inm}} = 248.15$ K, the corresponding ice nucleation rates for the non-air-pressurised and air-pressurised oils were $10^{8.99}\text{cm}^{-3}\text{s}^{-1}$ and $10^{6.14}\text{cm}^{-3}\text{s}^{-1}$, respectively. Compared to the theoretical

prediction for the HoN rate at $T = 248.15$ K (namely $10^{-26.56} \text{cm}^{-3} \text{s}^{-1}$ according to Pruppacher [44]), the ice nucleation rates achieved by this system were far higher, indicating that HeN was the dominant ice nucleation pathway. Without external assistance, the cooling temperature needed to be maintained at < 253.15 K to ensure a high f_{ice} , but at the cost of a low COP.

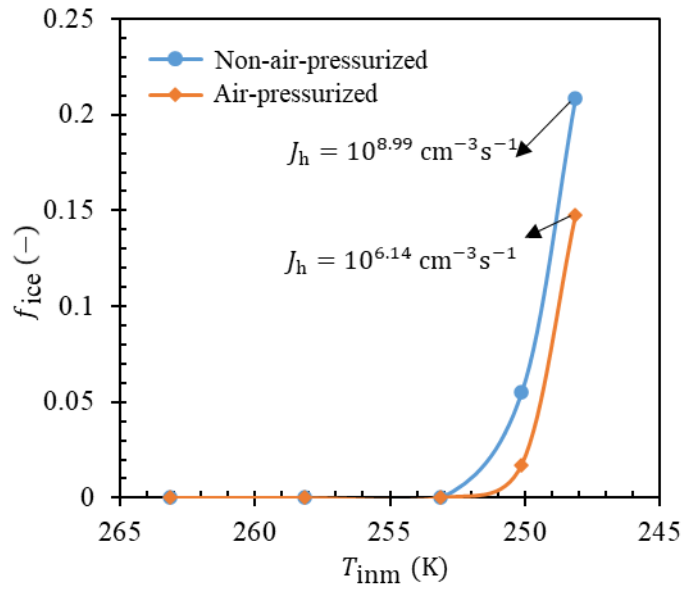


Figure 4.7. Ice nucleation of water droplets over temperatures without ultrasonic vibrations.

Under the effects of the ultrasonic vibrations, the interactions between the cavitation bubbles and the water droplets could induce ice nucleation. Figure 4.8 shows the effects of the temperature and sonicator power output on the ice nucleation of the water droplets. The temperature ranged from 269.65 K to 272.65 K and the sonicator power output ranged from 10% to 15%. It can be seen that, for temperatures above 271.65 K, the f_s increased with an increase in the sonicator power output and was insensitive to the temperature. For the power output $P_p \leq 10\%$, no ice nucleation events were recorded for the experimental temperature range, i.e., 269.65 K to 272.65 K.

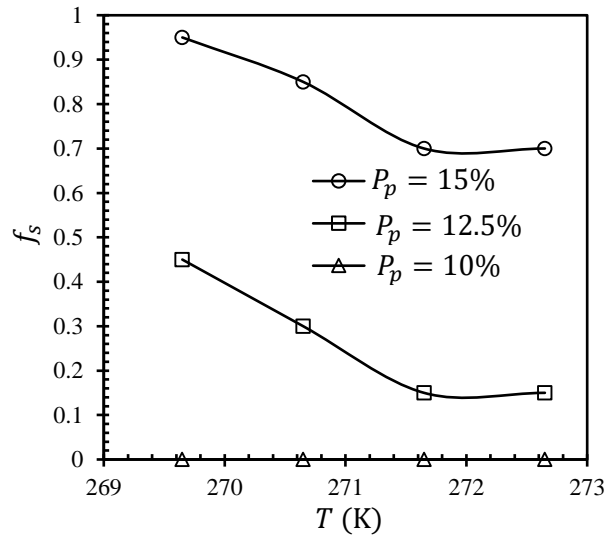


Figure 4.8. Effects of the temperature and sonicator power output on the ice nucleation of water droplets [pre-existing bubble size: 0.2 mm].

Furthermore, the effects of the pre-existing bubble sizes and the vibration induction times were studied and the results are shown in Figure 4.9 below. It can be seen that the f_s increased with an increase in the vibration induction time. However, the f_s decreased drastically when the pre-existing bubble sizes were increased. For a bubble size of 0.8 mm, there were no ice nucleation events observed. This might have been because when a pre-existing bubble size is similar to the inner diameter of the tube, the solid surface tends to reduce the pressure in the vicinity of the bubble, leading to a decrease in the bubble driving pressure [197, 244]. Hence, the bubble oscillation and small bubble shedding processes are much suppressed.

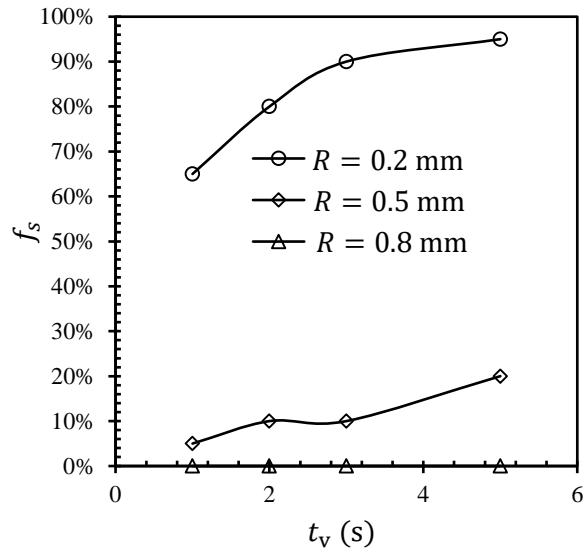


Figure 4.9. Effects of the pre-existing bubble sizes and vibration induction times on the ice nucleation of water droplets [$P_p = 15\%$, $T = 369.65$ K].

The experimental results above showed that the ice nucleation of the water droplets could be attributed to the strong interactions with the cavitation bubbles. However, the underlying mechanism of how the ice nucleation is triggered through the interactions between the droplets and the cavitation bubbles is still missing. In addressing this issue, the static water droplet ice nucleation was visualised using a high-speed camera. In the ultrasonic vibration field, the main bubble (mother) of around 0.6 mm in diameter underwent a strong surface oscillation process, as shown in Figure 4.10 below. This surface instability leads to the shedding of small bubbles (daughters) [245], as indicated in Figure 4.10 (a). The role of the mother bubble is to ensure the formation of enough daughter bubbles. These daughter bubbles are the main bodies that interact with the supercooled water droplet.

In this study, the focus was on the interaction with the cavitation bubbles outside the water droplet, which can produce ice particles with a high degree of roundness. In the ultrasonic

vibration field, the daughter bubbles moved anti-clockwise, which ensured sufficient interactions with the water droplets. The daughter bubbles d1 and d2 were examined. As shown in Figure 4.10 (a) - (c), the d1 bubble did not trigger ice nucleation. Whereas, when the d1 bubble moved to (d), dendrite ice started to grow, as circled by a red dashed-line. After 8.3 ms, the dendrite ice had spread vastly to the bottom part of the water droplet. This phenomenon might have been because the bottom part of the droplet was colder than the upper part. However, as can be seen in Figure 4.10 (a) - (f), ice nucleation was not induced by the d2 daughter bubble, even if the local temperature was equal to that of the d1 bubble.

Considering the review of ice nucleation related to cavitation bubbles in Section 2.3.2.2, there were three major mechanisms discussed, namely: (i) an extremely high pressure shock which originates from the collapse of the cavitation bubbles, (ii) ultra-low negative pressures associated with the collapse of the cavitation bubbles, and (iii) flow streams of stable cavitation bubbles. Mechanism (ii) requires a temperature of < 262 K which is out of the temperature range adopted in the present experiments. Flow streams apparently cannot exert its effects on the water droplet from the continuous medium. Whereas mechanism (i) features a strong shock wave or micro-jet which can directly impact on the interface of the water droplet, leading to a surge of local pressures. However, this shock wave or micro-jet induced ice nucleation is sensitive to distance. This sensitivity could explain the different ice nucleation abilities between d1 and d2 daughter bubbles. The d1 bubble was sandwiched between the water droplet and the tube wall, whereas the d2 bubble freely moved in the oil near the interface of the droplet. Therefore, it is expected that there will be a shorter distance between d1 bubble and water droplet than that between

d2 bubble and water droplet. The shorter the distance, the greater the possibility of an impact by pressure shock from the cavitation bubbles.

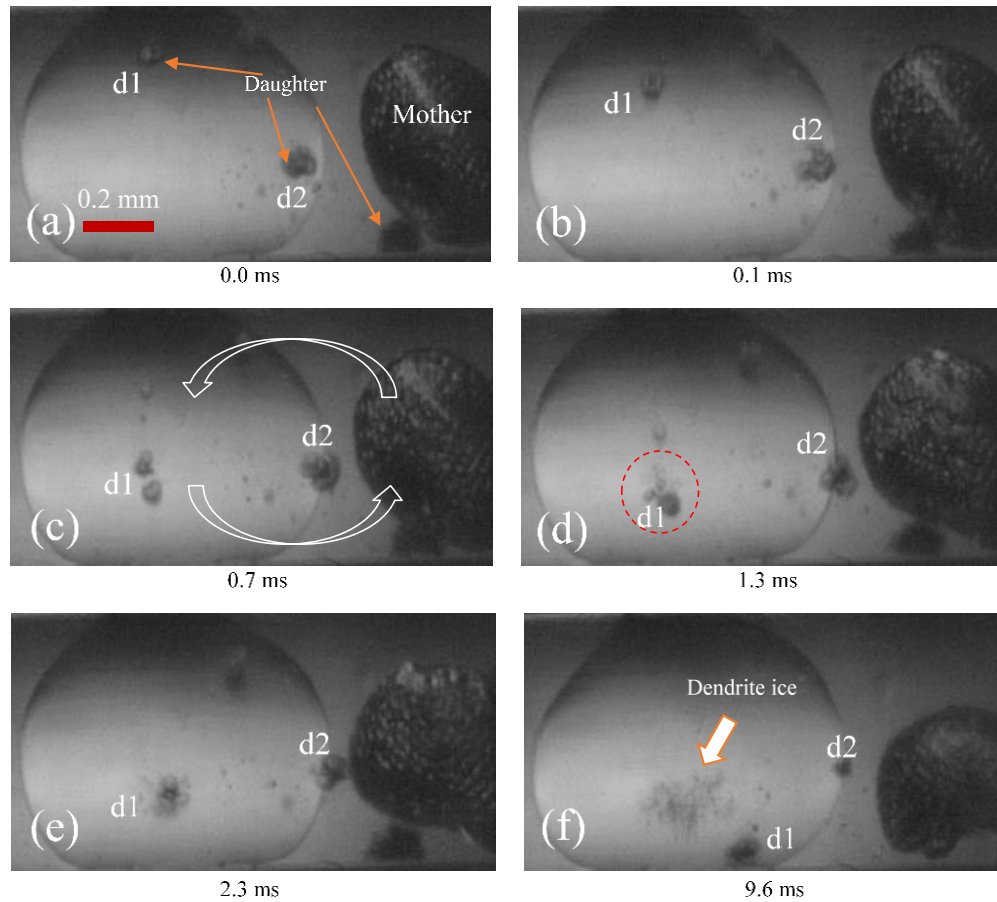


Figure 4.10. Time sequences for the ice nucleation of water droplets triggered by cavitation bubbles [$P_p = 15\%$].

To support the above discussions, a total of 25 ice nucleation events were recorded, and the corresponding nucleation sites are summarised in Figure 4.11 below where they are represented by a series of star symbols. Apparently, most of the nucleation sites were located at the bottom part of the water droplet, which is reasonable because the bottom part was colder than the upper part. In addition, the amplitudes of the high pressure shocks from the collapse of the bubbles varied drastically. A relatively small pressure amplitude required a relatively low ice nucleation temperature. Another interesting phenomenon

observed was that most of the nucleation occurred in the middle part of the water droplets (an area within the two red dashed lines in Figure 4.11). This part was nearly overlapped by the contact area between the water droplet and the tube wall. When the cavitation bubble moves into this area, or the narrow space as we can infer, the surface of the droplet will dent accordingly due to the presence of the bubble. This change in the shape of the surface of the droplets was favourable to the onset of the ice nucleation because most of the pressure shock could be absorbed by the droplet. Only three out of the twenty-five nucleation events occurred outside of the contact area, which again corroborated that the ice nucleation of water droplets triggered by cavitation bubbles is distance preferred. Therefore, one possible way to increase the nucleation rate is to well control the distance between the cavitation bubble and water droplet.

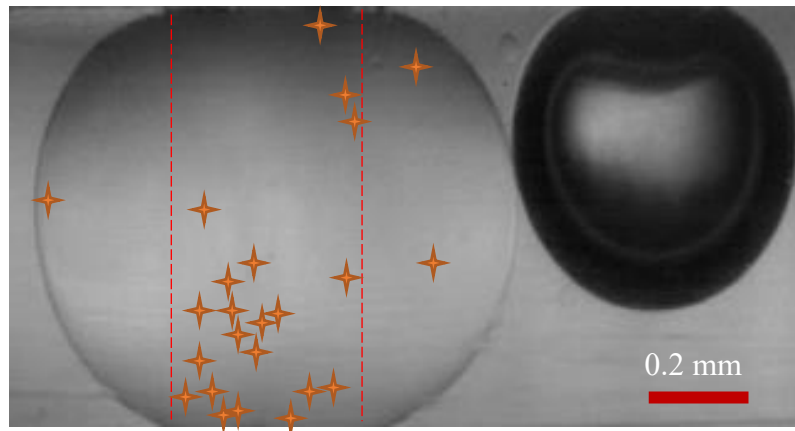


Figure 4.11. Distribution of the ice nucleation onset sites induced by cavitation bubbles.

4.4 Chapter summary

In this chapter, experimental studies were conducted to investigate: (i) the benchmark experiment on the ice nucleation of water droplets without introducing the ultrasonic vibrations, (ii) the ice nucleation of water droplets induced by the coupled effects of an

ultrasonic vibration field and solid particles, and (iii) the ice nucleation of water droplets in tubes triggered by cavitation bubbles formed in the continuous medium. The conclusions can be summarised as follows:

(i) The ice nucleation of water droplets suspended in oil without introducing an ultrasonic vibration field was investigated using two types of oil: air-pressurised and non-air-pressurised. The ice nucleation events occurred at $T < 253.15$ K. The ice nucleation rate of the water droplets using the air-pressurised oil was found to be lower than that when using the non-air-pressurised oil, primarily due to the reduced thermal conductivity due to the presence of air.

(ii) The ice nucleation of water droplets that contained glass bead particles (particles) in a field of weak ultrasonic vibrations was experimentally investigated. The ice nucleation was induced by the weak ultrasonic vibrations with the assistance of the glass particles. The nucleation onset sites were only observed in a region between the particle and the substrate. It was found that ice nucleation could not be initiated for water droplets with only one particle. When the number concentration of the particles was increased to 2 - 3 per droplet, the fraction of the frozen droplets (f_{ice}) increased to 5.6% at a temperature of 269.65 K. It was found that the f_{ice} could be increased by increasing the number concentration of the particles, or by reducing the initial temperature of the droplet. Additionally, the particle size also played an important role in determining the f_{ice} , particularly at low temperatures. The peaks of f_{ice} were constantly found when using particles with diameters of 180 μm - 250 μm at a vibration intensity of 0.0011 W/cm².

(iii) The ice nucleation of water droplets assisted by the cavitation bubbles in the continuous medium was systematically studied. It was found that ice nucleation induction could be attributed to the interactions between cavitation bubbles and water droplets in the ultrasonic vibrations field. Cavitation bubbles that could induce ice nucleation were found to be sensitive to the distance to the water droplet.

**CHAPTER 5. NUMERICAL STUDY OF ICE
NUCLEATIONS INDUCED BY CAVITATION BUBBLES**

5.1 Introduction

In previous chapter, cavitation bubbles have proved effective in inducing ice nucleation in small-volumes of water. However, due to the small scale of the cavitation bubble, the details of pressure and temperature distribution are very difficult if not impossible to be directly measured, which hinders the fully understanding of the underlying mechanism. In solving this issue, the numerical method is adopted. Therefore, this chapter focuses on the numerical investigation of ice nucleation induced by cavitation bubbles based on MRT-LBM coupled with an extended thermal LBM. The chapter begins with the development of MRT-LBM and the extension of the conventional thermal LBM. The numerical model is then used to gain insights into a number of phenomena, including: (i) the effects of the recalescence stage on the freezing process, (ii) the ice nucleation induced by cavitation bubbles, (iii) the evolution of the pressures of the cavitation bubbles inside the crevices, and (iv) the evolution of the pressures on the surfaces of the droplets in the vicinity of the collapsing cavitation bubbles. In the study of the ice nucleation induced by cavitation bubbles, two different cases are investigated: (i) the collapse of cavitation bubbles near a solid boundary, and (ii) the collapse of cavitation bubbles in a pressurised space. Aside from this, the simulation of the collapse of cavitation bubbles in a crevice is conducted in support of the experiment in Section 4.2. The structures of the crevices were simplified into three different types: (i) square-type, (ii) cone-type, and (iii) hemisphere-type. Lastly, the present model is applied to examining the propagation of the pressure waves and in determining the critical distances between the collapsed bubbles and the surfaces of the water droplets which are required to induce ice nucleation.

5.2 Development of a numerical model

5.2.1 Pseudo-potential MRT-LBM

Based on the discussions in Section 2.3.2.3, the pseudo-potential model proposed by Shan and Chen [185] was adopted to simulate the two-phase (liquid and vapour) and two components (water and oil) flow problems. The collision operator was replaced with the MRT model [246] to reduce the spurious current and to improve the numerical stability. With the MRT model, the collision process is carried out in moment space, while the streaming process is still performed in the velocity space. The evolution equation of the pseudo-potential MRT-LBM is expressed as:

$$\begin{aligned}
 f_\alpha(\mathbf{x} + \mathbf{e}_\alpha \delta_t, t + \delta_t) \\
 = f_\alpha(\mathbf{x}, t) - (M^{-1} \Lambda M)_{\alpha\beta} \left[f_\beta(\mathbf{x}, t) - f_\beta^{eq}(\mathbf{x}, t) \right] + \delta_t F_\alpha^*
 \end{aligned} \tag{5.1}$$

where f_α is the density distribution function, δ_t is the time step, \mathbf{e}_α is the discrete velocity along the α th direction, f_β^{eq} is the equilibrium distribution function, and F_α^* is the forcing term. For the two dimensional and nine-velocity (D2Q9) scheme, the \mathbf{e}_α is given as:

$$\mathbf{e}_\alpha = c \begin{bmatrix} 0 & 1 & 0 & -1 & 0 & 1 & -1 & -1 & 1 \\ 0 & 0 & 1 & 0 & -1 & 1 & 1 & -1 & -1 \end{bmatrix} \tag{5.2}$$

where $c = \frac{\delta_x}{\delta_t}$ is the lattice velocity, and δ_x is the lattice spacing. In Equation (5.1), the orthogonal transformation matrix, M , is given as:

$$M = \begin{bmatrix} 1 & 1 & 1 & 1 & 1 & 1 & 1 & 1 & 1 \\ -4 & -1 & -1 & -1 & -1 & 2 & 2 & 2 & 2 \\ 4 & -2 & -2 & -2 & -2 & -1 & -1 & -1 & -1 \\ 0 & 1 & 0 & -1 & 0 & -1 & -1 & -1 & 1 \\ 0 & -2 & 0 & 2 & 0 & 1 & -1 & -1 & 1 \\ 0 & 0 & 1 & 0 & -1 & 1 & 1 & -1 & -1 \\ 0 & 0 & -2 & 0 & 2 & 1 & 1 & -1 & -1 \\ 0 & 1 & -1 & 1 & -1 & 0 & 0 & 0 & 0 \\ 0 & 0 & 0 & 0 & 0 & 1 & -1 & 1 & -1 \end{bmatrix} \quad (5.3)$$

and the diagonal matrix, Λ , is expressed as:

$$\Lambda = \text{diag}(\tau_\rho^{-1}, \tau_e^{-1}, \tau_\zeta^{-1}, \tau_j^{-1}, \tau_q^{-1}, \tau_j^{-1}, \tau_q^{-1}, \tau_v^{-1}, \tau_v^{-1})^T \quad (5.4)$$

The relaxation times are chosen as follows [139]: $\tau_\rho^{-1} = \tau_j^{-1} = 1.0$, $\tau_e^{-1} = \tau_\zeta^{-1} = 1.1$,

and $\tau_q^{-1} = 1.1$. τ_v is in relation to the kinematic viscosity and is given by:

$$\nu = c_s^2 \left(\frac{1}{\tau_v} + 0.5 \right) \delta_t \quad (5.5)$$

where $c_s = \frac{1}{\sqrt{3}}$ is the lattice sound velocity.

f_α and f_α^{eq} are projected onto the momentum space via $m = Mf$ and $m^{eq} = Mf^{eq}$, respectively. For the D2Q9, m^{eq} can be given by:

$$m^{eq} = Mf^{eq} = \rho(1, -2 + 3|\mathbf{v}|^2, 1 - 3|\mathbf{v}|^2, v_x, -v_x, v_y, -v_y, v_x^2 - v_y^2, v_x v_y)^T \quad (5.6)$$

where $\rho = \sum_\alpha f_\alpha$ is the macroscopic density, and \mathbf{v} is the macroscopic velocity. The collision step in Equation (5.1) can be rewritten as:

$$m^* = [m - \Lambda(m - m^{eq}) + \delta_t S] \quad (5.7)$$

where I is the unit tensor, and S is the MRT forcing term in the momentum space. The streaming step of Equation (5.1) is then formulated as:

$$f_\alpha(\mathbf{x} + \mathbf{e}_\alpha \delta_t, t + \delta_t) = f_\alpha^*(\mathbf{x}, t) = M^{-1} m^* \quad (5.8)$$

The macroscopic velocity \mathbf{v} is calculated by:

$$\rho \mathbf{v} = \sum_\alpha \mathbf{e}_\alpha f_\alpha + \frac{\delta t}{2} \mathbf{F} \quad (5.9)$$

where \mathbf{F} is the total force acting on the system, including the fluid-fluid interactive force \mathbf{F}_{ll} , fluid-solid interactive force \mathbf{F}_{ls} , and the body force \mathbf{F}_b . For the pseudo-potential LBM model, \mathbf{F}_{ll} is given as:

$$\mathbf{F}_{ll} = -G\psi(\mathbf{x}) \sum_\alpha^N \omega(|\mathbf{e}_\alpha|^2) \psi(\mathbf{x} + \mathbf{e}_\alpha) \mathbf{e}_\alpha \quad (5.10)$$

For the single-component multiphase flow problem, the interaction strength G in Equation (5.10) is set as $G = -1$, and the weight coefficient $\omega(|\mathbf{e}_\alpha|^2)$ is $\omega(1) = \frac{1}{3}$ and $\omega(2) = \frac{1}{12}$. $\psi(\mathbf{x})$ is the interparticle potential, and is given by:

$$\psi(\mathbf{x}) = \sqrt{2(P_{EOS} - \rho c_s^2)/G} \quad (5.11)$$

in which P_{EOS} is the EoS for a non-ideal fluid. In this study, the Carnahan-Starling (CS) EoS is adopted, which is given by:

$$P_{EOS} = \rho RT \frac{1 + b\rho/4 + (b\rho/4)^2 - (b\rho/4)^3}{(1 - b\rho/4)^3} - a\rho^2 \quad (5.12)$$

where $a = 0.4963 (RT_c)^2/P_c$ and $b = 0.18727 RT_c/P_c$ with T_c and P_c are the critical temperature and pressure. We set $a = 0.5$, $b = 4$, $R = 1$. To improve the numerical stability, a dimensionless parameter k was introduced into the reduced EoS [21]. Equation (5.12) is then modified as:

$$P_{EoS} = k \left(\rho RT \frac{1 + b\rho/4 + (b\rho/4)^2 - (b\rho/4)^3}{(1 - b\rho/4)^3} - a\rho^2 \right) \quad (5.13)$$

For two-component flow problems, the interaction strength, G , in Equation (5.10) is set as $G = -3$, and $\varphi(\mathbf{x})$ is the function of the local densities and can be given as [185]:

$$\varphi(\mathbf{x}) = \rho_0 [1 - \exp(-\rho/\rho_0)] \quad (5.14)$$

The MRT forcing scheme proposed by Li et al. [201] was adopted to achieve thermodynamic consistency. Li et al.'s forcing scheme can be written as:

$$S = M^{-1} \left(I - \frac{\Lambda}{2} \right) M \omega_\alpha \left(\frac{\mathbf{e}_\alpha - \hat{\mathbf{v}}}{c_s^2} + \frac{\mathbf{e}_\alpha + \hat{\mathbf{v}}}{c_s^4} \right) \cdot \mathbf{F} \quad (5.15)$$

in which $\hat{\mathbf{v}}$ is defined as $\hat{\mathbf{v}} = \mathbf{v} + \sigma \mathbf{F} / \tau_\zeta \psi^2$. The parameter σ is applied to adjust the pseudo-potential model to satisfy the thermodynamic consistency, improve the numerical stability, and achieve a large density ratio. Moreover, combining the σ and k can realise the adjustment of the surface tension.

5.2.2 Thermal field

For the evolution of the temperature field, the widely used passive-scalar method [139] was adopted in this study, which is expressed as:

$$\frac{\partial T}{\partial t} + \nabla \cdot (\mathbf{v}T) = \nabla \cdot (\tilde{\alpha} \nabla T) + \phi_{1-v} + \phi_{1-i} \quad (5.16)$$

where $\tilde{\alpha}$ is the thermal diffusivity, ϕ_{1-i} and ϕ_{1-v} are the source terms responsible for the liquid-ice phase change and the liquid-vapour phase change, respectively. To solve the temperature equation, the BGK collision operator was adopted for the temperature field. The temperature distribution function is then given by [247]:

$$h_i(\mathbf{x} + \mathbf{e}_i \delta_t, t + \delta_t) = h_i(\mathbf{x}, t) - \frac{1}{\tau_h} [h_i(\mathbf{x}, t) - h_i^{eq}(\mathbf{x}, t)] + \delta_t \phi_{1-v} + \delta_t \phi_{1-i} \quad (5.17)$$

in which h_i and h_i^{eq} are the temperature distribution function and the equilibrium temperature distribution function, respectively. τ_h is the relaxation time for the temperature field, and can be calculated by:

$$\tilde{\alpha} = c_s^2(\tau_h - 0.5)\delta_t \quad (5.18)$$

The equilibrium temperature distribution function, h_i^{eq} , is given by:

$$h_i^{eq} = \omega'_i T \left(1 + \frac{\mathbf{e}_i \cdot \mathbf{v}}{c_s^2} \right) \quad (5.19)$$

where ω'_i is the weight coefficient for the D2Q5 model: $\omega'_0 = 1/3$, $\omega'_i = 1/6$ ($i = 1, 2, 3, 4$). The discrete velocities, \mathbf{e}_i , can be determined by:

$$\mathbf{e}_i = \begin{bmatrix} 0 & 1 & 0 & -1 & 0 \\ 0 & 0 & 1 & 0 & -1 \end{bmatrix} \quad (5.20)$$

The macroscopic temperature, T , is calculated by:

$$T = \sum_i h_i \quad (5.21)$$

The source term, ϕ_{1-v} , can be written as [244]:

$$\phi_{1-v} = T \left[1 - \frac{T}{\rho c_p} \left(\frac{\partial P}{\partial T} \right)_\rho \right] \nabla \cdot \mathbf{v} \quad (5.22)$$

In which c_p is the heat capacity, and $\nabla \cdot \mathbf{v}$ can be calculated using the second-order central difference scheme [248]:

$$\frac{\partial v}{\partial x_\alpha} = \sum_{j \neq 0} \frac{\omega_j \mathbf{e}_j \cdot \mathbf{i} [v(\mathbf{x} + \mathbf{e}_j \delta_t) - v(\mathbf{x} - \mathbf{e}_j \delta_t)]}{2c_s^2 \Delta t} \quad (5.23)$$

where \mathbf{i} is the unit vector of the i -coordinate axis.

The source term, ϕ_{1-i} , has the form as [247]:

$$\phi_{1-i} = \frac{\Delta h [f_s(\mathbf{x}, t) - f_s(\mathbf{x}, t - \delta_t)]}{c_p} \quad (5.24)$$

where Δh is the latent heat of the fusion of ice and f_s is the ice fraction.

5.2.3 Inclusion of the recalescence stage

The water remains in the metastable supercooled state prior to the recalescence stage, which commences when a stable ice nucleus is formed when the temperature drops below the ice nucleation temperature (T_{nuc}) [249]. The ice nucleus grows rapidly and spreads over the entire supercooled space in the form of dendritic ice, generating the initial spatial distributions of the ice fractions.

The recalescence stage is so rapid that it can be viewed as an “explosion” of ice, which is even more pronounced at high degrees of supercooling. Such a high growth speed for the dendritic ice can be attributed to the presence of local water clusters in which the bonded water molecules have relatively low kinetic energies, averaging 2 kJ/mol lower than unbonded ones [249]. This, in turn, allows the clusters to form the ice network more readily [249]. The lifetime and concentration of the hydrogen bonds of the water clusters are the sole functions of temperature [250]. Therefore, the growth speed of the ice dendrites strongly hinges on the local temperature of the surrounding unfrozen liquid. According to the empirical correlation of Lindenmeyer and Chalmers [251], the growth

speed of the dendritic ice, from a nucleated node (\mathbf{x}, t) to a neighbouring unfrozen node $(\mathbf{x} + \mathbf{e}_i \delta t, t)$, can be expressed by:

$$u_{i,\text{ice}} = 131 \times [\Delta T(\mathbf{x} + \mathbf{e}_i \delta t, t)]^{2.39} \quad (5.25)$$

where $\Delta T(\mathbf{x} + \mathbf{e}_i \delta t, t)$ is the degree of supercooling at the neighbouring node. It is worth mentioning that some other models of dendritic ice growth have been reported in the literature, including those in recent works such as [252-254]. These models generate different dendritic ice growth speeds, e.g., 16% deviation when using the latest modified Langer and Müller-Krumbhaar (LM-K) model [254] and the model of Lindenmeyer and Chalmers [251] for a supercooling degree of 293 K. However, the growth speed of the dendritic ice is far greater than the subsequent freezing (i.e., crystal growth) speed. For the supercooling degrees of 239.15 K, 253.15 K and 263.15 K, the calculated dendritic ice growth speeds were 1.04 m/s, 0.29 m/s and 0.06 m/s, respectively, whereas the predicted freezing speeds were 0.0025 m/s, 0.0006 m/s and 0.0003 m/s, which corresponded to the speed ratios of 416, 483 and 200, respectively. The recalescence stage can thus be viewed as instantaneous compared to the subsequent slow freezing stage of the small supercooled volume. Therefore, the application of different growth speed models for the dendritic ice would cause only marginal differences in the simulation results in terms of the distributions of the initial ice fractions and the subsequent freezing stage.

It is evident that for a given supercooled point it can be nucleated and generate ice by: (i) reaching T_{nuc} and forming a stable ice nucleus itself, or (ii) being positioned in the spreading path of the ice dendrites. The initial ice fraction, f_{s0} , generated at a nucleated

point in the recalescence stage is determined by the local temperature. In this study, the Stefan number (Ste) is used to calculate the local ice fraction [255] and is expressed as:

$$f_{s0}(\mathbf{x}, t) = Ste = \frac{c_p(\Delta T)}{\delta h} \quad (5.26)$$

where $f_{s0}(\mathbf{x}, t)$ is the local transient initial ice fraction, and ΔT is the local degree of supercooling.

The freezing stage, which is described as a slow crystal growth process [253], starts right after the onset of the recalescence stage. The evolution of this process is characterised by tracking the ice-water interface, which is governed by the enthalpy-based method [247, 256]:

$$f_s' = \begin{cases} 0 & H \geq H_l \\ \frac{H_l - H}{H_l - H_s} & H_s < H < H_l \\ 1 & H < H_s \end{cases} \quad (5.27)$$

where H_l and H_s are the enthalpies of the water at liquefying and solidifying points, respectively. The local enthalpy, H , is calculated by:

$$H = c_p T + f_s \times \delta h \quad (5.28)$$

f_s' and f_s are the local ice fractions in the present and last time steps, respectively. Evidently, if f_s in Equation (5.27) equals 0, the f_s' calculated by Equation (5.26) is the initial ice fraction. Hence, Equation (5.27) could also be used to calculate the initial ice fraction in the recalescence stage. In this study, both the enthalpy-based method and the Ste method are used and examined the predictions of the local ice fractions in the recalescence stage.

After obtaining the distributions of the initial ice fractions, the recalescence stage is included in the model as a source term [247, 257] of Equation (5.17) by Equation (5.24).

For the fluid field, the fully frozen node does not participate in the particle collision and migration. However, for the partially frozen node, the liquid part still has an effect on the flow field. For the accuracy of the simulation, the flow problem on the partially frozen node needs to be properly treated. This study has followed the percolation theory adopted by [258] for the treatment of porous media. Based on this theory, Equation (5.1) is then modified as:

$$\begin{aligned}
 f_\alpha(\mathbf{x} + \mathbf{e}_\alpha \delta_t, t + \delta_t) \\
 &= f_s f_\alpha(\mathbf{x} + \mathbf{e}_\alpha \delta_t, t) + (1 - f_s) \cdot M^{-1}[m - \Lambda(m - m^{\text{eq}}) \\
 &\quad + \delta_t S]
 \end{aligned} \tag{5.29}$$

obviously, when $f_s = 0$ the node is liquid; when $f_s = 1$ the node is totally solid; and when $0 < f_s < 1$ the node is a mixture of liquid and ice.

5.2.4 Ice nucleation onset temperature under pressure

During the collapse of cavitation bubbles, the inertia of the surrounding water causes an ultra-high pressure of several giga-pascals [37]. Under such high pressures, the water melting temperature varies dramatically. In this study, the Simon-Glatzel equation [228] was used to describe the ice melting curve as a function of the pressure:

$$T_m = T_0 \left(\frac{\Delta p}{a^*} + 1 \right)^{1/b^*} T_{\text{ref}} \tag{5.30}$$

where $\Delta p = \frac{p^{EOS}}{p_c} 22.06 - p'_0$, p'_0 and T_0 are the reference pressure and temperature, respectively, and T_{ref} is the reference temperature between the physical unit and the lattice unit. The values of p'_0 , T_0 , a^* and b^* for the ice phases are listed in Table 3.1.

For reasons of simplicity, efficiency and saving computational resources, an empirical equation was adopted for the ice nucleation temperature in this study, which has the form [37]:

$$T_{\text{hom}} = 0.86T_0 \left(\frac{\Delta P}{a^*} + 1 \right)^{1/b^*} \quad (5.31)$$

5.3 Model validation

5.3.1 Thermodynamic consistency

This section investigates the effects of the parameters k and σ on the thermodynamic consistency of the present MRT-LBM. A static droplet (radius: $R_{\text{drop}} = 40$), surrounded by vapour, is placed in the centre of a gravity-free computational domain. Note that all of the variables in LBM studies, if not specified, are in lattice units which can be converted into physical values based on the main reduced properties [259] (see Table 5.1 for the conversions of the units). For the lattice units, the unit of time is ts , the unit of length is lu , the unit of density is mu/lu^3 , and the unit of pressure is $mu/(lu.ts^2)$. The temperature is dimensionless.

Table 5.1. Unit conversion table.

Parameter	Lattice unit	Physics unit
Length	1	4.0×10^{-9} m

Time	1	1.6×10^{-12} s
Temperature	1	647.1 K
Viscosity ^a	0.1	1.0×10^{-6} m ² /s
Density	0.1	0.247 g/cm ³
Pressure	0.1	848.5 MPa

^a Values at 293 K.

The grid size was 201×201 and the periodic boundary scheme was applied to all four boundaries. The initial density of the liquid (vapour) was set according to the Maxwell construction. The density field in the computational domain was initialised by:

$$\rho(x, y) = \frac{\rho_l + \rho_v}{2} - \frac{\rho_l - \rho_v}{2} \left\{ \tanh \left[\frac{2\sqrt{(x - x_0)^2 + (y - y_0)^2} - R_{\text{drop}}}{W} \right] \right\} \quad (5.32)$$

For each k value, the σ value is adjusted to match the Maxwell construction curve. After the steady-state was achieved, the densities and pressures of the liquid and vapour were recorded.

Figure 5.1 (a) below shows the density coexistence curve of the present MRT-LBM. The left curve is the vapour branch and the right curve is the liquid branch. Clearly, the simulation results from the present model agree with the theoretical results predicted by the Maxwell equation. Moreover, with Li's forcing scheme, a large temperature range (i.e., $0.5T_c$ to T_c) can be achieved. Three different values of k are investigated, namely $k = 1.0$, $k = 0.5$ and $k = 0.1$. For $k < 1.0$, the σ value needs to be slightly tuned up to maintain the thermodynamic consistency. In addition, the reduced k value can further widen the temperature range, reaching temperatures as low as $T = 0.38T_c$ with $k = 0.1$ and $\sigma = 0.112$, which corresponded to the physical temperature of 245.9 K. The reduced surface tension, θ , was also realised at the same temperature. As shown in Figure

5.1 (b), the relationship of the pressure difference, Δp , across the vapour-liquid interface as a function of the droplet radius for $T_0 = 0.6T_c$ was obtained. It can be observed that the Δp increased linearly with the reduced droplet radii. The results were in line with the Laplace law which states that the pressure difference across the boundary of a droplet is inversely proportional to the droplet's radius [200].

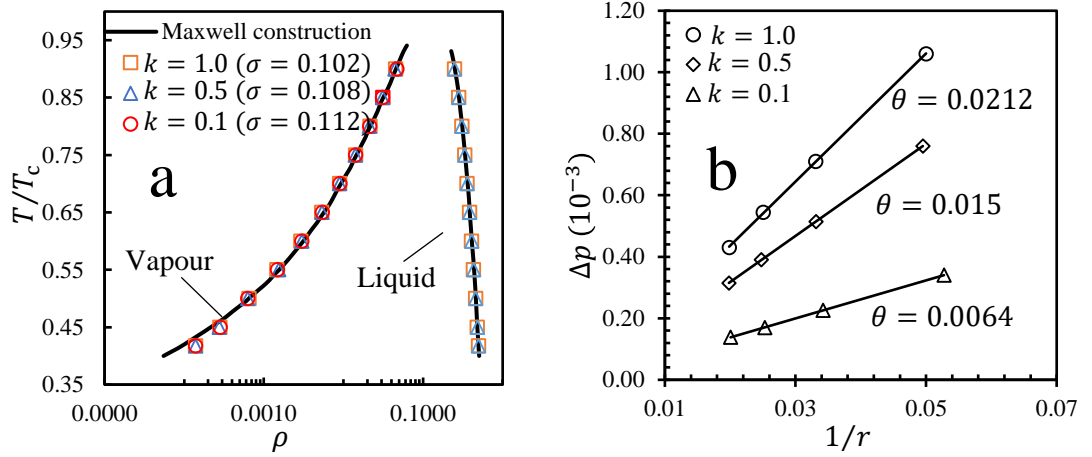


Figure 5.1. Thermodynamic consistencies: (a) comparison of the coexistence curve of the MRT-LBM with the Maxwell construction, (b) pressure differences between the liquid drop and the vapour phase as a function of $1/r$ at $T_0 = 0.6T_c$.

5.3.2 Free bubble growth and shrinkage

The evolution of a single bubble with an initial radius of R_0 in infinite space was simulated using the present model and was compared to the analytical solutions. The computational domain was set here as a 401×401 grid, the R_0 was set as 40, and the ρ_v was set as 0.0095, based on the density coexistence curve at $T_0 = 0.7T_c$. In order to simulate the growth and shrinkage of the cavitation bubbles, the initial density of the liquid was artificially changed to obtain a proper pressure difference, $\Delta p = p_l - p_v$. Under a critical pressure difference, Δp_{cri} , the bubble radius will remain unchanged, i.e.,

the bubble reaches its critical size (R_{cri}). This critical bubble size can be calculated through the Laplace law ($R_{\text{cri}} = -\theta/\Delta p_{\text{cri}}$). In other words, for a given initial bubble, if the $\Delta p > \Delta p_{\text{cri}}$ the vapour bubble will start shrinking rather than cavitating as condensation is preferable in terms of lowering the energy of the system. To the contrary, if the $\Delta p < \Delta p_{\text{cri}}$ the cavitating will dominate the evolution process of the bubble sizes. In order to have better accordance with the physical situation, the non-equilibrium extrapolation boundary scheme [247, 260] was applied for the four periodic boundaries.

The analytical solution for the evolution of the bubble sizes can be obtained by the R-P equation:

$$\rho_1 \left(R\ddot{R} + \frac{3}{2}\dot{R}^2 \right) = p_b - p(t) - p_0 + \frac{R}{c_1} \frac{d}{dt} p_b - 4\eta_l \frac{\dot{R}}{R} - \frac{2\theta}{R} \quad (5.33)$$

where p_b is the bubble pressure, $p(t)$ is the external driving pressure as a function of time, p_0 is the static pressure, c_1 is the sound velocity in liquid, η_l is the liquid viscosity, and θ is the surface tension. For a two-dimensional simulation, the R-P equation is boundary sensitive, as pointed out by Chen [261]. Therefore, following [139, 261], Equation (5.33) should be revised as:

$$\ln \left(\frac{R_{\text{bound}}}{R} \right) \rho_1 \left(R\ddot{R} + \frac{3}{2}\dot{R}^2 \right) + 2\eta_l \frac{\dot{R}}{R} + \frac{\theta}{R} = p_b - p_{\text{bound}} \quad (5.34)$$

where R_{bound} is the computational domain size and p_{bound} is the pressure at the boundary. The revised R-P equation can be solved using the 4th order Runger-Kutta integration algorithm. For a comparison between the analytical solutions and the simulation results, the lattice values are used for all variables in the R-P equation. The

viscosity can then be given as $\eta_l = (2\tau_v - 1)/6$ and the surface tension $\theta = 0.0191$ is obtained by the Laplace law [139].

Figure 5.2 below shows a comparison between the simulation results of the present LBM and the analytical solutions of the revised R-P equation. Clearly, the simulation results agreed with the revised R-P equation solutions. The critical pressure for $R_0 = 40$ is $\Delta p_{\text{cri}} = -4.8 \times 10^{-4}$. As predicted by the revised R-P equation, the bubble grows with $\Delta p > \Delta p_{\text{cri}}$, and shrinks with $\Delta p < \Delta p_{\text{cri}}$. It can be noticed that, for the bubble growth case, the simulation results of the present numerical model tended to yield a faster bubble expansion than the R-P equation in the early stages of the bubble growth. However, in the later stages of bubble growth, the bubble expansion was significantly affected by the limited computational domain size [262]. Therefore, the simulation predicted a slower growth rate than the revised R-P equation. For the shrinking of the bubble, the deviations between the simulation results and the revised R-P equation solutions lay in the treatment of the viscosity of the fluid. In the LBM, the liquid and vapour shared the same viscosity, while the revised R-P equation did not consider the viscosity of the vapour.

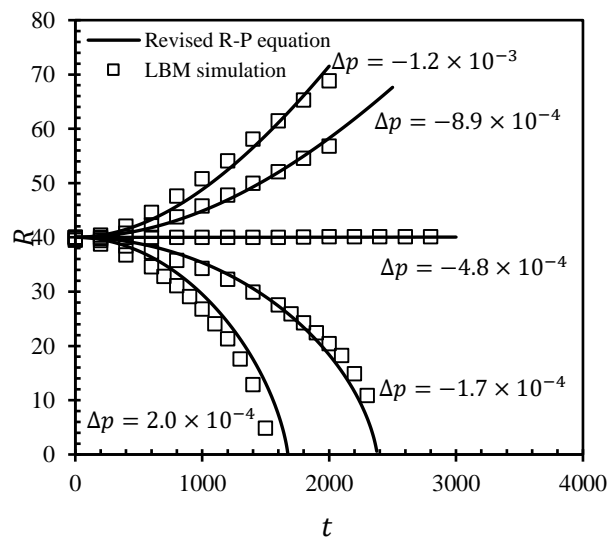


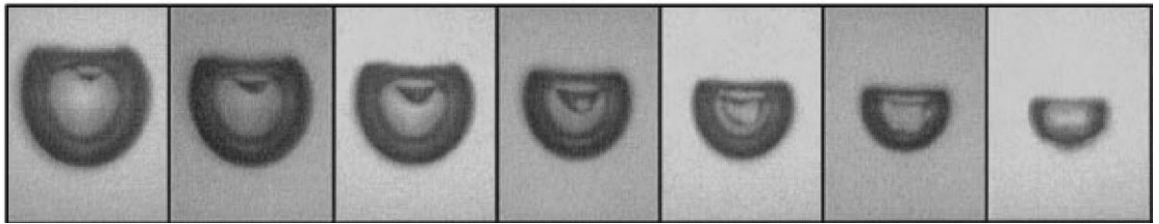
Figure 5.2. Comparison of the evolution of the sizes of the cavitation bubbles between the simulation results and the analytical solutions.

5.3.3 Evolution of the bubble profile in the neighbourhood of a solid boundary

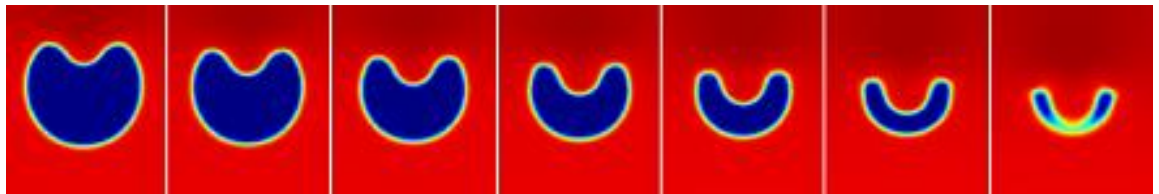
The collapse of cavitation bubbles in the vicinity of a solid boundary has been widely studied. The benchmark experimental measurements for the evolution of the bubble profiles, as also adopted in [263-265], was used to qualitatively validate the present model. The computational domain was set as a 401×401 grid. For the ice nucleation near a solid boundary, a dimensionless coefficient, λ , was assigned as the standoff distance. The λ was defined as $\frac{d_b}{R_0}$, where d_b is the distance between the initial centre of the bubble and the boundary of the solid. It is worth noting that in the LBM simulations of actual large-scale systems, due to the limits of the prohibitive computational overheads, a common practice to reduce the computational costs is to keep the key dimensionless numbers the same [139, 244]. In this study, λ is used as the key dimensionless number to ensure a consistent basis for comparison and the discussions. The bounce-back boundary condition was adopted for the bottom solid wall boundary. The periodic boundary was applied to the left and right boundary and was implemented through the non-equilibrium extrapolation method (NEM). The top boundary was treated as a pressure boundary implemented through NEM. The determination of the initial conditions was non-trivial due to the lack of data in the early stages of the laser-induced bubble generation, following the plasma recombination in the experiments [37]. Therefore, the initial conditions have been determined such that the radii of the bubbles and the standoff distances were the same as the available experimental data. The initial bubble radius (R_0) and the vapour bubble standoff distance (λ) were set as 80 and

1.6, respectively. Following the work of Chi et al. [244], the initial temperature was set at $0.6T_c$.

The simulation results for the evolution of the bubble profiles near a solid boundary were compared with the experimental data of Philipp et al. [264], as shown in Figure 5.3 below. For ease of identification, the density field of the simulation results is presented. Evidently, the simulation results qualitatively agreed with the experimental results. It can be noticed that an inward concave occurred on the top of the bubble and moved quickly to the internal bottom of the bubble. This unique bubble profile deformation was attributed to the presence of the solid boundary. It is believed that the solid boundary was able to break the symmetry of the external pressure distribution around the bubble [139, 205], resulting in a higher pressure above the bubble compared to the pressure below the bubble. When the top interface reaches the bottom interface, the bubble collapses. The resultant high pressures and temperatures will determine the onset of the ice nucleation, as detailed in the next section.



(a) Experimental photo: $\lambda = 1.6$, $R_0 = 1.45$ mm, $\Delta t = 10^{-6}$ s



(b) Simulated density field: $\lambda = 1.6$, $R_0 = 80$, $T_0 = 0.6T_c$, $\Delta t = 11$,
 $\Delta p = 0.0078$, $k = 1.0$, $\sigma = 1.02$

Figure 5.3. Comparison of the evolution of the bubble profiles between the simulation results and the experimental data: (a) experimental data, (b) LBM simulation results.

5.3.4 Evolution of the ice-water interface

To verify the present model’s capability of capturing the movements of the ice-water interface, a practical unidirectional freezing problem was simulated. Specifically, a capillary tube with a certain amount of water sample was employed to monitor the evolution of the ice-water interface. As depicted in Figure 5.4 below, the entire space surrounding the capillary tube was selected as the computational domain, which had a size of $10 \times 14 \text{ mm}^2$. In between the water sample and the bottom of the tube, there was a layer of oil (thickness: 1.0 mm; pour point: 173.15 K). The bottom of the domain was set as the cooling boundary.

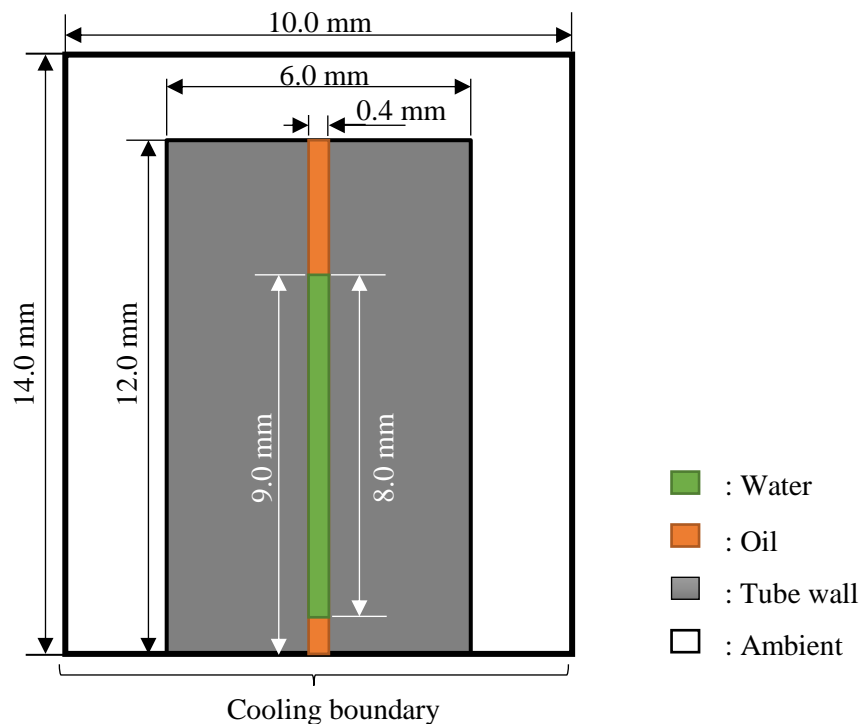


Figure 5.4. Schematic illustration of the computational domain.

For all of the boundaries, the NEM was adopted with the temperature of the cooling boundary fixed at the given temperature. The simulations were conducted strictly following the experimental set-up and operating conditions, as detailed in Appendix A, including the domain geometries, cooling module temperatures, cooling times and physiochemical properties of the liquids. For the simulations of cases with large time scales in this study, different lattice units were used (see Table 5.2). Note that this unit conversion table is only applicable to Section 5.3.4 and Section 5.4.1.

Table 5.2. Unit conversion table.

Parameter	Lattice unit	Physics unit
Length	1	3.3×10^{-5} m
Time	1	0.019 s
Temperature	1	1 K
Viscosity ^a	0.1	8.7×10^{-7} m ² /s
Density ^a	1	1 g/cm ³

^a Values at 293.15 K.

The quantitative comparisons between the LBM simulation results and the experimental data on the evolution of the ice-water interface are shown in Figure 5.5 below. Clearly, the model's predicted results using the *Ste* method can provide good agreement with the experimental data. It can be seen that the deviations between the LBM predictions and the experimental data increased with time, particularly after 4 seconds. This might have been because the experimental data, i.e., the ice-water interface, was greatly affected by the heat loss on the upper part of the capillary tube where the convective heat transfer was strong.

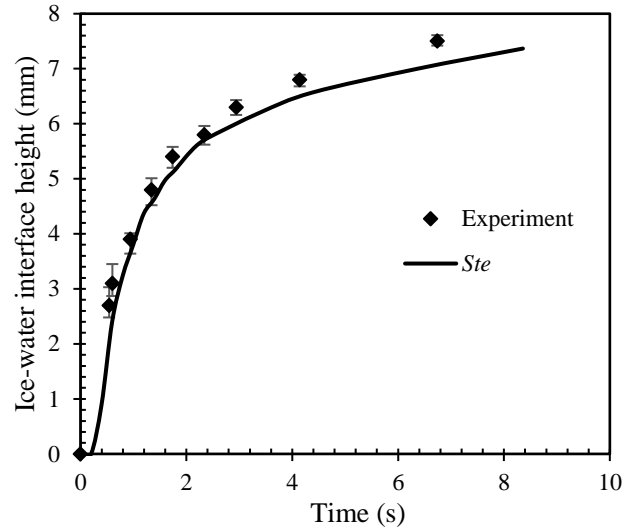


Figure 5.5. Comparison between the experimental data and the simulation results considering the recalescence stage [$T_0 = 293 \text{ K}$, $T_{cp} = 228 \text{ K}$, $T_{nuc} = 239 \text{ K}$ and $d_t = 0.4 \text{ mm}$].

5.4 Numerical studies

5.4.1 Effects of the recalescence stage on the freezing process

Once the supercooled water is nucleated, the solidification process undergoes three distinct stages, namely: recalescence (i.e., dendritic ice growth driven by the supercooling), freezing (i.e., crystal growth governed by the heat transfer), and solid cooling [247, 266]. The supercooled water phenomenon and the subsequent solidification process are commonly encountered in many natural and industrial processes, including spray crystallization [266], aircraft icing [267], freezing rain [268], plant freezing [269], and cold energy storage systems [1, 13, 270, 271]. The process of freezing the water presents a significant challenge to the safety, efficiency and performance of these processes.

Experimental investigations into the nucleation phenomenon and its subsequent freezing process have been carried out by many researchers, including their dependence on the presence of solid particles, solid surfaces and ultrasonic cavitation bubbles [e.g. 87, 272, 273-277]. However, to quantitatively describe the ice freezing process has proved very challenging using an experimental approach alone. Data such as the transient temperature field and the local distribution of ice fractions are difficult to acquire given the short times and length scales of the physics involved in the problem.

The recalescence stage features the rapid growth of dendritic ice over the entire supercooled space until the degree of supercooling is exhausted. Generally, two major changes take place after the recalescence stage: (i) a temperature rise due to the release of latent heat, and (ii) a distribution of dendritic ice in the entire supercooled space (henceforth referred to as the distribution of the initial ice fraction). It is evidently straightforward to consider the temperature change after the recalescence stage. Indeed, in most of the previous LBM simulations, the recalescence stage was conceptionally treated by simply initialising the system temperature to 273.15 K, yet the distribution of the initial ice fraction was completely ignored [247, 256, 278, 279].

The local initial ice fraction is mainly determined by the local degree of supercooling, i.e., the larger the degree of supercooling, the higher the ice fraction [255]. For small volumes of water that often bear a very large degree of supercooling (> 300 K), the role of the distribution of the initial ice fraction in dictating the subsequent freezing kinetics might be of great relevance.

In this study, both the Stefan number [280] (ratio of sensible heat to latent heat) and an enthalpy-based method [247, 256] were applied to calculate the initial ice fraction in the

recalescence stage. The effectiveness of these two methods has been examined and compared. Moreover, based on the developed model, the kinetics of the freezing characterised by the evolution of the variations in the local temperatures, the ice-water interface and the freezing rate have been analysed and discussed.

5.4.1.1 Numerical modelling

The computational domain size and boundary conditions were the same as the numerical model described in Section 5.3.4. Firstly, the simulations of the freezing process with and without the recalescence stage were conducted at a degree of supercooling of 34 K. Furthermore, to quantify the effects of the recalescence stage on the freezing process, different degrees of supercooling were applied (i.e., 0 K, 10 K, 20 K, and 34 K). In addition, to investigate the effects of the cooling boundary temperature on the evolution of the ice-water interface, T_{cp} was set to a range of 226 K to 230 K. The temperature of the computational domains was initialised as $T_0 = 293$ K.

5.4.1.2 Results and discussion

The measured cooling time (t_{nuc}) required for the water sample to reach the nucleation temperature and start to freeze under each T_{cp} is shown in Figure 5.6 below. It has been documented in the literature that T_{nuc} is a function of the water properties (e.g., volumes and impurities), and is independent of the T_{cp} and cooling time. An exponential correlation fitted between the t_{nuc} and T_{cp} was used to obtain the required time to reach the T_{nuc} for a given T_{cp} . By incorporating the value of t_{nuc} into the simulation, the T_{nuc} was consistently determined as ~ 239 K for the water samples used in the experiments for this study. It is worth noting that due to the surface hydrophilicity, the side of the water sample was presumably in direct contact with the capillary tube wall

(glass), as illustrated in Figure 5.4. It is likely that the roughness or impurities on the wall surfaces acted as nucleation sites and in turn induced the HeN [114]. However, it cannot be concluded with certainty that the surface topography of the tube wall or the impurities led to the occurrence of HeN, as the nucleation temperature was not far above the homogeneous limit [30, 281]. Significant work is required if we are to discriminate between HoN and HeN by accurately quantifying the role of the properties of the surfaces of the tube walls, which is certainly much beyond the scope of the present work. For this reason, $T_{nuc} = 239$ K is just considered as the nucleation temperature of the water samples used in the experiments in this study.

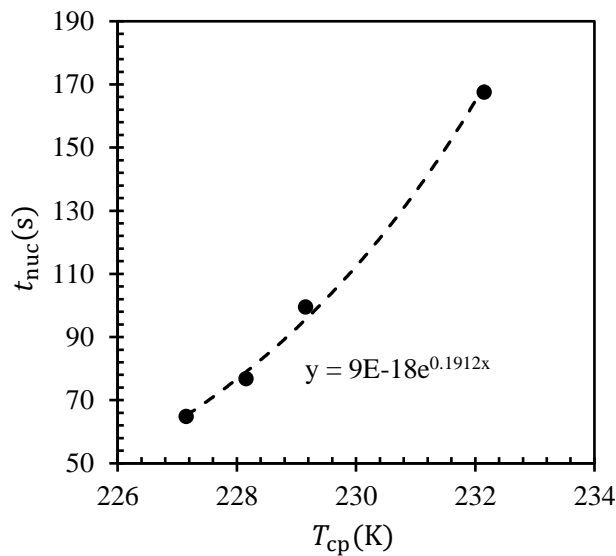


Figure 5.6. Cooling time (t_{nuc}) required to reach T_{nuc} at different T_{cp} ($T_0 = 293$ K and $d_t = 0.4$ mm). The *Ste* method was used to calculate the initial ice fraction generated in the recalescence stage. The dots represent the experimental data; the dashed-line represents the fitting curve.

Figure 5.7 below demonstrates the time series of the ice-water interface captured in the simulations and experiments. The images on the left-hand side and in the middle show the contours of the ice fraction predicted using the models without and with a

consideration of the recalescence stage, respectively, and the image on the right-hand side is the raw images taken from the experiments. It can be seen that the extended LBM with the inclusion of the recalescence stage accurately captured the kinetics of the freezing process. Specifically, the rapid recalescence stage completed in 0.19 s, with dendritic ice distributing over the entire supercooled domain. The freezing stage started after the onset of the recalescence stage. The ice-water interface slowly moved upwards along the tube height with a rate governed by the enthalpy change. The conical shape of the ice-water interface was due to the relatively high thermal conductivity of the walls of the capillary tube compared to those of water and oil, thus leading to a fast heat transfer rate and a large change in the temperature. By contrast, the model without the recalescence stage provided a poor description of the freezing kinetics that significantly deviated from the experimental measurements. For a consistent comparison and analysis, the position of the trough of the ice-water interface was used as the height of the ice-water interface.

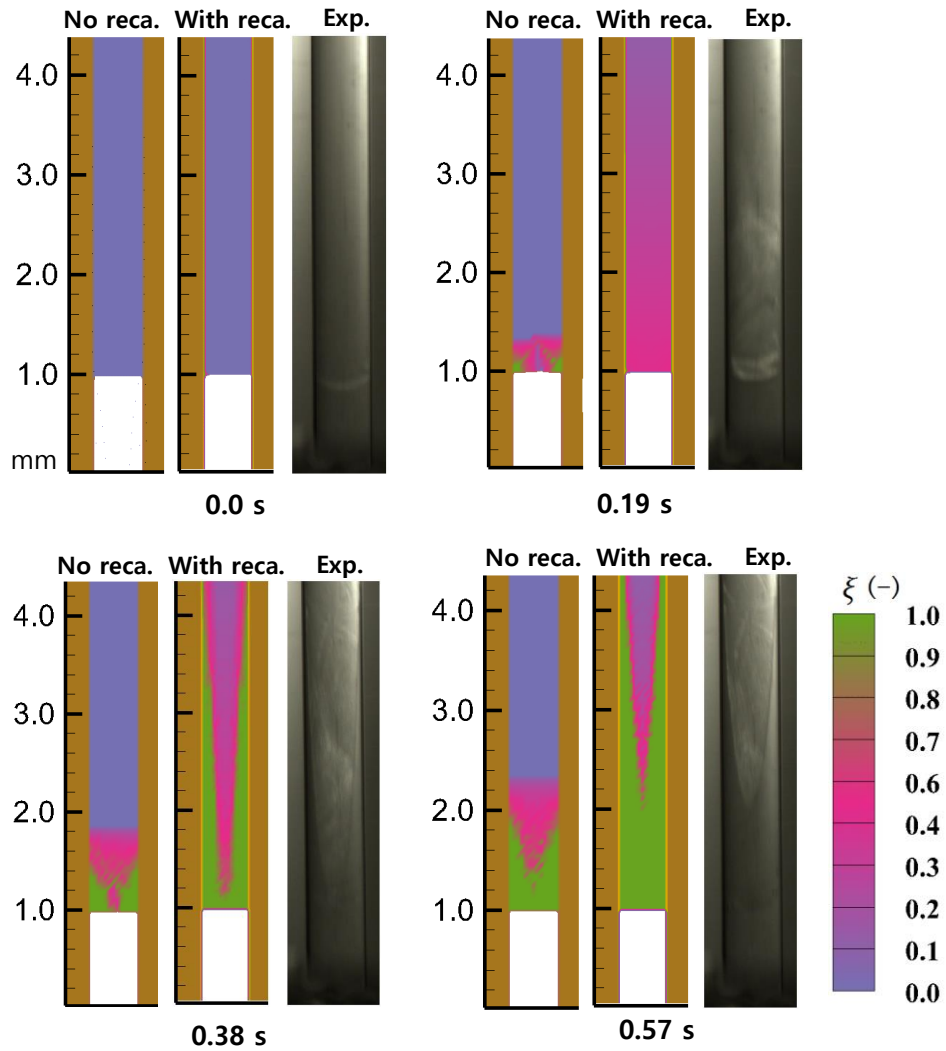


Figure 5.7. Time series of the ice-water interface captured in simulations and experiments ($T_0 = 293 \text{ K}$, $T_{cp} = 228 \text{ K}$, $T_{nuc} = 239 \text{ K}$ and $d_t = 0.4 \text{ mm}$). At each time instant, the image on the left-hand side is the predicted result using the model without considering the recalescence stage; the image in the middle is the results predicted by the extended LBM using the *Ste* method for calculating the initial ice fraction generated in the recalescence stage; and the image on the right-hand side is the raw data captured in experiments.

In Figure 5.8 below, the simulation data included the results predicted by the models that used the *Ste* method or the enthalpy-based method to calculate the initial ice fraction in the recalescence stage and the model which did not consider the recalescence stage. Clearly, the results predicted by the model without consideration of the recalescence stage

deviated most significantly from the experimental data. Though the time to complete the freezing stage was almost the same using the different models (e.g., 10 s), the model without consideration of the recalescence stage failed to predict the initial stage of the evolution of the ice-water interface.

It is also worth noting that the model that considered the recalescence stage using the enthalpy-based method to calculate the initial ice fraction also failed to predict the freezing stage, with the predicted ice-water interface being constantly lower than the measured values. When using the enthalpy method, the freezing process experienced an initial lag, after which the ice-water interface expanded at a similar rate to those measured in the experiments. This short lag can be explained by the initial ice fraction predicted by the enthalpy-based method in the recalescence stage. As shown in Figure 5.9 below, for temperatures above 245 K the enthalpy-based method and the *Ste* method predicted almost the same ice fraction. However, when the temperature dropped below 245 K, distinctly different results for the ice fraction were obtained using the two methods. Specifically, the *Ste* method predicted that the ice fraction was a monotonic function of the temperature, whereas the enthalpy-based method yielded a peak value of the ice fraction at $T = 245$ K. The monotonic increase of the ice fraction by the *Ste* method can be attributed to the abrupt increase in the water clusters upon the onset of the HoN [211]. However, the heat capacity of the water also increased when approaching the HoN temperature, leading to a high local enthalpy according to Equation (5.26). As a result, the initial ice fraction predicted by the enthalpy-based method plummeted at such low temperatures. In the present study, the estimated T_{nuc} was 239 K. Correspondingly, the initial ice fraction calculated by the enthalpy-based method was only 15%, which was much lower than that calculated by the *Ste* method (47%), resulting in the lag at the

beginning of the freezing stage. Therefore, for relatively high temperatures (≥ 245 K), both the *Ste* and the enthalpy methods might be valid for the prediction of initial ice fractions in the recalescence stage; whereas for temperatures lower than 245 K, the *Ste* method should be applied.

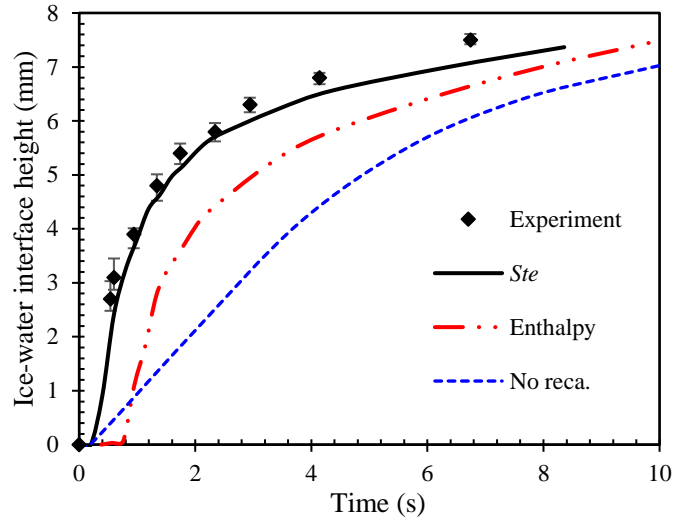


Figure 5.8. Comparison between the experimental data and the simulation results, with and without consideration of the recalescence stage [$T_0 = 293$ K, $T_{cp} = 228$ K, $T_{nuc} = 239$ K and $d_t = 0.4$ mm].

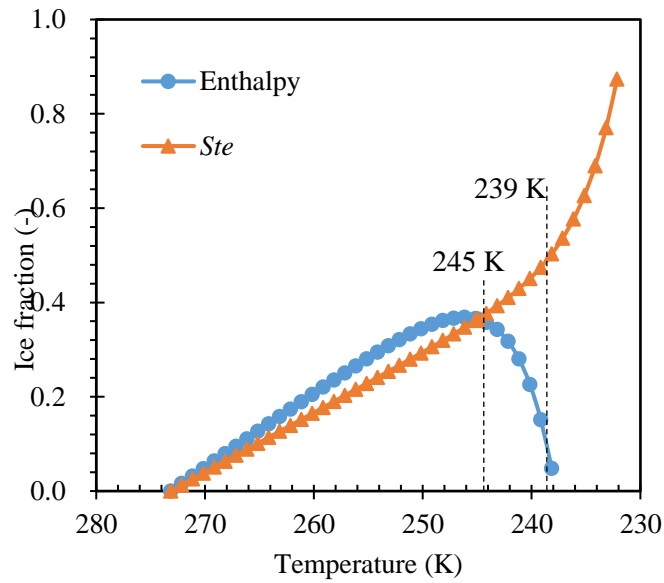


Figure 5.9. Initial ice fractions predicted by the enthalpy method and the *Ste* method over a wide range of temperatures.

Figure 5.10 below demonstrates the comparisons between the predicted results for the evolution of the ice-water interface using the models with and without consideration of the recalescence stage for the different degrees of supercooling. The *Ste* method was used to calculate the initial ice fraction in the model that considers the recalescence stage. When the degree of the supercooling was close to 273.15 K, the models with and without the recalescence stage generated identical results, with the two curves almost an exact overlap. As the degree of the supercooling increased, the discrepancies between the predicted results increased. This can be justified by the ice fraction generated in the recalescence stage under a certain degree of supercooling, as demonstrated in Figure 5.9. For the extreme case of a zero degree of supercooling, there was no ice generated in the recalescence stage. In other words, the recalescence stage did not exist. As the degree of the supercooling increased, the ice fraction increased and, accordingly, the role of the recalescence stage in determining the kinetics of the following freezing becomes more significant. It can also be seen that for the degree of supercooling of 293 K, the maximum deviation between the two sets of predicted results went up to 31% at 1.9 s ($\gamma = \Delta IH / IH_{Ste}$, where ΔIH is the maximum difference in the ice-water interface height and IH_{Ste} is the interface height predicted by the *Ste* method), indicating the necessity to consider the recalescence stage in the LBM simulation for such high degrees of supercooling (≥ 293 K).

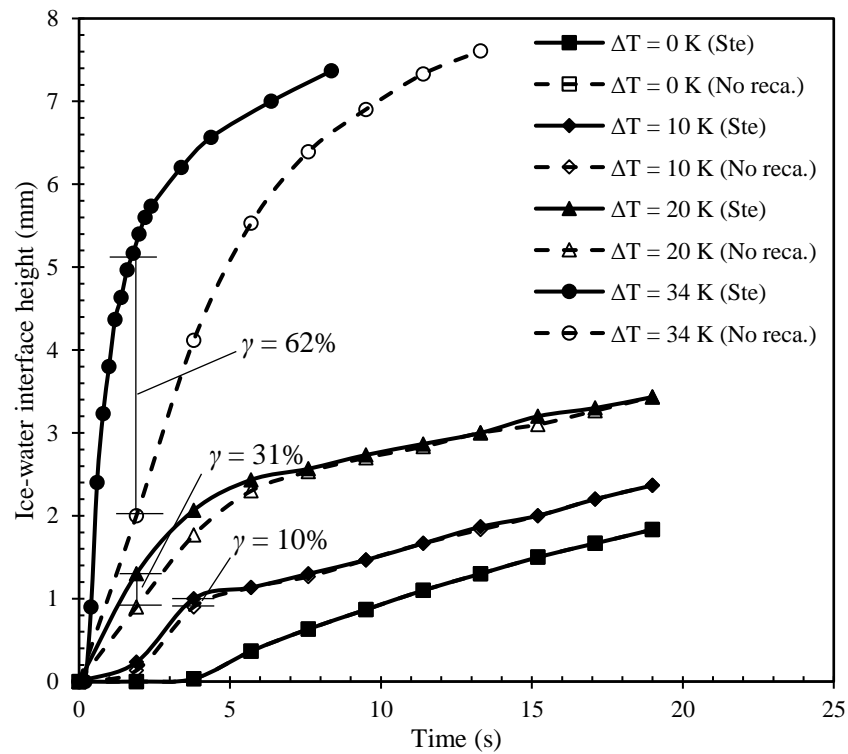


Figure 5.10. Comparison of the results predicted by the LBM model with and without consideration of the recalescence stage ($T_0 = 293\text{ K}$, $T_{cp} = 228\text{ K}$ and $d_t = 0.4\text{ mm}$). The *Ste* method was used to calculate the initial ice fractions in the model considering the recalescence stage.

The predicted freezing processes of the supercooled water under different T_{cp} (230 K, 228 K, and 226 K) is shown in Figure 5.11 below. The corresponding experimental data are also included. The results predicted by both the extended LBM model with the *Ste* method and the model without a consideration of the recalescence stage are included. Clearly, the results predicted by the extended LBM for the different T_{cp} all agreed with the experimental data, with the evolutionary trends being almost identical. The maximum deviation for all of the data points was 3.0%, within the limit of experimental error. The minor deviations may be attributed to the ideal (theoretical) conditions used in the simulations (e.g., constant nucleation temperature, constant water volume, and constant

oil height underneath the water), which were different, to some extent, to the practical and actual values in the experiments. Moreover, the limited operation errors and the inherent flaws of the methodologies for data acquisition in the experiments (e.g., the error in recording the cooling time) might have also contributed to the deviations.

It can also be seen that the freezing stage started earlier at the lower values of T_{cp} due to the greater heat flux induced by the larger temperature gradient (i.e., $\dot{q} \propto \Delta T$). However, the results also implied that the cooling time of the system before the water starts freezing (equal to t_{nuc}) was shorter for the lower T_{cp} values. In this study, the measured t_{nuc} was 65.0 s, 77.0 s and 100.0 s for the T_{cp} of 226 K, 228 K and 230 K, respectively. Clearly, under the higher T_{cp} values the system had been cooled for a longer duration at the instant the water sample started to freeze. The temperature fields of the system at $t_{nuc} + 0.19$ s for the different T_{cp} are shown in Figure 5.12 below. It can be seen that the temperature surrounding the tube channel in which the water freezing process was taking place was lower for the higher T_{cp} values. As a result, it is not surprising to find in Figure 5.11 that the predicted results using the no recalescence model also agreed with the experimental data at $T_{cp} = 226$ K, but deviated more significantly as the T_{cp} increased due to the increased degree of supercooling. The freezing rate that is measured by the slope of the evolutionary curve of the ice-water interface also increased as the T_{cp} increased on account of the greater temperature difference between the tube wall and the water (273.15 K after the recalescence stage).

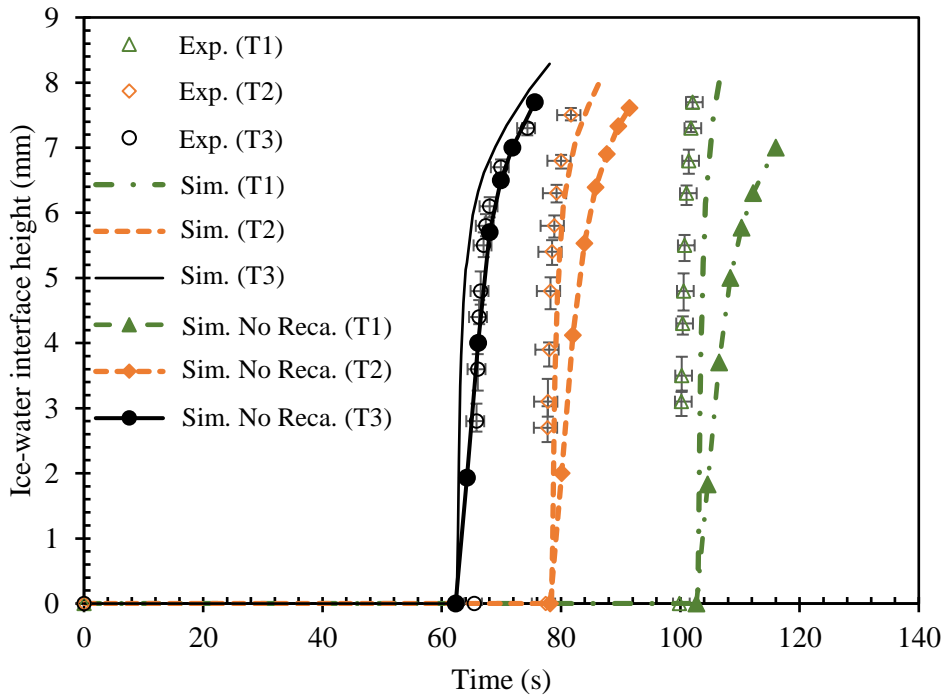


Figure 5.11. Evolution of the ice-water interface for different T_{cp} . [$T_0 = 293 \text{ K}$, $T_{nuc} = 239 \text{ K}$, and $d_t = 0.4 \text{ mm}$; the Ste method was used to calculate the initial ice fractions generated in the recalculation stage; T1, T2 and T3 were $T_{cp} = 230 \text{ K}$, $T_{cp} = 228 \text{ K}$, and $T_{cp} = 226 \text{ K}$, respectively]

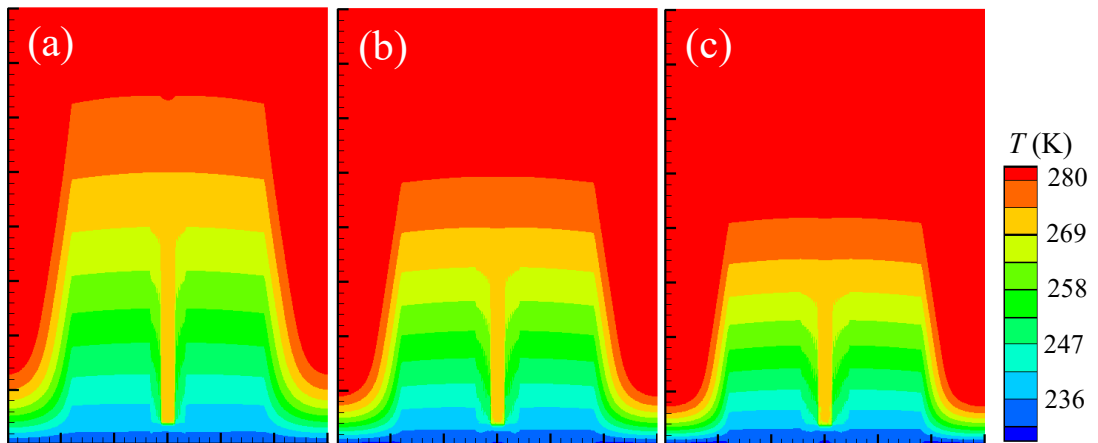


Figure 5.12. Temperature field at $t = 0.19 \text{ s}$ for three different T_{cp} after the onset of the nucleation: (a) $T_{cp} = 230 \text{ K}$, (b) $T_{cp} = 228 \text{ K}$, and (c) $T_{cp} = 226 \text{ K}$. The room temperature was set at 293 K , and the Ste method was used to calculate the initial ice fractions generated in the recalculation stage.

5.4.2 Ice nucleation induced by the collapse of cavitation bubbles

Cavitation is a very common phenomenon and is frequently found around a fast-rotating propeller [115, 135]. One can notice that the collapse of cavitation bubbles may result in severe damage to the surfaces of a material due to the extremely high pressure, high temperature and strong jet currents [115]. However, such phenomenal physical properties can also be utilised in achieving many other different purposes, such as ultrasonic cleaning [136], sonochemistry [137] and shockwave therapy [138]. In the past decades, ultrasonic cavitation has also been successfully used to induce ice nucleation [25, 32, 34, 116]. Though dozens of laudable experiments have been conducted to reveal the high efficiency of cavitation bubbles in triggering ice nucleation [32, 34, 37], there are many puzzles that remain unsolved, such as the pressure and temperature field distribution after the collapse of the cavitation bubbles. Due to the small scale and the rapid process, direct measurements of these relative parameters are quite difficult [139], therefore numerical simulations are usually adopted as a powerful tool to gain an understanding of these parameters.

To address the thermodynamic behaviours of the cavitation bubbles and the closely related phase change problem, a temperature equation needs to be incorporated into the LBM model. There are two popular strategies available in the literature: the double distribution function (DDF) scheme [247, 256, 257] and the finite difference (FD) scheme [282-284]. In the DDF thermal LBM, the temperature field is solved by using a source term incorporated into the thermal LB equation. Using the DDF scheme, Yang et al. [139] examined the thermodynamic behaviours of the cavitation bubbles. The simulation results satisfied the maximum temperature equation derived from the R-P equation. The FD scheme directly solved the discretised temperature equation that was coupled with the

LBM through the non-ideal EoS. By employing this FD-LBM hybrid model, Peng et al. [244] successfully reproduced a laser-induced process of cavitation bubble growth and collapse. As pointed out by Li et al. [285], the forcing term used in the DDF scheme would yield considerable errors in the LBM predictions of thermal flows due to the high spurious current. This error could be greatly reduced by the modified thermal LBM proposed by Gong et al. [286].

Overall, the above studies could well prove the capability of the LBM in simulating the phenomenon of cavitation bubbles. In the past decade, the LBM has been employed in studies of many research fields that have been related to cavitation bubbles. For example, Shan et al. [197] studied the collapse of cavitation bubbles near a solid boundary; Chen [287] investigated the phenomenon of natural cavitation formation under the shear flow due to pressure falls below the liquid vapour pressure; Peng et al. [262] simulated the heterogeneous cavitation nucleation in a crevice; and Mishra et al. [288] coupled the reaction kinetics and hydrodynamics in a collapsing cavity and demonstrated the concentrations of the highly heterogeneous solutes. However, to the best of the author's knowledge, there has been no LBM study that has extended to the examination of ice nucleation as a result of the pressure shocks from the collapse of cavitation bubbles. The effects of the collapsing pressure, temperature and jet currents on the distribution of the ice nucleation onset sites and the subsequent freezing process are still missing. Hence, it is vital to conduct a series of simulations of ice nucleation which have been induced by the collapse of cavitation bubbles.

In the present study, the pseudo-potential MRT-LBM with Li's forcing scheme was adopted for the density field distribution. To achieve a thermodynamic consistency, the non-ideal EoS was coupled with the pseudo-potential model. The temperature field was

solved by the thermal LBM proposed by Gong et al. [286] as the LBM scheme was computationally more efficient than the FD scheme. During the collapse of the cavitation bubbles, the evolution of the pressure and the temperature field are discussed. The corresponding melting temperature and the ice nucleation onset temperature as a function of the local pressure are estimated using the Simon-Glatzel equation [228] and an empirical equation, respectively. Following the onset of the ice nucleation, the recalescence stage of the freezing process [289] is considered for the distribution of the initial ice fractions. Two different scenarios for the collapse of the cavitation bubbles are discussed, namely: a collapse of the bubbles near a solid boundary, and a collapse with four pressure boundaries. The effects of the initial pressure differences, the bubble sizes and the standoff distances on the ice nucleation are also investigated.

5.4.2.1 Numerical modelling

In the present study, ice nucleations induced by the collapse of cavitation bubbles were numerically investigated in two scenarios: (i) near a solid boundary, and (ii) within a pressurised space. For both scenarios, the computational domain was set as a 401×401 grid. The temperature field was initialised as $T_0 = 0.4175T_c$ which corresponded to 270.15 K. The density of the vapour bubble was set as $\rho_v = 0.000138$.

For the first scenario, as shown in Figure 5.13(i), the bounce-back boundary condition was adopted for the bottom solid wall boundary; the periodic boundary was applied to the left and right boundary and was implemented through the non-equilibrium extrapolation method (NEM); the top boundary was treated as a pressure boundary implemented through NEM. The initial radii of the bubbles and the vapour bubble standoff distance ranged from 10 to 80 and 1.5 to 3.5, respectively. Another key parameter was the

initial density of the liquid, which determined the initial pressure difference, between the vapour bubble and the liquid phase. In this study, the ρ_l was set in a range from 0.52 to 0.53.

For the second ice nucleation scenario, all of the four boundaries were treated as the pressure boundaries with the NEM. The vapour bubble was fixed at the centre of the computational domain, as depicted in Figure 5.13(ii) below. The R_0 ranged from 10 to 80 and the ρ_l was set in a range from 0.506 to 0.52. The densities of the four boundaries were set as constant with the initial density of the liquid.

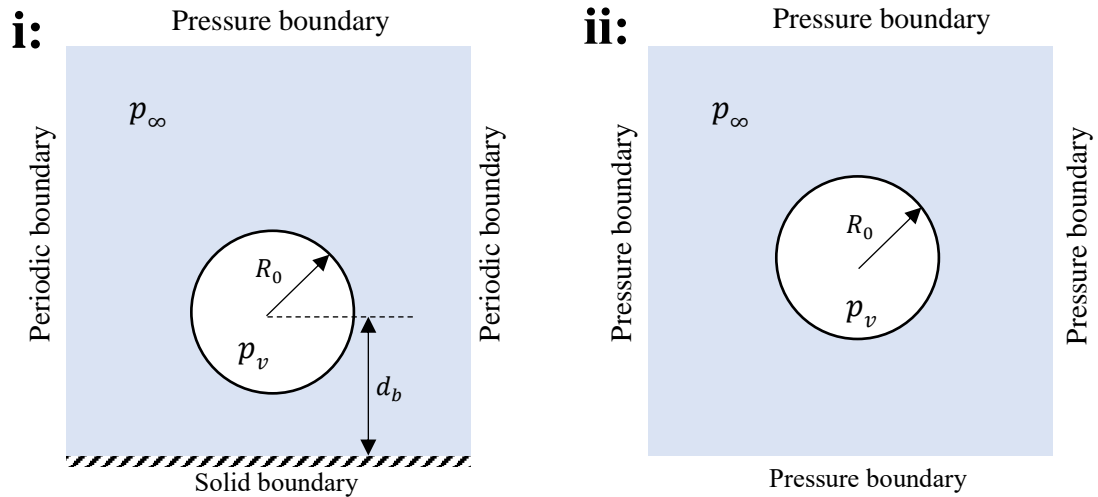


Figure 5.13. Computational domains for simulations of the collapse of cavitation bubbles and ice nucleation: (i) near a solid boundary, and (ii) within a pressurised space.

In order to simulate ice nucleation which have been induced by the collapse of cavitation bubbles, the simulation temperature needs to be reduced to $T < 0.422T_c$. The application of CS EoS with the coefficients $a = 0.5$ and $b = 4$ can successfully reach the above temperature range. However, Yuan et al. [290] found that the spurious current of the pseudo-potential LBM rose dramatically with an increase in the density ratio, i.e., by

reducing the temperature. To address this problem, three k values ($k = 1.0, k = 0.5, k = 0.1$) were tested with the corresponding σ adjusted to maintain the coexistence curve. A gravity-free computational domain of a 201×201 grid was applied. Periodic boundary schemes were applied to the four boundaries. A static bubble with an R_0 of 40 lattices surrounded by liquid was placed in the centre of the computational domain. The temperature range was $0.4T_c - 0.9T_c$. The initial density of the liquid (vapour) was set according to the Maxwell construction and was initiated by:

$$\rho(x, y) = \frac{\rho_l + \rho_v}{2} + \frac{\rho_l - \rho_v}{2} \left\{ \tanh \left[\frac{2\sqrt{(x - x_0)^2 + (y - \lambda r_0)^2} - R_0}{W} \right] \right\} \quad (5.35)$$

where ρ_l and ρ_v are the densities of the liquid and vapour, respectively, and (x_0, y_0) is the central point of the computational domain. The initial thickness of the interface, W , was set as 5 lattices.

As shown in Figure 5.14 below, the spurious current was as high as $\nu = 0.053$ at $k = 1.0$ and $T = 0.4T_c$. A high spurious current might lead to an erroneous temperature field or numerical instability due to the abrupt surge in the local density when the cavitation bubbles collapse. Hence, small k values were adopted to ensure numerical stability. As can be seen in Figure 5.14, for $T = 0.4T_c$, the spurious current was remarkably reduced, from $\nu = 0.053$ to $\nu = 0.00014$ by hundreds of times, as the value of k was decreased, from $k = 1.0$ to $k = 0.1$. Even smaller spurious currents could be achieved by further reducing the k value. However, the thickness of the interface became larger with a smaller k value. In a compromise between the thickness of the interface and the spurious current, and following the work of Zhu et al. [200], $k = 0.1$ was set for the simulations.

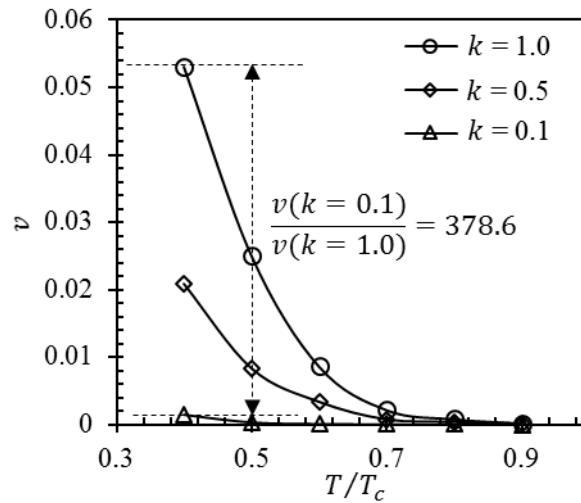


Figure 5.14. Effects of k and σ on the spurious current.

5.4.2.2 Results and discussion

5.4.2.2.1 Ice nucleation induced by the collapse of cavitation bubbles near a solid boundary

It was revealed in the results of both the experiments and the simulations that the collapse of cavitation bubbles near a solid boundary were significantly affected by the standoff distance, pressure difference and the initial radius of the bubbles [139, 197, 264, 265]. The focus here was on the ultra-high pressures and temperatures generated by the collapse of the cavitation bubbles, which are the two primary parameters affecting the onset of ice nucleation. For the fixed Δp and R_0 , it can be clearly seen in Figure 5.15 that the maximum collapse pressure (p_{\max}) increased with an increasing λ . The evolution curve of the p_{\max} against λ was seen to have an exponential increase for $\lambda < 2.8$, whereas the increase rate for the p_{\max} dropped down drastically for $\lambda \geq 2.8$. This change in p_{\max} against λ can be attributed to the reduced Δp , on account of the reduced pressures in the regions close to the solid boundary [244, 264]. When the cavitation bubbles are away from the solid boundary and are approaching the top pressure boundary, the p_{\max}

dramatically increased and then tended to level off due to the smaller pressure gradient near the pressure boundary.

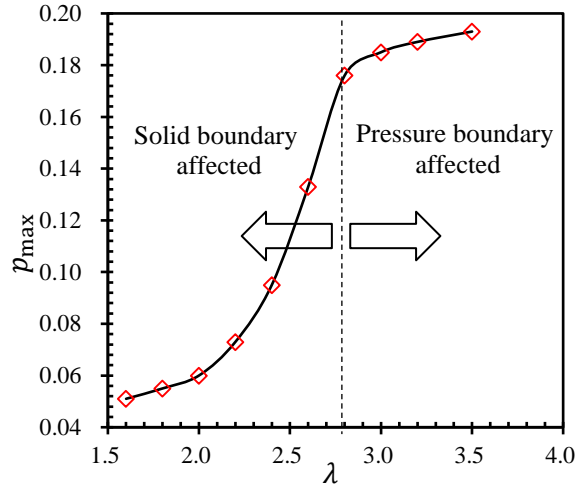


Figure 5.15. Effects of λ on p_{\max} [$\Delta p = 0.0027$, $T_0 = 0.4175T_c$, $R_0 = 80$].

The effects of Δp on the temperature field and p_{\max} are plotted in Figure 5.16 below. The R_0 was fixed at 80 and λ was fixed at 2.5 (i.e., the cavitation bubble is placed in the centre of the computational domain). The p_{\max} values were found to be positively related to the Δp . For the temperature field, the highest temperature inside the bubble and the lowest temperature outside the bubble were denoted as T_{high} and T_{low} , respectively, and they are the results for the fast-moving interface during the compression and rarefaction processes. Clearly, the T_{high} rose gradually with an increasing Δp , whereas the T_{low} decreased as the Δp increased. It is noteworthy that the T_{low} is very close to the HoN temperature and could lead to instantaneous ice nucleation. However, it cannot be certain whether such low temperatures result from the dynamics of bubble collapses or the instability of the solution to the temperature equation. Therefore, the possibility of ice nucleation induced by such low temperatures is not considered in this study.

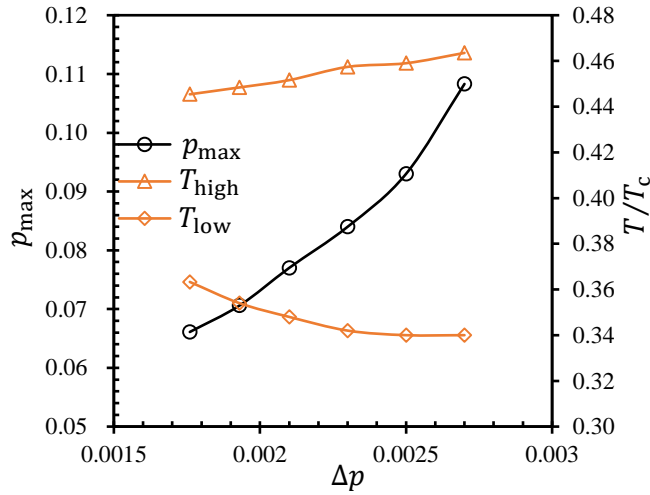


Figure 5.16. Effects of the initial Δp on p_{\max} and T [$\lambda = 2.5$, $T_0 = 0.4175T_c$, $R_0 = 80$].

When the λ and Δp values were fixed ($\lambda = 2.5$, $\Delta p = 0.0027$), the p_{\max} was first seen to increase sharply as the R_0 increased, and dropped drastically for $R_0 > 70$, as shown in Figure 5.17 below. The distance between the final positions of the cavitation bubbles and the bottom boundary were also recorded and denoted as y_p . The final position was defined as the centre of the cavitation bubble in the last phase of the collapse. The drop in p_{\max} can be explained by the change in the y_p . Clearly, for $R_0 < 60$, the value of y_p remained unchanged at 200. For $R_0 \geq 60$, the y_p decreased significantly as the pressure difference between the bubble-top and bubble-bottom was high enough to push the bubble towards the solid boundary. As discussed above, the p_{\max} tended to decrease with a reduced λ . Consequently, the p_{\max} values peak at around $R_0 = 70$. However, this peak p_{\max} was slightly lower than the one obtained with $\lambda = 3.5$.

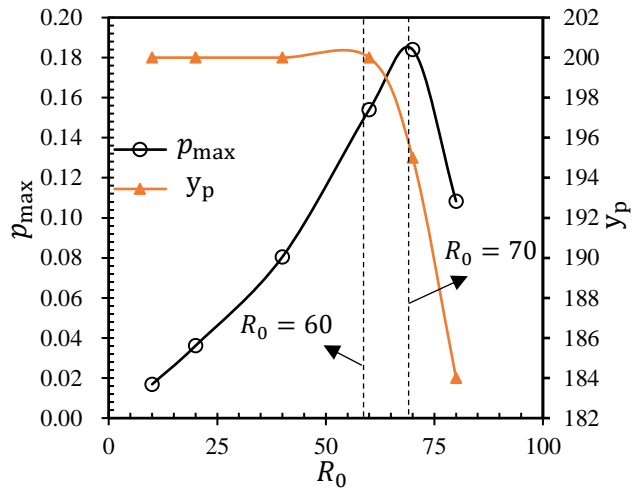


Figure 5.17. Effects of R_0 on p_{\max} [$\Delta p = 0.0027$, $T_0 = 0.4175T_c$, $\lambda = 2.5$].

Based on the above discussions, the values for the simulation conditions were chosen as $\lambda = 3.5$, $\Delta p = 0.0027$ and $R_0 = 80$. The pressure fields, temperature fields and distributions of the ice fractions are shown in Figure 5-18 below. Based on the surge in the pressure that comes after the last stage of the collapse of the bubbles, the complete collapse time-step can be determined. In this simulation, the bubble collapse was completed at $t = 1174$, and reached the highest pressure at $t = 1178$. Before this time-step, the bubble kept shrinking as the pressure surrounding the bubble rose gradually. As shown in Figure 5.18 (a), due to the presence of the solid bottom boundary, the pressure on top of the bubble was larger than that at the bottom of the bubble. It was also noticed that the bubble shape appeared to be flatter than those shown in Figure 5.3 during the later stages of the collapse of the cavitation bubbles. Moreover, the concave structure on the top surface of the bubble was absent due to the reduced surface tension. Therefore, a relatively high pressure gradient occurred at the top-right and top-left of the bubble. Driven by these two high pressure points, the bubble ended with an explosive collapse. Meanwhile, the temperature inside the bubble increased as a result of the process of

isentropic bubble collapse, as shown in Figure 5.18 (b). In addition, the wing-like distribution of low temperatures that appeared at the top-right and top-left of the bubble proved that the bubble interfaces at the two areas moved faster inwardly than those at the other parts due to the two high pressure points. For $t > 1178$, this high pressure started to spread around as a wave. Meanwhile, the amplitude of the pressure wave attenuated quickly with time.

As the cavitation bubble collapsed, mainly from the top-left and top-right, the spread of the pressure wave was biased in the Y direction, as confirmed by the elliptical pressure distribution (see Figure 5.18 (a) at $t = 1185$). Therefore, at $t = 1175$, the low temperature region ($T < 0.4T_c$) on top of the collapsing bubble was penetrated by the pressure wave, leading to a local pressure of $p = 0.139$ which corresponded to $T_{\text{hom}} = 0.43T_c$. Therefore, the ice nucleation started and continued outwardly along with the propagation of the pressure wave. The ice structure formed under this pressure was ice VI, for which the corresponding melting temperatures cover from 273.15 K (0.626 GPa) to 355 K (2.216 GPa). However, for $t \geq 1178$, the pressure dropped quickly and the ice formed inevitably underwent a process of transformation of its structures. The likely transformation pathway of the ice structures was: VI \rightarrow V \rightarrow III \rightarrow Ih where VI \rightarrow V and V \rightarrow III were two endothermic processes. Correspondingly, the enthalpy changes for the above two processes were 0.02 kJ/mol and 0.07 kJ/mol [291], respectively. The transition of III \rightarrow Ih was an exothermic process, for which the corresponding enthalpy change was -0.17 kJ/mol [291]. In addition, the local melting temperature first decreased to 251 K at 0.2 GPa and rose to close to 273.15 K with $p > 0.2$ GPa. As a result, the ice melted when the local temperature exceeded the melting temperature. As shown in Figure 5.18 (c), the ice at the collapse spot started to melt from

$t = 1178$. Therefore, for ice nucleations induced by the collapse of cavitation bubbles, a sufficient heat exchange between the ice particles and the surrounding supercooled liquid, or an initially large degree of supercooling, are required to ensure continuous freezing after the formation of the ice particles. The results can be indirectly confirmed by the probability of the phase change induced by the ultrasonic vibrations as a function of the degree of supercooling, as reported by Inada et al. [37], where cases with a small degree of supercooling tended to have a low probability of phase change.

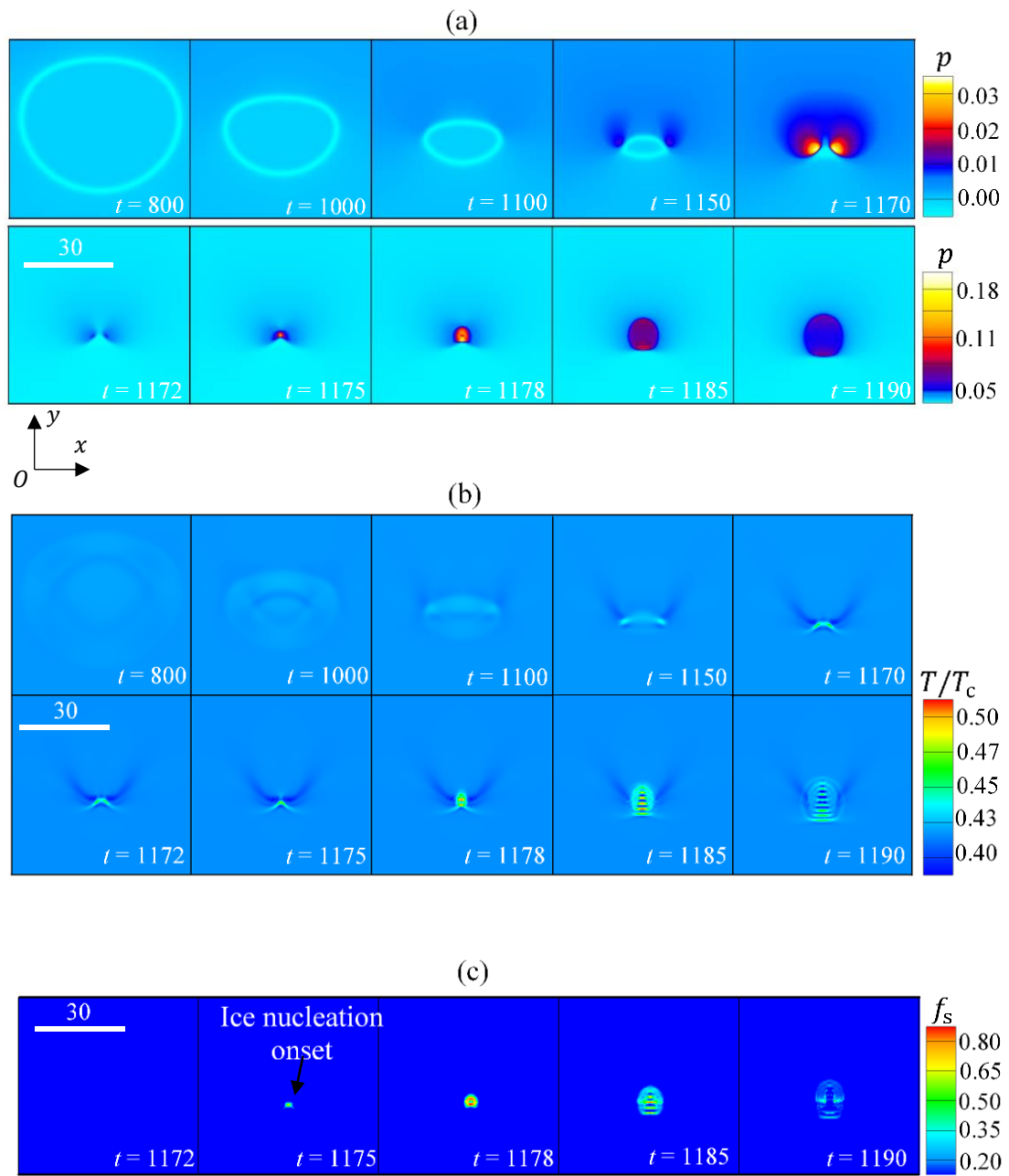


Figure 5.18. Pressure fields, temperature fields and distributions of the ice fractions before and after ice nucleation induced by the collapse of cavitation bubbles near a solid boundary [$T_0 = 0.4175T_c$, $\lambda = 3.5$, $\Delta p = 0.0027$ and $R_0 = 80$]: (a) pressure fields; (b) temperature fields; and (c) distributions of ice fractions.

5.4.2.2.2 Ice nucleation in a pressurised space

Figure 5.19 below shows the effects of the Δp on the temperature field and p_{\max} for the collapse of cavitation bubbles within a pressurized space. Clearly, the values of p_{\max} were positively related to the Δp for $\Delta p \in [0.00069, 0.002]$ with $R_0 = 80$. It is also found that T_{high} is positively related to Δp , whereas T_{low} slightly decreases as Δp increases. T_{high} generated in the last stage of cavitation bubble collapse is often experimentally measured at a much higher value in the literature ($\gg T_c$ [122]). This is primarily due to R_0 (corresponding to $0.32 \mu\text{m}$) is remarkably smaller than that applied in experiments (e.g. $50 \mu\text{m}$ [292]). Besides, a small surface tension is applied in the simulation, resulting in a decrease in the collapse intensity [293, 294]. In addition, the simulation considers a pure water-vapour system, i.e., the gas/air content is not included, leading to the reduction of the adiabatic ratio ($\gamma = c_p/c_v$, $\gamma_{\text{air}}: 1.4 > \gamma_{\text{vapour}}: 1.33$ [295]). A smaller adiabatic ratio incurs a lower collapse temperature ($T_{\text{collapse}} = \left(\frac{R_{\max}}{R_0}\right)^{3(\gamma-1)}$ [122]). Moreover, due to the limitation of the present model (i.e. for incompressible flow and hence unable to simulate the shock wave propagation after bubble collapse [245]), Δp is intentionally set to 0.00176 in this study to maintain the stability of the numerical model and achieve a p_{\max} that is high enough to induce ice nucleation.

For a fixed value of Δp , the effect of the R_0 on the p_{\max} was also investigated, and the results are plotted in Figure 5.20 below. The values for the p_{\max} were found to monotonically increase as the R_0 increased. For $R_0 > 80$, the results were numerically unstable for the final stages of the bubble collapse. This might have been because the jet current generated in the final stages of the collapse exceeded a supersonic velocity. As

discussed above, supersonic flows cannot be simulated in the present numerical model. Hence, the value of the R_0 was fixed at 80 to achieve a high p_{\max} value while maintaining the numerical stability.

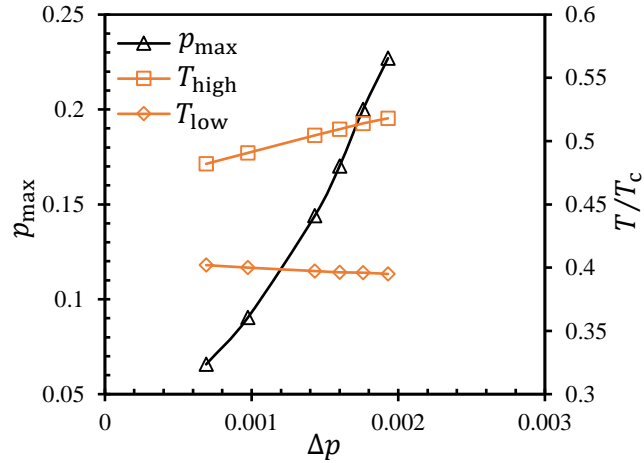


Figure 5.19. Effects of Δp on the p_{\max} , T_{high} and T_{low} of the cavitation bubble [$T_0 = 0.4175T_c$, $R_0 = 80$].

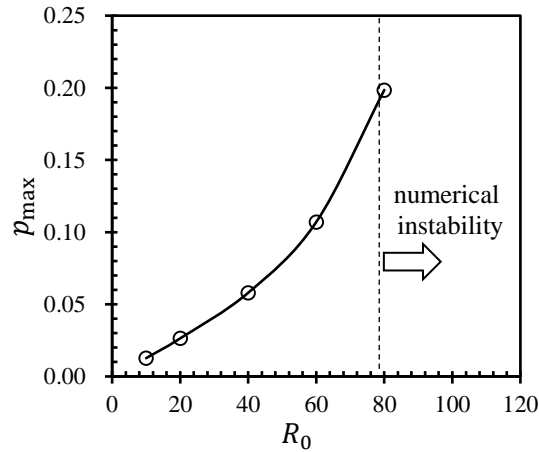


Figure 5.20. Effects of R_0 on the p_{\max} [$T_0 = 0.4175T_c$, $\Delta p = 0.00176$].

Based on the above discussions, the simulation conditions for the collapse of cavitation bubbles within a pressurised space were chosen as $\Delta p = 0.00176$ and $R_0 = 80$. The pressure fields, temperature fields and distribution of the ice fractions are shown in Figure

5.21 below. The collapse of the bubble was completed at $t = 1674$, with a $p_{\max} = 0.2$. For $t \leq 1674$, the cavitation bubbles kept shrinking as spherical bubbles. For $t > 1674$, the pressure wave at the collapse point started to spread into the surrounding water, resulting in a dramatic drop in the local pressures behind the pressure wavefront. The temperatures inside the bubbles first increased slowly with time and then rose sharply on approaching $t = 1670$. At $t = 1671$, the temperature of the bubble collapse reached as high as $T = 0.514T_c$. As clearly illustrated in Figure 5.21 (b), a relatively low-temperature region was formed around the bubble interface on the liquid side. The formation of this low-temperature region was mostly due to the fast contraction movements of the bubble wall. With the assistance of this low-temperature region, the hot spot at the point of bubble collapse (e.g., indicated by a black arrow in Figure 5.21 (b)) could be compensated for to some extent. Noting that at $t = 1674$, the local temperature at the collapse point had increased by $0.022T_c$ due to the latent heat released during the initial formation of the ice crystal. The onset of ice nucleation and the subsequent evolution of the distribution of the ice fractions are shown in Figure 5.21 (c). For $t < 1674$, the evolution of the T_{high} values and the corresponding T_{hom} values at the centre of the cavitation bubble upon ice nucleation are plotted in Figure 5.22 below. Clearly, the local T_{hom} value was smaller than the T_{high} value for the cavitation bubble at $t < 1674$. The ice nucleation was induced at $t = 1674$ when the collapse pressure reached its maximum (i.e., $p_{\max} = 0.2$). Once the ice was formed, the evolution of the ice structures was the same as discussed above in Section 5.4.2.2.1.

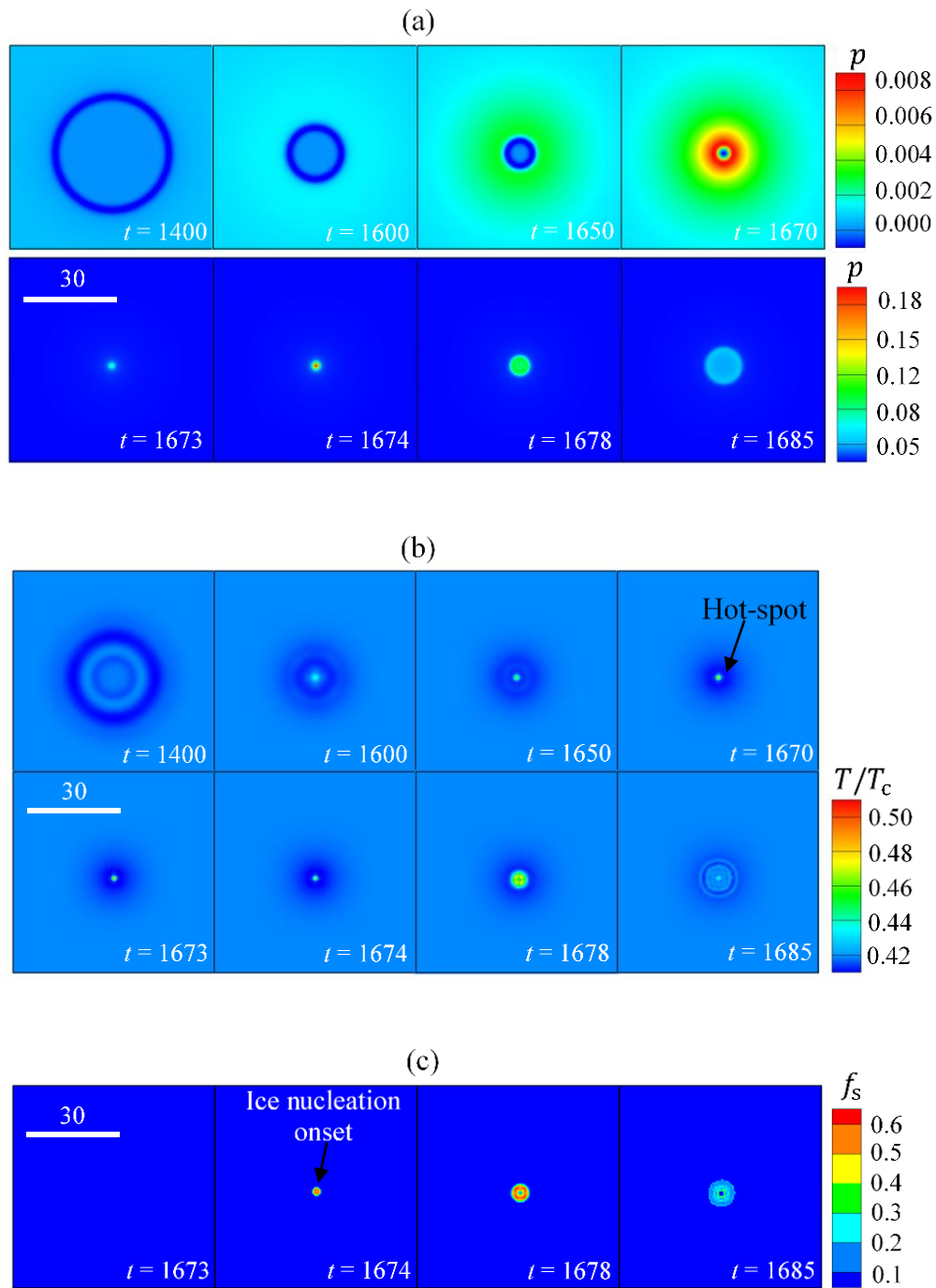


Figure 5.21. Pressure fields, temperature fields and distributions of the ice fractions before and after ice nucleation induced by the collapse of cavitation bubbles within a pressurised space [$T_0 = 0.4175T_c$, $\Delta p = 0.00176$ and $R_0 = 80$]: (a) pressure fields; (b) temperature fields; and (c) distributions of the ice fractions.

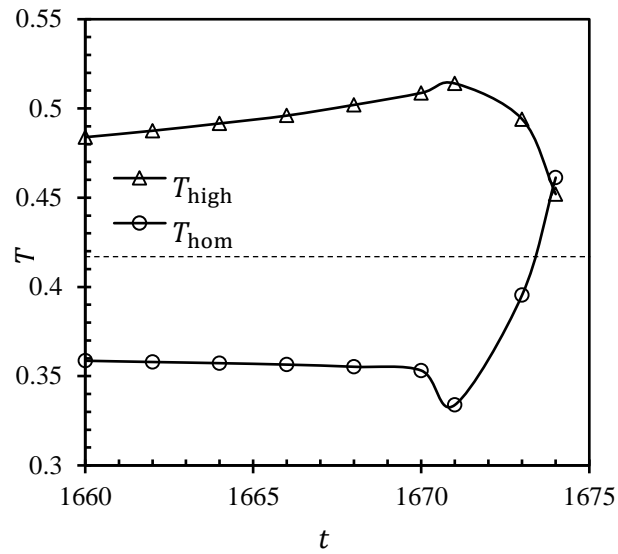


Figure 5.22. Evolution of the T_{high} values and the corresponding T_{hom} values at the centre of the cavitation bubble upon ice nucleation [Dashed-line represents the bulk water temperature].

5.4.2.2.3 Thermodynamic analysis of the formation and freezing of initial ice crystals

Considering the evolution profiles of the bubbles in the collapse process, Scenarios I and II can be described as the collapse of non-spherical cavitation bubbles and the collapse of spherical cavitation bubbles, respectively. Compared to the collapse of the non-spherical bubbles in Scenario I, the collapse of the spherical bubbles in Scenario II concentrated all of the fluid's energy from the bubble compression process, hence generating much higher collapse pressures under the same conditions (i.e., identical Δp , R_0 and λ), thus it could more readily initialise the ice nucleation. For both scenarios, the initially formed ice particles had a strong tendency to melt due to the fast dissipation of the pressure. Hence, a large initial degree of supercooling was required to ensure the continuous and complete freezing of water, as supported by the low probability of a phase change at small degrees of supercooling [37]. However, in Scenario I, the micro-jets which formed could impact on the local flow field [159] which, in turn, could lead to the migration of ice crystals

from the hot spot to the cold spot, and hence avoid melting. Therefore, the required degree of supercooling for continuous freezing in Scenario I might be lower than that in Scenario II.

To quantify and compare the required degrees of supercooling for the two scenarios, the simulation conditions for Scenario I were set as $R_0 = 80$, $\lambda = 2.5$, and $\Delta p = 0.00344$; and the simulation conditions for Scenario II were set as $R_0 = 80$ and $\Delta p = 0.00176$. Thus, the two scenarios could generate equal p_{\max} values. The initial temperature for both scenarios was set to range from $T = 0.4175T_c$ to $T = 0.4220T_c$, which corresponded to degrees of supercooling ranging from 2.96 K to 0.07 K. To evaluate the evolution of the f_{ice} , a new parameter of $f_{ice\text{-sum}}$ was assigned as the total amount of ice formed in the computational domain. The evolutions of $f_{ice\text{-sum}}$ over time for the two scenarios are shown in Figure 5.23 below. The evolution of $f_{ice\text{-sum}}$ can be divided into three distinct stages: (1) ice growing, (2) ice melting, and (3) ice stabilising.

Stage-1: The ice growth was attributed to the high pressures generated in the last stages of the bubble collapse. For Scenario I, the highest $f_{ice\text{-sum}}$ value was slightly higher than that in Scenario II, which was probably due to the T_{low} in Scenario I being lower than that in Scenario II, thus leading to a relatively larger degree of supercooling. According to the Stefan number, the ice fractions were positively related to the degree of the supercooling.

Stage-2: The initial ice melts due to the fast dissipation of the pressure. However, for Scenario I, part of the initial ice remained stable during the pressure dissipation process, even if the initial degree of the supercooling was close to 0 K. This might have been because the temperature of the formed ice was similar to, or lower than, the pressure-

dependent melting temperature. In contrast, in Scenario II an initial degree of supercooling of > 1.7 K was required to avoid the ice completely melting as the collapse of spherical cavitation bubbles generate a relatively higher temperature.

Stage-3: If the ice in Stage-2 is not completely melted, the remaining ice in Stage-3 will gradually regrow and finally become stabilised. The regrowth occurred due to the increase in the melting temperatures as the pressure decreased from 0.2 GPa to atmospheric pressure.

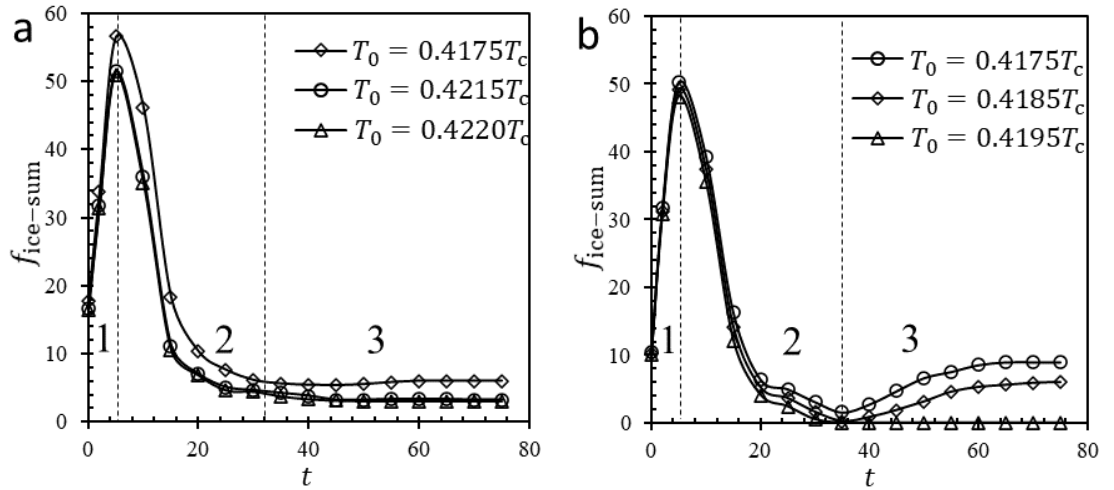


Figure 5.23. Evolution of $f_{ice-sum}$ over time [1, 2 and 3 in the figure represent the three stages of the evolution of $f_{ice-sum}$]: (a) Scenario I [$R_0 = 80$, $\lambda = 2.5$ and $\Delta p = 0.00344$]; (b) Scenario II [$R_0 = 80$ and $\Delta p = 0.00176$].

Despite its successful application in simulating the ice nucleation process triggered by the collapse of cavitation bubbles, the present model is limited to cases with small surface tensions. For cases with large surface tensions, further modifications to the model are required to reduce the spurious current for $T < 0.422T_c$. In addition, the compressibility effects of both the gas and liquid phases need to be included as they are deemed

responsible for the formation of secondary bubbly structures [296, 297], the propagation of shock waves and the high-speed jet current.

5.4.3 Evolution of the pressures of the cavitation bubbles inside the crevice

The current simulation is an extension of the study in Section 4.2. The glass beads had very rough surfaces which enabled the air bubbles to be trapped inside their numerous crevices when injected into the water droplets. Meanwhile, the water droplets were placed onto a vibrating substrate. During the strong collisions between the glass beads and the substrate, the trapped air bubbles worked as cavitation inception sites. Once the cavitation bubbles collapsed, extremely high pressures are released into the surrounding water which induced the ice nucleation. Considering the small scale of the crevices in the glass beads, it is beyond the capability of experimental approaches to obtain the evolution of the pressures during the collapse of the cavitation bubbles inside the crevices. Therefore, the numerical approach becomes a very powerful and useful tool for solving this problem.

During the vibration expansion process, the trapped bubbles worked as inception sites for the cavitation bubbles. However, the magnitude of the pressure in-between the vibrating substrate and the particles was not high enough for the cavitation bubbles to grow and detach from the crevices, which often requires a pressure amplitude of around -6 MPa [124, 125]. After a certain number of expansion and compression cycles, the trapped bubbles reached their maximum size and were likely to collapse, given the relatively high pressures built up during the collisions between the particles and the substrate. To numerically study the behaviour of the cavitation bubbles inside the crevices, a pseudo-potential LBM was applied, and the crevices on the surface of the glass beads were simplified into three basic structures: square-shape crevices, cone-shape crevices and

hemisphere-shape crevices (as shown in the colour white in Figure 5.24 below). The effects of the crevice sizes and the local collision pressures on the final collapse pressures are also examined and discussed.

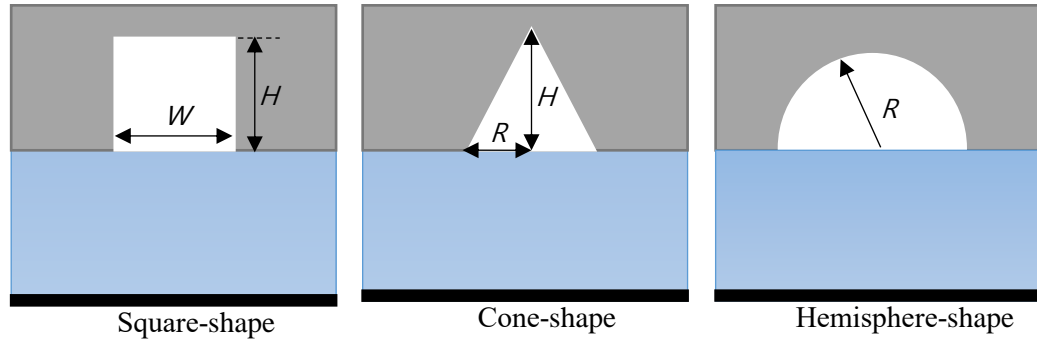


Figure 5.24. Simplified basic structures of the asperity crevices on the rough surfaces of the particles [Grey colour represents the body of the particle; light blue colour represents the liquid film; black colour represents the solid substrate].

5.4.3.1 Numerical modelling

The SEM images of the GB1 – GB4 particles showed that the asperities were densely distributed on the particle’s surfaces, as shown in Figure 5.25 below. During the strong collisions between the particles and the vibrating substrate, the water film between them was highly squeezed, leading to a surge in the local pressures. The balance between the gravitational force and the substrate inertial force was assumed to be in the water film. Accordingly, the direct collision pressure (p_d) generated by a single asperity in a collision could be simplified as:

$$p_d = \frac{4m_g \left(\frac{2\pi f P_v}{\rho c} + g \right)}{\pi D_a^2} \quad (5.36)$$

The first term in the bracket of Equation (5.36) is the substrate acceleration amplitude based on the intensity of the vibrations [25]. In Equation (5.36), m_g is the particle mass; f is the ultrasonic vibration frequency; ρ is the density of the water; c is the local sound speed; g is the gravitational acceleration; P_v is the absolute value of the maximum driving pressure from the substrate (as listed in Table 4.1); and D_a is the equivalent diameter of the asperity involved in the collision. Moreover, from the analysis of SEM images the values for D_a were estimated to be in the range of 1 μm – 10 μm . For $D_a < 1 \mu\text{m}$, the chance of contacting the substrate was negligible. The calculated p_d values were plotted in Figure 5.26 against the D_a values. Clearly, the p_d rose sharply as the D_a reduced from 10 μm to 1 μm . Meanwhile, the p_d values were positively related to the D_p values. Thus, the highest pressure, i.e., $p_d = 0.032 \text{ GPa}$, occurred at $D_a = 1 \mu\text{m}$ ($D_p = \text{GB4}$). At such a high pressure, according to Equation (5.31), the corresponding HoN temperature was $T_{\text{hom}} = 232.65 \text{ K}$. Therefore, the ice nucleation could not be triggered inside the water droplet for $T_o \geq 266.65 \text{ K}$. Moreover, the GB4 had the densest asperities (see Figure 5.25) as the total contact area was greatly increased, which may have brought the values of p_d down to some extent. This might explain why the f_{ice} values for GB4 were less than those of GB3 in Figure 4.4 (b). Overall, it is clear that direct collisions alone are not sufficient to induce ice nucleation for $T_o \geq 266.65 \text{ K}$.

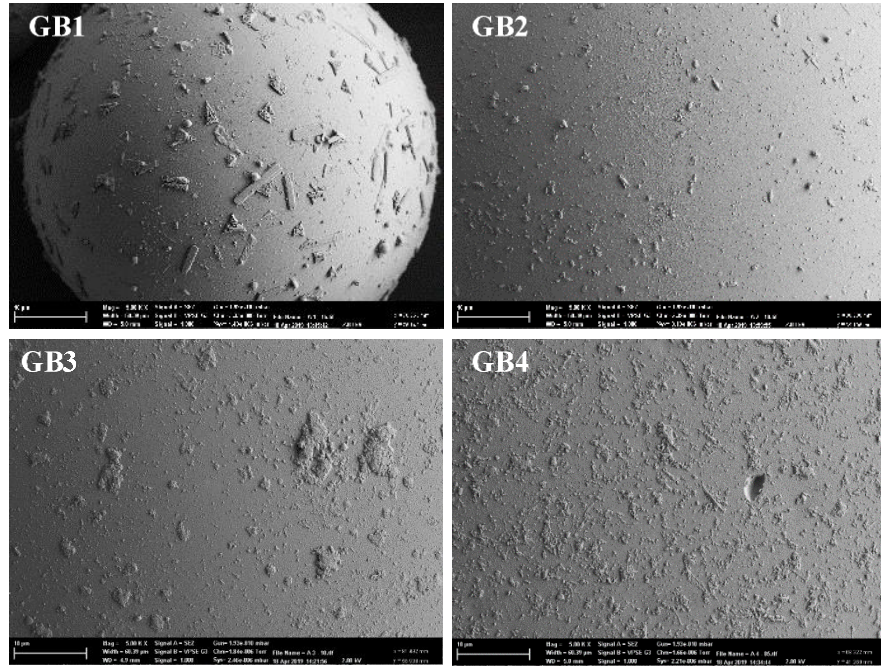


Figure 5.25. SEM images of glass beads in different groups [Scaled at 10 μm].

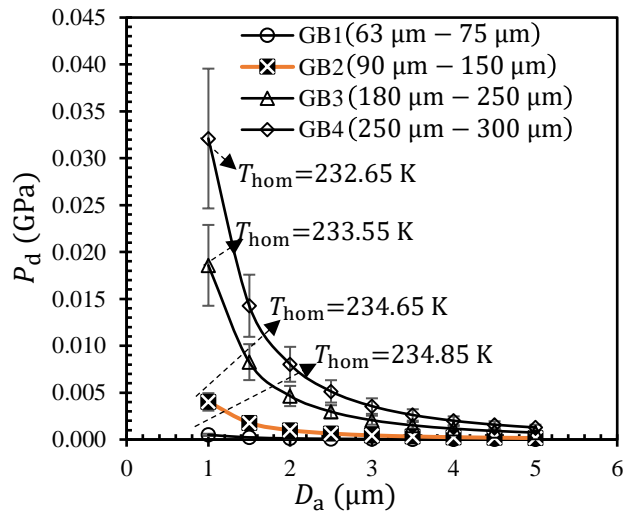


Figure 5.26. Effects of the asperity equivalent diameter on p_d [$E_v = 0.0011 \text{ W/cm}^2$].

Given that the cavitation bubbles in the crevices are frequently exposed to the build up high pressure fields in the water film, the cavitation bubbles are highly likely to collapse and generate much higher local pressures. To numerically investigate the dynamics of the bubble collapses in the crevices, the range of p_d values was chosen to be from 0.01 GPa

to 0.08 GPa. The three simplified crevice structures were investigated, namely: square-shape crevices, cone-shape crevices and hemisphere-shape crevices. The sizes of the crevices (i.e., radius, height and width) were set to vary around $0.5 \mu\text{m}$, corresponding to 125 lu. The conversions between the lattice units and the physical units were listed in Table 5.1. In the present study, a computational domain of a 401×401 grid ($1.6 \mu\text{m} \times 1.6 \mu\text{m}$) was applied for all of the three different crevices. The bottom half of the computational domain was set as the fluid region and the initial density was manually changed to obtain different p_d values. The top half of the computational domain was set as a solid region where the crevices rested, as shown in Figure 5.27 below using a hemisphere-shape crevice as an example. The left and right boundaries of the computational domain were set as periodic boundaries and the top and bottom boundaries were set as solid boundaries.

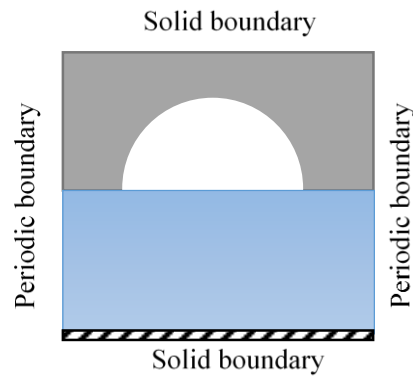


Figure 5.27. Boundary conditions of the computational domain.

5.4.3.2 Results and discussion

Figure 5.28 below shows the values for the maximum collapse pressures (p_{max}) generated when a cavitation bubble collapses in a square-shape crevice for different crevice heights (H_{sq}) and widths (W_{sq}) with $p_d = 0.08$ GPa. As shown in Figure 5.28

(a), with the value of W_{sq} fixed at $0.80 \mu\text{m}$, the p_{max} values increased with an increase in the H_{sq} . As shown in Figure 5.28 (b), when the value of H_{sq} was fixed at $0.72 \mu\text{m}$, the p_{max} values increased, first as the W_{sq} increased from $0.16 \mu\text{m}$ to $0.24 \mu\text{m}$, and then it dropped when the value of W_{sq} increased further to $0.48 \mu\text{m}$, and increased again when the W_{sq} became greater than $0.48 \mu\text{m}$. The first and second rises in the p_{max} values could be attributed to the primary and secondary bubble collapses, respectively. When the W_{sq} value was smaller than $0.24 \mu\text{m}$, the p_{max} was solely determined by the primary collapse. When the W_{sq} value was above $0.48 \mu\text{m}$, there were two secondary bubbles which formed after the primary collapse. Hence, the effect of the W_{sq} was different in three regions: (i): $W_{sq} \leq 0.24 \mu\text{m}$, where the primary collapse was dominant; (ii): $0.24 \mu\text{m} < W_{sq} \leq 0.48 \mu\text{m}$, the transition stage; and (iii): $0.48 \mu\text{m} < W_{sq}$, where the secondary collapse was dominant. In the transition stage, the decrease in the values of the P_{max} can be attributed to the energy consumed by the secondary collapse. The secondary bubbles collapsed under the high pressure wave released by the primary collapse. Figure 5.29 below shows the evolution of the pressures, from the primary collapse to the secondary collapse. The primary collapse is circled by the red dashed line and the secondary collapse is circled by the solid red line. The highest pressure generated by the collapse of cavitation bubbles in the square-shape crevice was $p_{\text{max}} = 0.68 \text{ GPa}$, which corresponded to a homogeneous ice nucleation temperature of $T_{\text{hom}} = 239 \text{ K}$. Clearly, the ice nucleation inside the droplet cannot be triggered at such low values of T_{hom} . Therefore, for $p_d \leq 0.08 \text{ GPa}$, the bubble collapses in the square-shape crevices could not generate pressures high enough to induce an ice nucleation.

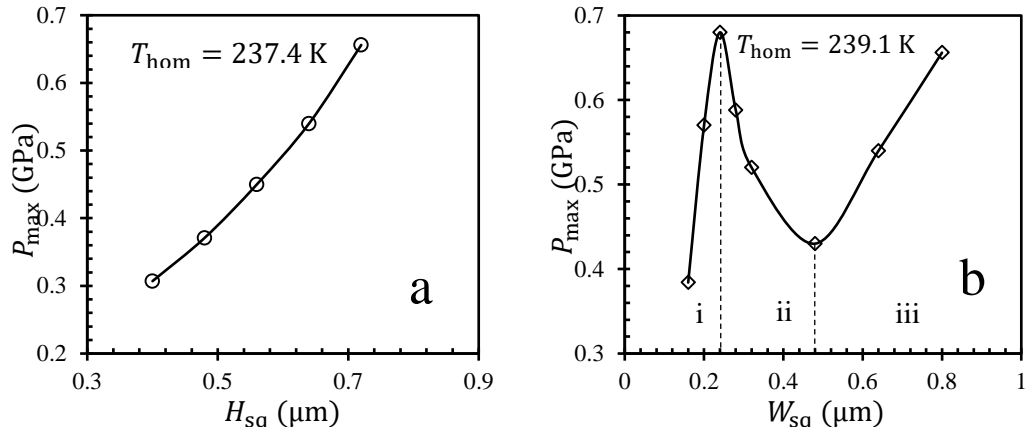


Figure 5.28. Effects of the height and width of the square-shape crevice on p_{\max} at $p_d = 0.08 \text{ GPa}$: (a) height effect on p_{\max} with width fixed at $0.80 \mu\text{m}$; (b) width effect on p_{\max} with height fixed at $0.64 \mu\text{m}$ [i: primary collapse dominant; ii: transition from dominant primary collapse to dominant secondary collapse; iii: secondary collapse dominant].

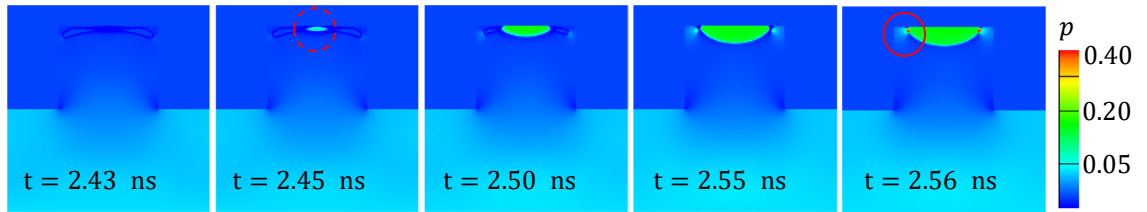


Figure 5.29. Pressure fields for the collapse of a cavitation bubble in a square-shape crevice [$H_{sq}: 0.64 \mu\text{m}$, $W_{sq}: 0.8 \mu\text{m}$; pressure unit: GPa]. The primary collapse is circled by the red dashed line and the secondary collapse is circled by the solid red line.

For the collapse of the cavitation bubbles in the cone-shape crevice with $p_d = 0.08 \text{ GPa}$, the effects of the crevice height (H_{co}) and radius (R_{co}) on the p_{\max} values are plotted in Figure 5.30 below. With the R_{co} value fixed at $0.8 \mu\text{m}$, the p_{\max} values increased with an increase in H_{co} . This increase was primarily due to the increased sizes of the cavitation bubbles. Oppositely, if the value of H_{co} was fixed at $0.72 \mu\text{m}$, the p_{\max} values decreased with a decrease in R_{co} . The highest pressure achieved in the cone-shape crevices was 0.89 GPa , which corresponded to $T_{\text{hom}} = 252.5 \text{ K}$. This was a big leap in

the values of T_{hom} compared to those from the square-shape crevice. However, considering the temperatures of the droplets (i.e., $T \in (264.15 \text{ K}, 273.15 \text{ K})$) applied in the experiment, 0.89 GPa was still not enough to trigger ice nucleation. Consequently, for $p_d \leq 0.08 \text{ GPa}$, the collapse of the cavitation bubbles could not trigger ice nucleation in the cone-shape crevices. Figure 5.31 below shows the distribution of the pressures in a typical collapse of cavitation bubbles in a cone-shape crevice. Due to the presence of the conical surface, the driving pressure was guided towards the left and right sides of the bubbles which formed two high pressure regions, as circled by the solid red line in Figure 5.31 below. Thus, the occurrence of secondary bubble collapses can be prohibited. Without the energy consumption of a secondary bubble collapse, the primary collapse in the cone-shape crevices can achieve a relatively higher collapse pressure than in the square-shape crevices.

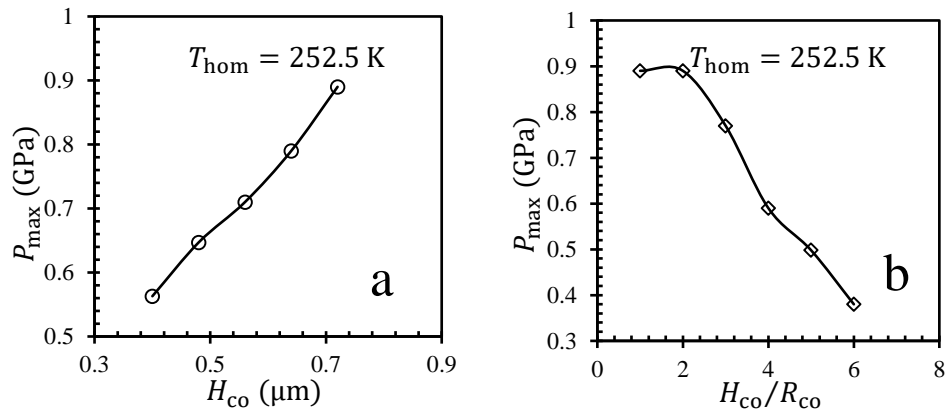


Figure 5.30. Collapse of cavitation bubbles in the cone-shape crevice at $p_d = 0.08 \text{ GPa}$: (a) effects of the crevice height on p_{max} with width fixed at $0.8 \mu\text{m}$; (b) effects of the crevice radius on p_{max} with height fixed at $0.72 \mu\text{m}$.

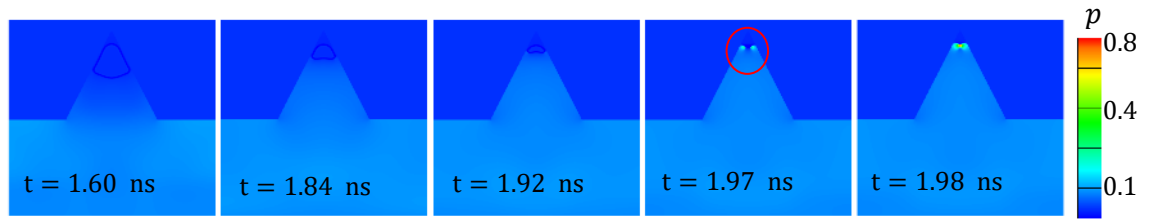


Figure 5.31. Pressure fields for the collapse of a cavitation bubble in a cone-shape crevice [R : $0.4 \mu\text{m}$; H : $0.72 \mu\text{m}$; pressure unit: GPa].

Figure 5.32 below shows the maximum collapse pressures for cavitation bubbles in the hemisphere-shape crevice. For $p_d > 0.05 \text{ GPa}$, the present model became unstable due to the supersonic currents generated by the collapse which were beyond the capabilities of the present model. Therefore, the value of p_d was reduced to 0.05 GPa to ensure numerical stability. As shown in Figure 5.32 (a), the P_{max} values were found to be positively related to the R_{he} values with the p_d value fixed at 0.05 GPa . When the R_{he} value reached $0.4 \mu\text{m}$, the collapse pressure achieved its peak at $p_{\text{max}} = 1.63 \text{ GPa}$, which corresponded to an ice nucleation temperature of $T_{\text{hom}} = 285.9 \text{ K}$. This T_{hom} value was theoretically high enough to induce ice nucleation in the water droplets for $T \in (264.15 \text{ K}, 273.15 \text{ K})$. With the R_{he} value was fixed at $0.4 \mu\text{m}$, the effects of the p_d values on the p_{max} was investigated and the results are plotted in Figure 5.32 (b). The distance between the final positions of the cavitation bubbles and the bottom boundary was also recorded and was denoted as Y_p . The final position was defined as the centre of the cavitation bubble in the last phase of the collapse. With an increase in the value of p_d , from 0.01 GPa to 0.016 GPa , the p_{max} values rose sharply, from 1.26 GPa to 1.56 GPa ; then the p_{max} values gradually dropped, from 1.56 GPa to 1.39 GPa , and the value of the p_d increased, from 0.016 GPa to 0.039 GPa ; and finally the p_{max}

values rose again, from 1.39 GPa to 1.63 GPa. The decrease in the p_{\max} for $p_d \in (0.016 \text{ GPa}, 0.039 \text{ GPa})$ was attributed to the reduction in the Y_p . As can be seen in Figure 5.32 (b), the value of the Y_p decreased with an increase in the p_d . When the value of Y_p reached below $0.495 \text{ }\mu\text{m}$, the bubble moved into the region where the local pressure was significantly reduced by the solid boundary [244, 264]. Therefore, the pressure difference across the bubble interface was greatly reduced. With further decreasing values of Y_p , the local pressure near the solid boundary became stable. Therefore, when $P_d \geq 0.039 \text{ GPa}$, the p_{\max} values started to rise again. For $p_d = 0.01 \text{ GPa}$, the value obtained for p_{\max} was 1.26 GPa, which corresponded to $T_{\text{hom}} = 271 \text{ K}$, which was in the range of experimental temperatures. Considering the pressure range of p_d in Figure 5.26, it can be concluded that the hemisphere-shape crevice was the only bubble collapse crevice structure which generated a pressure high enough to trigger ice nucleation inside the water droplets.

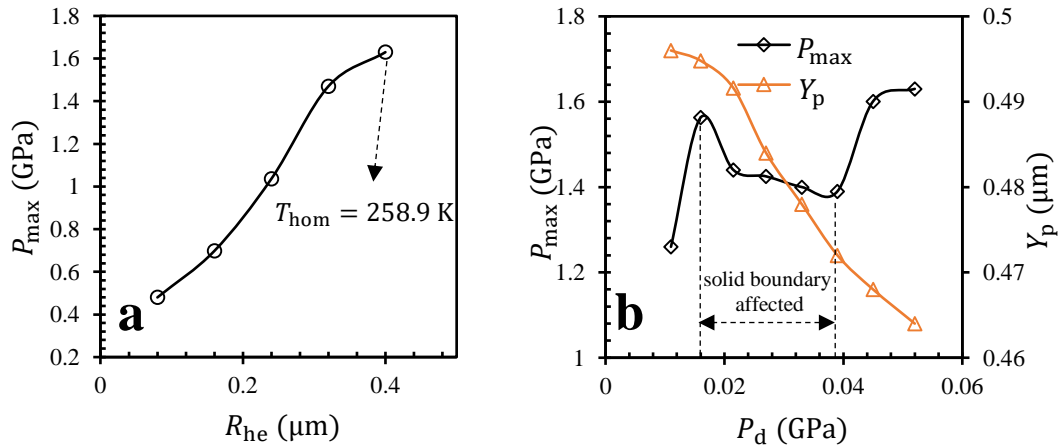


Figure 5.32. Maximum collapse pressures of cavitation bubbles in the hemisphere-shape crevice: (a) effects of the crevice radius on p_{\max} at $p_d = 0.05 \text{ GPa}$; (b) effects of p_d on p_{\max} with crevice radius fixed at $0.4 \text{ }\mu\text{m}$.

Figure 5.33 below shows the evolution of the pressures before and after the collapse of cavitation bubbles at $t = 2.109$ ns in a hemisphere-shape crevice. Compared to the square-shape and cone-shape crevices, the bubble collapse in the hemisphere-shape crevice generated relatively higher collapse pressures. Considering the different crevice structures, the cavitation bubbles in the hemisphere-shape crevice had much smaller contact areas with the solid boundaries during a collapse. As circled by a solid red line in Figure 5.33, in the final stages of a bubble collapse the bubble is entirely separated from the solid boundary. The presence of the solid boundary leads to the formation of a low-pressure region and breaks the symmetry of the external pressure distribution around the bubble [244]. Consequently, the cavitation bubbles in the hemisphere-shape crevice tended to have relatively higher pressure jumps across the bubble's interface than when in the other two crevices.

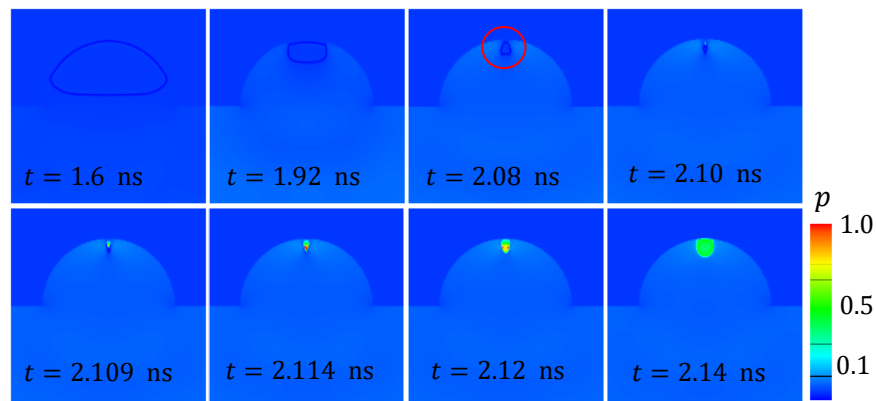


Figure 5.33. Pressure fields for the collapse of a cavitation bubble in a hemisphere-shape crevice [$R: 0.4 \mu\text{m}$; pressure unit: GPa].

Based on the above discussion on cavitation bubble dynamics in crevices, a conclusion can be reached that the collapse of cavitation bubbles in the crevice is structure sensitive. Not all cavitation bubble collapses in the crevice can induce ice nucleation and the bubble

collapse in the hemisphere-shape crevice proves capable of generating a pressure that is high enough for triggering ice nucleation in the water droplet. In addition, the above simulations are run for cases with a single asperity. Given the dense asperities at the particle surface, the number of asperities involved in the collision between the particle and the vibrating substrate should be way greater than one, leading to the dramatic increase in the contact area. As a consequence, P_d might be significantly reduced. This could be confirmed by the experimental result shown in Figure 4.4 (a) where the case with single particle has no ice nucleation. When two or more particles are contained in the droplet, the momentum transferred between each other could remarkably increase P_d . Also, though not captured by the high-speed camera in the experiments of this study, the microstreaming (or flow streams) caused by the oscillating cavitation bubbles could also contribute to (or even solely induce) the initialisation of ice nucleation [238, 240, 242]. Significant further work, albeit a valuable next step, is required to confirm and elucidate the contribution from bubble oscillation, which exceeds much beyond the scope of the current effort.

5.4.4 Evolution of the pressures on the surfaces of a droplet in the vicinity of a collapsing cavitation bubble

The present simulation study is a joint study of the ice nucleation of water droplets induced by the cavitation bubbles formed in a continuous medium. In an ultrasonic vibration field, the strongly collapsing bubbles interact with the water droplets and are likely to induce ice nucleation on the surfaces of the droplets. The experimental observations showed that the ice nucleation occurred when the collapsing bubbles were

in the vicinity of or were in contact with, the water droplets. Therefore, it is reasonable to conclude that, due to the fast dissipation of pressure waves in the liquid, the induction of ice nucleation on the water droplets closely hinged on the distance between the surface of the droplets and the centre of the cavitation bubbles. To obtain a good understanding of the impacts of the evolution of the pressures on the surfaces of the droplets, a series of numerical simulations were conducted. Based on the simulation results, a correlation can be established between the critical distances, the bubble sizes and the differential pressures.

5.4.4.1 Numerical modelling

As the present numerical model is limited to two-phase/two-component flows, the third phase/component cannot be properly treated, i.e., the water phase cannot be included in the simulation. However, given that the simulations conducted only investigate the evolution of the pressures on the surfaces of the water droplets, the water phase in the present model can be treated as a point with a distance of L_b to the point of collapse. It was also assumed that the surface of the droplet has no effect on the propagation of a pressure wave. The computational domain was set as a 401×401 grid. The two boundary conditions (collapse of spherical bubbles and non-spherical bubbles) applied in this simulation study were the same as described in Figure 5.13. In the simulations of the collapse of non-spherical cavitation bubbles, the standoff distance was set as $\lambda = 2.5$. The temperature field for all conditions was initialised as $T_0 = 0.4175T_c$, which corresponded to 270.15 K. The R_0 values ranged from 10 to 90. Another key parameter was the initial density, which determined the initial pressure difference between the vapour phase and the liquid phase. However, to the best of the author's knowledge, there is not an EoS equation for the oil (Fluoridrop 7500). Therefore, in this

study, the densities of the oil vapour and the liquid were approximated by using the densities of the water vapour and the liquid, respectively. Hence, the value for ρ_v was set as 0.000138 and the values for ρ_l were set to range from 0.5 to 0.52.

5.4.4.2 Results and discussion

In Section 5.4.2, the pressures generated in the last stages of the bubble collapses differed significantly for the spherical cavitation bubbles and the non-spherical bubbles. Therefore, this simulation study investigated the effects of both of the collapse types on the evolution of the pressures on the surfaces of the droplets. Figure 5.34 below shows the effects of the initial sizes of the cavitation bubbles on the propagation of the collapse pressure over L_b . Clearly, the collapse pressure dissipated quickly over L_b . In addition, the collapse pressure decreased dramatically with a decrease in the R_0 , which further shortened the critical distance (L_{cri}) that was to ensure the minimum pressure on the surface of the droplet needed to induce ice nucleation. In this study, the minimum pressure was set as $p = 0.1308$, which corresponded to 273.15 K. Thus, it can be seen that the values of L_{cri} decreased with a decrease in the collapse pressure or the size of the bubbles.

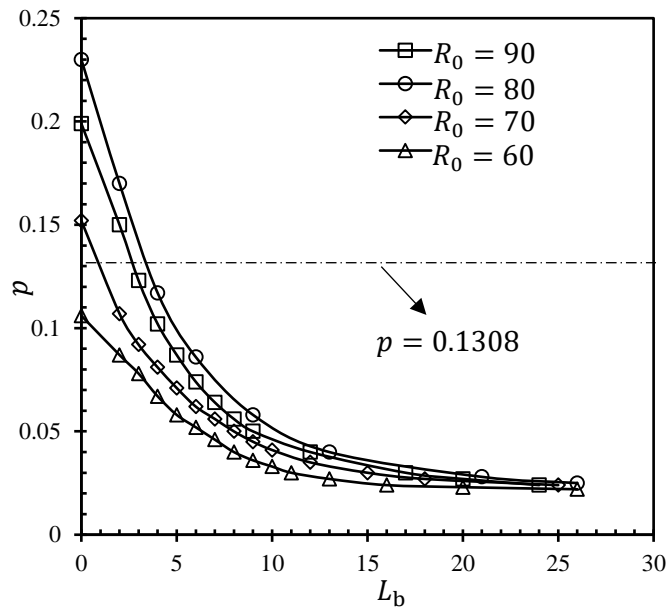


Figure 5.34. Effects of the initial sizes of the cavitation bubbles of the collapsed spherical bubbles on the propagation of the collapse pressure over L_b .

Furthermore, the effects of the collapse of non-spherical bubbles on the evolution of the surface pressures of droplets were investigated. For easy comparison, the pressure difference across the cavitation bubbles was increased to $\Delta p = 0.0334$ to ensure a collapse pressure similar to that of the collapse pressure of spherical bubbles. As shown in Figure 5.35 below, the collapse pressure decreased quickly over L_b , as well as when the initial size of the bubbles decreased. For a similar collapse pressure, the collapse of the non-spherical cavitation bubbles appeared to have a larger L_{cri} value compared to the collapse of the spherical bubbles, as shown in Figure 5.36 below. This might have been because the collapse of the non-spherical bubbles focused the pressure in one direction, thus having a higher momentum to propagate in the liquid, whereas the collapse of the spherical bubbles tended to dilute their pressure waves all around the liquid. However, the L_{cri} values achieved with these high pressures were still very small,

indicating that the collapse point needed to be very close to the surface of the droplet. As observed in the experimental study (see Section 4.3), the majority of the nucleation events occurred in the gap between the droplet and the tube wall.

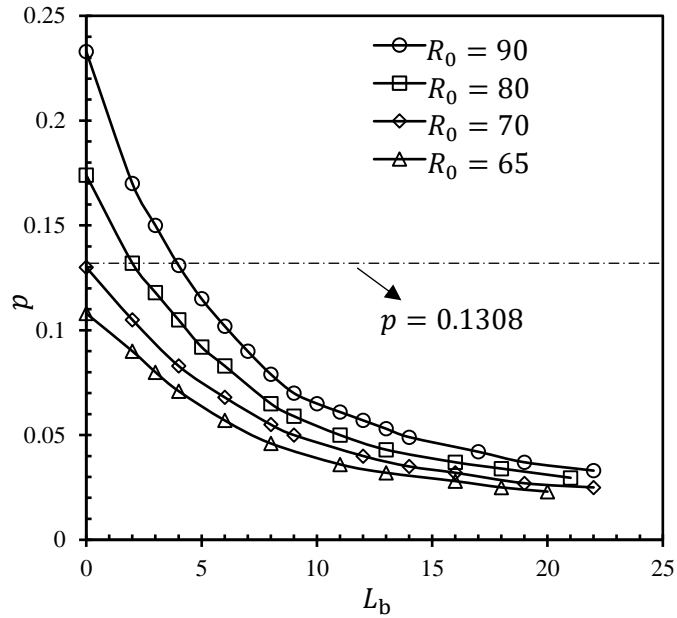


Figure 5.35. Effects of the initial sizes of the cavitation bubbles of the collapsed non-spherical bubbles on the propagation of the collapse pressure over L_b .

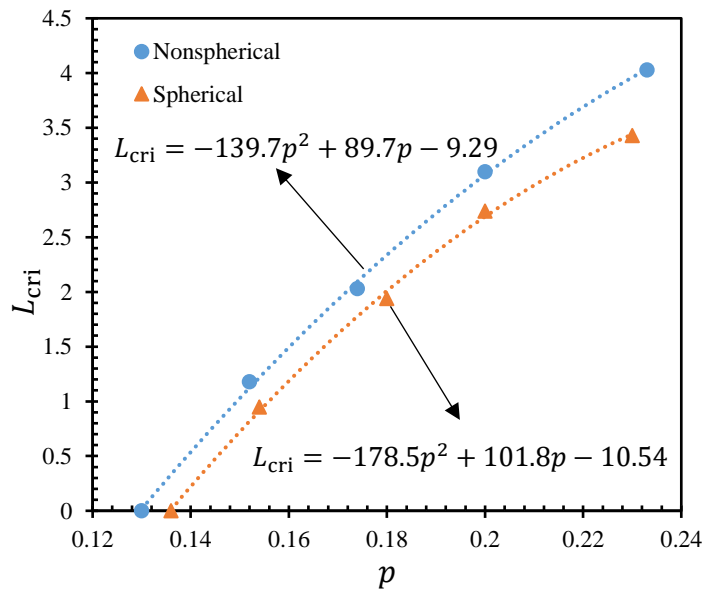


Figure 5.36. Effects of the collapse pressure on the critical distance between the surface of the droplet and the collapse point of the cavitation bubbles.

5.5 Chapter summary

In this chapter, numerical simulations were carried out to investigate: (i) the effects of the recalescence stage on the predictions for the freezing process; (ii) the process of ice nucleation induced by the collapse of cavitation bubbles; (iii) the evolution of the collapse pressures of the cavitation bubbles in the crevices of a solid surface immersed in water; and (iv) the evolution of the pressures on the surfaces of droplets imposed by the collapse of the cavitation bubbles in the continuous medium.

The recalescence stage was incorporated into the conventional lattice Boltzmann method (LBM) to examine the effects of the distribution of the initial ice fractions on the subsequent freezing processes of supercooled water. The predicted results of the extended LBM simulations using the Stefan number (Ste) for the initial ice fractions in the recalescence stage provided the best agreement with the experimental data. To the contrary, the predicted results of the model without consideration of the recalescence stage deviated most significantly from the experimental data. For relatively high temperatures (≥ 245 K), both the Ste and enthalpy-based methods might be valid for calculating the initial ice fraction in the recalescence stage, whereas for temperatures lower than ≥ 245 K the Ste method is recommended. When the degree of supercooling was close to 0 K, the models with and without consideration of the recalescence stage generated identical results, in terms of the evolution of the ice-water interface. However, for degrees of supercooling greater than 20 K, the recalescence stage should be considered in the LBM simulations to achieve predicted results with high accuracy. The present study sheds light on the importance of including the distributions of the initial ice fractions in the predictions for the freezing process of supercooled water.

The dynamics of the cavitation bubbles and the subsequent ice nucleation induced by the collapse of the bubbles were studied using a pseudo-potential MRT-LBM coupled with a thermal LBM. In the present model, the application of a dimensionless parameter, k , in the EoS equation and a dimensionless parameter, σ , in the forcing term enhanced the numerical stability, widened the range of simulation temperatures and reduced the spurious currents. Meanwhile, the thermodynamic consistency was well maintained. Thus, the present model realised simulations of the collapse of cavitation bubbles with temperatures lower than $0.422T_c$.

Ice nucleation induced by the collapse of cavitation bubbles was numerically investigated in two scenarios: (Scenario I) near a solid boundary, and (Scenario II) within a pressurised space. A series of simulations were conducted to investigate the effects of different parameters on the onset of the ice nucleation, including the standoff distances, the pressure differences and the sizes of the initial bubbles. The results showed that under the same conditions, much higher pressures were generated in the collapse of the cavitation bubbles in Scenario II compared to in Scenario I, and thus could more readily initialise the ice nucleation. With the same collapse pressures, the collapse of the non-spherical cavitation bubbles required much less degrees of supercooling for continuous freezing than was required for the spherical cavitation bubbles. The kinetics of the ice formation and growth were found to be strongly dependent on the evolution of the local temperature and pressure fields. After initialisation, the ice nucleation continued outwardly along with the propagation of the pressure wave from the collapse site towards the surrounding water. Due to the fast dissipating pressure, part of the initially formed ice then melted when the local temperature exceeded the melting temperature. To ensure the subsequent continuous

freezing of the water requires either a sufficient amount of heat exchange between the ice particles and the surrounding water or a large initial degree of supercooling.

Numerical simulations based on the LBM were conducted to examine the collapse dynamics of the cavitation bubbles in the asperity crevices on the surfaces of the particles. The maximum collision pressure, P_d , generated in the particle-substrate collision was estimated to be less than 0.04 GPa, which was insufficient to trigger the ice nucleation. The collapse of the cavitation bubbles in the asperity crevices on the rough surfaces of the particles that generated the extremely high point pressures could be responsible for the initialised nucleation. The simulation results showed that the collapse of the cavitation bubbles in the crevices was structure sensitive. For $P_d \leq 0.08$ GPa, it was found that only in the hemisphere-shape crevices could the collapse of the bubbles generate pressures that were high enough to induce ice nucleation inside the water droplets. Compared to the square-shaped and cone-shaped crevices, the collapsing bubbles in the hemisphere-shaped crevices generated relatively higher collapse pressures due to the smaller contact areas with the solid boundary during the collapse.

For the cavitation bubbles in the vicinity of a droplet, the pressure wave was found to dissipate quickly with the distance between the droplet and the collapse point. Therefore, to ensure the relatively high pressures that can induce ice nucleation, the final collapse point needs to be close enough to the surface of the droplet. The results also showed that the collapse of the non-spherical cavitation bubbles could render a relatively longer critical distance.

The numerical model developed in the present study could be adopted as a powerful tool for analysing the flow and temperature fields and the nucleation and freezing processes,

providing theoretical support to the analysis of experimental measurements as well as critical complementary data for understanding the underlying mechanisms of this complex phenomenon.

**CHAPTER 6. EXPERIMENTAL STUDY ON THE
CONTINUOUS PRODUCTION OF ICE PARTICLES**

6.1 Introduction

Previous chapters conducted a combined theoretical (Chapter 3), experimental (Chapter 4) and numerical (Chapter 5) studies of ultrasonic-assisted freezing of small water droplets. The results have demonstrated the ice nucleation ability of acoustic cavitation bubbles in micro-sized water droplets. This chapter, therefore, further studies the continuous production of ice particles from micro-sized water droplets assisted by the ultrasonic vibrations. The effectiveness of the ice nucleation triggering method employing cavitation bubbles for continuous production of micro-sized ice particles dispersed in an immiscible liquid is examined experimentally. Specifically, the yield and quality of the ice particles, in terms of their frozen droplet fractions, distribution of particle sizes and roundness ratios, were examined as a function of the ultrasonic characteristics, namely: the power output of the sonicator, vibration duty cycle and offset distance of the sonicator probe.

6.2 Experimental study

6.2.1 Experimental conditions and procedures

The experimental set-up in Section 4.3 was applied again for this study. For the continuous production of ice particles, the water droplets were generated through the microfluidic T-junction by controlling the flow rate of the water (ranging from 0.1 mL to 0.4 mL) and the oil phase (ranging from 11.0 mL to 15.0 mL). For the oil phase, a 10 mL syringe was filled with 9 mL oil and 1 mL air to ensure an air-pressurised condition. Once the temperature field was stabilized, the ultrasonic vibrations (power output, P_p , ranged from 10% to 20%) were imposed on the ice nucleation module through the sonicator probe. The morphologies of the droplets and ice particles were

monitored with a digital microscope. f_{ice} represented the fraction of frozen droplets out of the total number of water droplets, and R_r was the fraction of round ice particles out of the total number of ice particles. The total number of water droplets and the number of frozen droplets were determined by the observation numbers in a given period of time (300 s). The effects of the duty cycle, power output, P_p , offset distance of the sonicator, L_p , flowrates (q_o and q_w), and the cooling temperatures on the f_{ice} and R_r values were systematically investigated.

6.2.2 Stability analysis of the experimental set-up

The driving pressure inside the tube, P_d , was found to be the key to the inception, development, movement and the final collapse of the cavitation bubbles. The distributions of the P_d inside the tube were measured for different values of L_p and P_p and are shown in Figure 6.1 below. The P_d were the peak values of the pressure amplitudes measured in each duty cycle. For $P_p = 10.0\%$, the driving pressures at the centre of the sonicator probe were as high as $P_d \approx 1.9$ bar, while they linearly decreased to $P_d \approx 1.0$ bar with $L_p = 35$ mm. The same trend in the evolution of the P_d values was observed for different P_p values. It was these high pressures which were the warranty of cavitation inception events. Though all of the measured values for P_d were above the critical values (≈ 1 atm [144]), in each duty cycle the P_d values actually changed between 0 and $P_d|_{peak}$. Consequently, during the propagation of a pressure field, the water droplets may pass the nucleation module without interacting with any cavitation bubbles when the P_d is still on the way to its peak value. Therefore, for the supercooled water droplets to interact with the cavitation bubbles, increasing the P_p can ensure more time for the interactions to occur.

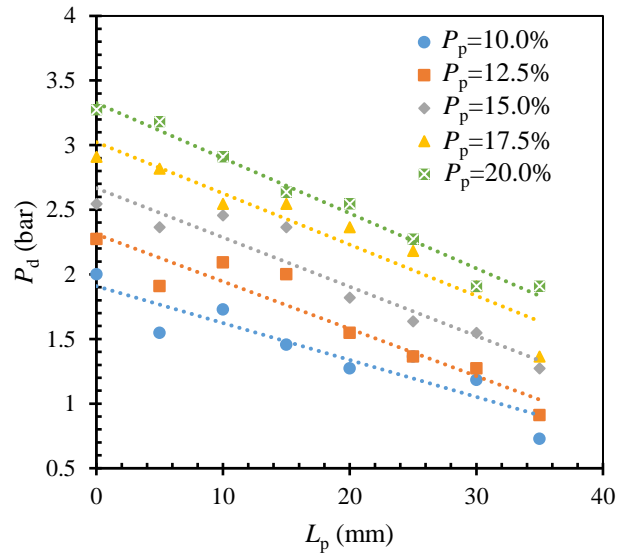


Figure 6.1. Evolution of the driving pressure amplitudes over different distances from the sonicator probe [V_{duty} : 10%].

The water droplet generation ability of the system at room temperature with different flowrates for the oil and water was also investigated. For each case, over 60 droplets were recorded and measured. The measurement resolution is 0.023 mm. The effects of the flowrates on the size distributions of the water droplets are shown in Figure 6.2 below. Clearly, when $q_o = 11$ mL/h, the sizes of the droplets mostly ranged between 0.53 mm and 0.59 mm, with the dominant size at around 0.55 mm. The fraction of this dominant droplet size increased with an increase in the ratio of the water/oil flow rate (i.e., from 50:1 to 10:1). Whereas, if the water flow rate was fixed at $q_w = 0.2$ mL/h, the fraction of the dominant droplet size moved up from 45% to 82%, with the rise in the oil flowrate from $q_o = 11$ mL/h to $q_o = 12$ mL/h, and then the fraction dropped significantly with a further increase in the oil flow rate (see Figure 6.3). Therefore, it can be concluded that flowrates with a high water/oil ratio tended to have relatively large droplets. This result was in line with the simulation findings of Liu et al. [298, 299].

Though the oil flowrate varied within a fairly large range, the capillary number ($C_a = \frac{\eta_c Q_c}{\gamma w_c}$) of the system only fell between 0.001 and 0.003, based on which the corresponding droplet sizes from literature range from 0.535 mm ($C_a = 0.003$) to 0.567 mm ($C_a = 0.001$) [299], which has a good agreement with the present experimental data, indicating that the microfluidic system has good stability and reliability in generating droplets with uniform sizes.

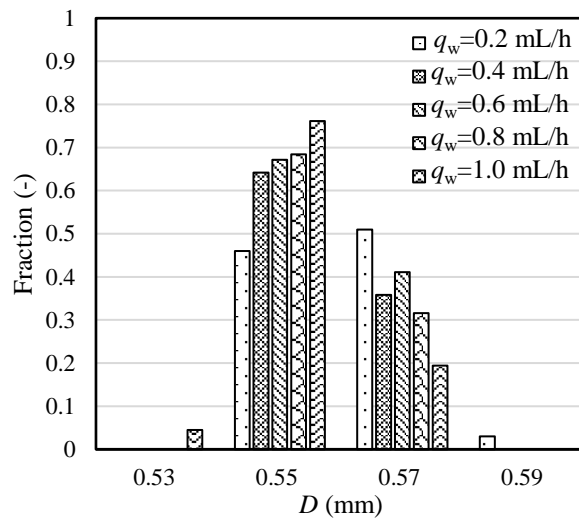


Figure 6.2. Effects of the water flowrate on the size distribution of the water droplets with $q_o = 11$ mL/h [$P_p = 0$].

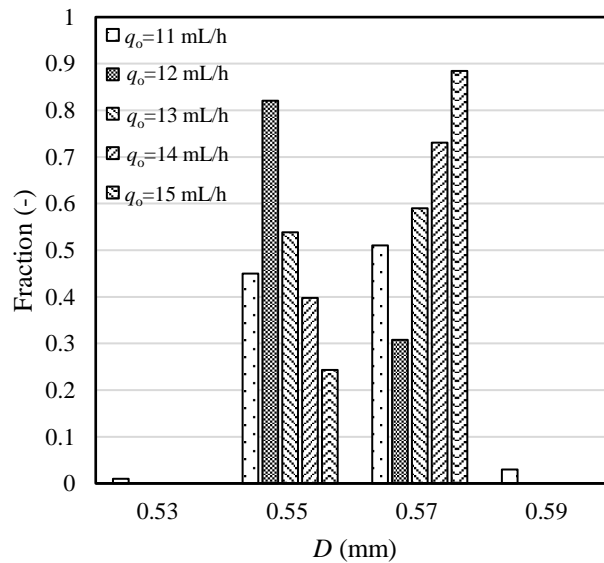


Figure 6.3. Effects of the oil flowrate on the size distribution of the water droplets with $q_w = 0.2 \text{ mL/h}$ [$P_p = 0$].

After generation, the droplets were introduced into the ice nucleation module where the effects of the temperature on the size of the droplets were investigated. As shown in Figure 6.4 below, the majority of the sizes of the water droplets remained between 0.55 mm and 0.57 mm due to the fixed flow rate ($q_o = 12 \text{ mL/h}$, $q_w = 0.5 \text{ mL/h}$). However, a small fraction of large droplets was observed when the temperature started to decrease. These large droplets were of a diameter in the range of 0.71 mm to 0.8 mm, and had been generated through the coalescence of two or more small droplets, as shown in the inset (a \rightarrow c) of Figure 6.4 below. The question is how the droplets catch up with each other before the coalescence? The answer might be because the viscosity of the oil changed, from 0.8 cSt to 0.1 cSt, with a decrease in the temperature, from 293.15 K to 283.15 K, which resulted in an increase in the drag force. In addition, the density ratio between the oil and water went up slightly with a decrease in the temperature, leading to an increase in the friction force between the droplets and the surface of the tube. Therefore, the droplets tended to slow down when they flowed into the cold section of the tube, leading to a coalescence of the water droplets.

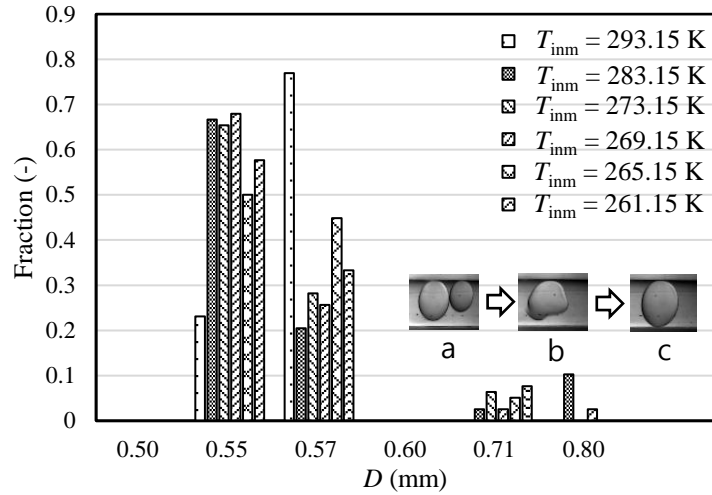


Figure 6.4. Effects of the temperature of the ice nucleation module on the distribution of water droplet sizes [$P_p = 0$; $q_o = 12$ mL/h; b: $q_w = 0.5$ mL/h].

6.3 Results and discussion

6.3.1 Initial bubble formation and distribution of sizes

According to the crevice model of cavitation bubble nucleation [300], the crevices or cracks on hydrophobic surfaces can facilitate the generation of bubbles. In this study, a circular crevice rested between a microfluidic T-junction and the expansion tube. When the air-pressurised oil flowed past this crevice, it was thought that the dramatic pressure drop might lead to the growth of cavitation bubbles in the crevice. To estimate the pressure drop from the syringe pump to the crevice, the flow type in the tube needed to be determined. The Reynolds number was calculated by:

$$Re = \frac{uD_H}{\nu} \quad (6.1)$$

where D_H is the hydraulic diameter of the tube (m), ν is the kinematic viscosity of the oil and u is the mean speed of the fluid obtained from the total flowrate. The inner tube

diameter between the syringe pump and the microfluidic T-junction was 0.00025 m, and the length was 0.3 m. In calculating the highest Reynolds number, the highest flowrate in this study was applied, namely 15 mL/h. The obtained Reynolds number was $Re = 27.6$, indicating a laminar flow type. Accordingly, the pressure drop was calculated by:

$$\Delta P = \frac{32 * L * \rho * u^2}{Re * D} \quad (6.2)$$

where L is the tube length and ρ is the density of the oil. Thus, the obtained pressure drop was 9.5 kPa. Based on this pressure drop, cavitation bubbles could be generated in the crevice. To observe this formation of the cavitation bubbles, the ultrasonic vibrations were turned off. As can be seen in Figure 6.5 below, a cavitation bubble was observed (as circled by dotted red circles). For reference, without the assistance of an ultrasonic field, the experimental results showed that cavitation bubbles could not form in the crevice if using non-air-pressurised oil. After the cavitation bubbles detached from the crevice, it kept growing when it moved into a region with much lower pressure. When this bubble moved into the field of intense ultrasonic vibrations, it became a bubble nucleus and expanded into a much larger cavitation bubble.

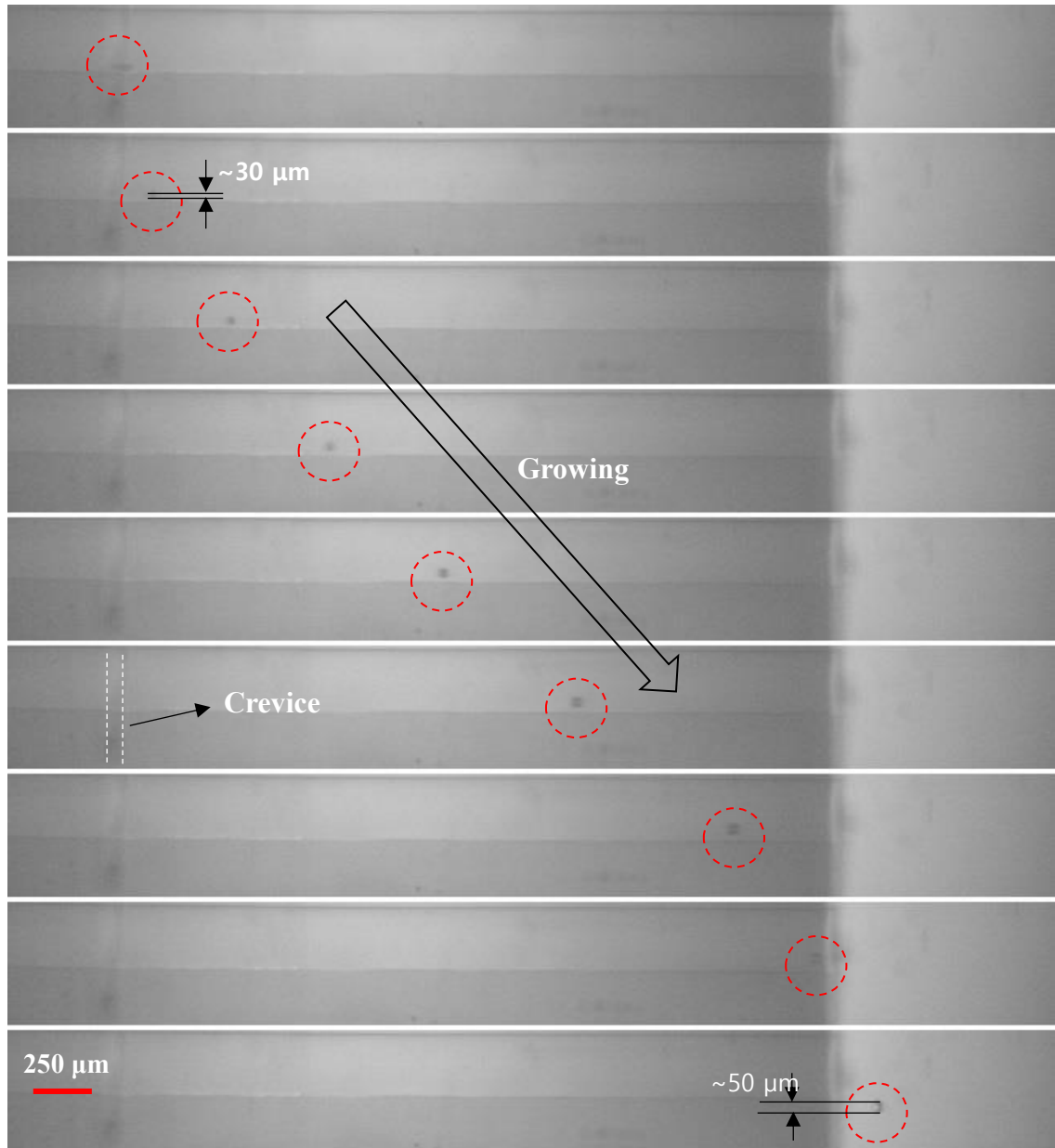


Figure 6.5. Formation of a cavitation bubble in a crevice without ultrasonic vibrations [$q_o = 12 \text{ mL/h}$].

6.3.2 Influential parameters and the quality of the ice particles

To evaluate the performance of the continuous ice nucleation of water droplets in tubes, the influential parameters were investigated in-depth, including the flowrates of the water and oil, the temperature of the ice nucleation module, the duty cycle of the ultrasonic

vibrations, and the position of the sonicator probe and its power output. The ice nucleation ability of the process was determined by the fraction of frozen droplets in a certain period of time and the quality of the ice particles was only evaluated by the roundness of the ice particles, as the observations in this study are two-dimensional.

Figure 6.6 below plots the effects of the oil flowrate on the f_{ice} at different temperatures. The corresponding evolution trend of the R_r at different temperatures is shown in Figure 6.7 below. The ratio of the flow rate was set at $q_o:q_w = 12:0.36$. As can be seen, the f_{ice} values increased significantly with a decrease in the temperature, whereas the values for R_r decreased drastically with a reduction in the temperature. The frozen droplets were observed at temperatures as high as 269 K. At a fixed T_{inm} value, lower flowrates tended to have higher f_{ice} values but had much lower values for R_r . This was because a lower flowrate could have a relatively longer residency time to achieve an adequate interaction with the cavitation bubbles. For example, take $q_o = 11$ mL/h and $q_o = 15$ mL/h, where the corresponding residency times were 6.56 s and 4.82 s, respectively. To achieve the same value of f_{ice} , a relatively lower value for T_{inm} was required in higher flowrate cases. It is noteworthy that the sensible heat carried by the oil phase should be critically evaluated, particularly for applying in high flowrate cases. If there's no efficient way of recycling the cold oil, the cold energy waste will increase dramatically with a lower T_{inm} .

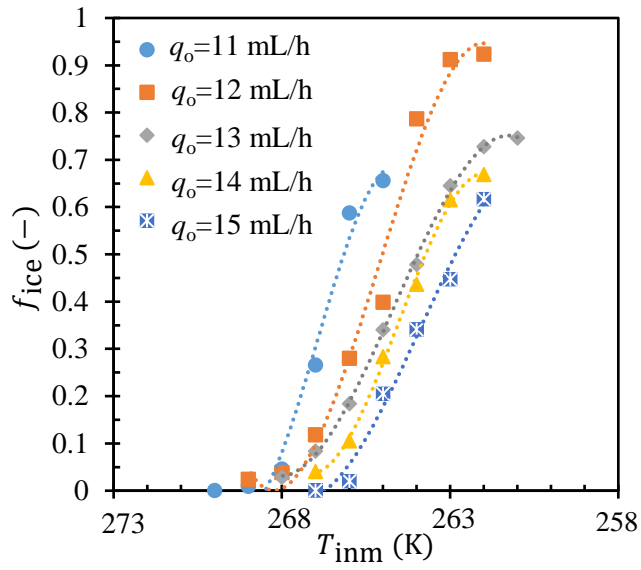


Figure 6.6. Effects of the flowrate on f_{ice} [$q_o:q_w = 12:0.36$; $P_p = 20\%$; $V_{duty} = 10\%$; $L_p = 0$ mm].

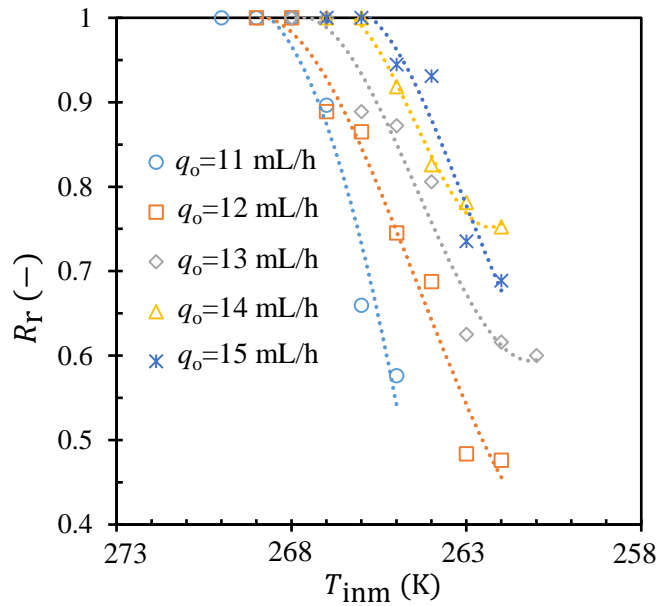


Figure 6.7. Effects of the flowrate on R_r [$q_o:q_w = 12:0.36$; $P_p = 20\%$; $V_{duty} = 10\%$; $L_p = 0$ mm].

The effects of the intensity of the ultrasonic vibrations on the f_{ice} values at different temperatures are shown in Figure 6.8 below. The corresponding R_r values at different

temperatures is presented in Figure 6.9 below. It was found that the values of f_{ice} increased remarkably with increased values of P_p . Increasing the P_p could increase the possibility of interactions between the cavitation bubbles and the water droplets due to the increased P_d . Consequently, at a given temperature (e.g., $T_{inm} = 262$ K), the fractions of the frozen droplets obtained with $P_p = 10.0\%$ and $P_p = 20.0\%$ were $f_{ice} \approx 1.2\%$ and $f_{ice} \approx 92.3\%$, respectively. Meanwhile, the R_r values decreased, from 100% to as low as 48%. For the same fraction (e.g., $f_{ice} \approx 28\%$), the corresponding R_r values for $P_p = 10.0\%$ and $P_p = 20.0\%$ were $R_r \approx 75\%$ and $R_r \approx 91\%$, respectively. These results indicated that the R_r can be significantly increased by increasing the P_p .

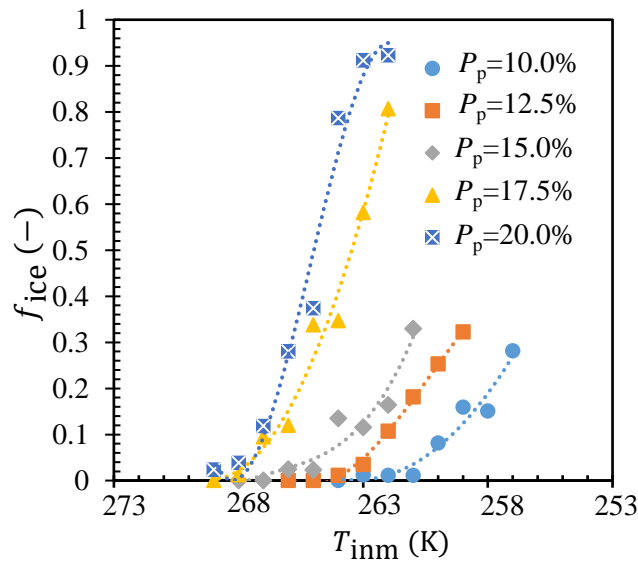


Figure 6.8. Effects of the vibration intensity on the f_{ice} at different temperatures [$q_o:q_w = 12:0.36$; $V_{duty} = 10\%$, $L_p = 0$ mm].

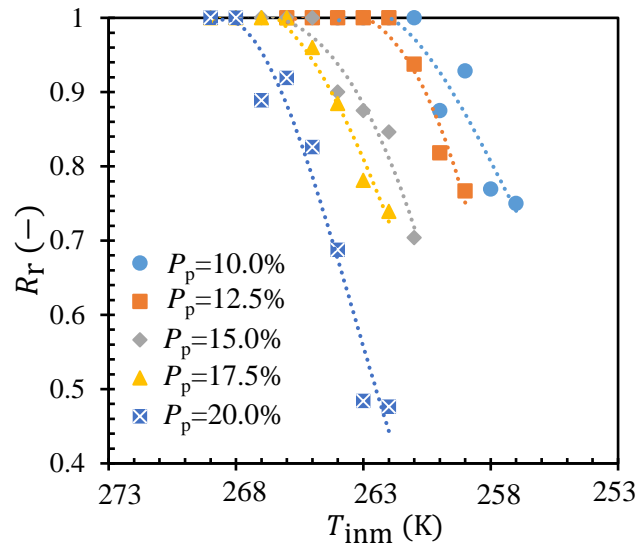


Figure 6.9. Effects of the intensity of the ultrasonic vibrations on the R_r at different temperatures [$q_o:q_w = 12:0.36$; $V_{duty} = 10\%$, $L_p = 0$ mm].

Other than the intensity of the vibrations, the closely related duty cycle also plays an important role in the ice nucleation of water droplets. Figure 6.10 below shows the effects of the vibration duty cycle on the f_{ice} values and its corresponding effects on the R_r values is plotted in Figure 6.11 below. Clearly, increasing the duty cycle could remarkably increase the values of f_{ice} , whereas the R_r values decreased. The increase in the duty cycle can be viewed as a way of increasing the interaction time between the water droplets and the cavitation bubbles, which is similar to increasing the P_p . If the duty cycle was increased (from 10% to 40%) and the P_p was simultaneously increased (from 10% to 15%), the values of the f_{ice} increased remarkably, from about 2.1% to 69.0%, at $T_{inm} = 262$ K. Meanwhile, the corresponding values for R_r decreased from 100% to 75%.

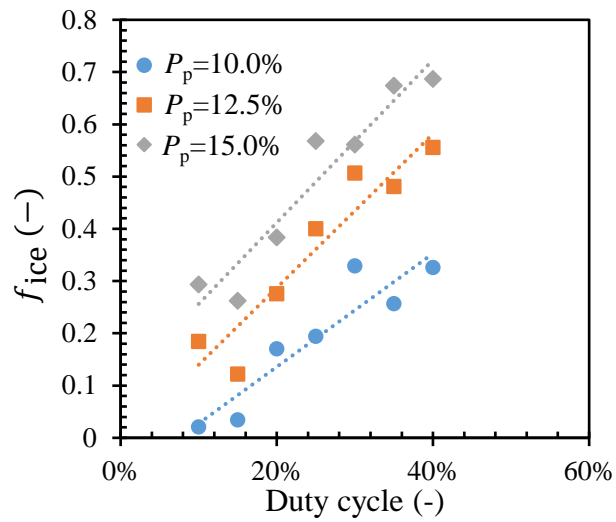


Figure 6.10. Effects of the vibration duty cycle on the f_{ice} [$q_o:q_w = 12:0.36$; $L_p = 0$ mm].

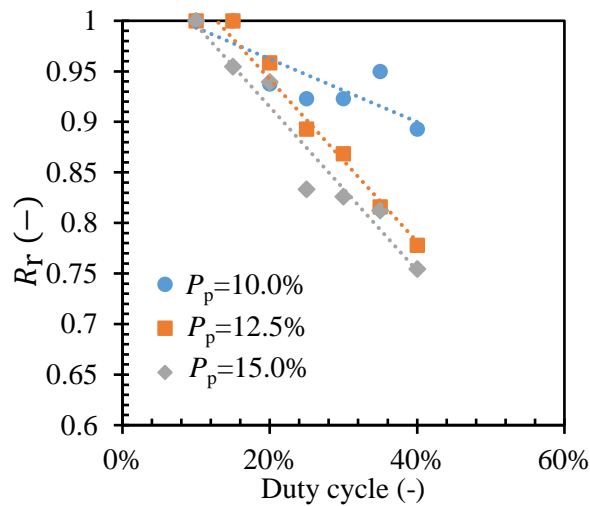


Figure 6.11. Effects of the vibration duty cycle on the R_r [$q_o:q_w = 12:0.36$; $L_p = 0$ mm].

The effects of the offset distance of the sonicator probe, L_p , versus the cooling module on the f_{ice} values at different temperatures are shown in Figure 6.12 below, and the corresponding R_r values are plotted in Figure 6.13 below. Three positions were

investigated, namely $L_p = 0$ mm, $L_p = 15$ mm and $L_p = 30$ mm. For $L_p = 0$ mm, the sonicator probe was at the water droplet inlet side, meaning that the highest intensity of vibrations was 30 mm away from the right-hand end of the cooling module where the droplet was deeply cooled down. For $L_p = 30$ mm, the sonicator probe was right above the deeply cooled droplet. For all three L_p values, with increasing temperatures, the values of the f_{ice} increased and the R_r values gradually decreased. However, for $L_p = 30$ mm, the f_{ice} values were much higher than those for $L_p = 0$ mm and $L_p = 15$ mm. This was understandable, as with $L_p \ll 30$ mm, the intensity of the vibrations was much reduced (as shown in Figure 6.1) where the water droplet was deeply cooled. Therefore, positioning the probe at the right-hand end of the cooling module could enhance the production of ice particles.

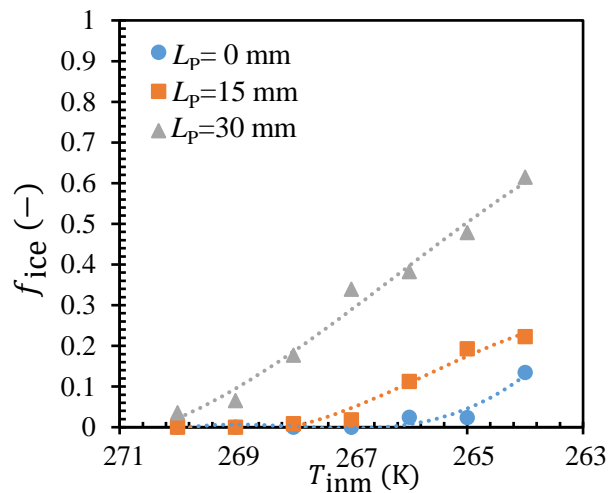


Figure 6.12. Effects of the offset distance of the sonicator probe on f_{ice} [$q_o:q_w = 12:0.36$; $P_p = 10\%$; $V_{duty} = 10\%$].

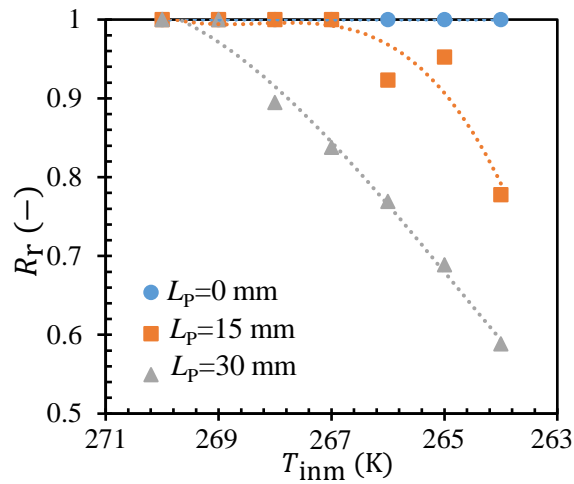


Figure 6.13. Effects of the offset distance of the sonicator probe on R_r [$q_o:q_w = 12:0.36$; $P_p = 10\%$; $V_{duty} = 10\%$].

It is worth noting that when the cavitation bubbles were absent from the ice nucleation module, ice nucleation in the water droplets could not be initiated, which confirmed that the ice nucleation closely hinged on the interactions with the cavitation bubbles. However, cavitation bubbles could not be directly formed for values of P_p in the range of 10% to 15% without the assistance of the bubbles generated from the crevice. Consequently, ice nucleation events could not be observed at the start of each experiment before the initial bubble moved into the ice nucleation module.

6.3.3 Characterisation of the ice particles

With strong interactions with cavitation bubbles, the ice nucleation of a water droplet is likely to occur at two places: (i) at the water-oil interface, where the ice nucleation is triggered by the interaction with the cavitation bubbles in the oil phase; (ii) inside the water droplet, where some of the cavitation bubbles may penetrate the oil-water interface and move into the droplet. The Case (i) ice nucleation of a water droplet generated a

spherical ice particle, as shown in Figure 6.14 (a) below. For the Case (ii) ice nucleation of a water droplet, the cavitation bubble may leave a conical shape in the ice particle when the cavitation bubble moves outside the partially frozen droplet. As clearly illustrated in Figure 6.14 (b), a large volume of air was trapped inside the ice particle, which was often observed at relatively low T_{inm} values. The lower the temperature, the faster the freezing rate. Moreover, the flow field could also be fiercely interfered with by the vibration field, resulting in the coalescence of droplets due to the sudden acceleration or slowing of the droplets. Therefore, relatively large ice particles were often observed, as shown in Figure 6.14 (c). Large ice particles were regarded as undesirable as they may block the tubing system.



Figure 6.14. Morphology of ice particles [scale bar: 0.4 mm].

The sizes of the ice particles at different temperatures and water flowrates are plotted in Figure 6.15 below. The irregular ice particles were not considered in the calculation of the mean diameter size of the ice particles. Apparently, for different flowrate ratios and temperatures, the sizes of the ice particles fluctuated between 0.45 mm and 0.6 mm. Compared to the droplet sizes without the ultrasonic vibrations (i.e., ~ 0.5 mm), the deviation was about +0.05 mm and -0.1 mm. This deviation indicated that the droplets broke up due to interactions with the cavitation bubbles which might occur during the ice particle production process. However, the deviation might be reduced

through the recollection of the tiny water droplets (less than 0.1 mm). As shown in Figure 6.16 below, a couple of small water droplets were collected by an ice particle.

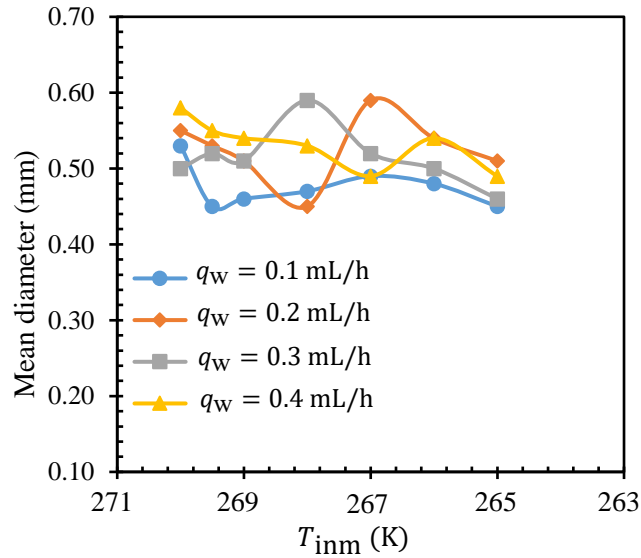


Figure 6.15. Ice particle mean-diameter over temperature and water flowrate [$q_o = 12$ mL/h; $P_p = 10\%$; duty cycle: 10%].



Figure 6.16. Recollection process by an ice particle of the small droplets [Time interval: 0.033 s; scale bar: 0.4 mm].

6.4 Chapter summary

The production of ice particles assisted by ultrasonic vibrations was systematically investigated in this chapter. The effects of different experimental parameters on the production of ice particles were studied in detail, including the intensity and duty cycle of the vibrations, the flowrates of the oil/water, the position of the sonicator probe and the temperature of the droplets. It was found that the f_{ice} values increased with an increase in the power output of the sonicator (i.e., P_p), the duty cycle of the vibrations (V_{duty}), the

position of the sonicator (L_p), and with decreasing temperatures in the ice nucleation module (T_{inm}). To the contrary, the roundness ratio of the ice particles, R_r , decreased with increasing values of P_p , V_{duty} , L_p , and with decreasing values of T_{inm} . The frozen droplets could be observed at temperatures as high as 269 K. The results also showed that increasing both the intensity and the duty cycle of the vibrations could dramatically increase the values of the f_{ice} and R_r . However, a balance needs to be established between the energy consumption and the efficiency of ice particle production.

**CHAPTER 7. CONCLUSIONS AND
RECOMMENDATIONS**

Motivated by the need for developing effective approaches for generating engineered ice particles of uniform sizes and spherical shapes, this research has been dedicated to investigating the ultrasonic-assisted freezing of micro-sized water droplets. A combined theoretical, experimental and numerical study has been conducted for obtaining an improved understanding of ice nucleation of micro-sized water droplets induced by high pressures from acoustic cavitation, and the subsequent effects on freezing temperatures of water droplets. Further, the acoustic cavitation was applied to continuous production of micro-sized ice particles. The main conclusions are summarised in section 7.1. The recommendations for future work are presented in section 7.2.

7.1 Conclusions

Firstly, a theoretical framework was built to clarify the relationship between ice nucleation and pressure based on the distribution of molecular kinetic energy. With this framework, the need was avoided to specify the ice-water interface energy and activation energy which are typically required for conventional methods. The predicted pressure-dependent homogeneous ice nucleation temperatures agreed well with the experimental results. A good agreement was obtained between the predicted homogeneous ice nucleation rate (J_h) and the experimental data collected from the literature for temperatures down to 190 K, indicating that the model was able to capture all the essential elements of ice nucleation phenomenon using a simplified approach. Significant improvements in the predictions were achieved after the fluctuations in the temperatures were included in the model. The J_h values were found to be strongly pressure-dependent for $T > 232$ K, but appeared to be weakly pressure-dependent for $T < 227$ K. Based on this theoretical study, it can be certain that ice nucleation rates for fine water droplets

can be significantly increased by extremely high pressure fields. With the measurable parameters as the inputs including the enthalpy of fusion, the hydrogen-bond energy, the pressure-dependent melting temperatures, and the pressure-dependent solid/liquid densities, this theoretical framework can be readily extended and applied to analyse the nucleation of other liquids with hydrogen-bonds.

The experimental work focused on the ice nucleation of confined volumes of water (i.e. micro-sized droplets). In particular, two mechanical ice nucleation triggering methods were developed based on acoustic cavitation. In the first method, fine solid particles submerged in a droplet were used to provide free sites for cavitation bubble inception. In the second method, cavitation bubbles were formed within the continuous medium carrying suspended droplets. Both methods used acoustic vibration to trigger ice nucleation. For the first method, the results showed that the ice nucleation could be induced by weak ultrasonic vibrations at temperatures as high as 271.15 K. The fraction of frozen droplets increased with an increase in the particle number concentration, vibration intensity, and vibration induction time. For water droplets with only one particle, the ice nucleation could not be initiated. When the water droplets had more than one particle, the ice nucleation events began to occur. It was evident that the nucleation sites for this approach were limited to the regions between solid particles and the vibrating substrate, in turn, indicating that the contact pressure due to particle collision with the substrate greatly influences ice nucleation onset. This method appears as a prominent way of inducing ice nucleation to the subjects that are sensitive to the ultrasonic vibrations. For the second method, the fraction of frozen droplets was also found increasing with increasing the vibration intensity and vibration induction time. The experimental observations showed that the sites for ice nucleation onset were at the droplet surface

where strong interactions between cavitation bubbles (formed in the continuous phase) and droplets (the dispersed phase) were encountered. It was evident that the cavitation bubble triggered the onset of ice nucleation. These results should find useful in designing the device for continuous production of ice particles.

Numerical studies based on lattice Boltzmann method (LBM) were carried out to gain a better understanding of the mesoscale underlying physics of the ice nucleation and freezing process for the above approaches, including the isentropic collapse process of cavitation bubbles, the propagation of the pressure waves and high temperatures generated, the rapid recalescence stage upon nucleation, and the evolution of the moving ice-water interface (the so-called ‘mushy zone’). Specifically, the conventional pseudo-potential multi-relaxation-time LBM (MRT-LBM) coupled with a thermal LBM was developed to investigate the cavitation bubble dynamics, including growth and collapse, and the subsequent ice nucleation and freezing process. The thermal LBM was extended by: i) inclusion of the recalescence stage (rapid growth of dendritic ice) and ii) inclusion of a criterion for the pressure-dependent ice nucleation onset. In this model, the Stefan number was used to determine the initial ice fraction for the entire spectrum of supercooling degrees in the recalescence stage. The Simon-Glatzel equation was applied to correlate the ice melting curve with the local pressure field which, in turn, governs the onset of ice nucleation. Both literature data and experimental data collected as part of this study were used to validate the model. The deviations fell within the limits of the experimental error.

The model was then used to gain an insight into a number of phenomena, including (i) the effect of recalescence stage on the freezing process, (ii) ice nucleation induced by

cavitation bubbles, (iii) pressure evolution of cavitation bubbles inside the crevice, and (iv) pressure evolution on the droplet surface in the vicinity of a collapsing cavitation bubble. Initially, the recalescence stage in the freezing process was experimentally and numerically studied. When the supercooling degree was close to 0 K, the models with and without consideration of the recalescence stage generated identical results, in terms of the evolution of the ice-water interface. The simulation results showed that the inclusion of the recalescence stage has a significant effect on the accuracy of predicting ice-water interface evolution for supercooling degrees greater than 20 K. Given that the freezing of a small droplet often bears a supercooling degree of more than 30 K, and the local supercooling degree could be significantly increased by the high pressure from the cavitation bubble collapse, hence an accurate description of the freezing can be achieved only when the recalescence stage has been taken into account.

To examine the more general cases of ice nucleation induced by cavitation bubbles, the numerical model was applied to investigate two practical scenarios: (Scenario I) near a solid boundary, and (Scenario II) within a pressurised space. Specifically, the effects of the key parameters on ice nucleation induced by the collapse of cavitation bubbles were studied, including the standoff distances, the pressure differences and the initial sizes of the bubbles. The results showed that under the same conditions, much higher pressures were generated in the collapse of the cavitation bubbles in Scenario II compared to in Scenario I, and thus could more readily initialise the ice nucleation. With the same collapse pressures, the collapse of non-spherical cavitation bubbles required much lower degrees of supercooling for the continuous freezing than were required for the collapse of spherical cavitation bubbles. The kinetics of the ice formation and growth were found to be strongly dependent on the evolution of the local temperature and pressure fields.

After initialisation, the ice nucleation continued outwardly from the collapse spot along with the propagation of the pressure wave towards the surrounding water. Due to the quickly dissipated pressure, part of the initially formed ice melted when the local temperature exceeded the melting temperature. These results suggest that maintaining a sufficiently large initial supercooling degree or use of additional mechanisms to force the ice crystals to migrate to low-temperature regions are essential to achieve complete freezing of water droplets.

A series of numerical simulations were conducted to examine the dynamics of the collapse of cavitation bubbles in the crevices of solid particles. The collapse dynamics of air bubbles trapped in the crevice at the solid particle surface was found to be sensitive to the crevice morphological characteristics. Compared to the square-shaped and cone-shaped crevices, the collapse of the bubbles in the hemisphere-shaped crevices generated relatively higher collapse pressures due to smaller contact areas with the solid boundaries during the collapse. The generated collapse pressures were as high as 1.63 GPa, which could theoretically induce ice nucleation at relatively high temperatures, which provides a potential theoretical explanation on how the presence of solid particles could assist with the initialisation of ice nucleation in a droplet. Lastly, the simulation results showed that the ice nucleation onset at the surface of the droplet strongly depends on the distance between the bubble collapse point and the droplet surface. The simulation results were used to develop a correlation for predicting the minimum distance required to initiate ice nucleation in the droplet as a function of key operating parameters, including the cavitation bubble size and external pressure amplitude.

The effectiveness of the ice nucleation triggering method of the cavitation bubble for continuous production of micro-sized ice particles dispersed in an immiscible liquid was examined experimentally. Specifically, the yield and quality of ice particles in terms of frozen droplets fraction, particle size distribution and ice particle roundness ratio, were examined as a function of ultrasonic characteristics, namely, the sonicator power output, vibration duty cycle, and sonicator probe offset distance. The increase in the yield, however, led to a loss of quality. The mean diameter of the water droplets used for producing ice particles was in the range from 535 μm to 567 μm . After ice nucleation by the cavitation bubbles, the mean diameter of the produced ice particles was measured in the range from 450 μm to 590 μm . The freezing temperature achieved was as high as 269 K with the frozen droplets fraction of 2% and the ice particle roundness ratio of 1. The highest frozen droplets fraction of about 92% was obtained at 262 K, whereas the ice particle roundness ratio drastically decreased to around 45%.

The results of the present study should prove useful in the application of the ultrasonic vibration-assisted nucleation of supercooled liquids in other fields, such as freezing of saline water droplets, solidification of molten metals, and freezing of biomaterials, in which the supercooling phenomenon is often encountered. The results also prove useful when developing a range of devices based on the application of ultrasonic-assisted nucleation of supercooled liquids. The data on pressure-dependent ice nucleation temperature could be applied to optimise the device design and achieve an efficient system operation. Moreover, the numerical model developed in the present study could be adopted as a powerful tool for analysing the flow and temperature fields and the nucleation and freezing processes, providing theoretical support to the analysis of

experimental measurements as well as critical complementary data for understanding the underlying mechanisms of this complex phenomenon.

7.2 Recommendations for future work

The results of the present study should prove useful when developing a range of devices based on the knowledge of ultrasonic-assisted nucleation of supercooled liquids. Specifically, the data on pressure-dependent ice nucleation temperature from the theoretical model may be applied to optimise the device operation conditions and achieve a high efficiency. For manipulating the local pressure, the acoustic vibrations were applied to generate cavitation bubbles and induce their collapse. The experimental results of the effects of a series of key operation parameters on the ice nucleation may be applied to optimise the device design. Moreover, the numerical models developed in the present study may be adopted as a powerful tool for analysing the flow and temperature fields and the nucleation and freezing processes, providing critical theoretical support to the inner working of the complex systems.

However, there are some aspects of this research discussed below which still need to be pursued in the future in order to gain broader insights into the mechanisms of ice nucleation induced by cavitation bubbles, and the operation and economic viability of an ultrasonic vibration-assisted ice particle generator.

- i) In this study, the ice nucleation induced by cavitation bubbles were attributed to the extremely high positive pressures generated by the collapse of the bubbles. However, it has been reported that the stable oscillation of cavitation bubbles can also induce ice nucleation, which therefore cannot be explained by a high pressure field. Some theories have been proposed which aim to

clarify the underlying mechanisms, such as the microstreaming [38]. However, there are still contradictions and debates about the underlying phenomenon that drives heterogeneous ice nucleation with lower supercooling degrees [40, 116] [38]. In addressing this problem, further experimental and theoretical work are required to dig deep into the underlying physics that governs the onset of the ice nucleation.

- ii) In the continuous production of ice particles, surfactants can be added to the carrier fluid to avoid the coalescence of the droplets during the continuous and fast production of the water droplets, thus increasing the generation rate. With the presence of surfactant on the oil-water interface, experiments are required to investigate the performance of the cavitation bubbles on the ice nucleation of water droplets. Moreover, with the increase in the generation rate of water droplets, the inception of the cavitation bubbles might be reduced due to the reduction in the oil content. An optimum generation rate for the water droplets needs to be determined in terms of a high efficiency in the ice nucleation of water droplets by cavitation bubbles.
- iii) In the cavitation bubble collapse process, shock waves and supersonic micro-jets are often encountered, and the compressibility incurred needs to be rigorously considered for the accurate prediction of the collapse dynamics of the cavitation bubbles. Thus, a computational fluid dynamics (CFD) model that incorporates the compressibility needs to be developed to investigate the evolutions of the pressure and temperature fields, particularly for the subsequent ice nucleation process. Further, the CFD model can be extended to a three-phase multi-component model to examine the ice nucleation of

water droplets induced by cavitation bubbles outside the droplet. Specifically, to investigate ice nucleation triggered by the supersonic micro-jet through the droplet's interface.

References

1. Zhang, P. and Z.W. Ma, *An overview of fundamental studies and applications of phase change material slurries to secondary loop refrigeration and air conditioning systems*. Renewable and Sustainable Energy Reviews, 2012. **16**(7): p. 5021-5058.
2. Kauffeld, M., et al., *Ice slurry applications*. International Journal of Refrigeration, 2010. **33**(8): p. 1491-1505.
3. Bellas, I. and S.A. Tassou, *Present and future applications of ice slurries*. International Journal of Refrigeration, 2005. **28**(1): p. 115-121.
4. Yau, Y.H. and B. Rismanchi, *A review on cool thermal storage technologies and operating strategies*. Renewable and Sustainable Energy Reviews, 2012. **16**(1): p. 787-797.
5. Kumano, H., et al., *Flow characteristics of ice slurry in narrow tubes*. International Journal of Refrigeration, 2010. **33**(8): p. 1513-1522.
6. Kitanovski, A., et al., *The fluid dynamics of ice slurry*. International Journal of Refrigeration, 2005. **28**(1): p. 37-50.
7. Haruki, N. and A. Horibe, *Flow and heat transfer characteristics of ice slurries in a helically-coiled pipe*. International Journal of Refrigeration, 2013. **36**(4): p. 1285-1293.
8. Bellas, J., I. Chaer, and S.A. Tassou, *Heat transfer and pressure drop of ice slurries in plate heat exchangers*. Applied Thermal Engineering, 2002. **22**(7): p. 721-732.
9. Thongwik, S., T. Kiatsiriroat, and A. Nuntaphan, *Heat transfer model of slurry ice melting on external surface of helical coil*. International Communications in Heat and Mass Transfer, 2008. **35**(10): p. 1335-1339.
10. Thongwik, S., et al., *Thermal analysis of slurry ice production system using direct contact heat transfer of carbon dioxide and water mixture*. International Communications in Heat and Mass Transfer, 2008. **35**(6): p. 756-761.
11. Stamatiou, E., J.W. Meewisse, and M. Kawaji, *Ice slurry generation involving moving parts*. International Journal of Refrigeration, 2005. **28**(1): p. 60-72.
12. Meewisse, J.W. and C.A. Infante Ferreira, *Validation of the use of heat transfer models in liquid/solid fluidized beds for ice slurry generation*. International Journal of Heat and Mass Transfer, 2003. **46**(19): p. 3683-3695.

13. Bédécarrats, J.-P., T. David, and J. Castaing-Lasvignottes, *Ice slurry production using supercooling phenomenon*. International Journal of Refrigeration, 2010. **33**(1): p. 196-204.
14. Wijesundera, N.E., et al., *Ice-slurry production using direct contact heat transfer*. International Journal of Refrigeration, 2004. **27**(5): p. 511-519.
15. Ltd, I.D.E.T., *Vacuum Ice Maker (VIM) for Thermal Energy Storage (TES)*. 2010.
16. Peng, Z., et al., *Ice Slurry Formation in a Cocurrent Liquid-Liquid Flow*. Chinese Journal of Chemical Engineering, 2008. **16**(4): p. 552-557.
17. Asaoka, T., et al., *Vacuum freezing type ice slurry production using ethanol solution 2nd report: Investigation on evaporation characteristics of ice slurry in ice production*. International Journal of Refrigeration, 2009. **32**(3): p. 394-401.
18. Asaoka, T., et al., *Vacuum freezing type ice slurry production using ethanol solution 1st report: Measurement of vapor-liquid equilibrium data of ethanol solution at 20 °C and at the freezing temperature*. International Journal of Refrigeration, 2009. **32**(3): p. 387-393.
19. Robert G. Dorsch and P.T. Hacker, *Photomicrographic investigation of spontaneous freezing temperature of supercooled water droplets*, in *National advisory committee for aeronautics*. 1950.
20. Svensson, E.A., et al., *Freezing of water droplets colliding with kaolinite particles*. Atmospheric Chemistry and Physics, 2009. **9**(13): p. 4295-4300.
21. Fraux, G. and J.P.K. Doye, *Note: Heterogeneous ice nucleation on silver-iodide-like surfaces*. The Journal of Chemical Physics, 2014. **141**(21): p. 216101.
22. Aleksandrov, V.D., A.A. Barannikov, and N.V. Dobritsa, *Effect of magnetic field on the supercooling of water drops*. Inorganic Materials, 2000. **36**(9): p. 895-898.
23. Zhang, X.-X., X.-H. Li, and M. Chen, *Role of the electric double layer in the ice nucleation of water droplets under an electric field*. Atmospheric Research, 2016. **178-179**: p. 150-154.
24. Rzesanke, D., et al., *On the role of surface charges for homogeneous freezing of supercooled water microdroplets*. Physical Chemistry Chemical Physics, 2012. **14**(26): p. 9359-9363.

25. Gao, P., et al., *Study on droplet freezing characteristic by ultrasonic*. Heat and Mass Transfer, 2017. **53**(5): p. 1725-1734.
26. Dalvi-Isfahan, M., et al., *Review on the control of ice nucleation by ultrasound waves, electric and magnetic fields*. Journal of Food Engineering, 2017. **195**: p. 222-234.
27. Wang, B., et al., *Heterogeneous ice nucleation and water uptake by field-collected atmospheric particles below 273 K*. Journal of Geophysical Research: Atmospheres, 2012. **117**(D21): p. n/a-n/a.
28. Murray, B.J., et al., *Ice nucleation by particles immersed in supercooled cloud droplets*. Chem Soc Rev, 2012. **41**(19): p. 6519-54.
29. Lüönd, F., et al., *Experimental study on the ice nucleation ability of size-selected kaolinite particles in the immersion mode*. Journal of Geophysical Research: Atmospheres, 2010. **115**(D14): p. n/a-n/a.
30. Stan, C.A., et al., *A microfluidic apparatus for the study of ice nucleation in supercooled water drops*. Lab Chip, 2009. **9**(16): p. 2293-305.
31. Cooper, C.F. and W.C. Jolly, *Ecological effects of silver iodide and other weather modification agents: A review*. Water Resources Research, 1970. **6**(1): p. 88-98.
32. Virone, C., et al., *Primary nucleation induced by ultrasonic cavitation*. Journal of Crystal Growth, 2006. **294**(1): p. 9-15.
33. Yu, D., B. Liu, and B. Wang, *The effect of ultrasonic waves on the nucleation of pure water and degassed water*. Ultrasonics Sonochemistry, 2012. **19**(3): p. 459-463.
34. Zhang, X., et al., *Active control of phase change from supercooled water to ice by ultrasonic vibration 2. Generation of ice slurries and effect of bubble nuclei*. International Journal of Heat and Mass Transfer, 2001. **44**(23): p. 4533-4539.
35. Hunt, J. and K. Jackson, *Nucleation of solid in an undercooled liquid by cavitation*. Journal of Applied Physics, 1966. **37**(1): p. 254-257.
36. Hickling, R., *Nucleation of freezing by cavity collapse and its relation to cavitation damage*. Nature, 1965. **206**(4987): p. 915-917.
37. Inada, T., et al., *Active control of phase change from supercooled water to ice by ultrasonic vibration 1. Control of freezing temperature*. International Journal of Heat and Mass Transfer, 2001. **44**(23): p. 4523-4531.

38. Zhang, X., T. Inada, and A. Tezuka, *Ultrasonic-induced nucleation of ice in water containing air bubbles*. Ultrasonics Sonochemistry, 2003. **10**(2): p. 71-76.
39. Saclier, M., R. Peczalski, and J. Andrieu, *A theoretical model for ice primary nucleation induced by acoustic cavitation*. Ultrasonics Sonochemistry, 2010. **17**(1): p. 98-105.
40. Louisnard, O., F.J. Gomez, and R. Grossier, *Segregation of a liquid mixture by a radially oscillating bubble*. Journal of Fluid Mechanics, 2007. **577**: p. 385-415.
41. Marcolli, C., *Ice nucleation triggered by negative pressure*. Scientific Reports, 2017. **7**(1): p. 16634.
42. Matsumoto, M., S. Saito, and I. Ohmine, *Molecular dynamics simulation of the ice nucleation and growth process leading to water freezing*. Nature, 2002. **416**(6879): p. 409-413.
43. Turnbull, D. and J.C. Fisher, *Rate of nucleation in condensed systems*. The Journal of chemical physics, 1949. **17**(1): p. 71-73.
44. Pruppacher, H.R., *A New Look at Homogeneous Ice Nucleation in Supercooled Water Drops*. Journal of the Atmospheric Sciences, 1995. **52**(11): p. 1924-1933.
45. Murray, B.J., et al., *Kinetics of the homogeneous freezing of water*. Physical Chemistry Chemical Physics, 2010. **12**(35): p. 10380-10387.
46. Türkmen, I.R., *Homogeneous Nucleation Rates of Ice in Supercooled Binary Liquid Mixtures of Water+ Non-electrolytes: A combined Theoretical and Experimental Study*. 2007, Freie Universität Berlin.
47. Koop, T., et al., *Water activity as the determinant for homogeneous ice nucleation in aqueous solutions*. Nature, 2000. **406**: p. 611.
48. Pruppacher, H.R. and J.D. Klett, *Microphysics of Clouds and Precipitation: Reprinted 1980*. 2012: Springer Science & Business Media.
49. Ickes, L., et al., *Classical nucleation theory of homogeneous freezing of water: thermodynamic and kinetic parameters*. Physical Chemistry Chemical Physics, 2015. **17**(8): p. 5514-5537.
50. Huang, J. and L.S. Bartell, *Kinetics of homogeneous nucleation in the freezing of large water clusters*. The Journal of Physical Chemistry, 1995. **99**(12): p. 3924-3931.
51. Stöckel, P., et al., *Rates of homogeneous ice nucleation in levitated H₂O and D₂O droplets*. The Journal of Physical Chemistry A, 2005. **109**(11): p. 2540-2546.

52. Krämer, B., et al., *Homogeneous nucleation rates of supercooled water measured in single levitated microdroplets*. *The Journal of Chemical Physics*, 1999. **111**(14): p. 6521-6527.
53. Hagen, D.E., R.J. Anderson, and J.L. Kassner, *Homogeneous Condensation—Freezing Nucleation Rate Measurements for Small Water Droplets in an Expansion Cloud Chamber*. *Journal of the Atmospheric Sciences*, 1981. **38**(6): p. 1236-1243.
54. Manka, A., et al., *Freezing water in no-man's land*. *Physical Chemistry Chemical Physics*, 2012. **14**(13): p. 4505-4516.
55. Broto, F., et al., *A study by differential scanning calorimetry of the crystallization and the melting of D₂O and D₂O+ H₂O droplets dispersed within emulsions*. 1979. **257**(3): p. 302-308.
56. Bartell, L. and Y. Chushak, *In Water in Confining Geometries*. Buch, V. and Devlin, JP, Eds. 2003, Springer-Verlag, Berlin & Heidelberg.
57. Hung, H.-M., A. Malinowski, and S.T. Martin, *Kinetics of Heterogeneous Ice Nucleation on the Surfaces of Mineral Dust Cores Inserted into Aqueous Ammonium Sulfate Particles*. *The Journal of Physical Chemistry A*, 2003. **107**(9): p. 1296-1306.
58. Hoose, C., et al., *A Classical-Theory-Based Parameterization of Heterogeneous Ice Nucleation by Mineral Dust, Soot, and Biological Particles in a Global Climate Model*. *Journal of the Atmospheric Sciences*, 2010. **67**(8): p. 2483-2503.
59. Atkinson, J.D., et al., *The importance of feldspar for ice nucleation by mineral dust in mixed-phase clouds*. *Nature*, 2013. **498**: p. 355.
60. Mujumdar, A.S., *Effects of Electric and Magnetic Field on Freezing and Possible Relevance in Freeze Drying AU - Woo, M. W*. *Drying Technology*, 2010. **28**(4): p. 433-443.
61. Lee, C.P. and T.G. Wang, *The effects of pressure on the nucleation rate of an undercooled liquid*. *Journal of Applied Physics*, 1992. **71**(11): p. 5721-5723.
62. Dolan, D.H., et al., *A metastable limit for compressed liquid water*. *Nature Physics*, 2007. **3**: p. 339.
63. Vonnegut, B., *The Nucleation of Ice Formation by Silver Iodide*. *Journal of Applied Physics*, 1947. **18**(7): p. 593-595.

64. Lupi, L., A. Hudait, and V. Molinero, *Heterogeneous Nucleation of Ice on Carbon Surfaces*. Journal of the American Chemical Society, 2014. **136**(8): p. 3156-3164.
65. Shen, J.H., K. Klier, and A.C. Zettlemoyer, *Ice Nucleation by Micas*. Journal of the Atmospheric Sciences, 1977. **34**(6): p. 957-960.
66. Niedermeier, D., et al., *Heterogeneous freezing of droplets with immersed mineral dust particles ¹³C measurements and parameterization*. Atmos. Chem. Phys., 2010. **10**(8): p. 3601-3614.
67. Min, Q.L., et al., *Impacts of mineral dust on ice clouds in tropical deep convection systems*. Atmospheric Research, 2014. **143**: p. 64-72.
68. Knopf Daniel, A. and T. Koop, *Heterogeneous nucleation of ice on surrogates of mineral dust*. Journal of Geophysical Research: Atmospheres, 2006. **111**(D12).
69. Pummer, B., et al., *Ice nucleation by water-soluble macromolecules*. 2015. **15**(8): p. 4077-4091.
70. Fortes, A.D., et al., *No evidence for large-scale proton ordering in Antarctic ice from powder neutron diffraction*. The Journal of Chemical Physics, 2004. **120**(24): p. 11376-11379.
71. McCauley, J.W., R.E. Newnham, and G.V. Gibbs, *Crystal structure analysis of synthetic fluorophlogopite*. American Mineralogist: Journal of Earth and Planetary Materials, 1973. **58**(3-4_Part_1): p. 249-254.
72. Shevkunov, S.V., *Nucleation of water vapor on the surface of a silver iodide crystal: Numerical experiment*. Journal of Experimental and Theoretical Physics, 1995. **81**(4): p. 753-769.
73. Wang, L., et al., *Molecular dynamics simulation study of the interaction of mixed cationic/anionic surfactants with muscovite*. Applied Surface Science, 2015. **327**: p. 364-370.
74. Diehl, K., et al., *The ice nucleating ability of pollen.: Part II. Laboratory studies in immersion and contact freezing modes*. Atmospheric Research, 2002. **61**(2): p. 125-133.
75. Deadmore, D.L. and H.E. Sliney, *Hardness of CaF₂ and BaF₂ solid lubricants at 25 to 670 C*. 1987: National Aeronautics and Space Administration, Lewis Research Center.
76. Conrad, P., et al., *Ice nucleation on BaF₂(111)*. The Journal of Chemical Physics, 2005. **122**(6): p. 064709.

77. Goodwin, J.H., *Analcime and K-feldspar in tuffs of the green river formation, Wyoming*. American Mineralogist: Journal of Earth and Planetary Materials, 1973. **58**(1-2): p. 93-105.
78. Li, X., H. Li, and G. Yang, *Promoting the Adsorption of Metal Ions on Kaolinite by Defect Sites: A Molecular Dynamics Study*. Scientific Reports, 2015. **5**(1): p. 14377.
79. Murray, B.J., et al., *Heterogeneous freezing of water droplets containing kaolinite particles*. Atmos. Chem. Phys., 2011. **11**(9): p. 4191-4207.
80. Hu, X.L. and A.J.S.S. Michaelides, *Ice formation on kaolinite: Lattice match or amphotericism?* 2007. **601**(23): p. 5378-5381.
81. Croteau, T., A. Bertram, and G.J.T.J.o.P.C.A. Patey, *Adsorption and structure of water on kaolinite surfaces: Possible insight into ice nucleation from grand canonical Monte Carlo calculations*. 2008. **112**(43): p. 10708-10712.
82. Edwards, G.R. and L.F. Evans, *Ice Nucleation by Silver Iodide: III. The Nature of the Nucleating Site*. Journal of the Atmospheric Sciences, 1968. **25**(2): p. 249-256.
83. Edwards, G.R. and L.F. Evans, *Effect of surface charge on ice nucleation by silver iodide*. Transactions of the Faraday Society, 1962. **58**(0): p. 1649-1655.
84. Curland, S., et al., *The Contribution of Pyroelectricity of AgI Crystals to Ice Nucleation*. Angewandte Chemie, 2018. **130**(24): p. 7194-7197.
85. Yan, J.Y. and G.N. Patey, *Heterogeneous Ice Nucleation Induced by Electric Fields*. The Journal of Physical Chemistry Letters, 2011. **2**(20): p. 2555-2559.
86. Fletcher, N.H., *Size Effect in Heterogeneous Nucleation*. The Journal of Chemical Physics, 1958. **29**(3): p. 572-576.
87. Welti, A., et al., *Influence of particle size on the ice nucleating ability of mineral dusts*. Atmos. Chem. Phys., 2009. **9**(18): p. 6705-6715.
88. Dufour, L., *Ueber das Gefrieren des Wassers und über die Bildung des Hagels*. Annalen der Physik, 1862. **190**(12): p. 530-554.
89. Rau, W.J.Z.f.N.A., *Eiskeimbildung durch dielektrische Polarisierung*. 1951. **6**(11): p. 649-657.
90. Wei, S., et al., *Effects of dipole polarization of water molecules on ice formation under an electrostatic field*. Cryobiology, 2008. **56**(1): p. 93-99.

91. Shichiri, T. and Y. Araki, *Nucleation mechanism of ice crystals under electrical effect*. Journal of Crystal Growth, 1986. **78**(3): p. 502-508.
92. Petersen, A., et al., *A new approach for freezing of aqueous solutions under active control of the nucleation temperature*. 2006. **53**(2): p. 248-257.
93. Pruppacher, H.R., *The effect of an external electric field on the supercooling of water drops*. 1963. **68**(15): p. 4463-4474.
94. Stan, C.A., et al., *Externally Applied Electric Fields up to 1.6×10^5 V/m Do Not Affect the Homogeneous Nucleation of Ice in Supercooled Water*. The Journal of Physical Chemistry B, 2011. **115**(5): p. 1089-1097.
95. Doolittle, J.B. and G. Vali, *Heterogeneous Freezing Nucleation in Electric Fields*. Journal of the Atmospheric Sciences, 1975. **32**(2): p. 375-379.
96. Nakajima, A., et al., *Effect of electrification conditions on the freezing of supercooled water droplets on a hydrophobic coating*. 2007. **36**(8): p. 1020-1021.
97. Löwe, J.-M., et al., *EXPERIMENTAL INVESTIGATION OF ELECTRO-FREEZING OF SUPERCOOLED WATER DROPLETS*, in *9th World Conference on Experimental Heat Transfer, Fluid Mechanics and Thermodynamics*. 2017: Iguazu Falls, Brazil.
98. Otero, L., et al., *Effects of Magnetic Fields on Freezing: Application to Biological Products*. Comprehensive Reviews in Food Science and Food Safety, 2016. **15**(3): p. 646-667.
99. Inaba, H., et al., *Effect of the magnetic field on the melting transition of H₂O and D₂O measured by a high resolution and supersensitive differential scanning calorimeter*. 2004. **96**(11): p. 6127-6132.
100. Pang, X.-F., B. Deng, and B.J.M.P.L.B. Tang, *Influences of magnetic field on macroscopic properties of water*. 2012. **26**(11): p. 1250069.
101. Pang, X., B.J.S.i.C.S.G.P. Deng, Mechanics, and Astronomy, *Investigation of changes in properties of water under the action of a magnetic field*. 2008. **51**(11): p. 1621-1632.
102. Zhou, K.X., et al., *Monte Carlo simulation of liquid water in a magnetic field*. Journal of Applied Physics, 2000. **88**(4): p. 1802-1805.
103. Toledo, E.J.L., T.C. Ramalho, and Z.M. Magriotis, *Influence of magnetic field on physical-chemical properties of the liquid water: Insights from experimental and theoretical models*. Journal of Molecular Structure, 2008. **888**(1): p. 409-415.

104. Chang, K.-T. and C.-I. Weng, *The effect of an external magnetic field on the structure of liquid water using molecular dynamics simulation*. Journal of Applied Physics, 2006. **100**(4): p. 043917.
105. Zhang, G., W. Zhang, and H. Dong, *Magnetic freezing of confined water*. The Journal of Chemical Physics, 2010. **133**(13): p. 134703.
106. Hu, H., H. Hou, and B. Wang, *Molecular Dynamics Simulations of Ice Growth from Supercooled Water When Both Electric and Magnetic Fields Are Applied*. The Journal of Physical Chemistry C, 2012. **116**(37): p. 19773-19780.
107. Tagami, M., et al., *Solidification of levitating water in a gradient strong magnetic field*. Journal of Crystal Growth, 1999. **203**(4): p. 594-598.
108. Amiri, M.C. and A.A. Dadkhah, *On reduction in the surface tension of water due to magnetic treatment*. Colloids and Surfaces A: Physicochemical and Engineering Aspects, 2006. **278**(1): p. 252-255.
109. Holysz, L., A. Szczes, and E. Chibowski, *Effects of a static magnetic field on water and electrolyte solutions*. Journal of Colloid and Interface Science, 2007. **316**(2): p. 996-1002.
110. Colic, M. and D. Morse, *The elusive mechanism of the magnetic 'memory' of water*. Colloids and Surfaces A: Physicochemical and Engineering Aspects, 1999. **154**(1): p. 167-174.
111. Vallée, P., et al., *Effects of Pulsed Low-Frequency Electromagnetic Fields on Water Characterized by Light Scattering Techniques: Role of Bubbles*. Langmuir, 2005. **21**(6): p. 2293-2299.
112. Vallée, P., et al., *Effects of pulsed low frequency electromagnetic fields on water using photoluminescence spectroscopy: Role of bubble/water interface*. The Journal of Chemical Physics, 2005. **122**(11): p. 114513.
113. Bi, Y., B. Cao, and T.J.N.c. Li, *Enhanced heterogeneous ice nucleation by special surface geometry*. 2017. **8**: p. 15372.
114. Campbell, J.M., F.C. Meldrum, and H.K. Christenson, *Is Ice Nucleation from Supercooled Water Insensitive to Surface Roughness?* The Journal of Physical Chemistry C, 2015. **119**(2): p. 1164-1169.

115. Zhang, Y., et al., *A review of microscopic interactions between cavitation bubbles and particles in silt-laden flow*. Renewable and Sustainable Energy Reviews, 2016. **56**: p. 303-318.
116. Zhang, X., T. Inada, and A.J.U.S. Tezuka, *Ultrasonic-induced nucleation of ice in water containing air bubbles*. 2003. **10**(2): p. 71-76.
117. Chow, R., et al., *A study on the primary and secondary nucleation of ice by power ultrasound*. Ultrasonics, 2005. **43**(4): p. 227-230.
118. Pecha, R. and B. Gompf, *Microimplosions: Cavitation Collapse and Shock Wave Emission on a Nanosecond Time Scale*. Physical Review Letters, 2000. **84**(6): p. 1328-1330.
119. Ohsaka, K. and E.H. Trinh, *Dynamic nucleation of ice induced by a single stable cavitation bubble*. Applied Physics Letters, 1998. **73**(1): p. 129-131.
120. Pallares, G., et al., *Equation of state for water and its line of density maxima down to -120 MPa*. Physical Chemistry Chemical Physics, 2016. **18**(8): p. 5896-5900.
121. Brothie, A., F. Grieser, and M. Ashokkumar, *Effect of Power and Frequency on Bubble-Size Distributions in Acoustic Cavitation*. Physical Review Letters, 2009. **102**(8): p. 084302.
122. Rooze, J., et al., *Dissolved gas and ultrasonic cavitation – A review*. Ultrasonics Sonochemistry, 2013. **20**(1): p. 1-11.
123. Marschall, H.B., et al., *Cavitation inception by almost spherical solid particles in water*. Physics of Fluids, 2003. **15**(2): p. 545-553.
124. Borkent, B.M., et al., *The acceleration of solid particles subjected to cavitation nucleation*. Journal of Fluid Mechanics, 2008. **610**: p. 157-182.
125. Arora, M., C.-D. Ohl, and K.A. Mørch, *Cavitation Inception on Microparticles: A Self-Propelled Particle Accelerator*. Physical Review Letters, 2004. **92**(17): p. 174501.
126. Zobrist, B., et al., *Heterogeneous Ice Nucleation Rate Coefficient of Water Droplets Coated by a Nonadecanol Monolayer*. The Journal of Physical Chemistry C, 2007. **111**(5): p. 2149-2155.
127. Eow, J.S. and M. Ghadiri, *Electrostatic enhancement of coalescence of water droplets in oil: a review of the technology*. Chemical Engineering Journal, 2002. **85**(2): p. 357-368.

128. Diehl, K., et al., *The ice nucleating ability of pollen.: Part II. Laboratory studies in immersion and contact freezing modes*. 2002. **61**(2): p. 125-133.
129. Carpenter, K. and V. Bahadur, *Electrofreezing of Water Droplets under Electrowetting Fields*. *Langmuir*, 2015. **31**(7): p. 2243-2248.
130. Smith, M.H., R.F. Griffiths, and J. Latham, *The freezing of raindrops falling through strong electric fields*. *Quarterly Journal of the Royal Meteorological Society*, 1971. **97**(414): p. 495-505.
131. Olmo, A., R. Baena, and R. Risco, *Use of a droplet nucleation analyzer in the study of water freezing kinetics under the influence of ultrasound waves*. *International Journal of Refrigeration*, 2008. **31**(2): p. 262-269.
132. Caupin, F. and E. Herbert, *Cavitation in water: a review*. *Comptes Rendus Physique*, 2006. **7**(9): p. 1000-1017.
133. Vukasinovic, B., M.K. Smith, and A.R.I. Glezer, *Dynamics of a sessile drop in forced vibration*. *Journal of Fluid Mechanics*, 2007. **587**: p. 395-423.
134. Kaci, M., et al., *Emulsification by high frequency ultrasound using piezoelectric transducer: Formation and stability of emulsifier free emulsion*. *Ultrasonics Sonochemistry*, 2014. **21**(3): p. 1010-1017.
135. Ji, B., et al., *Partially-Averaged Navier–Stokes method with modified $k-\epsilon$ model for cavitating flow around a marine propeller in a non-uniform wake*. *International Journal of Heat and Mass Transfer*, 2012. **55**(23): p. 6582-6588.
136. Niemczewski, B., *Observations of water cavitation intensity under practical ultrasonic cleaning conditions*. *Ultrasonics Sonochemistry*, 2007. **14**(1): p. 13-18.
137. Pradhan, A.A. and P.R. Gogate, *Degradation of p-nitrophenol using acoustic cavitation and Fenton chemistry*. *Journal of Hazardous Materials*, 2010. **173**(1): p. 517-522.
138. Brujan, E.A., T. Ikeda, and Y. Matsumoto, *Jet formation and shock wave emission during collapse of ultrasound-induced cavitation bubbles and their role in the therapeutic applications of high-intensity focused ultrasound*. *Physics in Medicine and Biology*, 2005. **50**(20): p. 4797-4809.
139. Yang, Y., et al., *Thermodynamic of collapsing cavitation bubble investigated by pseudopotential and thermal MRT-LBM*. *Ultrasonics Sonochemistry*, 2020. **62**: p. 104873.

140. Rayleigh, L., *VIII. On the pressure developed in a liquid during the collapse of a spherical cavity*. The London, Edinburgh, and Dublin Philosophical Magazine and Journal of Science, 1917. **34**(200): p. 94-98.
141. Plesset, M.S. and S.A. Zwick, *The Growth of Vapor Bubbles in Superheated Liquids*. Journal of Applied Physics, 1954. **25**(4): p. 493-500.
142. Plesset, M.S. and A. Prosperetti, *Bubble dynamics and cavitation*. J Annual review of fluid mechanics, 1977. **9**(1): p. 145-185.
143. Plesset, M.S., *The dynamics of cavitation bubbles*. Journal of applied mechanics, 1949. **16**: p. 277-282.
144. Hilgenfeldt, S., et al., *Analysis of Rayleigh–Plesset dynamics for sonoluminescing bubbles*. Journal of fluid mechanics, 1998. **365**: p. 171-204.
145. Tinguely, M., et al., *Energy partition at the collapse of spherical cavitation bubbles*. Physical Review E, 2012. **86**(4): p. 046315.
146. Brennen, C.E., *New York Oxford Oxford University Press*. 1995.
147. Keller, J.B. and M. Miksis, *Bubble oscillations of large amplitude*. The Journal of the Acoustical Society of America, 1980. **68**(2): p. 628-633.
148. Prosperetti, A., *The equation of bubble dynamics in a compressible liquid*. The Physics of Fluids, 1987. **30**(11): p. 3626-3628.
149. Shen, Y., et al., *Study on the spatial distribution of the liquid temperature near a cavitation bubble wall*. Ultrasonics Sonochemistry, 2016. **29**: p. 394-400.
150. Yasui, K., *Variation of Liquid Temperature at Bubble Wall near the Sonoluminescence Threshold*. Journal of the Physical Society of Japan, 1996. **65**(9): p. 2830-2840.
151. Yasui, K., *Effects of thermal conduction on bubble dynamics near the sonoluminescence threshold*. The Journal of the Acoustical Society of America, 1995. **98**(5): p. 2772-2782.
152. Yasui, K., *Alternative model of single-bubble sonoluminescence*. Physical Review E - Statistical Physics, Plasmas, Fluids, and Related Interdisciplinary Topics, 1997. **56**(6): p. 6750-6760.
153. Fujikawa, S. and T. Akamatsu, *Effects of the non-equilibrium condensation of vapour on the pressure wave produced by the collapse of a bubble in a liquid*. Journal of Fluid Mechanics, 1980. **97**(3): p. 481-512.

154. Merouani, S., et al., *Theoretical estimation of the temperature and pressure within collapsing acoustical bubbles*. Ultrasonics Sonochemistry, 2014. **21**(1): p. 53-59.
155. Shen, Y., et al., *A model for the effect of bulk liquid viscosity on cavitation bubble dynamics*. Physical Chemistry Chemical Physics, 2017. **19**(31): p. 20635-20640.
156. Lechner, C., et al., *Pressure and tension waves from bubble collapse near a solid boundary: A numerical approach*. The Journal of the Acoustical Society of America, 2017. **142**(6): p. 3649-3659.
157. Koukouvinis, P., et al., *Numerical simulation of a collapsing bubble subject to gravity*. Physics of Fluids, 2016. **28**(3): p. 032110.
158. Ming, L., N. Zhi, and S. Chunhua, *Numerical simulation of cavitation bubble collapse within a droplet*. Computers & Fluids, 2017. **152**: p. 157-163.
159. Liu, B., et al., *Cavitation Bubble Collapse Near a Heated Wall and Its Effect on the Heat Transfer*. Journal of Heat Transfer, 2013. **136**(2).
160. Liu, B., J. Cai, and X. Huai, *Heat transfer with the growth and collapse of cavitation bubble between two parallel heated walls*. International Journal of Heat and Mass Transfer, 2014. **78**: p. 830-838.
161. Noh, W.F. and P. Woodward. *SLIC (Simple Line Interface Calculation)*. in *Proceedings of the Fifth International Conference on Numerical Methods in Fluid Dynamics June 28 – July 2, 1976 Twente University, Enschede*. 1976. Berlin, Heidelberg: Springer Berlin Heidelberg.
162. Hirt, C.W. and B.D. Nichols, *Volume of fluid (VOF) method for the dynamics of free boundaries*. Journal of computational physics, 1981. **39**(1): p. 201-225.
163. Youngs, D.L., *Time-dependent multi-material flow with large fluid distortion*. Numerical methods for fluid dynamics, 1982.
164. Wang, Q.X. and J.R. Blake, *Non-spherical bubble dynamics in a compressible liquid. Part 1. Travelling acoustic wave*. Journal of Fluid Mechanics, 2010. **659**: p. 191-224.
165. Blake, J.R., B.B. Taib, and G. Doherty, *Transient cavities near boundaries. Part 1. Rigid boundary*. Journal of Fluid Mechanics, 1986. **170**: p. 479-497.
166. Brujan, E.A., et al., *The final stage of the collapse of a cavitation bubble close to a rigid boundary*. Physics of Fluids, 2001. **14**(1): p. 85-92.

167. Nagrath, S., et al., *Hydrodynamic simulation of air bubble implosion using a level set approach*. Journal of Computational Physics, 2006. **215**(1): p. 98-132.
168. Sussman, M., P. Smereka, and S. Osher, *A level set approach for computing solutions to incompressible two-phase flow*. 1994.
169. Sussman, M., et al., *An Adaptive Level Set Approach for Incompressible Two-Phase Flows*. Journal of Computational Physics, 1999. **148**(1): p. 81-124.
170. Koshizuka, S. and Y. Oka, *Moving-Particle Semi-Implicit Method for Fragmentation of Incompressible Fluid*. Nuclear Science and Engineering, 1996. **123**(3): p. 421-434.
171. Tian, W., et al., *Numerical computation of thermally controlled steam bubble condensation using Moving Particle Semi-implicit (MPS) method*. Annals of Nuclear Energy, 2010. **37**(1): p. 5-15.
172. Frisch, U., B. Hasslacher, and Y. Pomeau, *Lattice-Gas Automata for the Navier-Stokes Equation*. Physical Review Letters, 1986. **56**(14): p. 1505-1508.
173. Qian, Y.H., D.D. Humières, and P. Lallemand, *Lattice BGK Models for Navier-Stokes Equation*. EPL (Europhysics Letters), 1992. **17**(6): p. 479.
174. McNamara, G.R. and G. Zanetti, *Use of the Boltzmann Equation to Simulate Lattice-Gas Automata*. Physical Review Letters, 1988. **61**(20): p. 2332-2335.
175. Higuera, F.J. and J. Jiménez, *Boltzmann Approach to Lattice Gas Simulations*. EPL (Europhysics Letters), 1989. **9**(7): p. 663.
176. Chen, L., et al., *A critical review of the pseudopotential multiphase lattice Boltzmann model: Methods and applications*. International Journal of Heat and Mass Transfer, 2014. **76**: p. 210-236.
177. He, X., X. Shan, and G.D. Doolen, *Discrete Boltzmann equation model for nonideal gases*. Physical Review E, 1998. **57**(1): p. R13-R16.
178. Guo, Z., C. Zheng, and B. Shi, *Discrete lattice effects on the forcing term in the lattice Boltzmann method*. Physical Review E, 2002. **65**(4): p. 046308.
179. Wagner, A.J., *Thermodynamic consistency of liquid-gas lattice Boltzmann simulations*. Physical Review E, 2006. **74**(5): p. 056703.
180. McCracken, M.E. and J. Abraham, *Multiple-relaxation-time lattice-Boltzmann model for multiphase flow*. Physical Review E, 2005. **71**(3): p. 036701.

181. Li, Q., et al., *Lattice Boltzmann methods for multiphase flow and phase-change heat transfer*. Progress in Energy and Combustion Science, 2016. **52**: p. 62-105.
182. Grunau, D., S. Chen, and K. Eggert, *A lattice Boltzmann model for multiphase fluid flows*. Physics of Fluids A: Fluid Dynamics, 1993. **5**(10): p. 2557-2562.
183. Swift, M.R., et al., *Lattice Boltzmann simulations of liquid-gas and binary fluid systems*. Physical Review E, 1996. **54**(5): p. 5041-5052.
184. He, X. and G.D. Doolen, *Thermodynamic Foundations of Kinetic Theory and Lattice Boltzmann Models for Multiphase Flows*. Journal of Statistical Physics, 2002. **107**(1): p. 309-328.
185. Shan, X. and H. Chen, *Lattice Boltzmann model for simulating flows with multiple phases and components*. Physical Review E, 1993. **47**(3): p. 1815-1819.
186. Ahrenholz, B., et al., *Prediction of capillary hysteresis in a porous material using lattice-Boltzmann methods and comparison to experimental data and a morphological pore network model*. Advances in Water Resources, 2008. **31**(9): p. 1151-1173.
187. Huang, H., et al., *ON SIMULATIONS OF HIGH-DENSITY RATIO FLOWS USING COLOR-GRADIENT MULTIPHASE LATTICE BOLTZMANN MODELS*. International Journal of Modern Physics C, 2013. **24**(04): p. 1350021.
188. Swift, M.R., W.R. Osborn, and J.M. Yeomans, *Lattice Boltzmann Simulation of Nonideal Fluids*. Physical Review Letters, 1995. **75**(5): p. 830-833.
189. Zheng, H.W., C. Shu, and Y.T. Chew, *A lattice Boltzmann model for multiphase flows with large density ratio*. Journal of Computational Physics, 2006. **218**(1): p. 353-371.
190. Inamuro, T., et al., *A lattice Boltzmann method for incompressible two-phase flows with large density differences*. Journal of Computational Physics, 2004. **198**(2): p. 628-644.
191. Fakhari, A. and M.H. Rahimian, *Investigation of deformation and breakup of a moving droplet by the method of lattice Boltzmann equations*. International Journal for Numerical Methods in Fluids, 2010. **64**(8): p. 827-849.
192. Shao, J.Y., et al., *Free-energy-based lattice Boltzmann model for the simulation of multiphase flows with density contrast*. Physical Review E, 2014. **89**(3): p. 033309.
193. Shan, X. and G. Doolen, *Multicomponent lattice-Boltzmann model with interparticle interaction*. Journal of Statistical Physics, 1995. **81**(1): p. 379-393.

194. Sbragaglia, M., et al., *Generalized lattice Boltzmann method with multirange pseudopotential*. Physical Review E, 2007. **75**(2): p. 026702.
195. Shan, X., *Pressure tensor calculation in a class of nonideal gas lattice Boltzmann models*. Physical Review E, 2008. **77**(6): p. 066702.
196. Sussman, M., *A second order coupled level set and volume-of-fluid method for computing growth and collapse of vapor bubbles*. Journal of Computational Physics, 2003. **187**(1): p. 110-136.
197. Shan, M.-l., et al., *Investigation of cavitation bubble collapse near rigid boundary by lattice Boltzmann method*. Journal of Hydrodynamics, 2016. **28**(3): p. 442-450.
198. Huang, H., M. Sukop, and X. Lu, *Multiphase lattice Boltzmann methods: Theory and application*. 2015: John Wiley & Sons.
199. Huang, H., M. Krafczyk, and X. Lu, *Forcing term in single-phase and Shan-Chen-type multiphase lattice Boltzmann models*. Physical Review E, 2011. **84**(4): p. 046710.
200. Zhu, W., M. Wang, and H. Chen, *Study on multicomponent pseudo-potential model with large density ratio and heat transfer*. International Communications in Heat and Mass Transfer, 2017. **87**: p. 183-191.
201. Li, Q., K.H. Luo, and X.J. Li, *Forcing scheme in pseudopotential lattice Boltzmann model for multiphase flows*. Physical Review E, 2012. **86**(1): p. 016709.
202. Blake, J.R. and D.C. Gibson, *Cavitation Bubbles Near Boundaries*. Annual Review of Fluid Mechanics, 1987. **19**(1): p. 99-123.
203. Church, C.C., *A theoretical study of cavitation generated by an extracorporeal shock wave lithotripter*. The Journal of the Acoustical Society of America, 1989. **86**(1): p. 215-227.
204. Liu, B., et al., *Simulation of heat transfer with the growth and collapse of a cavitation bubble near the heated wall*. Journal of Thermal Science, 2013. **22**(4): p. 352-358.
205. Xue, H.-H., et al., *Cavitation Bubble Collapse near a Curved Wall by the Multiple-Relaxation-Time Shan–Chen Lattice Boltzmann Model*. Chinese Physics Letters, 2017. **34**(8): p. 084301.
206. Chahine, G.L., et al., *Modeling of surface cleaning by cavitation bubble dynamics and collapse*. Ultrasonics Sonochemistry, 2016. **29**: p. 528-549.

207. Ohl, S.W., E. Klaseboer, and B.C. Khoo, *The dynamics of a non-equilibrium bubble near bio-materials*. *Physics in Medicine and Biology*, 2009. **54**(20): p. 6313-6336.
208. Aghdam, A.H., et al., *Characterization of the interaction of two oscillating bubbles near a thin elastic membrane*. *Experiments in Fluids*, 2012. **53**(6): p. 1723-1735.
209. Shervani-Tabar, M.T., et al., *Numerical analysis of a cavitation bubble in the vicinity of an elastic membrane*. *Fluid Dynamics Research*, 2013. **45**(5): p. 055503.
210. Koukouvinis, P., et al., *Simulation of bubble expansion and collapse in the vicinity of a free surface*. *Physics of Fluids*, 2016. **28**(5): p. 052103.
211. Moore, E.B. and V. Molinero, *Structural transformation in supercooled water controls the crystallization rate of ice*. *Nature*, 2011. **479**(7374): p. 506-508.
212. Stanley, H.E., et al., *Liquid Polyamorphism: Some Unsolved Puzzles of Water in Bulk, Nanoconfined, and Biological Environments*. *AIP Conference Proceedings*, 2008. **982**(1): p. 251-271.
213. Jeffery, C. and P. Austin, *Homogeneous nucleation of supercooled water: Results from a new equation of state*. *Journal of Geophysical Research: Atmospheres*, 1997. **102**(D21): p. 25269-25279.
214. Langer, J.S., R.F. Sekerka, and T. Fujioka, *Evidence for a universal law of dendritic growth rates*. *Journal of Crystal Growth*, 1978. **44**(4): p. 414-418.
215. Ohsaka, K. and E.H. Trinh, *Apparatus for measuring the growth velocity of dendritic ice in undercooled water*. *Journal of Crystal Growth*, 1998. **194**(1): p. 138-142.
216. Shibkov, A.A., et al., *Crossover from diffusion-limited to kinetics-limited growth of ice crystals*. *Journal of Crystal Growth*, 2005. **285**(1-2): p. 215-227.
217. Rastogi, A., A.K. Ghosh, and S. Suresh, *Hydrogen bond interactions between water molecules in bulk liquid, near electrode surfaces and around ions*. *Thermodynamics-physical chemistry of aqueous systems*, 2011: p. 351-364.
218. Koga, Y., *Two-dimensional characterization of the effect of solute on H₂O: A thermodynamic probing methodology*. *Journal of Molecular Liquids*, 2015. **205**: p. 31-36.
219. Suresh, S.J. and V.M. Naik, *Hydrogen bond thermodynamic properties of water from dielectric constant data*. *The Journal of Chemical Physics*, 2000. **113**(21): p. 9727-9732.
220. Smith, J.D., et al., *Energetics of Hydrogen Bond Network Rearrangements in Liquid Water*. *Science*, 2004. **306**(5697): p. 851.

221. Heggie, M.I., et al., *Cooperative polarisation in ice Ih and the unusual strength of the hydrogen bond*. Chemical Physics Letters, 1996. **249**(5): p. 485-490.
222. Levashov, V.A., et al., *Equipartition theorem and the dynamics of liquids*. Physical Review B, 2008. **78**(6): p. 064205.
223. Waghe, A., J.C. Rasaiah, and G. Hummer, *Filling and emptying kinetics of carbon nanotubes in water*. The Journal of Chemical Physics, 2002. **117**(23): p. 10789-10795.
224. Billeter, S.R., P.M. King, and W.F. van Gunsteren, *Can the density maximum of water be found by computer simulation?* The Journal of Chemical Physics, 1994. **100**(9): p. 6692-6699.
225. Rowlinson *, J.S., *The Maxwell–Boltzmann distribution*. Molecular Physics, 2005. **103**(21-23): p. 2821-2828.
226. Mason, B.J., *The supercooling and nucleation of water*. Advances in Physics, 1958. **7**(26): p. 221-234.
227. Sellberg, J.A., et al., *Ultrafast X-ray probing of water structure below the homogeneous ice nucleation temperature*. Nature, 2014. **510**: p. 381.
228. Choukroun, M. and O. Grasset, *Thermodynamic model for water and high-pressure ices up to 2.2GPa and down to the metastable domain*. The Journal of Chemical Physics, 2007. **127**(12): p. 124506.
229. Speedy, R.J., *Thermodynamic properties of supercooled water at 1 atm*. The Journal of Physical Chemistry, 1987. **91**(12): p. 3354-3358.
230. Mukhopadhyay, A., W.T.S. Cole, and R.J. Saykally, *The water dimer I: Experimental characterization*. Chemical Physics Letters, 2015. **633**: p. 13-26.
231. Laksmono, H., et al., *Anomalous Behavior of the Homogeneous Ice Nucleation Rate in "No-Man's Land"*. The journal of physical chemistry letters, 2015. **6**(14): p. 2826-2832.
232. Mishima, O., *Volume of supercooled water under pressure and the liquid-liquid critical point*. The Journal of Chemical Physics, 2010. **133**(14): p. 144503.
233. Butorin, G. and V. Skripov, *Crystallization in supercooled water*. Kristallografiya, 1972. **17**(2): p. 379-&.
234. Bhabhe, A., H. Pathak, and B.E. Wyslouzil, *Freezing of Heavy Water (D2O) Nanodroplets*. The Journal of Physical Chemistry A, 2013. **117**(26): p. 5472-5482.

235. Amaya, A.J. and B.E. Wyslouzil, *Ice nucleation rates near ~225 K*. The Journal of Chemical Physics, 2018. **148**(8): p. 084501.
236. Li, T., D. Donadio, and G. Galli, *Ice nucleation at the nanoscale probes no man's land of water*. Nature Communications, 2013. **4**: p. 1887.
237. Matula, T.J., *Inertial cavitation and single-bubble sonoluminescence*. Philosophical Transactions of the Royal Society of London. Series A: Mathematical, Physical and Engineering Sciences, 1999. **357**(1751): p. 225.
238. Chow, R., et al., *The microscopic visualisation of the sonocrystallisation of ice using a novel ultrasonic cold stage*. Ultrasonics Sonochemistry, 2004. **11**(3): p. 245-250.
239. Dodds, J., et al., *The Effect of Ultrasound on Crystallisation-Precipitation Processes: Some Examples and a New Segregation Model*. Particle & Particle Systems Characterization, 2007. **24**(1): p. 18-28.
240. Hu, F., et al., *Effects of pre-existing bubbles on ice nucleation and crystallization during ultrasound-assisted freezing of water and sucrose solution*. Innovative Food Science & Emerging Technologies, 2013. **20**: p. 161-166.
241. Hunt, J.D. and K.A. Jackson, *Nucleation of the Solid Phase by Cavitation in an Undercooled Liquid which expands on Freezing*. Nature, 1966. **211**(5053): p. 1080-1081.
242. Kiani, H., et al., *Ultrasound assisted nucleation of some liquid and solid model foods during freezing*. Food Research International, 2011. **44**(9): p. 2915-2921.
243. Zheng, L. and D.-W. Sun, *Innovative applications of power ultrasound during food freezing processes—a review*. Trends in Food Science & Technology, 2006. **17**(1): p. 16-23.
244. Peng, C., et al., *Simulation of laser-produced single cavitation bubbles with hybrid thermal Lattice Boltzmann method*. International Journal of Heat and Mass Transfer, 2020. **149**: p. 119136.
245. Lauterborn, W. and T. Kurz, *Physics of bubble oscillations*. Reports on Progress in Physics, 2010. **73**(10): p. 106501.
246. Lallemand, P. and L.-S. Luo, *Theory of the lattice Boltzmann method: Dispersion, dissipation, isotropy, Galilean invariance, and stability*. Physical Review E, 2000. **61**(6): p. 6546-6562.

247. Sun, J., J. Gong, and G. Li, *A lattice Boltzmann model for solidification of water droplet on cold flat plate*. International Journal of Refrigeration, 2015. **59**: p. 53-64.
248. Chang, X., H. Huang, and X.-Y. Lu, *Thermal lattice Boltzmann study of three-dimensional bubble growth in quiescent liquid*. Computers & Fluids, 2017. **159**: p. 232-242.
249. Matsumoto, M., S. Saito, and I. Ohmine, *Molecular dynamics simulation of the ice nucleation and growth process leading to water freezing*. Nature, 2002. **416**: p. 409.
250. Sciortino, F., et al., *Lifetime of the bond network and gel-like anomalies in supercooled water*. Physical Review Letters, 1990. **64**(14): p. 1686-1689.
251. Lindenmeyer, C.S. and B. Chalmers, *Growth Rate of Ice Dendrites in Aqueous Solutions*. The Journal of Chemical Physics, 1966. **45**(8): p. 2807-2808.
252. Berberović, E., et al., *Computational modeling of freezing of supercooled water using phase-field front propagation with immersed points*. International Journal of Multiphase Flow, 2018. **99**: p. 329-346.
253. Schremb, M., et al., *Ice Layer Spreading along a Solid Substrate during Solidification of Supercooled Water: Experiments and Modeling*. Langmuir, 2017. **33**(19): p. 4870-4877.
254. Wang, T., et al., *Dendritic Growth Model Involving Interface Kinetics for Supercooled Water*. Langmuir, 2019. **35**(15): p. 5162-5167.
255. Hindmarsh, J.P., D.I. Wilson, and M.L. Johns, *Using magnetic resonance to validate predictions of the solid fraction formed during recalescence of freezing drops*. International Journal of Heat and Mass Transfer, 2005. **48**(5): p. 1017-1021.
256. Zhao, X., et al., *An improved enthalpy-based lattice Boltzmann model for heat and mass transfer of the freezing process*. Applied Thermal Engineering, 2017. **111**: p. 1477-1486.
257. Zhao, J., X. Li, and P. Cheng, *Lattice Boltzmann simulation of a droplet impact and freezing on cold surfaces*. International Communications in Heat and Mass Transfer, 2017. **87**: p. 175-182.
258. Semma, E., et al., *Investigation of flows in solidification by using the lattice Boltzmann method*. International Journal of Thermal Sciences, 2008. **47**(3): p. 201-208.
259. Gong, S. and P. Cheng, *Numerical investigation of droplet motion and coalescence by an improved lattice Boltzmann model for phase transitions and multiphase flows*. Computers & Fluids, 2012. **53**: p. 93-104.

260. Guo, Z., B. Shi, and C. Zheng, *A coupled lattice BGK model for the Boussinesq equations*. International Journal for Numerical Methods in Fluids, 2002. **39**(4): p. 325-342.
261. Chen, X., *Simulation of 2D cavitation bubble growth under shear flow by lattice Boltzmann model*. J Communications in Computational Physics, 2010. **7**(1): p. 212.
262. Peng, C., et al., *Single-component multiphase lattice Boltzmann simulation of free bubble and crevice heterogeneous cavitation nucleation*. Physical Review E, 2018. **98**(2): p. 023305.
263. Plesset, M.S. and R.B. Chapman, *Collapse of an initially spherical vapour cavity in the neighbourhood of a solid boundary*. Journal of Fluid Mechanics, 1971. **47**(2): p. 283-290.
264. Philipp, A. and W. Lauterborn, *Cavitation erosion by single laser-produced bubbles*. Journal of Fluid Mechanics, 1998. **361**: p. 75-116.
265. Lauterborn, W. and H. Bolle, *Experimental investigations of cavitation-bubble collapse in the neighbourhood of a solid boundary*. Journal of Fluid Mechanics, 1975. **72**(2): p. 391-399.
266. Hindmarsh, J.P., A.B. Russell, and X.D. Chen, *Experimental and numerical analysis of the temperature transition of a suspended freezing water droplet*. International Journal of Heat and Mass Transfer, 2003. **46**(7): p. 1199-1213.
267. Gent, R., N. Dart, and J. Cansdale, *Aircraft icing*. Philosophical Transactions of the Royal Society of London A: Mathematical, Physical and Engineering Sciences, 2000. **358**(1776): p. 2873-2911.
268. Zerr, R.J., *Freezing rain: An observational and theoretical study*. Journal of Applied Meteorology, 1997. **36**(12): p. 1647-1661.
269. Pearce, R.S., *Plant freezing and damage*. Annals of Botany, 2001. **87**(4): p. 417-424.
270. Kousksou, T., et al., *Crystallisation kinetics with nucleation phenomenon: Ice slurry system*. International Journal of Refrigeration, 2012. **35**(7): p. 1921-1930.
271. Egolf, P.W., et al., *Cold storage with ice slurries*. INTERNATIONAL JOURNAL OF ENERGY RESEARCH, 2008. **32**: p. 187-203.
272. Zhang, C., et al., *Influence of Characteristics and Roughness of Nucleation in Conical Pits on Surface Heterogeneous Nucleation*. Procedia Engineering, 2015. **121**: p. 1281-1288.

273. Vali, G., *Freezing Rate Due to Heterogeneous Nucleation*. Journal of the Atmospheric Sciences, 1994. **51**(13): p. 1843-1856.
274. Rosinski, J., B. Kopcewicz, and N. Sandoval, *Heterogeneous nucleation of ice at the liquid-liquid interface*. Journal of Aerosol Science, 1990. **21**(1): p. 87-96.
275. Okawa, S., A. Saito, and T. Matsui, *Nucleation of supercooled water on solid surfaces*. International Journal of Refrigeration, 2006. **29**(1): p. 134-141.
276. Niedermeier, D., et al., *Heterogeneous ice nucleation: exploring the transition from stochastic to singular freezing behavior*. Atmos. Chem. Phys., 2011. **11**(16): p. 8767-8775.
277. Fitzner, M., et al., *The Many Faces of Heterogeneous Ice Nucleation: Interplay Between Surface Morphology and Hydrophobicity*. Journal of the American Chemical Society, 2015. **137**(42): p. 13658-13669.
278. Voller, V.R. and C. Prakash, *A fixed grid numerical modelling methodology for convection-diffusion mushy region phase-change problems*. International Journal of Heat and Mass Transfer, 1987. **30**(8): p. 1709-1719.
279. Bourdillon, A.C., P.G. Verdin, and C.P. Thompson, *Numerical simulations of water freezing processes in cavities and cylindrical enclosures*. Applied Thermal Engineering, 2015. **75**: p. 839-855.
280. Chaudhary, G. and R. Li, *Freezing of water droplets on solid surfaces: An experimental and numerical study*. Experimental Thermal and Fluid Science, 2014. **57**: p. 86-93.
281. Tobo, Y., *An improved approach for measuring immersion freezing in large droplets over a wide temperature range*. Scientific Reports, 2016. **6**: p. 32930.
282. Li, Q., et al., *Lattice Boltzmann modeling of boiling heat transfer: The boiling curve and the effects of wettability*. International Journal of Heat and Mass Transfer, 2015. **85**: p. 787-796.
283. Li, Q., P. Zhou, and H.J. Yan, *Pinning–Depinning Mechanism of the Contact Line during Evaporation on Chemically Patterned Surfaces: A Lattice Boltzmann Study*. Langmuir, 2016. **32**(37): p. 9389-9396.
284. Hu, A., R. Uddin, and D. Liu, *Discrete methods of the energy equations in the pseudo-potential lattice Boltzmann model based simulations*. Computers & Fluids, 2019. **179**: p. 645-654.

285. Li, Q. and K.H. Luo, *Effect of the forcing term in the pseudopotential lattice Boltzmann modeling of thermal flows*. Physical Review E, 2014. **89**(5): p. 053022.
286. Gong, S. and P. Cheng, *A lattice Boltzmann method for simulation of liquid–vapor phase-change heat transfer*. International Journal of Heat and Mass Transfer, 2012. **55**(17): p. 4923-4927.
287. Chen, X., *Simulation of 2D cavitation bubble growth under shear flow by lattice Boltzmann model*. Communications in Computational Physics, 2010. **7**(1): p. 212.
288. Mishra, S.K., et al., *Modeling the coupling of reaction kinetics and hydrodynamics in a collapsing cavity*. Ultrasonics Sonochemistry, 2010. **17**(1): p. 258-265.
289. Gai, S., et al., *Effect of ultrasonic vibration on the nucleation onset of temperature of micro-sized water droplets*, in *Chemeca 2018*. 2018: Queenstown, NZ. p. 234.
290. Yuan, P. and L. Schaefer, *Equations of state in a lattice Boltzmann model*. Physics of Fluids, 2006. **18**(4): p. 042101.
291. Fletcher, N.H., *Other forms of ice*, in *The Chemical Physics of Ice*, N.H. Fletcher, Editor. 1970, Cambridge University Press: Cambridge. p. 49-72.
292. Flannigan, D.J., et al., *Measurement of Pressure and Density Inside a Single Sonoluminescing Bubble*. Physical Review Letters, 2006. **96**(20): p. 204301.
293. Jarman, P., *Measurements of Sonoluminescence from Pure Liquids and some Aqueous Solutions*. Proceedings of the Physical Society, 1959. **73**(4): p. 628-640.
294. Nozaki, K., S.-i. Hatanaka, and S. Hayashi, *Dynamics of single sonoluminescing bubble in concentrated aqueous alkaline halide solutions*. Japanese journal of applied physics, 2004. **43**(9R): p. 6481.
295. Dean, J.A., *Lange's handbook of chemistry*. Vol. 15. 1992: McGraw-Hill New York.
296. Obreschkow, D., et al., *Cavitation Bubble Dynamics inside Liquid Drops in Microgravity*. Physical Review Letters, 2006. **97**(9): p. 094502.
297. Kamaev, P.P., et al., *Quantification of Optison bubble size and lifetime during sonication dominant role of secondary cavitation bubbles causing acoustic bioeffects*. The Journal of the Acoustical Society of America, 2004. **115**(4): p. 1818-1825.
298. Liu, H. and Y. Zhang, *Droplet formation in a T-shaped microfluidic junction*. Journal of Applied Physics, 2009. **106**(3): p. 034906.

299. Wang, X., et al., *Pressure drop-based determination of dynamic interfacial tension of droplet generation process in T-junction microchannel*. *Microfluidics and Nanofluidics*, 2015. **18**(3): p. 503-512.
300. Atchley, A.A. and A. Prosperetti, *The crevice model of bubble nucleation*. *The Journal of the Acoustical Society of America*, 1989. **86**(3): p. 1065-1084.

Appendix A: Experimental set-up for recalescence stage analysis

The schematic of the experimental setup for the recalescence stage analysis is shown in Figure A1. A semiconductor cooling module (MULTICOMP Peltier Element) was used to maintain a constant low temperature. The temperature to which the cooling module is set, or the cooling module surface temperature, is denoted by T_{cp} . A capillary glass tube (length: 300 mm), the bottom of which was sealed with an ultrathin plastic film (100 μm), was placed vertically on top of the cooling module surface. Two tubes with the inner diameter (d_t) of 0.4 mm and 1.2 mm were used. The gap between the capillary tube and the cooling module was filled up with the thermal-paste to reduce the contact thermal resistance. In each experiment, Q-water (from Milli-Q integrate water purification system) was sandwiched between two layers of the fluorocarbon oil to prevent contamination to the water. Once nucleation starts, the appearance changes of water in the recalescence stage (i.e. from transparent to opaque) and the subsequent evolution of ice-water interface in the freezing stage were captured using a high-speed camera (PIXELINK, Canada, up to 4000 fps). A K-type thermocouple (application range: 233 K – 1023 K) with the 0.5 mm probe was used to measure the local sample temperature in the 1.2 mm capillary tube. Another K-type thermocouple (application range: 198 K – 523 K) was used for monitoring the temperature of the cooling module surface. The thermocouples were calibrated in a water-bath using a mercury thermometer as the reference. Due to the low operating temperature, frost is constantly observed on the cold surface of the capillary tube, which obstructs the camera vision and undermines the image quality. In this study, the capillary tube and the cooling module are enclosed by a transparent glass cover. Prior to experiments, nitrogen is purged into the enclosure to

expel the humid air, thus ensuring the entire process can be viewed even at ultralow temperatures, and the freezing process occurs in a stable environment.

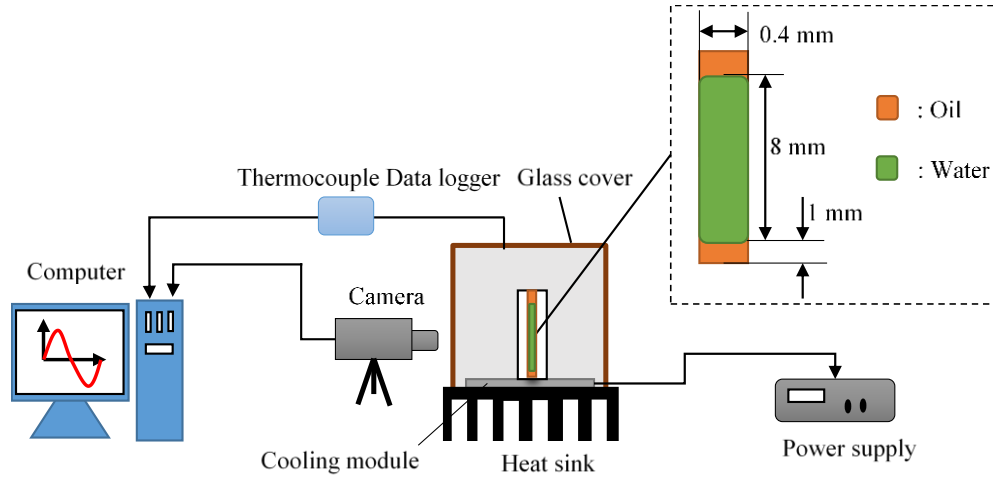


Figure A1. Schematic of the experimental set-up.

The core of this experiment is the observation of the recalescence stage in the freezing process, which the freezing rate closely hinges on the local supercooling degree. Hence, a large supercooling degree is required for investigating the effect of the supercooling degree on the freezing rate. To obtain a large supercooling degree, the water needs to be ultra-pure. In this study, a water sample from Milli-Q integrate water purification system was adopted. The resistivity of Milli-Q water can reach as high as $18.2 \text{ M}\Omega \cdot \text{cm}$. During the experiment, the Milli-Q water sample was placed in-between two layers of Fluoridrop 7500 liquid to maintain the high quality.

The room temperature (T_0) was kept constant at 293 K to maintain the heat transfer consistency between the system and the ambient. The other operating parameters are listed in Table A1. The cooling fan of the heat sink was powered on prior to switching on the cooling module to protect the cooling module from overheating. As soon as the

cooling module surface temperature reached 253 K, the high-speed camera was turned on to start recording the freezing process of the supercooled water. Each experiment was repeated for at least 3 times to minimise the operation error and also cancel out errors induced by the instabilities of the measuring equipment. In-between two experiments, a waiting time of 20 minutes is set to ensure the initial temperature of the system is close to the room temperature.

Table A1. Operation parameters.

Parameter	Value	Unit
Initial temperature (T_0)	293	K
Cooling module temperature (T_{cp})	223 – 240	K
Thermal conductivity (λ):		
Water ^b	0.598	W/(m·K)
Oil ^{b, c}	0.065	W/(m·K)
Capillary tube wall	1.2	W/(m·K)
Specific heat (c):		
Water ^b	4.157	kJ/(kg·K)
Oil ^{b, c}	1.128	kJ/(kg·K)

^a See more details in the following section.

^b Temperature-dependent parameter; the value at 293 K was shown and chosen as the initial value.

^c Fluoridrop 7500.